EVOLUTION OF PROTOPLANETARY DUST-DISK SIZES

by

Nathanial Hendler

A Dissertation Submitted to the Faculty of the

DEPARTMENT OF PLANETARY SCIENCES

In Partial Fulfillment of the Requirements
For the Degree of

DOCTOR OF PHILOSOPHY

In the Graduate College

THE UNIVERSITY OF ARIZONA

THE UNIVERSITY OF ARIZONA
GRADUATE COLLEGE

As members of the Dissertation Committee, we certify that we have read the dissertation prepared by Nathanial Phillip Hendler
entitled Evolution of Protoplanetary Dust-Disk Sizes
and recommend that it be accepted as fulfilling the dissertation requirement for the Degree of Doctor of Philosophy.

Renu Malhotra — Date: 20 May 2020

Isamu Matsuyama — Date: 20 May 2020

Ilaria Pascucci — Date: 20 May 2020

Paola Pinilla — Date: 20 May 2020

Andrew Youdin — Date: 20 May 2020

Final approval and acceptance of this dissertation is contingent upon the candidate's submission of the final copies of the dissertation to the Graduate College.
I hereby certify that I have read this dissertation prepared under my direction and recommend that it be accepted as fulfilling the dissertation requirement.

Dissertation Director: Ilaria Pascucci — Date: 20 May 2020

ACKNOWLEDGEMENTS

As an undergraduate at the University of Arizona, I began working with Ilaria Pascucci as a research assistant. Without her influence and encouragement, I would not have become a graduate student much less written this dissertation. Thank you Ilaria for everything. Working with you as been one of the most rewarding things I have ever done. I truly can not overstate the metamorphic influence you've had on me. I am so lucky to have been exposed to your scientific verve. I look forward to watching you continue to explore the science of protoplanetary disks (and even exo-planets I guess). I hope that someday I will be able to contribute to your work again.

The path I have taken to complete this dissertation is unique to me, and could not have been accomplished without the influence and aid of many people. Some of these people were mentors and teachers, while others held important roles of encouragement and/or distraction.

I owe a debt of gratitude to Pima Community College which allowed me to explore my interests and develop my academic footing while working full time. Without a public community college, I would not have been able to begin this journey. In particular I would like to acknowledge and thank Anthony Pitucco.

As an undergraduate in the Geosciences department of the University of Arizona, there were three professors that opened my eyes to both research and science: Jay Quade, George Gherels and George Davis. Dr. Gherels gave me my first opportunity to perform research, which I found wildly rewarding. Dr. Quade and Dr. Davis both acted as mentors and teachers to me and gave me opportunities to really sink my teeth into scientific studies for the first time.

At LPL, there are many people to thank and acknowledge. I would like to thank Mary Guerrieri, Bertha Orosco and Maria Schuchardt for always being there for me. I would like to thank Tom Zega and Renu Malhotra both for inspiring me as an undergrad and graduate student. I would like to thank Alessondra Springmann for being a great office mate and friend who was there with humor and good advice when I needed it. Thanks to Andrea Banzatti for our lunches and so much more.

I would like to thank and acknowledge my entire committee, Ilaria Pascucci, Renu Malhotra, Isamu Matsuyama, Paola Pinilla and Andrew Youdin, all of whom have impacted my career as a graduate student beyond their participation as committee members. The diversity of their approaches and styles for problem solving has served me well, and I certainly strive to emulate different aspects of each. Collaborations with Renu Malhotra and Paola Pinilla resulted in significant positive impacts on my development as a scientist and I consider them to both be important mentors.

There's no easy way to enumerate the reasons for thanking some people. Thanks

to my mom and dad. Thank you Tracy, I suspect you don't really know how important you have been. Thank you Hamish. Thank you Tim Smith and Kojo Plange. Thank you Dragoon. Thank you Tucson.

More than anyone else, one person in the world has encouraged, supported and challenged me to do this thing that I wanted. There's zero chance that this dissertation would have happened without Sarah Meadows.

Thanks again to everyone. It's been lots of fun and lots of pain. Consider this an official declaration that "I owe you one", and once this pandemic is over, I'll buy a round.

DEDICATION

Dedicated to Augusta Meadows.

TABLE OF CONTENTS

TABLE OF CONTENTS – *Continued*

LIST OF FIGURES

LIST OF FIGURES – *Continued*

LIST OF FIGURES – *Continued*

LIST OF FIGURES – *Continued*

LIST OF FIGURES – *Continued*

LIST OF FIGURES – *Continued*

LIST OF TABLES

ABSTRACT

The planets of our Solar System formed within a disk of dust and gas 4.5 billion years ago. While the Solar System's primordial protoplanetary disk is now gone, we can begin to understand its possible properties by looking out to the disks within nearby star-forming regions. To understand planet formation, dust observations are used to constrain the mechanics and evolution of planet formation. The properties of disks around brown dwarfs and very-low mass stars (hereafter VLMOs) provide important boundary conditions on the process of planet formation and inform us about the numbers and masses of planets than can form in this regime. Radiative transfer models are fit to the spectral energy distributions of 11 VLMOs with known disks and find that these VLMOs do not follow previously derived disk temperature-stellar luminosity relationships if the disk outer radius scales with stellar mass. The 3 mm continuum observation of the highly inclined transition disk around the star T Cha reveals multiple dust structures: an inner disk, a spatially resolved dust gap, and an outer ring. When compared with previously published 1.6μm VLT/SPHERE imagery, it is found that the location of the outer ring is wavelength dependent. More specifically, the peak emission of the 3 mm ring is at a larger radial distance than that of the 1.6 μm ring, suggesting that millimeter-sized grains in the outer disk are located further away from the central star than micron-sized grains. The most likely origin of the dust gap is from an embedded planet or planets. The dust disk size of 152 protoplanetary disks is estimated from archival ALMA observations. This sample is combined with 47 disks from Tau/Aur and Oph whose dust disk radii were estimated, as here, through fitting radial profile models to visibility data. These 199 homogeneously derived disk sizes are used to identify empirical disk-disk and disk-host property relations as well as to search for evolutionary trends. In agreement with previous studies, we find that dust disk sizes and millimeter luminosities are

correlated, but show for the first time that the relationship is not universal between regions. We find that disks in the 2-3 Myr-old are not smaller than disks in other regions of similar age, and confirm the Barenfeld et al. (2017) finding that the 5-10 Myr USco disks are smaller than disks belonging to younger regions. Finally, we find that the outer edge of the Solar System, as defined by the Kuiper Belt, is consistent with a population of dust disk sizes which have not experienced significant truncation.

CHAPTER 1

Introduction

1.1 Protoplanetary Disks

Understanding the origins of the Earth has been held in common as a pursuit by humans going back to at least the beginning of recorded history. The field of astronomy has revealed the Earth's place in the universe, while the field of geology has given scientists the ability to unearth much of the early Earth's history. But, if we are to learn of the formation of the Earth, we must first understand the formation of the Solar System, and to do that, we look to the newly forming nearby stars and the disks of circumstellar dust and gas that surround them for answers.

Star formation begins with the collapse of a molecular cloud of dust and gas. Whatever small amounts of angular momentum are contained within the cloud are conserved, and as the cloud collapses, the angular velocity increases. Consequently, radial infall of material towards the forming star is slowed, and a disk of dust and gas forms around the young protostar (e.g. Terebey et al., 1984).

Making up only a small fraction of the system's total mass, the gas and dust found in protoplanetary disks define the environment and materials of planet formation. While the disk has as much as 100 times more gas than dust, it is the thermal emission of the dust – in excess beyond the blackbody emission of the host star – at IR and longer wavelengths that is responsible for the discovery and identification of these disks.

Dust grains, assumed to be in thermal equilibrium, absorb light from their host protostar and re-radiate it at longer wavelengths back into the disk, or out into space. Grains of sizes ranging from sub-micron to centimeter can be observed, with the wavelength at which they most efficiently emit corresponding approximately to the grain's size (e.g. Evans, 1994). This fact, combined with the effects of optical

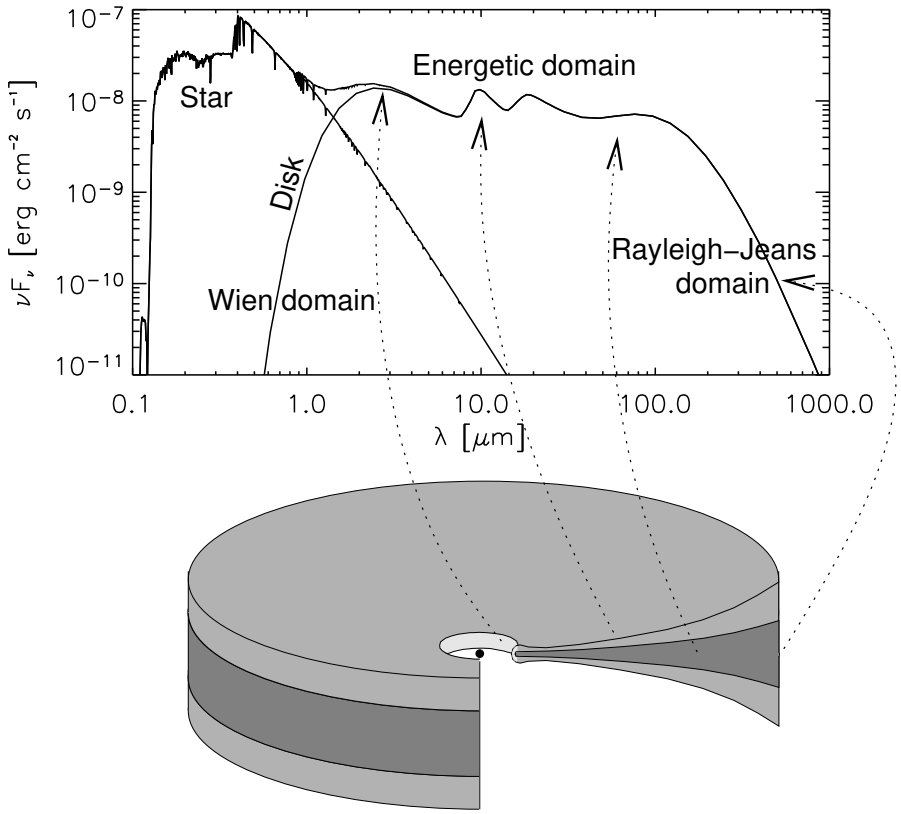

Figure 1.1 A spectral energy diagram (SED) and schematic of a protoplanetary disk. In this figure from Dullemond et al. (2007) we see within the SED the thermal excess emission emitted by the dust. The corresponding regions of the physical disk are connected to the SED with arrows, underscoring the dependence on wavelength for probing different regions of the disk.

depth and variations in the disk's temperature profile (in both the axial and vertical directions) dictates that observations at different wavelengths must probe different regions and dust-size populations of the disk. This is shown in schematically in Figure 1.1. Typically, the observed near-infrared emission originates from small grains near the surface of the inner disk while progressively longer wavelengths probe progressively colder and larger grains at larger disk radii with millimeter observations ultimately probing the largest observable grains near the midplane.

By collecting the photometric observations of a single disk at many wavelengths, spectral energy distributions (SEDs) can be constructed (see Figure 1.1). The mor-

phology of SEDs have been generalized into an empirical classification scheme that has been taken to reflect the formation and evolution of the star and disk system. The Lada Sequence defines Class 0 (embedded core), Class I (protoplanetary disk and envelope), Class II (protoplanetary disk), Class III (debris disk) Lada and Wilking (1984); Lada (1987).

The SEDs of Class I and Class II systems both contain excess continuum emission in the near-infrared. By examining the fraction of these systems in nearby low-mass star-forming regions (e.g. Taurus, Chamaeleon), the lifetime of a typical protoplanetary disk – defined as the time it takes for 50% of the stars within a region to not have a disk detected at IR wavelengths – has been estimated to be 3-6 Myrs (Ribas et al., 2014). This assumes that a single evolutionary course from Class 0 to Class III is taken by all systems. Additionally, extrinsic disk properties such as inclination can impact the Class assigned to a system, for example, an edge-on Class I system may appear to be Class 0.

While SEDs contain information regarding the structure, composition and viewing geometry of disks, the recent advent of observatories with higher sensitivities and spatial resolution has allowed us to better consider the evolution of disk properties (e.g. dust disk mass and disk outer radius). Interferometers, such as the Submillimeter Array (SMA) and in particular the Atacama Large Millimeter/submillimeter Array (ALMA) have provided the spatial resolution needed to resolve protoplanetary disks. Perhaps more importantly, ALMA's high sensitivity has made possible the observations of the many disks necessary to complete demographic surveys of individual star-forming regions (e.g. Ansdell et al., 2016; Pascucci et al., 2016; Barenfeld et al., 2016). VLT/SPHERE and Gemini/GPI, using adaptive optics, detect the spatial distribution of the smallest (micron-sized) grains. These small grains, observed in scattered light, are well coupled to the gas and reveal the dust at large scale heights within the flared disk. Alternatively, observations in the sub-mm/mm regime made by facilities like SMA and ALMA probe the majority of the disk's dust mass and the larger dust grains which have settled to the midplane (the assumed location of planet formation within the disk) in the outer parts of the disk.

Characterized by T Tauri stars and a dearth of massive stars, nearby low-mass star-forming regions provide a laboratory of stars with (and without) disks for scientific study. These regions are critically important to this thesis for three reasons in particular. The first is that the regions are close enough to the Solar System (approximately 100-200 pc) that many of the disks can be spatially resolved. This makes it possible to examine the distribution of dust, and of particular importance to this work: measure the dust outer radius for many of the disks. Secondly, each region provides a significant population of young stars with which to study the demographics of disk evolution and planet formation. We can look for trends of the disk properties within each region, and also compare trends between regions, in order to better understand which properties of these systems may be universal, and which may be a function of initial conditions for example. Lastly, there exists a spread in the ages of the regions. While the uncertainties in the ages of the individual disks are large, the age of each star forming region is determined by hundreds of stars, resulting in reliable relative ages between regions (see Soderblom et al., 2014). Because there are regions representing young (1-3 Myr) and old (5-10 Myr) regions, as well as regions with overlapping ages, the evolution of disks through time can be examined. For this work there are 5 low-mass star-forming regions which are relevant. Presented in order of age, they are: Ophiuchus ($\sim$1-2 Myr), the Taurus & Auriga Complex ($\sim$1-3 Myr), Lupus ($\sim$1-3 Myr), Chamaeleon I ($\sim$2-3 Myr), and the Upper Scorpius OB association ($\sim$5-11 Myr).

The sensitivity and resolution of the ALMA interferometer has revolutionized the field of protoplanetary disk observing. Figure 1.2 shows disks observed by ALMA bearing gaps, rings, spirals and asymmetries. However, most protoplanetary disks have not been observed at the sensitivity and spatial scales required to resolve these structures. While the detection and location of sub-structures for the majority of disks may not be know, ALMA has performed several surveys of different low-mass star-forming regions (e.g. Lupus, Ansdell et al. (2016); ChaI, Pascucci et al. (2016); USco, Barenfeld et al. (2016)) at spatial scales and sensitivities sufficient for determining the location of the disk's outer-dust radius. While not all disks share

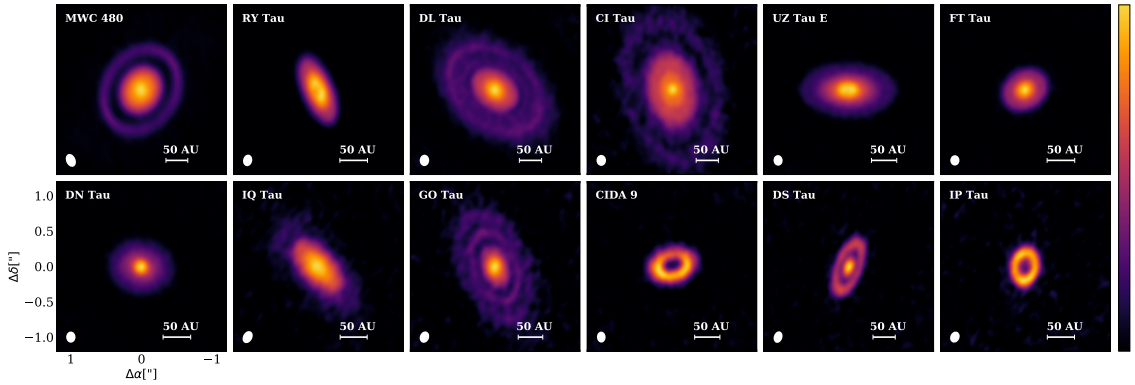

Figure 1.2 1.33 mm continuum emission images of disks from the Taurus star forming region highlighting a diversity of substructures. Long et al. (2018).

each structure (gaps, spirals, etc), at the very least, each resolved disk has an outer radius, making this feature an obvious common denominator to use when comparing disks.

1.2 Modeling and Methods

This thesis uses two different methods of estimating the basic disk properties (such as dust disk mass and the location of the dust outer radius) of observed disks. In both cases, model disks are constructed, and then compared against the observed data to determine that model's likelihood.

Radiative transfer modeling includes many of the intrinsic physical properties (e.g. grain size distributions, density structure, grain opacity) and extrinsic properties (e.g. disk inclination, position angle) of a disk in order to numerically simulate radiative transfer through the disk. With Monte Carlo radiative transfer, photon packages emanating from the central star propagate through the disk. Probabilities determine if the simulated photos interact (via scattering or absorption) with the modeled dust and gas. This process results in many valuable outputs, such as disk temperatures, optical depth at different wavelengths, multi-wavelength images and SEDs. The last two, images and SEDs can be compared directly against observations in order to understand the most probable conditions of the observed disks.

In the second chapter of this thesis, the 2D Monte Carlo radiative transfer code `MCMax` (Min et al., 2009) is used. This code iteratively solves the vertical hydrostatic equilibrium of the disk, includes dust settling and viscous heating.

While radiative transfer models numerically solve for many of the physics that are relevant to disks, and the results include many disk properties of interest, the approach is computationally expensive.

If we are interested in measuring the structures observed within the dust disk (e.g. the dust outer radius, or location of a ring's inner edge), we can turn to visibility fitting if we have observations of sufficient spatial resolution and sensitivity. In visibility fitting, a model of the sky brightness is compared with interferometric visibilities.

The fundamental observable of an interferometer (like ALMA), visibilities are complex quantities measuring the amplitude and phase of interference between two antennas. Consequently, visibilities are measurements of the 2D Fourier transform of the observed sky brightness.

Figure 1.3 shows the visibility plots of two different disks. Observations that are unresolved (point sources) appear as flat lines in real amplitude vs uv-distance plots (as shown in the left panel of Figure 1.3). For resolved sources, real amplitude varies with uv-distance, and the shape of this function is determined by the resolved structure of the source. For example, looking at the resolved example in the right panel of Figure 1.3, it is possible to tell that this source has one large ring because the amplitude falls to zero, goes below, and then rises once again to positive values. Disks with multiple rings will do this multiple times, while full disks will fall to zero as the uv-distance increases. For observations of objects that are centered and axisymmetric, the imaginary value of the amplitude will be uniformly zero across uv-distance. Deviations of the imaginary value from zero indicate asymmetries within the field of view.

In this work, axis-symmetric radial intensity profiles are created to model sky brightness which are then compared against observations using the visibility fitting code `Galario` (Tazzari et al., 2017).

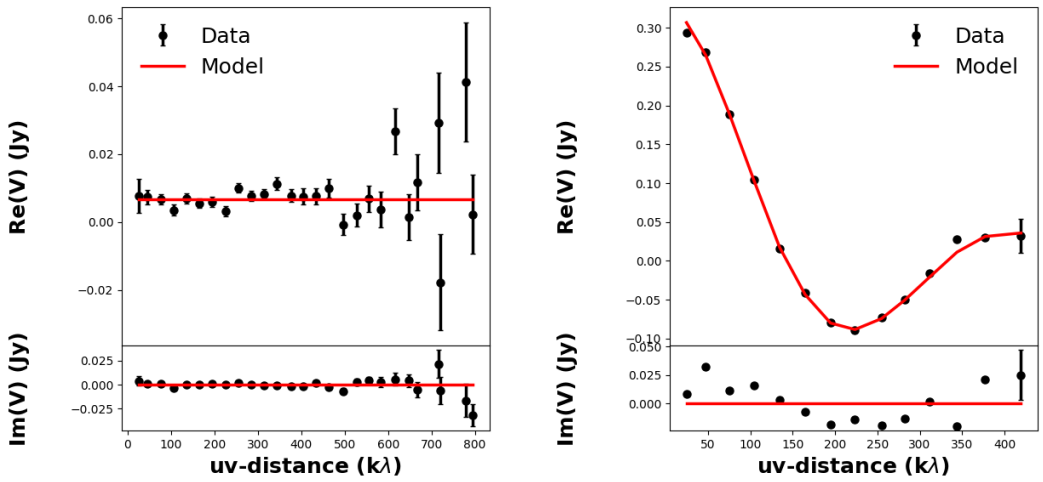

Figure 1.3 Each plot shows the real (Re) and imaginary (Im) components of amplitude. On the left, because the real component of the amplitude stays constant with uv-distance, we can tell that this source is unresolved. Resolved sources have a real amplitude that varies with uv-distance. An example of a resolved source is shown on the right.

This approach of fitting visibilities with a radial intensity profile makes as few assumptions as possible about disk properties to measure the dust outer radius (a disk parameter that is fundamentally measurable unlike disk mass for example).

This approach of measuring the dust outer radius (a disk parameter that is fundamentally measurable, unlike disk mass for example) by fitting visibilities with a radial intensity profile makes few assumptions about disk properties. Previous attempts to study this parameter have used physical models which require assumptions about surface density profiles and, vertical structure (e.g. Barenfeld et al., 2017; Tazzari et al., 2017) that are not necessary with radial profile visibility fitting.

1.3 Summary: Thesis Outline

In this thesis, disk modeling is performed, and compared to observations, in order to better understand the properties of protoplanetary disks.

In Chapter 2, continuum and [OI] 63 μm line emission observations of disks around 11 brown dwarfs and very low mass stars are used to investigate the prop-

erties of disks in the low-mass regime of planet formation. By measuring the line emission, and fitting grids of radiative transfer models to the SEDs of these disks within the Taurus and Chamaeleon I star-forming regions, we find:

- Disks around these sources are underluminous in [OI] 63 μm when compared to more massive T Tauri disks.
- We estimate that the dust disks of these sources have outer radii in the range of 1.3–78 au, with a median size of 4.2 au – much smaller than found around solar-mass stars.
- These disks are likely warmer than suggested by previously derived disk-temperature/stellar-luminosity relationships, resulting in lower disk mass estimates.
- We infer that the inner emission is compact (≤ 1 au in radius), the gap width is between 18-28 au, and the emission from the outer ring peaks at ~ 36 au. We compare our ALMA image with previously published 1.6μm

In Chapter 3, we compare 3mm and 1.6μm observations of the transition disk T Cha, i.e. a disk with a dust inner cavity based on SED modeling. Our 3mm ALMA continuum map reveals an inner disk (≤ 1 au in radius), a large gap (located from 18-28 au) and a dust ring (~ 36 au). Sky-brightness models fit to the ALMA visibilities allow us to estimate the location of the dust ring's peak emission along with its inner and outer edges. When compared with a previously published VLT/SPHERE 1.6μm image and model, we find the 3mm ring to be located farther from the central star than the 1.6μm ring. This, along with the observed inner disk, suggests that the gap in T Cha is a result of planet-disk interactions.

Previous works have measured the dust-disk sizes for disks within individual star-forming regions. Because these regions represent different ages and cluster formation environments, comparisons between these different works were quickly made in order to determine if evolutionary trends can be seen in the data. However,

these comparisons stand on shaky ground because the sizes for each region are based on differing assumptions and modeling techniques.

It is the goal of Chapter 4 to estimate the dust-disk sizes in a homogeneous way so that disk-disk and disk-star trends can be searched for and compared across star-forming regions. This is accomplished by estimating the sizes of disks from ALMA observations of sources within the regions of Lupus, Chamaeleon I and Upper Scorpius OB using the same radial profile modeling and visibility fitting approach as Tripathi et al. (2017a) used for their disk size estimates of disks within Ophiuchusand Taurus & Auriga Complex.

In agreement with previous results, we confirm that disk radii are correlated with millimeter luminosity, but find that the $\log R_{\rm eff} - \log L_{\rm mm}$ relation is not universal as suggested by Andrews et al. (2018b). The slope of this relationship becomes flatter for the older regions of Chamaeleon I and Upper Scorpius OB .

Additionally, we attempt to understand what is a *typical* protoplanetary disk size. We compare the Solar System's size with our sample of 1-3 Myr disks and conclude that the Solar System's size, if primordial in origin, is not an outlier.

CHAPTER 2

Hints for Small Disks around Very Low-Mass Stars and Brown Dwarfs

2.1 Introduction

Brown dwarfs are sub-stellar objects that represent the low-mass end of the star formation process. Similar to their stellar counterparts, T Tauri (TT) stars, young (1-2 Myr) brown dwarfs possess protoplanetary disks of dust and gas (e.g. Luhman et al., 2007) that are the environment of planet formation (e.g. Apai et al., 2005). Indeed, the recent discovery of the TRAPPIST-1 exoplanet system at the sub-stellar boundary (Gillon et al., 2016, 2017) suggest that brown dwarfs may be capable of forming planetary systems. Observing protoplanetary disks in this regime allows us to observe the lower-boundary conditions of planet formation.

The conditions in protoplanetary disks are strongly dependent on stellar mass. In particular, scaling laws have been identified between host star mass and protoplanetary dust disk mass (e.g. Pascucci et al., 2016). Planet formation models typically adopt these scaling laws to predict the planets that may form around low-mass stars (e.g. Raymond et al., 2007; Mordasini et al., 2012). However, disks around the lowest-mass stars may not be scaled down versions of their higher-mass counterparts. Disks around brown dwarfs show differences in their dust and gas evolution (Pascucci et al., 2009). There are also indications that disks around brown dwarfs have a different disk geometry (e.g. Szűcs et al., 2010; Daemgen et al., 2016), though this is not always found (Harvey et al., 2010; Mulders and Dominik, 2012).

Because brown dwarfs are significantly fainter than TT stars, only limited observations are present to directly constrain their dust masses (e.g. Mohanty et al., 2013; Pascucci et al., 2016, and references therein). Several studies have used Herschel far-infrared photometry (e.g. Harvey et al., 2012; van der Plas et al., 2016; Daemgen et al., 2016) and ALMA (e.g. van der Plas et al., 2016) to estimate dust masses.

Table 2.1. Source Properties

2MASS	Common Name	Region	SpTy	Ref.	A_v	log L_{bol} ($L_\odot$)	Ref.	T_{eff} (K)	M_* ($M_\odot$)
J04141760+2806096	CIDA-1	Taurus	M5	L17	4.6	-0.7	R10	3125	0.19
J04193545+2827218	FR Tau	Taurus	M5.25	L17	0.0	-0.9	R10	3090	0.14
J04233539+2503026	FU Tau A	Taurus	M7	L17	2.0	-0.72	L09	2880	0.16
J04295950+2433078	CFHT-20	Taurus	M5	L17	4.6	-0.7	R10	3125	0.19
J04381486+2611399	J04381486	Taurus	M7.25	L17	3.5	-2.3	R10	2846	0.05
J04382134+2609137	GM Tau	Taurus	M5	L17	2.0	-1.15[a]	H08	3125	0.14
J04393364+2359212	J04393364	Taurus	M5	L17	1.3	-1.0	R10	3125	0.18
J04394748+2601407	CFHT-4	Taurus	M7	L17	4.4	-1.0	R10	2880	0.11
J11062554–7633418	ESO Hα 559	Cha I	M5.25	L07	3.58[b]	-1.28	L07	3088	0.14
J11071668–7735532	Cha Hα 1	Cha I	M7.75	L07	0.0[b]	-1.82	L07	2765	0.04
J11105597–7645325	Hn 13	Cha I	M5.75	L07	2.91[b]	-0.89	L07	3021	0.14

Note. — A distance of 137 and 162 pc is assumed for the Taurus (R10) and Chamaeleon I sources (L07).

[a]GM Tau luminosity from D14

[b] L07 report the extinction at J band. From those values we computed the A_V in this table using the interstellar extinction law in Mathis (1990) and an Rv of 3.1.

References. — Davies et al. (2014) (D14); Herczeg and Hillenbrand (2008) (H08); Luhman et al. (2007) (L07); Luhman et al. (2009) (L09); Luhman et al. (2017) (L17); Rebull et al. (2010) (R10)

One parameter that has remained largely unexplored in these studies is the dust disk outer radius. From a theoretical perspective, disks around brown dwarfs are predicted to form with smaller gas disks (Bate, 2012) and experience more efficient radial drift leading to smaller dust disks (Pinilla et al., 2013). Observations with ALMA of a handful of spatially resolved brown dwarf dust and gas disks range in size from 20 au to 140 au (Ricci et al., 2013, 2014; Testi et al., 2016), smaller than TT disks (22–440 au with a mean size of 165 au) (Isella et al., 2009; Andrews et al., 2010; Guilloteau et al., 2011).

In this work, we explore the impact of smaller disk radii around brown dwarfs and very-low mass stars (hereafter VLMOs) on observables related to the dust and the gas in those disks. We present a Herschel survey of [OI] 63 μm for 11 VLMOs probing the disk gas in § 2.2 and § 2.3.1. Detailed thermo-chemical models of protoplanetary disks have shown that this transition can be used as an order of magnitude disk mass estimator (e.g. Woitke et al., 2010), hence a large survey toward T Tauri stars (Dent et al., 2013) was carried out. We perform radiative transfer modeling of the spectral energy distribution (SED) of these sources in § 2.3.2 starting from the zero-order assumption that the disk geometry and dust opacity are stellar-mass independent. We also run two radiative transfer grids with and without a stellar-mass dependent disk radius to quantify the difference in disk temperature in § 2.3.3. We examine the underluminosity of [OI] 63 μm in our VLMO disks in § 2.4.1, while in § 2.4.2 we compare the likelihoods of small and large disk models by testing model grids against the SEDs of our VLMO sample. We also show how smaller disk radii lead to higher disk temperatures than previously assumed and impacts estimates of the dust disk mass.

2.2 Observations and Data Reduction

2.2.1 Sample

Our sample comprises 11 very low-mass stars and brown dwarfs from two nearby star-forming regions, Taurus and Chamaeleon I ($d = 162$ pc, Luhman 2008). Because

we use stellar parameters from Rebull et al. (2010) for the majority of our Taurus sources, we adopt their distance of 137 pc for the Taurus star-forming region (Torres et al., 2007, 2009). Ten of the sources were selected by us and observed with the Herschel/PACS spectrograph as part of Proposal ID `OT2_ipascucc_2`, see § 3.2 for more details. CIDA-1 is the only other very low-mass star observed with the same setting (Proposal ID `OT1_ascholz_1`), hence we include it in our analysis.

We chose to focus on the Taurus and Chamaeleon I star-forming regions because the low-mass end of the stellar population is well characterized and, unlike ρ Oph, suffer from minimal contamination from extended cloud emission. In addition to being very low-mass stars/brown dwarfs, our targets were selected to posses a dust disk (based on infrared excess emission) and to have a flux density at 24 μm (F_{24}) greater than 50 mJy (Guieu et al., 2007; Luhman et al., 2008; Rebull et al., 2010). CIDA-1 also fits these criteria. The 24 μm flux limit was applied to ensure bright 70 μm fluxes (F_{70}), greater than $\sim$ 70 mJy, based on the empirical relation $\nu_{70}F_{70} \sim 0.5 \times \nu_{24}F_{24}$ from the VLMO disk sample of Harvey et al. (2012). Because of the known positive correlation between the far-infrared continuum and the [OI] 63 μm emission line (e.g. Howard et al., 2013; Keane et al., 2014), our target selection criteria were intended to maximize the detection of the [OI] forbidden line (see also § 3.2).

Table 2.1 provides the main properties of our targets. Spectral types are converted to effective temperatures for each object using the relationship given in Luhman et al. (2003). Because this relationship deviates from linearity between spectral types M6 and M9, quadratic interpolation was used to estimate temperatures for non-integer spectral types. Stellar masses were computed by comparing each source position in the Hertzsprung-Russell diagram to the Baraffe et al. (1998) evolutionary tracks. While this is a standard approach and the only one available for our sample, one should keep in mind that model-inferred masses have large uncertainties of 50-100% below 1 $M_{\odot}$ as demonstrated by Stassun et al. (2014) using a sample of eclipsing binary systems.

Two of our sources, FU Tau and Hn 13, are multiple. FU Tau has an M9.25

companion at a separation of 5.″7, and may have an additional spectroscopic binary companion (Luhman et al., 2009). Hn 13 has a 0.″13 near-equal mass companion (imaged by Ahmic et al. (2007)).

2.2.2 Herschel/PACS Spectroscopy

Our sample was observed in February and March 2013 with the ESA *Herschel Space Observatory* (Pilbratt et al., 2010) Spectrograph (PACS; Poglitsch et al., 2010) which provides an IFU with a 5×5 array of spaxels, each with a pixel size of 9.″4. The sources were observed under two different programs (`OT2_ipascucc_2` 10 sources and `OT1_ascholz_1` for CIDA-1). Both programs used the standard point-source spectroscopy line scan mode with chop/nod, the chopper throw set to small and the standard faint line mode selected (high grating sampling density). Spectra were centered on the [OI] 63 μm line and covered from 62.93 to 63.43 μm. The red channel observations were a bonus and covered from 188.77 to 190.35 μm.

We set the exposure times for the ten `OT2_ ipascucc_2` sources by extrapolating the 63 μm continuum-line relationship from Howard et al. (2013) down to a minimum flux density of 70 mJy (see § 2.2.1) and found a corresponding [OI] 63 μm line flux of $4{\times}10^{-18}$ W/m^2. The exposure time was set to 16,420 seconds to achieve a 3σ detection on this line, i.e. a sensitivity of $1.4{\times}10^{-18}$ W/m^2, about three times better than that achieved for TT stars with the GASPS survey (Dent et al., 2013). CIDA-1, the brightest source in our sample and observed under `OT1_ascholz_1`, has a shorter exposure time of 9,868 seconds. The particulars of the observations including the *Herschel* observation identification numbers (ObsIDs) are listed in Table 2.2.

The data were reduced from level 0 using the *Herschel* Interactive Processing Environment (HIPE; Ott, 2010) version 14.0.1 with calibration set product 72. Because the targets are all faint point-sources, the "ChopNodBackgroundNormalization" (version 1.38.4.3) pipeline script was used for reduction. This pipeline flags bad data (e.g. mechanism movements, saturation, overly-noisy or bad pixels), applies signal corrections (e.g. non-linearities, crosstalk, transients, capacitance ratios), performs wavelength and flux calibration, and corrects data for spacecraft velocity. For

Table 2.2. Herschel/PACS Sample and Observations

Target Name	ObsID	Obs Date	Duration (s)
CIDA-1	1342268646	2013-03-25	9868.0
FR Tau	1342263516	2013-02-12	16420.0
FU Tau A	1342264241	2013-02-25	16420.0
CFHT-20	1342265469	2013-02-16	16420.0
J04381486	1342265470	2013-02-16	16420.0
GM Tau	1342264239	2013-02-25	16420.0
J04393364	1342263934	2013-02-19	16420.0
CFHT-4	1342264240	2013-02-25	16420.0
ESO Hα 559	1342263489	2013-02-11	16420.0
Cha Hα 1	1342263459	2013-02-10	16420.0
Hn 13	1342263492	2013-02-11	16420.0

the final cube rebinning, the wavelength grid was sampled using `oversample=2` and `upsample=4`. Proper flatfielding was verified interactively from within HIPE for each target.

Because telescope jitter and pointing errors can result in flux beyond the central spaxel, the appropriate spectra output from the task `extractCentralSpectrum` must be chosen as described in the *PACS Data Reduction Guide: Spectroscopy* (section 8.4.1). The central spaxel with the application of the c1-to-total point-source correction was used to extract the final spectrum. To further test this choice the spectra of neighboring spaxels were examined for extended emission using the "comboplot" output. All neighboring spaxels were confirmed to have no signal above the rms. For all of our sources the central spaxel (`c1`) spectra had the best SNR and a signal that was comparable to those extracted from the 3x3 corrected spectra. The absolute flux calibration uncertainty for the PACS spectrograph at $\sim$63 μm is estimated to be 10% (PACS Observer Manual; HERSCHEL-HSC-DOC-0832, Version 2.5.1). The final spectra for all of our targets are shown in Figure 2.1.

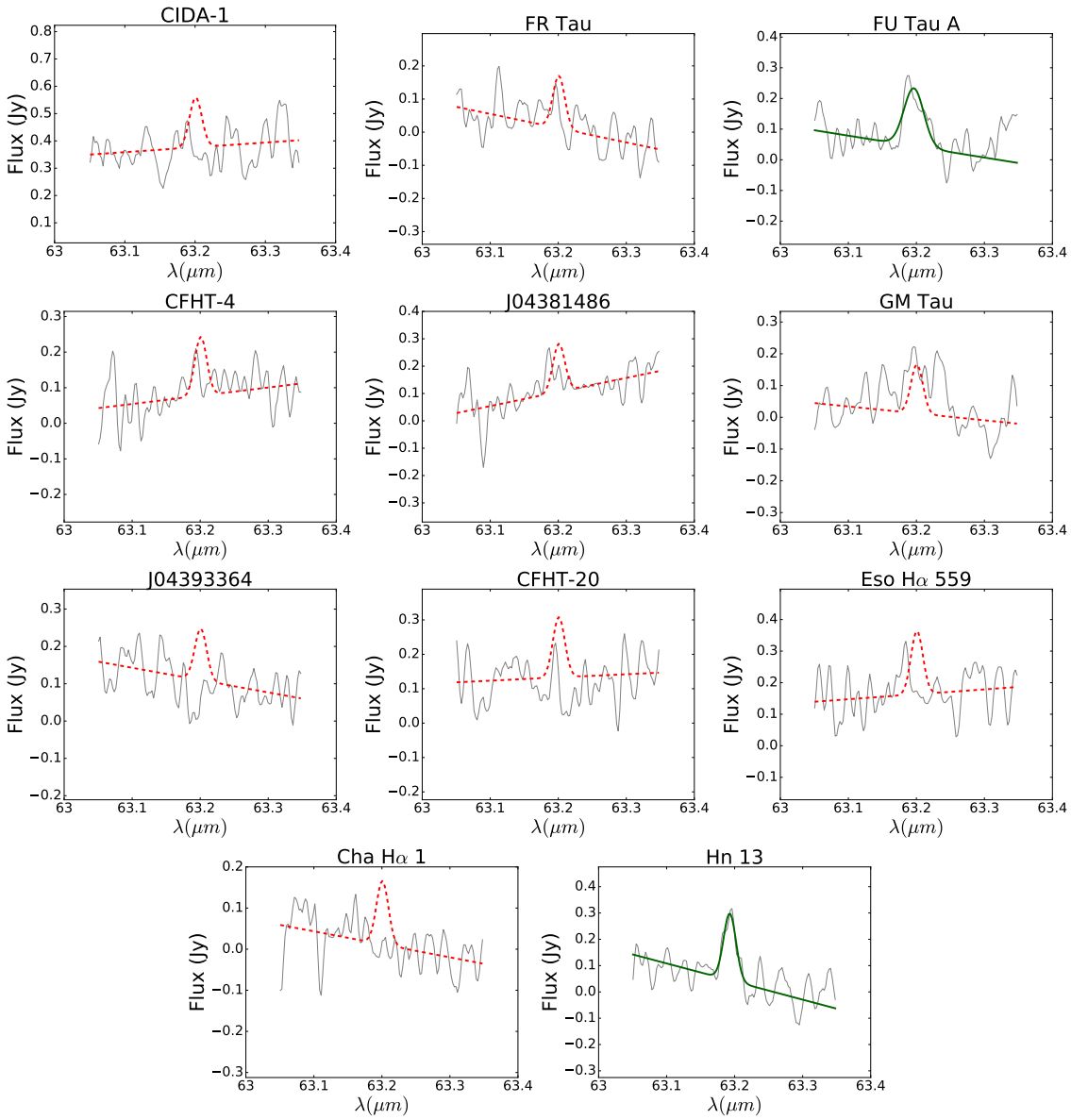

Figure 2.1 Herschel/PACS spectroscopy measurements of the wavelength region around the [OI] 63 μm emission line (solid gray line). Greater than 3σ Gaussian fits (detections) are overplotted as solid green lines. Hypothetical 3σ upper limits (FWHM of unresolved line) are shown as red dashed lines.

2.3 Analysis

Our analysis is separated into 3 sub-sections. In § 2.3.1 we present our findings for the 63 μm [OI] line emission and continuum, and 189 μm continuum for 11 *Herschel Space Observatory* observations. The [OI] 63 μm emission informs us about the gas content, especially in the disk atmosphere (e.g. Woitke et al., 2010), while the continuum emission about the dust in the disk.

This is followed by two separate sets of radiative transfer modeling schemes. The first, § 2.3.2, investigates VLMO dust disk properties by fitting our source SEDs. § 2.3.3 describes the grid of models we used to analyze the relationship between the disk outer radius and the derived disk mass.

2.3.1 [OI] Line and Continuum Detections

While [OI] 63 μm emission is not fully understood (e.g. Howard et al., 2013), envelopes, disks and outflows could all contribute to [OI] emission lines. As a forbidden line, [OI] 63 μm emission require a low density environment. A correlation between 63μm continuum emission and [OI] 63 μm lines suggests a disk origin, and it has been suggested that a [OI] emission can be used to distinguish between populations of outflows, full disks and transition disks (Howard et al., 2013; Keane et al., 2014). However, Howard et al. (2013) found no correlation between the dust disk mass and the [OI] line. Assuming that the dust mass traces the bulk of the disk mass, this suggests that the line is optically thick, and does not trace well the gas mass. In relation to the disk origin, models predict that the [OI] 63um line traces the surface of the disk and is sensitive to the average temperature of the region being probed.

To identify [OI] 63 μm detections, we smooth the spectrum using a uniform filter (width of 3 resolution elements) before fitting each spectrum within $\pm$0.1 μm of the line using a Levenberg-Marquardt algorithm assuming a Gaussian for the line profile and a first-order polynomial for the continuum. The 1σ uncertainties on the line fluxes are evaluated from the standard deviation of the pixels in the spectrum minus the best-fit model. We consider a line to be detected when its flux is greater than 3

Table 2.3. Observed continuum flux densities and line fluxes.

Source	$F_{[OI]}$	F_{63}	F_{189}	F_{70}	Ref.
	(10^{-18} W/m^2)	(mJy)	(mJy)	(mJy)	(F_{70})
CIDA-1	≤ 3.01	358.7 ± 50.9	270.4 ± 83.3	266 ± 2	B14
FR Tau	≤ 2.62	≤ 120.7	≤ 145.4	46 ± 3	B14
FU Tau A	5.17 ± 1.04	≤ 98.9	≤ 131.3	86 ± 17	R10
CFHT-20	≤ 2.89	≤ 127.6	≤ 154.5	128 ± 4	B14
J04381486	≤ 2.91	≤ 132.0	≤ 152.5	95 ± 2	B14
GM Tau	≤ 2.54	≤ 121.5	≤ 66.8	36 ± 2	B14
J04393364	≤ 2.28	100.3 ± 32.4	≤ 140.0	70 ± 1	B14
CFHT-4	≤ 2.73	≤ 110.6	≤ 161.9	109 ± 5	B14
ESO Hα 559	≤ 3.30	174.0 ± 45.6	317.7 ± 42.2		
Cha Hα 1	≤ 2.55	≤ 112.5	172.6 ± 40.0		
Hn 13	4.35 ± 1.30	≤ 114.0	≤ 76.7		

Note. — 3σ upper limits are reported for non-detections.

times the 1σ uncertainty. In case of non-detections, we fit the same spectral range with a first-order polynomial and we provide in Table 2.3 the 3σ upper limits from the rms in the baseline-subtracted spectrum using a Gaussian with a width equal to that of an unresolved line (FWHM of 98 km/s at 63.18 μm). Sources are considered detected in the continuum if the S/N at 63.2 μm is greater than 3.

Following this approach we detect the [OI] 63 μm line of two sources in our sample (toward FU Tau A and Hn 13) and the continuum of three bright disks (CIDA-1, J04393364, and ESO Hα 559). Two of these bright disks (CIDA-1 and ESO Hα 559) are also detected in the continuum at 189 μm. FU Tau A has a known molecular outflow (Monin et al., 2013), and it is possible that the outflow contributes to the [OI] 63 μm line, in which case the flux we report in Table 2.3 would be an upper limit for the disk emission.

Riviere-Marichalar et al. (2016) analyzed 362 Herschel sources, which included our 11 targets, using HIPE 12.0. Our results are consistent with Riviere-Marichalar et al. except for FU Tau A where we report an $\sim 5\sigma$ [OI] 63 μm detection ($5.17 \pm 1.04 \times 10^{-18}$ W/m^2) while Riviere-Marichalar et al. report a 3σ upper limit of ($< 3 \times 10^{-18}$ W/m^2).

All of the eight Taurus sources were also observed with the PACS photometer by Bulger et al. (2014). Literature 70 μm flux densities are reported in the last column of Table 2.3. Two of the sources (FR Tau and GM Tau) are fainter than the 70 mJy flux density estimated from the 24 μm photometry available at the time of the proposal submission. Except for CIDA-1, our continuum values and upper limits are consistent with the literature values within 1σ of the uncertainties we quote. In the case of CIDA-1 the 63 and 70 μm flux densities are within 2σ. It is possible that source variability further contributes to the flux discrepancy for this source as 70 μm variability can be close to $\sim$ 20% even for non-embedded young low-mass stars (Class II SEDs, see Billot et al. 2012). Given the better sensitivity of the PACS photometer and smaller uncertainty of the 70 μm photometric values, we will use them, when available, in the analysis that follows.

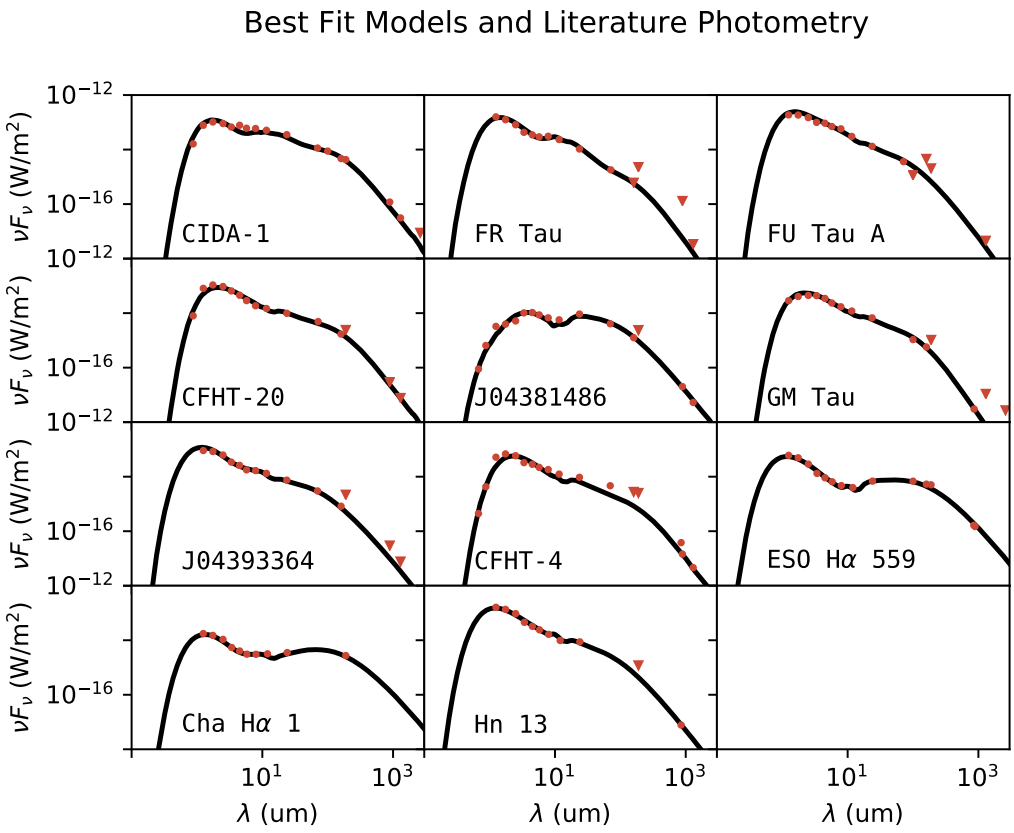

Figure 2.2 SEDs of our Herschel sources. Orange: photometric fluxes from literature; triangles: upper limits. The best-fit radiative transfer models for each source are displayed for each target (black line).

2.3.2 Continuum Radiative Transfer Modeling of Individual Sources

Table 2.4. Source photometry.

Source	Wavelength (μm)	Flux (mJy)
CIDA-1	0.88, 1.25, 1.75, 2.50, 3.35, 4.49, 5.73, 7.87, 11.56, 23.67, 70.00, 100.00, 160.00, 189.00, 890.00, 1300.00, 2600.00	0.0047, 0.033, 0.06, 0.075, 0.075, 0.12, 0.12, 0.16, 0.2, 0.28, 0.
FR Tau	1.25, 1.75, 2.50, 3.35, 4.49, 5.73, 7.87, 11.56, 23.67, 71.42, 160.00, 189.00, 890.00, 1300.00	0.066, 0.073, 0.068, 0.048, 0.052, 0.056, 0.081, 0.09, 0.083, 0.0
FU Tau A	1.25, 1.75, 2.50, 3.35, 4.49, 5.73, 7.87, 11.56, 23.67, 71.42, 100.00, 160.00, 189.00, 1300.00	0.078, 0.11, 0.12, 0.11, 0.14, 0.13, 0.15, 0.12, 0.1, 0.086, 0.039
CFHT-20	0.88, 1.25, 1.75, 2.50, 3.35, 4.49, 5.73, 7.87, 11.56, 23.67, 71.42, 160.00, 189.00, 890.00, 1300.00	0.0023, 0.034, 0.063, 0.079, 0.073, 0.068, 0.055, 0.049, 0.057,
J04381486	0.68, 0.88, 1.25, 1.75, 2.50, 3.35, 4.49, 5.73, 7.87, 11.56, 23.67, 70.00, 160.00, 189.00, 890.00, 1300.00	2e-05, 0.00019, 0.0014, 0.0023, 0.0043, 0.011, 0.016, 0.017, 0.0
GM Tau	1.25, 1.75, 2.50, 3.35, 4.49, 5.73, 7.87, 11.56, 23.67, 100.00, 160.00, 189.00, 860.00, 1300.00, 2600.00	0.012, 0.024, 0.037, 0.049, 0.052, 0.045, 0.045, 0.046, 0.053, 0.
J04393364	1.25, 1.75, 2.50, 3.35, 4.49, 5.73, 7.87, 11.56, 23.67, 70.00, 160.00, 189.00, 890.00, 1300.00	0.038, 0.049, 0.052, 0.038, 0.039, 0.034, 0.044, 0.051, 0.059, 0.
CFHT-4	0.68, 0.88, 1.25, 1.75, 2.50, 3.35, 4.49, 5.73, 7.87, 11.56, 23.67, 70.00, 160.00, 189.00, 850.00, 890.00, 1300.00	0.0001, 0.0013, 0.022, 0.04, 0.049, 0.037, 0.043, 0.042, 0.048,
ESO Hα 559	1.25, 1.75, 2.50, 3.40, 4.50, 5.80, 8.00, 12.00, 24.00, 100.00, 160.00, 189.00, 850.00, 890.00	0.025, 0.029, 0.024, 0.015, 0.014, 0.013, 0.013, 0.016, 0.055, 0.
Cha Hα 1	1.25, 1.75, 2.50, 3.40, 4.50, 5.80, 8.00, 12.00, 24.00, 189.00	0.0073, 0.0088, 0.009, 0.0061, 0.0061, 0.006, 0.0081, 0.013, 0.0
Hn 13	1.25, 1.75, 2.50, 3.40, 4.50, 5.80, 8.00, 12.00, 24.00, 189.00, 850.00	0.067, 0.079, 0.079, 0.052, 0.049, 0.047, 0.044, 0.039, 0.07, 77.

Note. — Photometric observations used to create SEDs for model fitting. A machine readable version of this table is available online.

References. — (B14) Bulger et al. (2014); (G06) Guieu et al. (2006); (L10) Luhman et al. (2010); (M01) Martín et al. (2001); (R10) Rebull et al. (2010); (C03) Cutri et al. (2003); (W10) Klein et al. (2003); (G07) Guieu et al. (2007); (L00) Luhman (2000) (P16) Pascucci et al. (2016); (H17) This work.

We combine continuum observations at multiple wavelengths and carry out continuum radiative transfer (hereafter, RT) modeling to constrain some of the main disk properties,

with focus on the outer disk radius as it might affect the [OI] 63 μm emission (e.g. Kamp et al., 2011). Each source's spectral energy distribution (SED) is shown in Figure 2.2 and individual fluxes and references are given in Table 2.4 and available online.

We model the SEDs with the 3D axisymmetric Monte Carlo RT code MCMax (Min et al., 2009). MCMax self-consistently calculates the disk vertical structure for a given dust surface density profile and gas-to-dust ratio, assuming hydrostatic equilibrium and $T_{\rm gas} = T_{\rm dust}$. The vertical structure of the dust is calculated from an equilibrium between dust settling and vertical mixing as described in Dullemond and Dominik (2004). Calculation of the disk temperature and density structure are iterated until a self-consistent solution is reached. For a given grain size distribution, the only free parameter controlling the vertical structure is the turbulent mixing strength, which was not found to be different in modeling the median SEDs of Herbig stars, T Tauri stars, and brown dwarfs by Mulders and Dominik (2012).

We begin by fitting the stellar parameters and disk inclinations of our sources using a genetic algorithm. The stellar luminosity and temperature are taken from Table 1 and allowed to vary only within their typical uncertainties, 30% for the luminosity and $\pm$100 K for the temperature (Luhman et al., 2007). Higher luminosities were required for CFHT-4 (2 times higher) and J04381486 (10 times higher) in order to achieve good fits. This is likely due to the high inclination of these disks. Ricci et al. (2014) estimate a disk inclination of 77° from a resolved millimeter continuum image of CFHT-4, and Luhman et al. (2007) estimate an inclination of $67 - 71°$ for J04381486 using a *Hubble Space Telescope* scattered light observation. GM Tau required a $T_{\rm eff}$ that was 189 K lower the the literature value in order to fit the optical/NIR portion of the SED. These quantities are used to compute stellar radii from the Stefan-Boltzmann relation. The source distance is fixed to that reported in Table 2.1. The literature extinction in Table 2.1 provides a good fit for all sources.

Table 2.5. Maximum likelihood parameters for source models.

Source	i (°)	$R_{\rm in}$ (au)		$R_{\rm out}$ (au)		Log $M_{\rm dust}$ ($M_\odot$)		$< T_{\rm d} >$ (K)
CIDA-1	35	0.32	$^{+1.5}_{-0.31}$	7.6	$^{+60}_{-3.9}$	-4.9	$^{+0.55}_{-0.92}$	48
FR Tau	77	0.32	$^{+1.5}_{-0.32}$	3.2	$^{+25}_{-2.3}$	-6.1	$^{+0.92}_{-1.3}$	46
FU Tau A	56	0.00032	$^{+0.017}_{-0.00026}$	1.3	$^{+36}_{-0.47}$	-7.2	$^{+1.3}_{-0.92}$	140
CFHT-20	56	0.0001	$^{+0.018}_{-4.4\times10^{-5}}$	4.3	$^{+46}_{-2.7}$	-5.7	$^{+0.92}_{-1.3}$	64
J04381486	70	0.032	$^{+0.025}_{-0.031}$	10	$^{+5.6}_{-3.6}$	-4.9	$^{+0.55}_{-0.18}$	33
GM Tau	35	0.0032	$^{+0.015}_{-0.0031}$	1.8	$^{+3.2}_{-0.92}$	-6.8	$^{+3.1}_{-0.55}$	73
J04393364	35	0.01	$^{+0.55}_{-0.0094}$	4.3	$^{+4.6}_{-3.4}$	-5.7	$^{+2.4}_{-1.3}$	42
CFHT-4	80	0.01	$^{+0.0078}_{-0.0099}$	78	$^{+43}_{-66}$	-5.3	$^{+0.18}_{-0.92}$	15
ESO Hα 559	35	0.032	$^{+0.53}_{-0.03}$	33	$^{+18}_{-17}$	-4.2	$^{+1.7}_{-0.18}$	18
Cha Hα 1	35	0.1	$^{+0.46}_{-0.099}$	33	$^{+88}_{-24}$	-3.1	$^{+1.3}_{-0.55}$	16
Hn 13	35	0.01	$^{+0.0078}_{-0.0099}$	3.2	$^{+13}_{-2.3}$	-6.1	$^{+0.92}_{-1.3}$	64

Note. — The maximum likelihood values are shown for the parameters: $R_{\rm in}$, $R_{\rm out}$ and $M_{\rm dust}$, along with their corresponding 1σ confidence intervals. $< T_{\rm d} >$ is calculated from the best-fit model selected for the source as described in § 2.3.2.

Eight equally spaced (in cosine) inclinations are sampled to constrain the viewing angle of the disk.

The general setup for all modeling follows the one described in Mulders and Dominik (2012) to fit the median SEDs of TT stars and brown dwarfs. Given the rather coarse SED sampling at long wavelengths, and degeneracies in SED modeling (e.g. Woitke et al., 2016), we limit the number of free parameters. The surface density is a power-law of the form $\Sigma \propto r^{-1}$ while the minimum and maximum grain sizes are $a = 0.1\mu$m and 1 mm with a particle size distribution proportional to $a^{-3.5}$, following Mulders and Dominik (2012). With this approach, we can explore the impact of the outer radius on the SED under the explicit assumption that the surface density slope and grain size distribution are stellar-mass independent.

To estimate confidence intervals, we run a grid of 4400 models for each source which explores the disk structure (inner and outer radius) and the disk mass. For the disk dust mass, 20 logarithmically spaced steps between 10^{-2} and $10^{-9} M_{\odot}$ are sampled. The disk inner radius is explored using 11 logarithmically spaced steps between 10^{-4} and 10^{1} au. For outer radius, 20 logarithmically spaced steps from 1 to 250 au are used. These ranges are chosen such that there is a peak in the Bayesian proability distribution. For sources where a clear peak is not observed, physically unrealistic values justify the boundaries of our grids (e.g., dust masses $> 25\%$ stellar mass, $R_{\rm in} <<$ silicate sublimation radius).

We also determine the likelihood of each model in order to establish confidence intervals for the parameter space of our model grids. The likelihood of each model is calculated by comparing photometric data with model flux densities using $\exp(-\chi^2_R/2)$, where χ^2_R is the reduced chi-squared metric. For photometric detections, we assume a typical uncertainty of 20% for each flux measurement. Upper limits are included in our fitting by using the modified χ^2 statistic described by Sawicki (2012).

Relative probabilities are then calculated for each parameter by summing the likelihood of common parameter values normalized by the sum of all likelihoods. 68.3% confidence intervals for the parameters $R_{\rm out}$, $R_{\rm in}$ and $M_{\rm dust}$ are estimated

from Bayesian probability distributions and reported in Table 2.5. Figure 2.3 shows the probability distribution and confidence interval for $R_{\rm out}$ for each source. See Appendix A.2 for additional information on the confidence intervals and for examples of probability distributions for $R_{\rm in}$ and $M_{\rm dust}$.

Along with the resulting parameters of our best fit models we also report the mass-averaged disk temperature ($< T_{\rm d} >$) in Table 2.5. Here, we take $< T_{\rm d} >$ to be the average of the dust temperature at each model grid point weighted by the dust mass at that point. In order to demonstrate the relationship between this value and the disk outer radius, we choose the model with the maximum likelihood from the set of models containing the most probable outer radius value as our fiducial model with which to calculate $< T_{\rm d} >$.

Because we find maximum likelihood values of $R_{\rm out}$ that are substantially smaller than those of disks around TT stars (~ 10 times smaller on average), we also run a second grid of models keeping $R_{\rm out}$ fixed to 200 au, a typical value used for modeling TT disks. These models use the same 20 and 11 steps of $M_{\rm dust}$ and $R_{\rm in}$, respectively, outlined above. We use these grids to similarly derive a $< T_{\rm d} >$ with which to compare our first grid of variable $R_{\rm out}$ against (see Figure 2.5).

Because heating of the dust in the outer disks of VLMOs by interstellar radiation may be significant, all of our models include an isotropic interstellar radiation field (approximated by a diluted 20,000K black body) in combination with a cosmic microwave background temperature of 2.7 K to properly compute the temperature in the outer disk (see Woitke et al., 2009).

2.3.3 Outer Radius Parameter Study

In addition to modeling individual sources, we carry out two sets of RT models to assess the impact of the disk outer radius ($R_{\rm out}$) on the derived disk mass and $< T_{\rm d} >$. Both parameter studies are calculated for a range of stellar masses but in one case $R_{\rm out}$ is held fixed at 200 au (hereafter, *fixed* $R_{\rm out}$ study) while in the other case (hereafter, *variable* $R_{\rm out}$ study) $R_{\rm out}$ scales linearly with stellar mass (see also Table 2.6). For both studies, the scaling of disk mass with stellar mass is chosen to

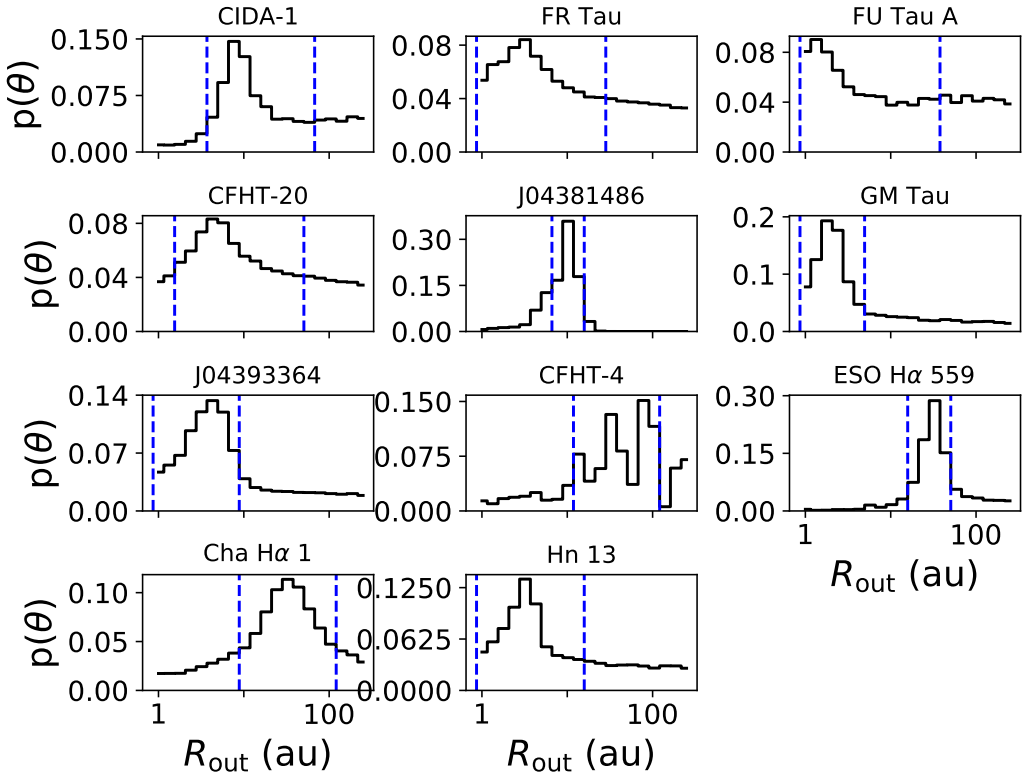

Figure 2.3 Bayesian probability distribution of $R_{\rm out}$ values. Vertical blue lines are 1σ confidence intervals reported in Table 2.5.

Table 2.6. Parameter Study Model Inputs.

Parameter	Variable $R_{\rm out}$	Fixed $R_{\rm out}$
$R_{\rm out}$(au)	$200(M_*/M_\odot)$	200
$M_{\rm dust}$	$\propto M_*^{2.0}$	$\propto M_*^{1.2}$
M_* ($M_\odot$)	0.05 - 2.239	
$R_{\rm in}$(au)	$0.05 \times L_*^{0.5}$	

reproduce the best fit relation to the 887,μm flux densities versus stellar masses in the Chameleon I star-forming region (Pascucci et al., 2016).

To cover a large range in stellar mass we combine the evolutionary tracks from Baraffe et al. (2015) and Feiden (2016) as in Pascucci et al. (2016). To find corresponding luminosities and temperatures for each stellar mass we use the 2 Myr isochrone because this age is a good match to the age of the star-forming regions we consider in this study. We set 15 equally log-spaced stellar masses from 0.05 $M_\odot$ to 2.239 $M_\odot$ which cover from 0.019 $L_\odot$ to 6.33 $L_\odot$.

All models adopt the same dust properties, turbulent mixing strength, and surface density power law profiles as those to fit individual SEDs (§ 2.3.2). Inner radii follow a scaling relationship consistent with the temperature at which silicate sublimation would occur. All parameters are summarized in Table 2.6.

One important difference between the two parameter studies is the scaling of disk mass with stellar mass. The *fixed* $R_{\rm out}$ study requires a shallower disk mass-stellar mass relation to reproduce the best-fit 887,μm flux, and yields a different temperature-luminosity relation. Implications of this parametric study will be discussed in § 2.4.3.

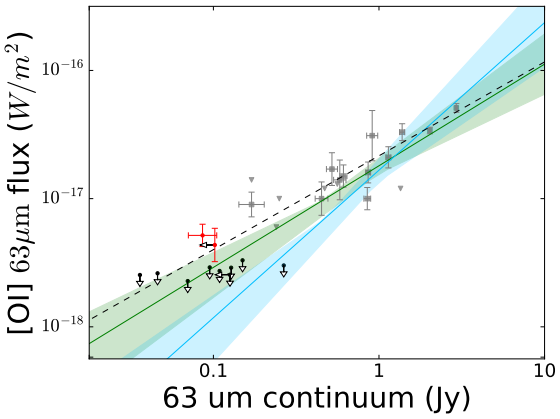

Figure 2.4 Fluxes are scaled to a distance of 140pc as in Howard et al. (2013). Red points are [OI] detections from this work. Black points are this work with arrows indicating upper limits in continuum and/or line flux observations. Grey points are full disks from Howard et al. (squares are detections and triangles are upper limits), with the dashed line showing their best fit. Green line is a refitting of the Howard et al. data using their upper limits. Blue line is the fit including our sources. Shaded areas are 1σ confidence intervals.

2.4 Results

2.4.1 Faint [OI] 63 μm emission from very low-mass star and brown dwarf disks

As mentioned in § 2.3.1 we detect the [OI] 63 μm line only toward 2 out of the 11 VLMO disks in the sample. Figure 2.4 shows the [OI] line flux versus the continuum of our sample (red and black symbols) in the context of literature values for more luminous/massive objects (grey symbols). The non-detections are somewhat surprising given that most sources should have been detected if they followed the line luminosity-continuum relation for TT stars with no known jets from Howard et al. (2013) (dashed line). This suggests that VLMO disks may be under-luminous in the [OI] 63 μm line.

In order to consider the possibility that the trend in the line flux-continuum relation does not extend to the VLMO regime and that the VLMO [OI] 63 μm emission is under-luminous, we have re-fit the same data and included the TT sources with upper limits which Howard et al. omitted from their fit. By doing this we are able to then re-fit the full TT sample (detections and upper limits) with our VLMO

Table 2.7. [OI] vs 70um Continuum Fitting Results

	Linear Regresion	
Description	Intercept	Slope
TT Disks	0.89 ± 0.18	-16.74 ± 0.06
TT + VLMO	1.14 ± 0.22	-16.78 ± 0.09

non-detections [1] (see Figure 2.4).

To do this we use the Bayesian method of regression fitting described in Kelly (2007)[2] which takes into account non-detections and errors bars.

We exclude FU Tau A from the fitting because it is a known outflow source Monin et al. (2013). Table 2.7 gives the fit coefficients.

The blue line in Figure 2.4 shows the best fit with the addition of our sources. VLMO disks may be under luminous in the [OI] $63\,\mu$m line, as suggested by the brightest (in continuum) half of the VLMO sample with no [OI] detection, but the upper limits are not stringent enough to conclude that they are actually under luminous at a confidence greater than 89%. On average our samples appear to be under-luminous by a factor of 1.8.

2.4.2 Small dust disks

Our RT modeling suggests greater likelihoods for outer disk radii that are smaller (maximum likelihoods $\leq$ 78 au with a mean value of 15 au) than typical values ($>$ 150 au) for disks around T-Tauri stars (e.g. Isella et al., 2009; Andrews et al., 2009; Guilloteau et al., 2011). We also note that for every source, the confidence

[1] We consider only non-detections from our sample. Of the two VLMOs with detected [OI] lines, one is excluded from our analysis because it has a known jet, and the other is excluded because it has only an upper limit for its $63, \mu$m continuum.

[2] Implemented by Josh Meyers in Python (Jan 16 2016 commit).

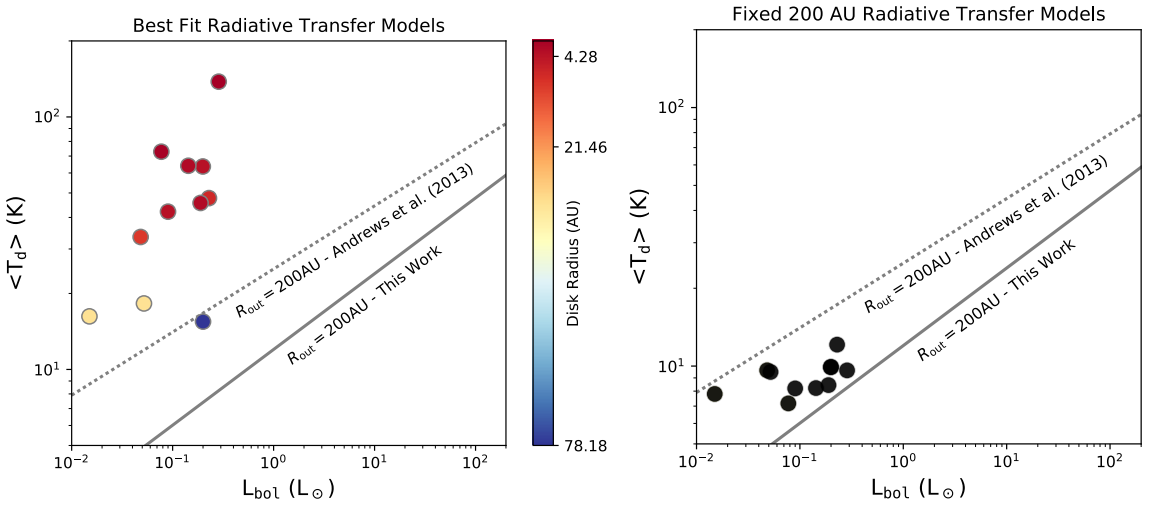

Figure 2.5 Circles are outputs from the RT modeling of our *Herschel* sources. The left panel shows the best fit of these models where the outer disk radius is a free parameter. The right panel shows the best fits where disk radius is fixed at 200 au. Both panels show the best-fit temperature-luminosity relation of our fixed radius parameter study models (lower solid line) and the Andrews et al. (2013) fit (dotted line).

intervals (see Figure 2.3) lie entirely well below 200 au. In fact, with the exception of CFHT-4, the confidence intervals lie entirely below 100 au, and the Bayesian probability distributions decrease towards larger outer radii.

Although these best fit models may not be unique solutions and stellar-mass dependencies in other disk parameters might yield equally good fits (e.g. Woitke et al., 2016), this approach shows that smaller disks around sub-stellar objects are consistent with the SEDs.

Disk sizes are mostly unknown in the brown dwarf regime. For our sample spatially resolved millimeter images exist only for CIDA-1, CFHT-4, and ESO Hα 559 (Ricci et al., 2014; Pascucci et al., 2016). Detailed modeling has been carried out for the first two with estimated disk radii of $66\pm^{14}_{12}$ au for CIDA-1 and greater than 80 au for CFHT-4 (Ricci et al., 2014). ESO Hα 559 was resolved at 887, μm and a fitted elliptical Gaussian resulted in a FWHM of 0.23″x 0.15″ (37 au x 24 au, Pascucci et al. (2016)). The maximum likelihood outer radius values found by our

modeling of CFHT-4 (78 au) and ESO Hα 559 (33 au) are in good agreement with these findings.

Ricci et al. (2014) find an outer radius for CIDA-1 which differs significantly from our value of 7.6 au, however, our modeling does not reject large sizes and the 1σ confidence interval of 60 au is consistent with the estimate of Ricci et al. These three disks are all larger than the median VLMO disks in our sample but they are also three of the four brightest disks. This suggests that smaller disks are indeed more common in the brown dwarf regime (see also Testi et al. (2016)). Additionally, Luhman et al. (2007) found that their models of J04381486 with outer radii of 20 and 40 au agreed "reasonably well" with *Hubble* Wide Field Planetary Camera observations. These values are larger than our finding of $R_{\rm out} = 10^{+5.6}_{-3.6}$ au, in line with observations showing that sub-micron grains and gas disks, as probed via scattered light images, are typically larger than dust disks traced at millimeter wavelengths (e.g. de Gregorio-Monsalvo et al., 2013).

If VLMO disks are indeed smaller than those around TTs, an important implication is that they are hotter than we would estimate if they were the same size as disks around TTs, i.e. their $< T_{\rm d} >$ is higher.

The left panel of Figure 2.5 illustrates this point: circles are our best fit values color-coded by disk outer radius while the dotted and solid lines are the $< T_{\rm d} > - L_{\rm bol}$ relations by Andrews et al. (2013) and by our *fixed* $R_{\rm out}$ models (§ 2.3.3). In both models the dust disk radius is 200 au regardless of stellar luminosity/mass but our *fixed* $R_{\rm out}$ models are significantly cooler because we compute the disk vertical structure self-consistently which results in less vertically extended disks. Regardless of these differences, it is clear that our best-fit RT models point to disk radii smaller than 200 au and higher $< T_{\rm d} >$ for VLMO disks than typically assumed. The SED fits with fixed $R_{\rm out}$ have temperatures in between those predicted by the Andrews et al. (2013) and our *fixed* $R_{\rm out}$ grid relations (right panel of Figure 2.5).

Note that the *Herschel* models with fixed 200 au outer radius fall above (and not on) the trend-line produced by our 200 au parameter models for two reasons. First, the Herschel sources were selected to be brighter, and hence hotter, disks

Table 2.8 Effect of model assumptions on total disk mass (gas + dust) estimates

	Fixed Radius Estimates						Scaled Radius Estimates		
	This work			Andrews et al. (2013)			This work		
	Disk Mass		$< T_{\rm d} >$	Disk Mass		$< T_{\rm d} >$	Disk Mass		$< T_{\rm d} >$
	($M_{\odot}$)	(M_{*})	(K)	($M_{\odot}$)	(M_{*})	(K)	($M_{\odot}$)	(M_{*})	(K)
CIDA-1	0.017	0.09	7.40	0.0036	0.019	16.71	0.0040	0.021	15.67
J04381486	0.274	5.05	2.45	0.0039	0.071	6.65	0.0005	0.008	20.29
GM Tau	0.008	0.11	3.25	0.0003	0.004	8.42	0.0001	0.001	18.99
CFHT-4	0.004	0.03	6.01	0.0006	0.005	14.06	0.0004	0.004	16.45
ESO Hα 559	0.069	0.48	4.96	0.0078	0.055	11.97	0.0043	0.030	17.21

whereas the model grid was fit to the median disk mass in Chameleon. Second, the parameter models use disk masses and inner disk radii that scale with stellar mass and bolometric luminosity respectively, whereas our best-fit SED models allow these value to vary for a best fit with photometry.

Interestingly, our variable $R_{\rm out}$ grid VLMO models are found to be optically thick at 63, μm for all of our sources with the exception of CFHT-4 (the source with the largest $R_{\rm out}$) and at 850, μm for all but two (CFHT-4 and FR Tau). This is different than what is proposed in Harvey et al. who, however, targeted a fainter 70, μm sample of brown dwarf disks. Measuring dust disk sizes will be important to establish if, and by how much, brown dwarf disks are optically thick at these wavelengths.

2.4.3 Disk Temperature-Stellar Luminosity Relation

A typical approach to measure dust disk masses is to obtain a sub-mm/mm data point, a source distance, assume optically thin emission and dust opacity, and an average dust temperature ($< T_{\rm d} >$) to be used in the Planck function (e.g. Beckwith et al., 1990). This same approach has been recently used to estimate dust disk masses for hundreds of stars in nearby star-forming regions and associations. As discussed in Pascucci et al. (2016) such estimates, as well as the disk mass-stellar mass scaling relation, are very sensitive to the assumed $< T_{\rm d} >$ and how it scales with stellar luminosity.

In the previous section we showed that the SEDs of VLMOs can be well reproduced with disks that have smaller radii than TT disks and, as such, do not fall on the temperature-luminosity relation derived by Andrews et al. (2013). Instead, they are hotter, plotting above this relation (see Figure 2.6 and Table 2.5). We use the two RT grids discussed in § 2.3.3 to quantify the difference in the $< T_{\rm d} > -L_{\rm bol}$ relation for fixed outer radii disks and radii scaling with stellar mass (see Figure 2.6). The *fixed* $R_{\rm out}$ models result in mass-averaged disk temperatures that decrease with stellar luminosity and become lower than 10 K for brown dwarfs. This is somewhat surprising given that dust grains in giant molecular clouds, heated by the interstellar radiation field, stabilizes at $\sim$ 10 K (Mathis et al., 1983). We remind the reader that we have included interstellar radiation in our modeling (see § 2.3.2) but, as also found in van der Plas et al. (2016), this extra heating does not change appreciably the dust disk temperature (see in particular their Figure 5d).

In the very different assumption of outer radii scaling with stellar mass, $< T_{\rm d} >$ remains confined within $\sim$10-20 K over four orders of magnitude in luminosity and shows an opposite behaviour by slightly increasing toward the lower-luminosity/lower-mass objects. For example, the difference in $< T_{\rm d} >$ for the two assumptions when $L_* = 0.1 L_\odot$ is 10.4 K which results in mass estimates that differ by a factor of 9.

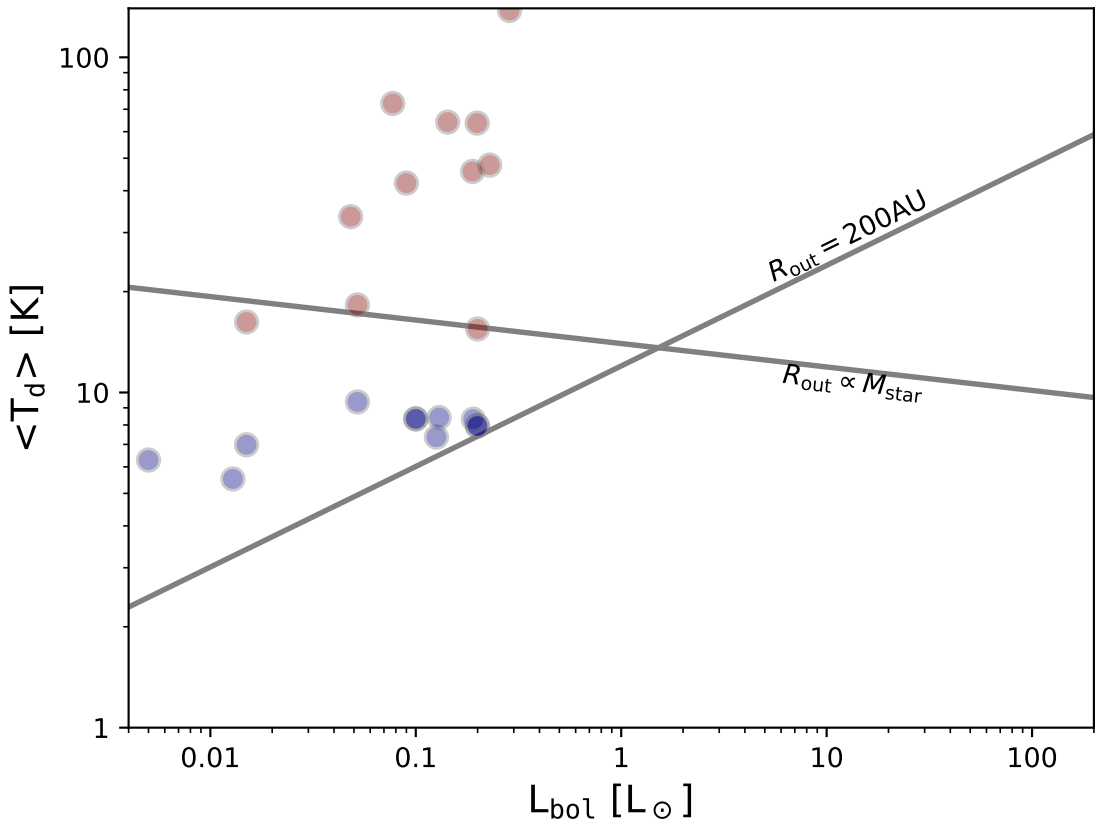

Figure 2.6 $R_{out} \propto M_{star}$ shows the best fit of our grid of RT models where the disk's outer radius is scaled to the stellar mass. $R_{out} = 200$ au shows the best fit of our grid of RT models where the disk's outer radius is fixed to 200 au (it is the same line seen in the right and left panels of Figure 2.5). Red dots are our best fit models (figure 2.5 left panel) and the blue dots are the *fixed* $R_{\rm out}$ grid (200 au) models (Figure 2.5 right panel).

2.5 Discussion

In this paper we start from the zero-order assumptions that disk geometry and dust opacity are stellar-mass independent. With these assumptions, our RT modeling of each source suggests that dust disk outer radii range from 1.3 to 78 au. This is significantly less than the 200 au radius typically assumed for TT disks. Although small disk radii may not be a unique solution, they agree well with the few previously resolved VLMO disks. As such, it becomes necessary to consider the effect of smaller disk sizes when calculating their masses and interpreting the [OI] 63 μm line emission.

2.5.1 Mass estimates for small disks

Disk mass estimates using a $< T_{\rm d} >$ taken from a $L_{\rm bol}$ relationship with a fixed outer radius will ultimately result in temperatures that are too low for low luminosity objects and temperatures that are too high for high luminosity objects (Fig. 2.6). Consequently this will result in over-predicting and under-predicting the dust disk masses of low and high luminosity sources respectively.

$< T_{\rm d} >$ can vary by a factor of 3 to 5 times for luminosities between 0.01 and 100 $L_{\odot}$. If we consider VLMOs to be represented by $L_{\rm bol} \in [0.005, 0.2] L_{\odot}$ (The range of our Herschel sample) we find $< T_{\rm d} >$ to be lower by a factor of 8 to 2 with a mean difference (in logarithmic space) of 5 times. The disagreement in the two treatments is much less for TT objects where considering typical $L_{\rm bol} \in [1.5, 8] L_{\odot}$ (comparable to the TT disks considered by Howard et al 2013) results in a overestimate of $< T_{\rm d} >$ by a factor ~ 1.5. In addition, the fixed outer radius relationship gives too low of a $< T_{\rm d} >$ in the VLMO regime. Luminosities below $0.053 L_{\odot}$ (which would include 4 of our 11 sources) result in $< T_{\rm d} >$ under 5 K.

Ultimately these disagreements in $< T_{\rm d} >$ are significant because they result in an even greater discrepancy in mass predictions. For example, using the fixed $< T_{\rm d} > - L_{\rm bol}$ relationships and applying them to the source J04381486 ($0.005 L_{\odot}$; $F_{890,\mu{\rm m}} = 6$ mJy), a total disk mass (assuming a gas-to-dust radio of 100) of 5 and

$0.07M_*$ is estimated (depending on whether the vertical structure is self consistently calculated or not) due to the low $< T_{\rm d} >$ of 6.7 K and 2.5 K respectively. Table 2.8 compares the effects of model assumption on estimated disk masses for the 5 sources in our sample with $\sim 887, \mu$m detections.

Because the dust disk size likely depends on many factors including disk mass, height, turbulent mixing, age, grain-growth and drift rates, perhaps even more so than it depends upon host luminosity, characterizing the dust-disk outer radius becomes critical in understanding disk masses.

2.5.2 [OI] emission in small disks

For our 11 observed sources we had only 2 [OI] 63 μm line detections. Figure 2.4 shows the fit (dashed line) to TT disks found by Howard et al. (2013) which we used to set the sensitivity of our observations. Based on this we expected more detections but over two-thirds of our sources resulted in upper limits which fall below their fit.

In order to assess how feasible it is that these disks are under-luminous (and to pinpoint a likely origin of this under-luminosity), we compare our observations to the thermochemical models by Greenwood et al. (2017). These models use 2D RT and a complex chemical network on top of a parametrized disk structure, allowing investigations into the effects of disk geometry on the [OI] 63 μm line flux by computing a grid of models of varying disk masses and radii.

Figure 2.7 shows that for a given mass, a decreasing of the disk size leads to a decrease in [OI] emission while continuum emission increases or stays constant. This is consistent with the [OI] underluminosity of VLMOs being caused by smaller disk sizes.

The reason for the reduced [OI] emission is due to the radii at which the emission originates. Figure 2.8 shows the radius within which 70% of the [OI] and continuum emissions originate normalised to the taper radius[3] , a measure of the disk size. For all disk sizes, the [OI] emission originates from larger radii than the continuum. For

[3]Taper radius is the location of an exponential tapering-off of the disk density power law. $R_{\rm taper} = R_{\rm out}/8$.

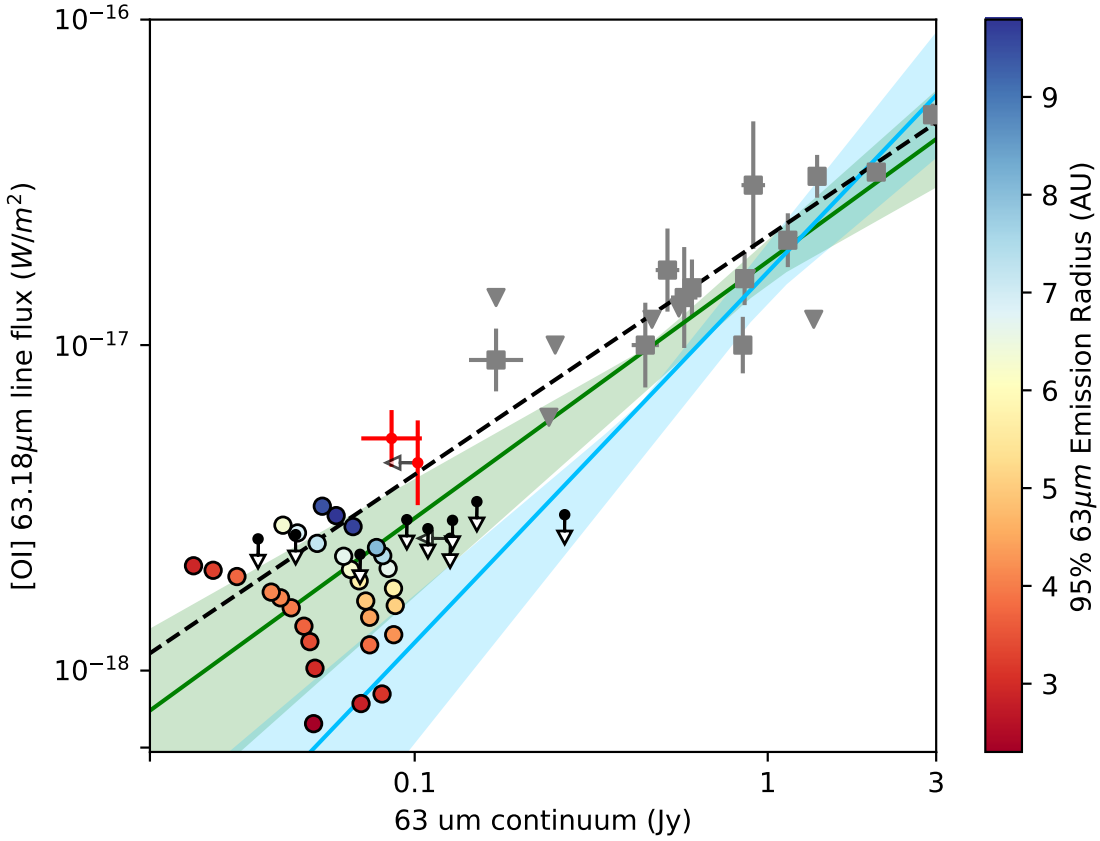

Figure 2.7 Line and continuum emission from thermochemical models by Greenwood et al. (2017) (color-filled circles) superimposed on data and fits described in Figure 2.4. Isarithms of constant mass (1, 4, and 8 $\times 10^{-4} M_{\odot}$) and flaring index show how smaller disks lead to a rapid decrease in [OI] line flux.

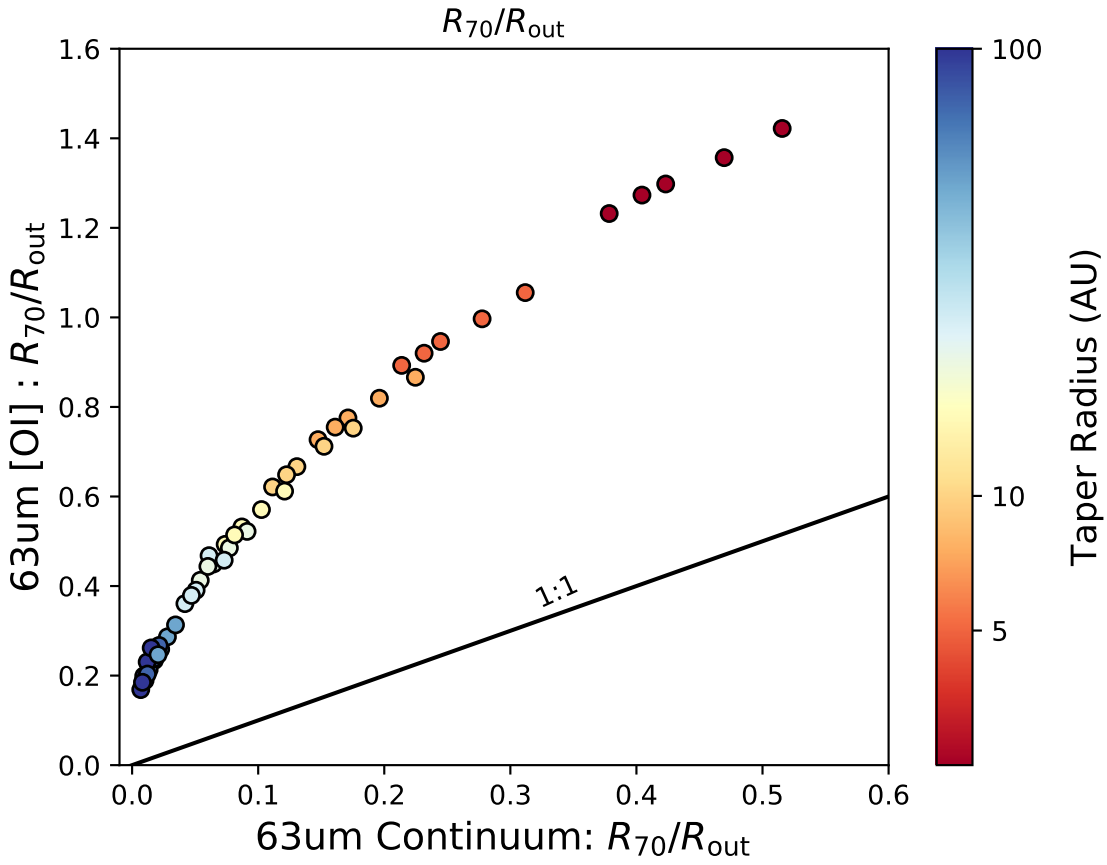

Figure 2.8 Line and continuum emission from thermochemical models by Greenwood et al. (2017) showing that 70% of [OI] 63 μm emission comes from larger relative distances as the disk size decreases. 70% of the given emission ([OI] or continuum) originates from within the R_{70} radius.

large disks, the majority of the emission is well within the taper radius for both the [OI] 63 μm line flux and the continuum flux density. However, as the disks become smaller (going from blue to red in the figure), the area of [OI] 63 μm line emission falls beyond the taper radius while the continuum emission remains well within. Thus, one possible contribution to the observed under-luminosity is that the line-emitting area of [OI] 63 μm is disproportionately small in VLMO disks.

Another contributing factor may be that VLMO disks tend to be less flared than their higher-mass counterparts, for which there is some observational evidence

(Szűcs et al., 2010; Liu et al., 2015, however see Harvey et al. 2012). The models by Greenwood et al. (2017) show that changing the flaring index (β) from 1.2 to 1.15, 1.10, and 1.05 decreases the [OI] 63 μm emission in a VLMO disk to 73% and 40%, and 13% of the $\beta = 1.2$ levels respectively, while the continuum emission decreases to 87%, 40%, and 19% of the $\beta = 1.2$ levels (Greenwood, personal communication). These results suggest that the [OI] 63 μm line flux is more sensitive to disk flaring than the continuum flux, causing a sample of weakly-flared disks to be under-luminous in their [OI] 63 μm emission.

2.6 Summary and Conclusions

Starting from a sample of 11 luminosity-selected very low-mass stars and brown dwarfs with disks, we use the PACS spectrometer aboard the *Herschel Space Observatory* to measure the [OI] 63 μm line fluxes and model the spectral energy distributions. The analysis of 10 out of our 11 sources is consistent with the previous analysis by Riviere-Marichalar et al. (2016), however using a newer data reduction pipeline, we report a new [OI] 63um detection toward FU Tau A.

Our main findings are:

- We detect only two sources in [OI] 63 μm despite a 3 times better sensitivity than for T Tauri disks, suggesting that disks around very low-mass star and brown dwarf disks are underluminous in [OI] 63 μm.

- Assuming that the disk geometry and opacity are stellar-mass independent, we find that disk models with outer radii in the range of 1.3–78 au have the highest maximum likelihood values when compared to SEDs. These radii are significantly smaller than those of T Tauri star disks (22–440 au).

- If very low-mass star and brown dwarf disks are indeed smaller and hotter than T Tauri disks they do not follow previously derived temperature-luminosity relationships. A disk outer radius that scales linearly with stellar mass results

in almost flat $< T_{\rm d} > -L_{\rm bol}$ relationship. This results in higher average temperatures for VLMO disks and smaller disk mass estimates.

- Using thermochemical models we find that smaller disks result in lower [OI] 63 μm fluxes which may explain the non-detections in the sample.

A smaller size of protoplanetary disks around sub-stellar objects has a large impact on the derived disk masses from large surveys of star-forming regions. High-resolution ALMA observations are necessary to quantifying how the disk radius scales with stellar mass to correctly gauge the planet-forming potential of very low-mass stars and brown dwarfs.

2.7 Acknowledgements

The Herschel spacecraft was designed, built, tested, and launched under a contract to ESA managed by the Herschel/Planck Project team by an industrial consortium under the overall responsibility of the prime contractor Thales Alenia Space (Cannes), and including Astrium (Friedrichshafen) responsible for the payload module and for system testing at spacecraft level, Thales Alenia Space (Turin) responsible for the service module, and Astrium (Toulouse) responsible for the telescope, with in excess of a hundred subcontractors. HIPE is a joint development by the Herschel Science Ground Segment Consortium, consisting of ESA, the NASA Herschel Science Center, and the HIFI, PACS and SPIRE consortia. An allocation of computer time from the UA Research Computing High Performance Computing (HPC) and High Throughput Computing (HTC) at the University of Arizona is gratefully acknowledged. This material is based upon work supported by the National Science Foundation under Grant No. 1228509. Support for this work, part of the NASA Herschel Science Center Theoretical Research/Laboratory Astrophysics Program, was provided by NASA through a contract issued by the Jet Propulsion Laboratory, California Institute of Technology under a contract with NASA (Grant No. 1483963).

This research has made use of the SIMBAD database and the VizieR catalogue access tool, CDS, Strasbourg, France.

CHAPTER 3

A likely planet-induced gap in the disk around T Cha

3.1 Introduction

Transition disks are a sub-set of disks that display a significantly reduced near-infrared emission but large mid- to far-infrared emission in their spectral energy distribution (SED, Strom et al., 1989). This SED-identified characteristic is associated with a depletion of warm dust particles in the inner disk, which is why transition disks are thought to be crucial to understand how planet-forming material is cleared out.

Recently, many transition disks have been spatially resolved at different wavelengths reveling a variety of structures: gaps or cavities[1] (e.g. Pérez et al., 2014; Dong et al., 2017), spiral arms (e.g. Muto et al., 2012), shadows (some of them variable with time, e.g. Pinilla et al., 2015a), and lopsided asymmetries (e.g. van der Marel et al., 2013; Casassus et al., 2013). These observations highlight that the SED-classified transition disks are a heterogeneous group of objects (e.g. Espaillat et al., 2014), only a subset of which may be truly caught in the act of dispersing (e.g. Ercolano & Pascucci, 2017). For instance, disks shaped by planet-disk interaction are not necessarily dispersing as planet formation may occur early in disk evolution and be a long lived process.

The combination of near-infrared (tracing micron-sized particles) and millimeter imagery (mm/cm-sized grains) provides important insights into the origin of structures in transition disks. In particular, cavities and gaps resulting from pressure bumps in the gas are most pronounced at millimeter wavelengths as mm/cm-sized

[1]We use the term "gap" to refer to an empty or depleted annular region separating an inner and an outer disk while we use "cavity" for an empty or depleted region that extends from the central star out to an outer disk.

grains concentrate in pressure maxima, while micron-sized dust follows the gas (e.g. Brauer et al., 2008). In the case of planet-induced pressure bumps, the location of the peak emission at near-infrared and mm wavelengths can be also used to estimate the planet mass (e.g. de Juan Ovelar et al., 2013; Garufi et al., 2013).

In this letter, we present ALMA 3 mm high-angular resolution ($0.11'' \times 0.06''$) observations of the transition disk around T-Chamaeleontis (T Cha). We also compare our data with the similarly high-resolution ($\sim 0.04''$) 1.6 μm SPHERE/VLT imagery recently published by Pohl et al. (2017). This comparison makes T Cha one of two systems, along with TW Hya (van Boekel et al., 2017), for which millimeter and near-infrared emission can be investigated at similar spatial scales (e.g. 2.5-4.3 au with SPHERE and 1.6-10 au with ALMA).

T Cha is a T-Tauri star (spectral type G8, Alcala et al., 1993) located in the ϵ-Cha association (at 107 ± 3 pc, Gaia Collaboration et al. 2016) with an estimated age between 2-10 Myr (Fernández et al., 2008; Ortega et al., 2009). The presence of a gap in this disk was first inferred via SED modeling (Brown et al., 2007) and then later by the analysis of NIR interferometric data (Olofsson et al., 2011, 2013). High-resolution mid-infrared spectroscopy found evidence for a disk wind beyond the dust gap whose properties are compatible with a slow star-driven photoevaporative wind (Pascucci & Sterzik, 2009; Sacco et al., 2012). ALMA Cycle 0 observations at 0.85 mm could not resolve the gap but identified two emission bumps separated by 40 au, suggesting a cavity of 20 au in size (Huélamo et al., 2015). Interestingly, a candidate exoplanet has been reported inside the cavity (Huélamo et al., 2011), although its existence is debated (Sallum et al., 2015). The recent SPHERE/VLT scattered polarized light images (Pohl et al., 2017) resolve the outer ring-like emission. By fitting the observations with radiative transfer models, the inner edge of the outer ring is found at ~ 30 au. Pohl et al. (2017) also give upper limits for potential embedded planets. Using hot-start models, planets more massive than $\sim 8.5\,M_{Jup}$ are ruled out at a distance from $0.1''$to $0.3''$(10.7 to 32.1 au) from the central star. At larger separations, the limit is $\sim 2.0\,M_{Jup}$.

In the hot-start model, planet formation occurs from the collapse of disk material

due to gravitational instability, resulting in high initial entropy. This scenario may be unrealistic, especially within the 10.7 to 32.1 au disk region (Stamatellos and Whitworth, 2009; Helled et al., 2014). In a core accretion formation model, gas falling onto the solid core is shock heated, and the gravitational potential energy of the gas is efficiently liberated via radiation. This model, sometimes referred to as a cold start, results in a planet with lower initial entropy, and will have a lower contrast with the nearby disk material, when compared to a hot-start model. If core accretion is considered a more appropriate formation scenario, a planet greater than $\sim 8.5\,M_{Jup}$ can not be ruled out. Determining which formation model is more appropriate is complicated by effects such as stellar-metallicity, disk lifetime and opacity (e.g. Stamatellos and Whitworth, 2009; Helled et al., 2014).

Here, we present our ALMA 3 mm observations (Sect. 3.2), then our visibility fitting approach (Sect. 3.3), and summarize our results, including the comparison with the SPHERE/VLT images (Sect. 3.4). We discuss our findings and address different origins for shaping the wavelength dependent size of gaps and cavities (Sect. 3.5). We conclude that the most likely explanation for T Cha's gap is from planet-disk interaction.

3.2 Observation and Data Reduction

Our ALMA Cycle 3 observations (Project ID: 2015.1.00979.S, PI I. Pascucci) were carried out on October 27 and 29, 2015 with 48 12 m antennas. Of the four Band 3 spectral windows, three were utilized for the continuum emission and one was centered around the hydrogen recombination line H(41)α at 92.03 GHz, which might trace a disk wind (Pascucci et al., 2012). The on-source time ($\sim$2 h) was set to achieve a sensitivity of 9μJy/beam in the aggregate continuum bandwidth of 6.6 GHz.

The ALMA data were calibrated using the Common Astronomy Software Applications (CASA, McMullin et al., 2007). The initial reduction scripts were provided by the North American ALMA Science Center and included phase, bandpass, and

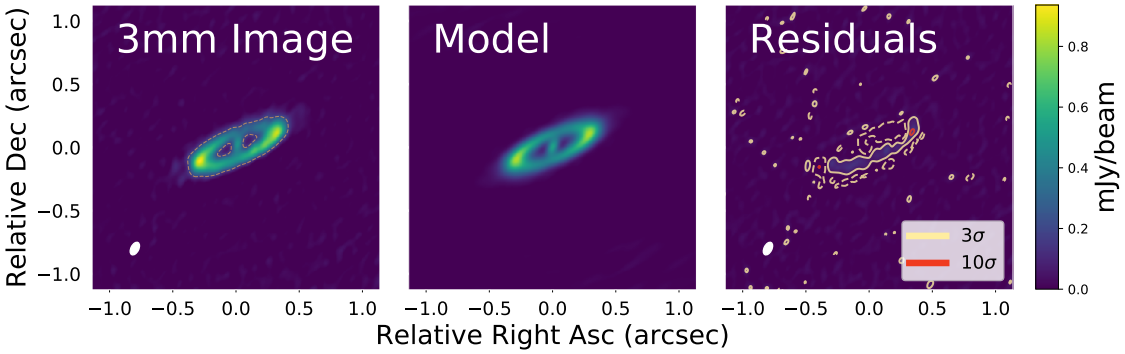

(a)

Figure 3.1 Left: Cleaned 3 mm ALMA image of T Cha (Project ID: 2015.1.00979.S). Beam is shown as ellipse in lower left and 1σ level is 1.6mJy. Countour shows 5σ region integrated for flux density measurement reported in Section 3.2. Center: Best-fit model. Right: The residuals of our best-fit model (center panel) subtracted from the unbinned ALMA image (left panel).

flux calibration. We ran the scripts using CASA 4.7.1 and created images in the continuum and in the line using Briggs weighting and robustness parameter equal to 0.5 (for the line we also applied a 2Mλ tapering to increase the sensitivity). The continuum emission at an average frequency of 99.16 GHz (3.0 mm) is spatially resolved and detected at high sensitivity, see Figure 3.1 where the image rms is 9μJy/beam and the beam is $0.11'' \times 0.06''$ with a position angle of -18.11°. The H recombination line is not detected even when rebinning in spectral resolution to tens of km/s, the expected line width. Applying self-calibration did not significantly improve the continuum image while resulting in lower spatial resolution and did not lend a line detection. Hence, we will focus this letter on the properties of the continuum 3 mm emission using the non self-calibrated data.

On the image shown in Figure 3.1 we draw a 5σ contour and measure a total flux density of 16.5±1.6 mJy (the quoted uncertainty includes an absolute flux calibration uncertainty of 10%). The peak S/N from our cleaned image is 110. Our value is ∼2.5 higher than that found by ATCA at 3.2 mm (Ubach et al., 2012), which, in combination with the flux reported by Huélamo et al. (2015) (198±4 mJy at 0.85 mm), results in a integrated millimeter spectral index of $\sim 1.97 \pm 0.08$. This

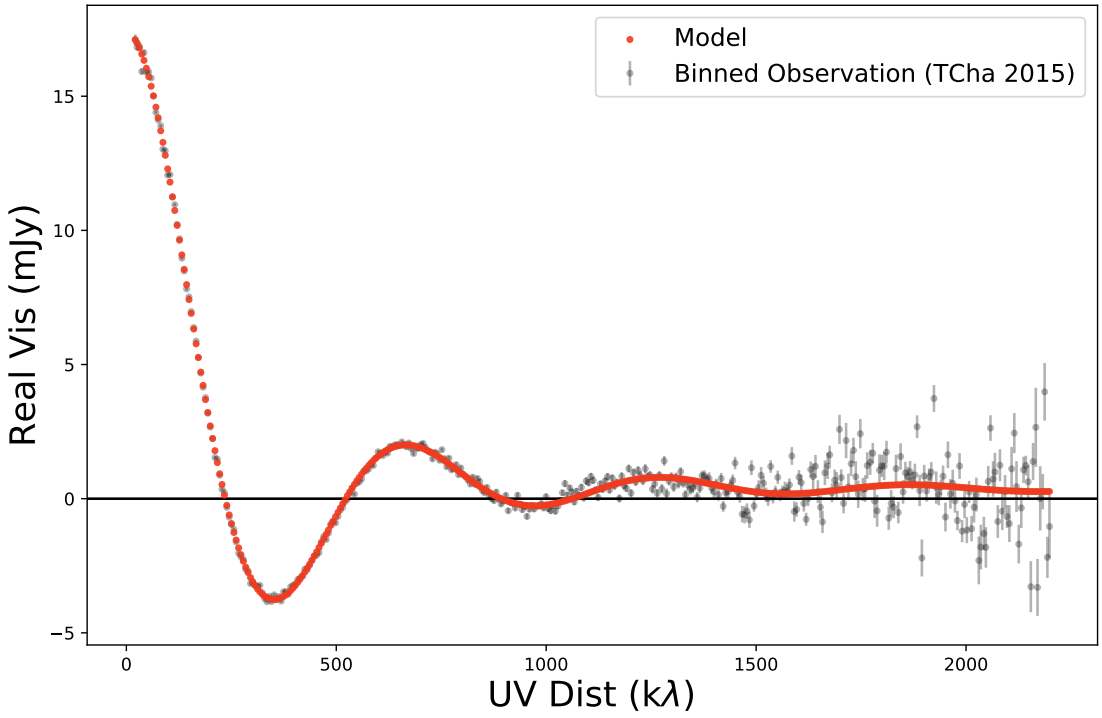

Figure 3.2 Deprojected real visibilities from Band 3 observation. Data are shown in gray with error bars. Model is overlaid in red.

value is close to the relationship between spectral index and cavity size introduced by Pinilla et al. (2014) for transition disks and could be an indication of mm-sized grains trapped at the outer edge of a planet-induced gap.

3.3 Analysis

The T Cha 3 mm continuum map (hereafter: 3 mm image, Figure 3.1) reveals a disk with three distinct components: an inner emission, a spatially resolved gap, and an outer ring. In order to quantify the location and size of these structures we use two methods – fitting model radial profiles to the visibilities and direct measurements from the 3 mm image. We then compare our results with previously published findings at shorter wavelengths in order to examine the wavelength dependence of these features.

Symbol	Parameter	Range	Best Fit	Unit
	Nuker Profile – Outer Disk			
$R_{\rm peak}$	transition radius	[10–60]	37.09 ± 0.07	(au)
γ	inner disk index	[-6–1]	-3.10 ± 0.06	
α	transition index	[10–85]	53.73 ± 12.81	
β	outer disk index	[5–8]	6.49 ± 0.04	
	Gaussian – Inner Disk			
A/B	amplitude ratio	[30–500]	336.0 ± 109.1	
$R_{\rm width}$	gaussian width	[0–4]	1.01 ± 0.28	(au)

Table 3.1 *Model parameters, parameter space (Range), and best fit modeling results.*

Assuming an axisymmetric disk, we model the sky brightness by fitting parametric models to the dust continuum emission in the visibility domain. To prepare the visibilities for fitting, we center, deproject and bin the data. The visibilities were centered using the routines `uvmodelfit()` and `fixvis()` within CASA. CASA's `disk` model provided the best centering fit, resulting in a center with α_{ICRS} =11h57m13.29s and δ_{ICRS} =-79d21m31.68s. The observed (u, v) points from the three spectral windows are deprojected and binned, reducing the number of unflagged data points used for fitting from 7×10^7 to 3×10^4. During this process, we minimize the residuals between the unbinned image and our axisymmetric binned image in order to find a fit for the inclination and position angle (PA). We find that the optimal values for the inclination and PA are 73° and 113°, respectively, which are within 2σ of the values and uncertainties reported in the literature (e.g. Olofsson et al., 2013; Pohl et al., 2017).

To model the three disk components, we assume radial intensity profiles that combine a Nuker profile and a Gaussian. Tripathi et al. (2017) showed that a Nuker profile (Lauer et al., 1995) reproduces well the visibilities of a variety of disks, including full and transition disks, with few input parameters. It does this by producing a decreasing monotone function for full disks, or a symmetric/asymmetric function about a single maximum for rings. The addition of a Gaussian centered at the stellar location is necessary to fit the inner emission seen in Figure 3.1. The

radial profile of our model is given by

$$I(r) = A\ \exp\left(-\frac{r^2}{2R_{\rm width}^2}\right) + B\left(\frac{r}{R_{\rm peak}}\right)^{-\gamma}\left[1+\left(\frac{r}{R_{\rm peak}}\right)^{\alpha}\right]^{(\gamma-\beta)/\alpha} \tag{3.1}$$

where the first term in the equation is the central Gaussian and the second term is the Nuker profile. In the equation, r is the radial distance and the remaining symbols are defined in Table 3.1. When Fourier transformed this symmetric brightness profile can be expressed with the zeroth-order Bessel function of the first kind J_0 (Berger & Segransan, 2007). We then fit the model visibilities to the binned real part of the observed visibilities using the *emcee* (Foreman-Mackey et al., 2013) implementation of the Markov chain Monte Carlo method. For our radial grid, we use $r \in [0-500]$ au with steps of 0.025 au. Our parameter space is sampled with 1000 walkers having 500 steps each. The parameter space explored, and the results of our fitting are shown in Table 3.1. Posterior probability distributions of the sampled parameter space are available online.

Our best-fit model is imaged using the same (u, v) coordinates as our ALMA observations. Our model visibilities are shown in Figure 3.2, while Figure 3.1 shows the model image and the residuals between our unbinned observations and our best-fit model, i.e. data − model. Note that the residuals are at most 10σ, and below 1σ when we subtract the model from the binned data. Our residuals reveal a positive residual in the south spanning from east-to-west, and negative residuals in the south and north . Because positive and negative residuals are aligned with the disk major axis, we argue that this may result from optical-depth effects.

3.4 Results

Radial intensity profiles along the disk's PA of 113° are shown in Figure 3.3a for our ALMA 3 mm image. We also compare in Figure 3.3b the best-fit model profiles from our visibility analysis and the best model fit to the SPHERE/VLT 1.6 μm image from Pohl et al. (2017). From these profiles we extract values for the location of the ring's peak emission ($R_{\rm peak}$). In addition to $R_{\rm peak}$, we report $R_{\rm wall}$ defined

as in de Juan Ovelar et al. (2013), i.e. the radial location where the intensity is half of the difference between the gap minimum intensity and the outer ring peak intensity. The radial position of $R_{\rm peak}$ resulting from our 3mm ALMA observations agree well (within 1 au) with our best-fit model (see Table 3.2). Comparing our visibility modeling with the NIR model provided by Pohl et al. (2017), we find that the 3mm $R_{\rm peak}$ is at a greater radial distance than the 1.6μm $R_{\rm wall}$ by 8.8 au.

The central emission is unresolved by our beam of $\sim$10 au diameter and our visibility modeling suggests that it is confined within a radius of only $\sim$ 1 au. The flux density measured over the ALMA beam is 0.55 ± 0.06 mJy. By extrapolating the hot (1400K) NIR SED-component (Olofsson et al., 2013) out to 3 mm, we find that only $\sim$2% of the measured flux density could come from close-in micron-sized grains. In addition, from the long-wavelength portion of the SED (Pascucci et al., 2014) we calculate that no more than $\sim$ 30% of the central emission arises from free-free emission. As such, most of the detected central emission is thermal dust emission, likely from millimeter-sized grains. By detecting the central 3 mm emission *and* spatially resolving the outer ring, our ALMA image demonstrates that the disk of T Cha has a gap at millimeter wavelengths and not a cavity.

Using the definition of $R_{\rm wall}$ for the locations of the inner and outer edge of the gap, we estimate from our image a gap size of $\sim$ 17.7 au. This should be considered a lower limit as we do not spatially resolve the central mm emission. The location of the gap's outer edge found from our observation and modeling are 22.9 and 27.8 au respectively, with the latter being very similar to the 28.3 au reported by Pohl et al. (2017) from modeling the SPHERE images. By taking the model $R_{\rm wall}$ to be the location of the gap outer edge, we find an upper limit on the gap width of < 27.8 au (any larger and the gap would extend to zero au and become a cavity).

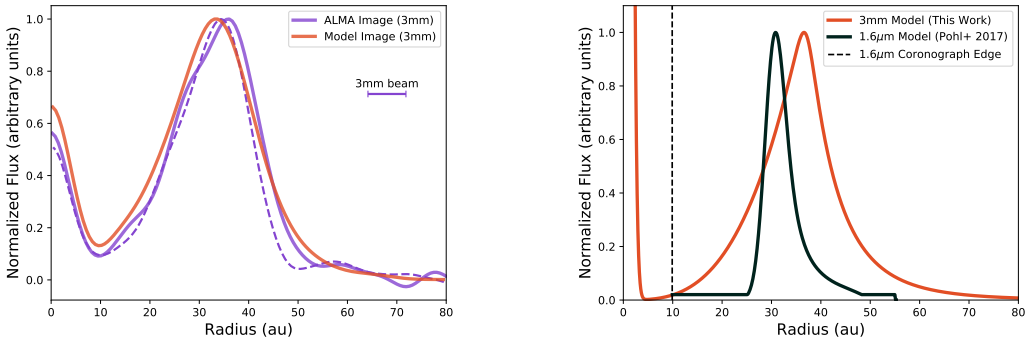

(a) (b)

Figure 3.3 (a) Comparison of radial intensities profiles (normalized to the intensity of the ring peak) from our ALMA image and best-fit model image (using same u,v spacing). For the ALMA image (purple), the solid line is taken radially along T Cha's PA towards the NE, while the dashed lines is taken along the same line extending to the SW. Because our model is axisymmetric, we show only one profile (red). The ALMA/3mm beam width along T Cha's PA is 0.072″. (b) Comparison of ring location at different wavelengths. Radial intensities taken from best-fit models.

λ	Source	Location
3mm	Image $R_{\rm peak}$	36.1±0.8 au
	Model $R_{\rm peak}$	37.1 au
	Image $R_{\rm wall}$	22.9 au
	Model $R_{\rm wall}$	27.8 au
1.6μm	Model $R_{\rm peak}$	30.8 au
	Model $R_{\rm wall}$	28.3 au

Table 3.2 *Radial locations of the outer-ring emission found from images and best-fit models.*

3.5 Discussion

Our continuum ALMA observations reveal a disk around T Cha with three main dust components: an inner emission, gap, and an outer ring. By modeling the real part of the visibilities with a Nuker profile and a Gaussian, we can constrain the physical properties of these three components.

Our main result is the detection of an unresolved inner disk ($\leq$ 1 au radius, based on visibility modeling), where most of the 3 mm flux density arises from thermal dust emission, likely from mm-sized grains (see Sect. 4). This, combined with the already known outer emission, implies that the disk of T Cha has a gap in the population of millimeter-sized grains. Previous work has also inferred a very compact inner disk in the NIR ($R_{\rm out} \leq 0.17$ au, Olofsson et al., 2011, 2013). Hence, whatever is the physical origin of the gap, it has to allow a detectable inner disk at multiple wavelengths.

The detection of a gap, and not of a cavity, in combination with other properties inferred from our analysis, enables us to exclude several mechanisms for the origin of the structures in the disk of T Cha. For instance, particle trapping at the outer edge of a dead zone can create structures as observed in transition disks (e.g. Flock et al., 2015; Ruge et al., 2016). Inside a dead zone, where turbulent velocities of particles are low, grain growth is efficient and small grains are depleted. As a result, we expect to observe a NIR and a mm-cavity of the same size. When an MHD disk wind acts together with a dead zone, smaller cavities will be present at shorter wavelengths. However, this latter scenario does not preserve a long-lived inner disk because the MHD wind removes efficiently the inner material, leaving a cavity, not a gap (Pinilla et al., 2016b). As a consequence, a dead zone, or a dead zone *and* MHD disk wind, is not a likely origin for the observed *gap* in the disk of T Cha.

Photons from the central star can heat the upper layers of the disk gas, increasing the thermal velocity of the gas to the point where it becomes gravitationally unbound to the star-disk system. This thermally driven wind, or photoevaporation, contributes to disk mass loss, the removal of disk material from the inside out

(Ercolano & Pascucci, 2017) and gap formation (second disk evolutionary stage in Figure 6 of Alexander et al., 2014).

While there is evidence in T Cha of a disk wind that can be photoevaporative in nature (Pascucci & Sterzik, 2009; Sacco et al., 2012), photoevaporation predicts only a specific combination of mass accretion rate and gap size (see Figure 6 in Ercolano & Pascucci, 2017). T Cha shows strong photometric variability and UX Ori-like behavior, inferred from significant changes of prominent emission lines, such as H_α. If this variability is due to accretion episodes, the mean accretion rate of T Cha is $4 \times 10^{-9}\, M_\odot$/year (Schisano et al., 2009). With this mass accretion rate and our gap size estimate $\geq$20 au, star-driven photoevaporation does not appear to be a plausible mechanism to open the gap seen in the T Cha disk. This argument is valid even in the presence of variability because the timescale for the hole to grow from the initial gap opening radius to $\sim$20 au is longer than the timescale for draining material by accretion. If the accretion rate in the outer disk is variable then there will be episodes when the inner disk refills and there is accretion onto the star, which will reduce the gap size.

Both cavities and gaps are expected from planet-disk interactions. While a cavity can be opened by a massive planet, Pinilla et al. (2016a) demonstrated that an inner disk can be maintained at timescales greater than 1 Myr for planets of mass $\sim 1.0\, \mathrm{M_{Jup}}$. More massive planets filter out all kind of grains (from micron- to mm/cm-sized particles), and as a result the inner disk is gone after few million years of evolution.

The spatial segregation of small and large particles seen in T Cha, as observed in the NIR and mm-emission respectively, is another expected outcome of planet-disk interactions, because the small grains are expected to follow the gas while the large grains move and accumulate in pressure maxima. Indeed, radial segregation of small vs. large grains has been observed in different transition disks following the expected results from planet-disk interaction models (Garufi et al., 2013; Pinilla et al., 2015b). Using the wavelength-dependent grain size relationships resulting from the 2D hydrodynamical and dust evolution models of de Juan Ovelar et al.

(2013), we can constrain the mass of the potential embedded planet inside the gap. With the values reported in Table 3.2, we find $R_{\rm wall,NIR}/R_{\rm peak,mm} = 0.8$ which implies a $1.2\,{\rm M_{Jup}}$ planet in the single-planet scenario and with the specific disk properties assumed in de Juan Ovelar et al. (2013) (model outcomes are sensitive to disk properties, especially viscosity). The planet mass is consistent with the upper limits reported in Pohl et al. (2017), leaving open the possibility that the gap in the disk of T Cha is carved by a giant planet.

While a large millimeter gap can be consistent with a single planet, Dong & Fung (2017) show that the width of a single-planet gap observed at near-infrared wavelengths should be only $\sim 30-40\%$ of the gap radial location. Using $R_{\rm wall,NIR}$ from Table 3.2 and the coronagraph mask diameter of 185 mas gives a minimum NIR gap width of $\sim 18\,{\rm au}$, which is $\geq$64% of the gap's radial location. As such it is unlikely that the gap in the disk of T Cha is opened only by one planet. Rather multiple embedded planets, whose individual gaps overlap, contribute to open the large observed gap.

In summary, we find that the most likely origin for the gap in the disk of T Cha is due to planet-disk interactions. If the gap is carved by a single planet, we find that a mass of $1.2\,{\rm M_{Jup}}$ is required. However, because of the large gap width, multiple less massive planets with overlapping gaps are more probable. Future ALMA observations could constrain the size of a potential gap in the gas surface density (e.g. van der Marel et al., 2016), which is crucial to distinguish between single or multiple planets (e.g. Zhu et al., 2011).

CHAPTER 4

The evolution of dust-disk sizes from a homogeneous analysis of 1-10 Myr-old stars

4.1 Introduction

Protoplanetary disks, consisting of gas and dust around young ($\sim$1–10 Myr) stars, are the sites of planet formation. Because the expected population of planetesimals (km-sized bodies) or larger planetary embryos within these disks is not directly observable, we rely on millimeter observations sensitive to the largest detectable dust grains to constrain the timing, location, and mechanics of planet formation. The radial distribution of these mm/cm sized grains within the disk is a key parameter governing the planet making potential of a disk. For instance, in the pebble accretion scenario, the total amount of millimeter-sized grains and their inward flux are critical to form planets (e.g Ormel et al., 2017).

Millimeter surveys of protoplanetary disks reveal typical disk properties, as well as their spread, and can be used to identify empirical relationships between disk properties and disk/host-star properties. Such relations are essential to test and inform planet formation (e.g. Mulders et al., 2015; Pascucci et al., 2018), as well as in understanding the diversity of observed exo-planetary systems.

ALMA surveys of the nearby low-mass star-forming regions of Lupus, Chamaeleon I and USco (Ansdell et al., 2016; Pascucci et al., 2016; Barenfeld et al., 2016, respectively) each found a positive correlation between the mass in millimeter grains (hereafter,$M_{\rm dust}$) and stellar mass (hereafter, $M_\star$) for their respective region. It was also shown that the relationship steepens with the age of the region (Pascucci et al., 2016), suggesting that the amount of pebbles available to form planets decreases faster for disks around low-mass stars.

Pre-ALMA observations of the brightest disks in different star-forming regions reported dust disk outer radii ranging from 22 to 440 au (Isella et al., 2009; Andrews

et al., 2010; Guilloteau et al., 2011). In addition, a correlation between disk size and disk luminosity ($L_{\rm mm}$) was identified early on (Andrews et al., 2010). However, only the ~ 3 times larger SMA sample analyzed by Tripathi et al. (2017a) could quantify the relation and found that $L_{\rm mm}$ scales as the square of the dust disk radius.

Dust disk size estimates from ALMA surveys have been carried out for Lupus (Tazzari et al., 2017; Andrews et al., 2018b), USco (Barenfeld et al., 2017) and the Orion Nebula Cluster (Eisner et al., 2018), yet each has been performed with different modeling techniques and assumptions. Tazzari et al. (2017) estimated Lupus disk sizes by fitting a two layer model (Chiang and Goldreich, 1997) to visibilities, and found that Lupus disks tend to be larger than previously reported disk sizes in Tau/Aur and Oph observed at similar angular resolutions. Andrews et al. (2018b) estimated the disk sizes of Lupus by fitting Nuker brightness profiles, and compared them to the disk sizes of Tau/Aur and Oph as estimated by Tripathi et al. (2017a) and did not come to the same conclusion that the Lupus disks are generally larger. While both works analyzed sub-samples of the same ALMA campaign, the Andrews et al. (2018b) sample was ~ 2 times larger than the Tazzari et al. (2017) sample which had a 4 mJy cutoff, excluded unresolved disks as well as disks with resolved gaps or cavities. However, both works determined that disks within Lupus have a positive correlation between disk size and $L_{\rm mm}$. Barenfeld et al. (2017) estimated the sizes of disks within the older USco region by fitting radiative transfer models to visibilities using a truncated power law for surface density. They found USco disks to be typically three times smaller than the disks in Oph, Tau/Aur and Lupus, and suggested that USco followed the same positive correlation between disk size and $L_{\rm mm}$ as Tripathi et al. (2017a). Finally, Eisner et al. (2018) measured disks within the Orion Nebula Cluster by fitting a 2D elliptical Gaussian to ALMA continuum maps. Their work found a correlation between disk size and $L_{\rm mm}$ as well, and additionally suggested that Chamaeleon I disks, using HWHM measurements from Pascucci et al. (2016) for Chamaeleon I disk sizes, are significantly smaller than Oph, Tau/Aur, and Lupus.

While trends seen within each region are robust, inferences among regions might

be compromised by the use of varying modeling techniques (i.e. image plane measurements, radiative transfer modeling, visibility fitting with profiles generated by different functions) and assumptions (i.e. opacity, paramaterized disk height, fixed surface density slope, disk temperature, inner radius location). Andrews et al. (2018b) addressed this problem by comparing the regions of Oph, Tau/Aur and Lupus in a homogeneous way, finding that mm-luminosity scales as the square of the dust-disk radius was common to all three regions. This suggests that the scaling law between disk radius and stellar luminosity may be universal.

In this work we expand on the results of Tripathi et al. (2017a) and Andrews et al. (2018b), using the same modeling techniques in order to present a homogeneously derived census of disk sizes within five regions of varying ages. In Section 4.2 we discuss our sample selection, consisting of a combination of disk size estimates from literature for Oph and Tau/Aur (Section 4.2.1) with our own estimates for disks within Lupus, Chamaeleon I and USco (Section 4.2.2). Our reduction of the ALMA observations is discussed in Section 4.3. To estimate disk sizes, we model observed sky brightnesses using axisymmetric radial-profile models which are fit to ALMA visibilities (see Section 4.4). Because not every source is detected, or results in a model that provides a disk size estimate, Section 4.4.1 provides details on the selection criteria we use for the final sample of disks used in our analysis. In Section 4.5 we summarize our results and compare disk sizes between regions. We use a variety of statistical tests to assess if relationships exist between disk properties and stellar-host properties in Section 4.5.1. Finally, we discuss and summarize our results in Sections 4.6 and 4.7.

4.2 Initial Sample Selection

We aim to obtain a representative sample of stars with protoplanetary disks from different regions spanning a range of ages. In order to make a proper comparison, we have also chosen regions observed at similar wavelengths and spatial scales (see Table 4.1). Each of the disks included in this work belongs to the following 5 regions:

Table 4.1. Regions included in our analysis

Region	Telescope	λ (μm)	Typical Beam (arcsec)
Oph	SMA	880	$0.41 - 0.78$
Tau/Aur	SMA	880	$0.41 - 0.78$
Lupus	ALMA	935-954	$0.28 - 0.35$
Chamaeleon I	ALMA	884-887	$0.5 - 0.7$
USco	ALMA	876-975	$0.35 - 0.75$

Ophiuchus which is $\sim$1-2 Myr (Luhman and Rieke, 1999), hereafter Oph; the Taurus & Auriga Complex which is $\sim$1-3 Myr (Luhman, 2004), hereafter Tau/Aur; Lupus which is $\sim$1-3 Myr (Comerón, 2008; Alcalá et al., 2014); Chamaeleon I which is $\sim$2-3 Myr (Luhman, 2008), hereafter Cha I; and the Upper Scorpius OB association which is $\sim$5-11 Myr (Preibisch et al., 2002; Pecaut et al., 2012; Slesnick et al., 2008), hereafter USco.

We use previously published disk sizes for Oph and Tau/Aur with observations obtained by the Submillimeter Array (SMA; see Section 4.2.1 for more details), while we estimate sizes for disks in Lupus, Cha I, and USco from archival ALMA data (Section 4.2.2). Stellar masses are also derived homogeneously for the latter three regions after re-scaling literature stellar luminosities to the Gaia DR2 distances (Section 4.2.2).

4.2.1 Oph and Tau/Aur

We include in our analysis previously derived disk sizes for sources in the Oph and Tau/Aur star-forming regions (Tripathi et al., 2017a), relying on the Gaia-updated values reported in Andrews et al. (2018b). From the entire sample of 50 disks we

exclude TW Hya, HD 163296, and LkHα 330 because they do not belong to Oph nor Tau/Aur.

Andrews et al. (2018b) derived disk sizes also for 56 sources belonging to the Lupus star-forming region, from ALMA observations originally presented in Ansdell et al. (2016). We use these literature values only to verify that our modeling approach delivers the same results (Section 4.2.2 and Appendix B.1.1) and justify the extended comparison of disk sizes carried out here. We note, however, that the Oph and Tau/Aur samples come from flux-limited SMA observations, and consequently are biased towards brighter objects than the Lupus, Chamaeleon I, and USco samples. We take this bias into account when interpreting the results.

4.2.2 Lupus, Chamaeleon I, and USco

To test if our approach for estimating disk sizes delivers the same results as Tripathi et al. (2017a) and Andrews et al. (2018b), we re-reduce and re-analyze the ALMA data from the Lupus star-forming region. We include in our sample all the 62 detections from the ALMA project `2013.1.00220.S` (PI: Johnathan Williams) as presented in Ansdell et al. (2016). As discussed in Appendix B.1.1 and shown in Figures B.1 and B.2, our method retrieves the same disk sizes as those in Andrews et al. (2018b) for most sources, as well as the same disk size-millimeter luminosity relation within the quoted uncertainties. Because the uncertainties reported in Andrews et al. (2018b) are systematically lower than ours (see Appendix B.1.1), we prefer to use the inferred disk sizes from our modeling in the analysis and discussion sections of this paper in order to have consistent uncertainties across all of our samples.

For the Chamaeleon I region, we include as part of our sample the 66 detections reported in Pascucci et al. (2016) from ALMA project `2013.1.00437.S` (PI: Pascucci, I.). Five detections and nine non-detections from that project were re-observed at 5 times higher sensitivity in project `2015.1.00333.S` (PI: Pascucci, I.). We use the 11 detections reported in Long et al. (2018), giving us a total of 72 Chamaeleon I disks.

Finally, USco was observed in projects 2011.0.00526.S and 2013.1.00395.S (PI: Carpenter, J.) and results were originally presented in Carpenter et al. (2014) and Barenfeld et al. (2016) respectively. To estimate disk sizes we have selected those 50 USco targets that were detected.

Stellar masses

For Lupus, Chamaeleon I, and USco we also re-derive stellar masses in order to (a) have self-consistent values for the ALMA datasets, and (b) take advantage of the newer Gaia DR2 distances. Stellar masses are determined following the Bayesian inference approach described in Pascucci et al. (2016). First, we collect stellar effective temperatures and bolometric luminosities from the literature: For Lupus we rely on Alcalá et al. (2014); Biazzo et al. (2017); Frasca et al. (2017); Andrews et al. (2018b); For Chamaeleon I on Manara et al. (2016, 2017); while for USco we rely on Barenfeld et al. (2016). Then, we scale these luminosities to the new Gaia DR2 distances. For sources in Chamaeleon I and USco we query distances from the Bailer-Jones et al. (2018) Gaia catalogue. When there is no DR2 distance available, we use the median sample distance of 190 pc for Chamaeleon I and 144 pc for USco, both of which agree with the values obtained from all members of each region (see Roccatagliata et al. 2018 and de Zeeuw et al. 1999). For our Lupus sample, we take the GAIA DR2 distances as presented in Andrews et al. (2018b). J11072825-7652118 (Chamaeleon I) and J16141107-2305362 (USco) have anomalously large DR2 distances (744 pc, and 6011 pc respectively). For these three sources we also use the median distance of each region as given above. Following Pascucci et al. (2016), we assume an uncertainty of 0.02 dex in the stellar temperature for spectral types earlier than M3 and 0.01 dex for later spectral types and a 0.1 dex uncertainty on all stellar luminosities. Table B.1 within Appendix B.2 summarizes the adopted and inferred stellar parameters for Lupus, Chamaeleon I, and USco.

4.3 ALMA Observations and Data Reduction: Lupus, Cha I and USco

We re-reduce band 7 ($\sim 880 - 975\mu$m) observations of similar sensitivity for the sample of disks presented in Section 4.2.2. The data reduction steps that lead to the calibrated visibilities are described below.

In general, the raw data is taken from the ALMA archive and measurement sets are built using the calibration scripts created by the North American ALMA Science Center (NAASC). For this step we use the same version of the Common Astronomy Software Applications (CASA, McMullin et al. 2007b) as used by the NAASC noted within the downloaded scripts. These scripts perform phase, bandpass and flux calibrations and create the standard CASA measurement sets containing the visibilities.

Because the 8 outermost edge channels in each spectral window are typically noisy, we remove them from our measurement sets. Next, we average the measurement sets in time and by channel. The parameters used to do time averaging and spectral window averaging are unique to each source with the goal of ending up with similarly sized (in number of data points) data sets. Typically, we average spectral windows by widths of 19 channels. We average our data in time by a variable number of seconds based on the total amount of data available to us (this varies by exposure time and number of baselines). However, we constrain all time averaging to be between 2 and 30 seconds. For these steps, we use `CASA` version `4.7.2-el6`.

Measurement sets from the project `2011.0.00526.S` (USco) were directly provided by the PI and co-author J. Carpenter. For these sources we used a width of 22 channels for the spectral window averaging.

Calibration of the sources in projects `2015.1.00333.S` (Chamaeleon I) and `2013.1.00395.S` (USco) were performed using `CASA` version `4.7.2-el6`. Calibration of the sources in science goal `A001_X11d_X13` (Chamaeleon I) and project `2013.1.00220.S` (Lupus) was performed using `CASA` version `5.1.1-5.el7`. These exceptions were required due to incompatibilities between the NAASC provided calibration scripts and system libraries.

In addition, for the 10 brightest Chamaeleon I disks[1], we use self-calibrated visibilities from Pascucci et al. (2016). The disk sizes resulting from self-calibrated visibilities are the same as those derived from non-self-calibrated visibilities, hence we do not apply self calibration to the other regions.

4.4 Modeling Method

In this section we describe our approach to model the calibrated continuum visibilities and our procedure for determining the dust disk outer radius ($R_{\rm eff}$). To expand upon the results presented in Tripathi et al. (2017a) and Andrews et al. (2018b), we use a similar method to derive disk sizes for Lupus, ChaI and USco.

As high-contrast asymmetries seem to be uncommon even in high-resolution ALMA images (Long et al., 2018; Andrews et al., 2018a), we assume axisymmetric disks and use a parametric radial intensity profile to fit the disk intensity in the visibility domain.

For all modeling, we fit disk inclination (i), position angle (PA), and disk center offsets (dRA, dDec) in addition to the free parameters connected to the chosen radial profile function described below. All modeling also includes a *nuisance* parameter (lnwcorr) defined as the natural logarithm of the factor by which the weights of the observed visibilities are overestimated.

For all disks, we test two different functions for generating the radial profile shape: a Nuker profile (Lauer et al., 1995b) and a Dirac delta function (point source). By comparing the best-fit models of each function (using the reduced χ^2) for a given source, we are able to determine if the disk is resolved (Nuker fits better) or not (point source fits better).

The Nuker profile was shown by Tripathi et al. (2017a) to be a useful radial profile function thanks to its ability to reproduce the sky brightness of both full and transition disks. The radial intensity of a Nuker profile is expressed as:

[1]These disks are: J10581677–7717170, J10590699–7701404, J11022491–7733357, J11040909–7627193, J11074366–7739411, J11080297–7738425, J11081509–7733531, J11092379–7623207, J11094742–7726290, and J11100010–7634578.

$$I(r) = F_0 \left(\frac{r}{R_{\rm t}} \right)^{-\gamma} \left[1 + \left(\frac{r}{R_{\rm t}} \right)^{\alpha} \right]^{(\gamma-\beta)/\alpha} \tag{4.1}$$

where r is the radial distance, F_0 is the amplitude coefficient, $R_{\rm t}$ is the transition radius, α is the transition index, while γ and β are indexes that define the inner and outer cutoff, respectively. Figure 2 in Tripathi et al. (2017a) nicely illustrates how each parameter affects the shape of the Nuker profile.

For a given profile (Nuker or point source), we produce a synthetic disk image which is Fourier transformed and sampled at the same spatial frequencies as our observational data using `GALARIO` (Tazzari et al., 2018). Our modeled visibilities are fit to the real and imaginary parts of the observed visibilities using the `emcee` implementation (Foreman-Mackey et al., 2013b) of the Markov Chain Monte Carlo method (MCMC). Uniform priors are used over a parameter space defined as: $R_{\rm t} \in [0.005, 3]$ au, $\gamma \in [-11, 4]$, $\log \alpha [0.3, 1.3]$, $\beta \in [1, 17]$, $\log F_0 \in [3, 12]$ Jy/Sr, $i \in [0, 90]$ deg, PA $\in [0, 179]$ deg, dRA $\in [-3, 3]$ arcsec, dDec $\in [-3, 3]$ arcsec, lnwcorr $\in [-10, 10]$. We cover this parameter space with 70 chains (ensemble sample walkers) which individually take 100,000 steps in order to sample the posterior probability distribution function (PDF). The location of each walker is initialized using random draws from a truncated normal distribution about the median value for each parameters following an initial MCMC burn in cycle using 100 walkers and 1000 steps. An example best fit model for the source J16085468-3937431, is given in Figures 4.1 and 4.2, all other fits are provided in the electronic version of this paper.

MCMC fitting produces a chain of models. We use the autocorrelation length as a guide to understand at what point in the chain convergence occurs. This typically happens well before 10^4 steps per walker, leaving us with approximately 6.99×10^6 samples per disk. We then conservatively ignore half of the converged chain length and only consider the 3.5×10^6 samples from the end of the MCMC chain to estimate the posterior probability density function (PDF), and parameter uncertainties.

The bounds of the parameter space explored by the MCMC walkers for the variables i, PA, dRA, dDec and lnwcorr is the same for all regions. The remaining free parameters explored is determined by the radial profile being modeld (Nuker or

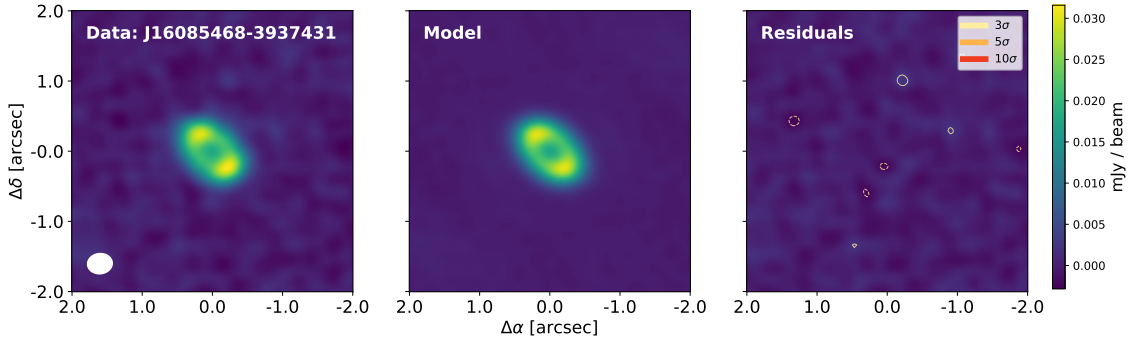

Figure 4.1 Comparison of the ALMA 887 μm observation of J16085468-3937431 with our best-fit model. The first panel shows the ALMA observation as a continuum map generated using the CASA `clean` command with Briggs weighting with a robustness parameter of 0.5. The middle panel shows a continuum map generated from our model using the same UV spacings as the ALMA observation. The last panel shows the residuals between the first two panels (residuals of 3, 5, and 10 sigma are denoted as outlines).

point-source). For these parameters, the bounds are adjusted for each star-forming region based on prior exploration of the parameter space to ensure no truncation of the posterior distributions. The boundaries we chose are similar to those in Tripathi et al. (2017a) and Andrews et al. (2018a), and are chosen to cover well the posterior distribution.

At this point it is important to point out that the physical parameter we are interested in, disk size, is not one of the free parameters being fit, and additionally, the Nuker profile has no distinct outer edge. To deal with these two issues and following Tripathi et al. (2017a), we estimate the *effective radius* ($R_{\rm eff}$), the radius at which a given fraction (x) of the cumulative flux is contained. Here, we compute two $R_{\rm eff}$: R_{68}, the radius containing 68% of the flux, to connect our results to the low- and medium-resolution disk surveys (Tripathi et al., 2017a; Andrews et al., 2018b); and R_{90}, the radius containing 90% of the flux. The latter is done primarily to test how well low- and medium-resolution surveys recover disk radii obtained via high-resolution ALMA surveys (Long et al., 2018; Huang et al., 2018), although we also find it useful when comparing our disk sizes with dynamical features in the Solar System (see Section 4.6.2).

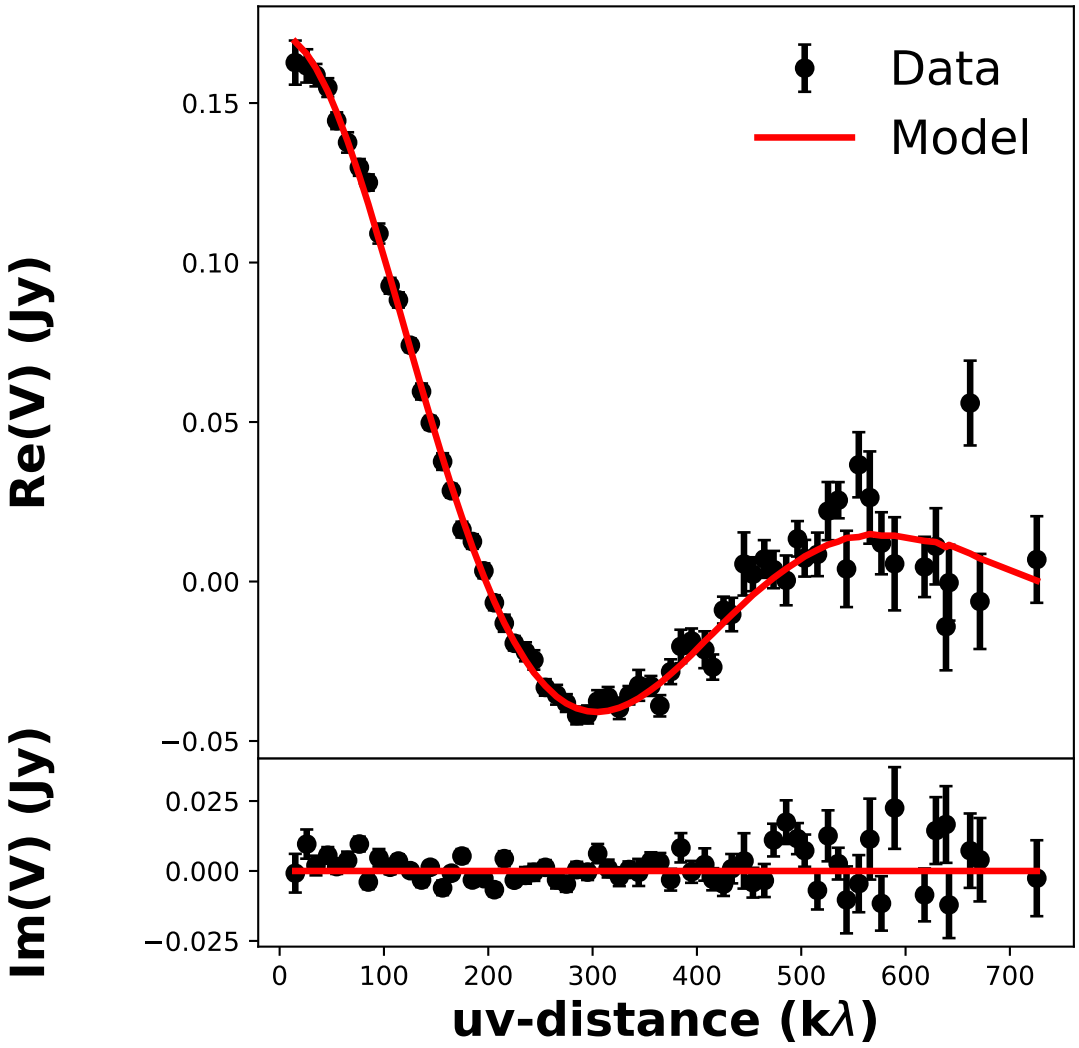

Figure 4.2 A comparison of our model with the observed visibilities for the source J16085468-3937431. The real and imaginary components of the observed visibilities (filled circles) are azimuthally averaged and deprojected. For the clarity of the figure, the visibility data is further binned in increments of 10kλ. Our best-fit (Nuker profile) model is plotted in red. Plot made with the UVPLOT package (Tazzari, 2017).

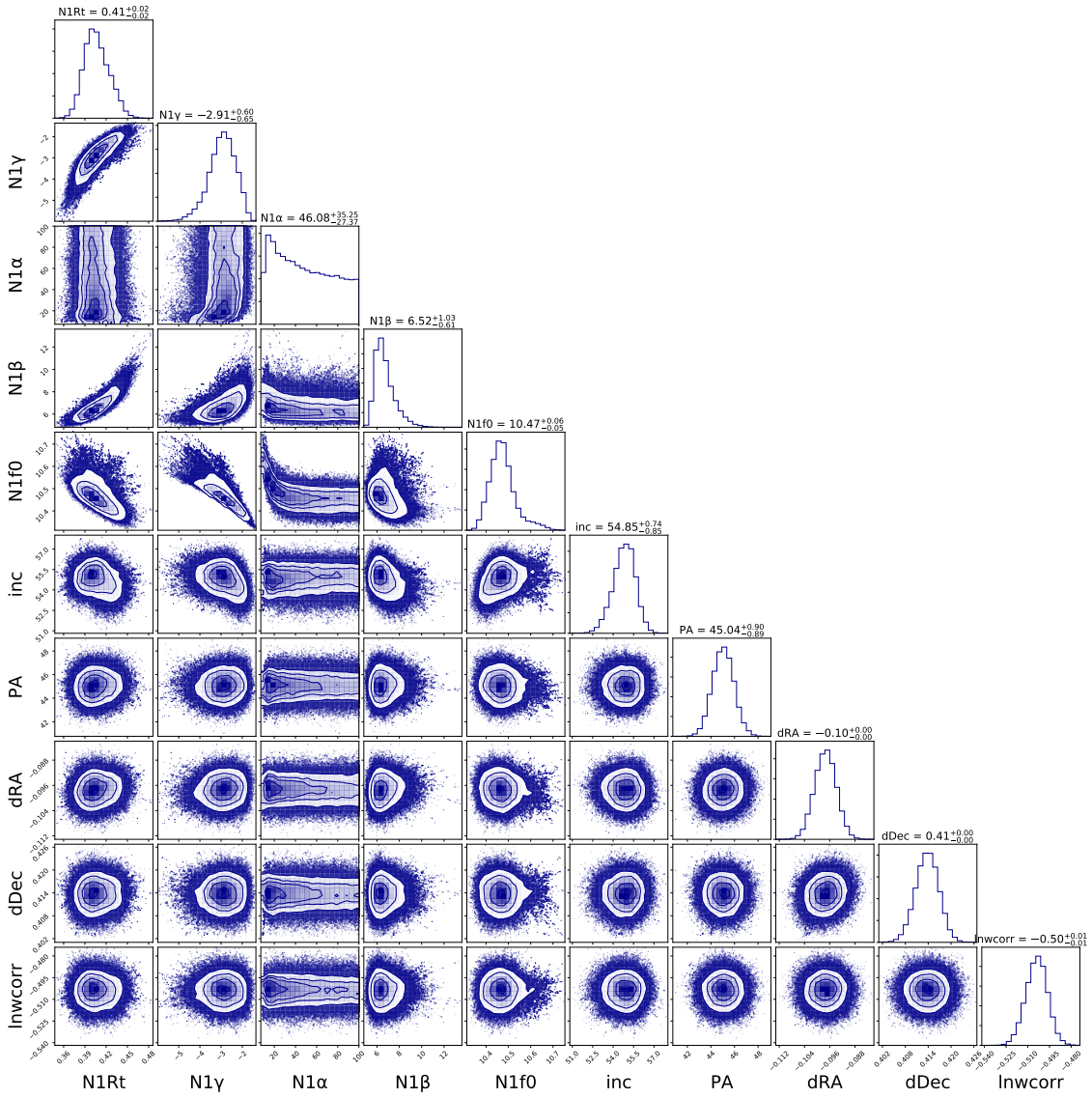

Figure 4.3 Corner plot of the free parameters generated from the MCMC fitting of J16085468-3937431. Marginalized distributions are shown as histograms at the top of each column. Parameters with names preceded by "N1" refer to the corresponding Nuker parameters (see Equation 4.1). Parameters used to deproject and center the disk are inclination (inc), position angle (PA), right ascension offset (dRA), and declination offset (dDec). The last column is the fitted weight correction factor (lnwcorr; see Section 4.4).

We randomly sample 5000 models from the second half of our MCMC chain, and for each model we calculate $R_{\rm eff}$. This gives us a posterior distribution of disk sizes. We take the median value to be our $R_{\rm eff}$ estimate, and quantiles of 16 and 84% as our upper and lower confidence intervals.

In order to determine wheter the observations resolve the source or not, we independently fit and test models created by both a Nuker profile (resolved) and a point source (unresolved) for each observation. The reduced chi-square statistic of the best Nuker profile and best point source model are compared. In cases where the point-source results in a better fit, we determine that the source is unresolved. To compute the upper-limit on the size of unresolved sources, we take the results of the Nuker model, and use the 84th percentile $R_{\rm eff}$ (what would be the upper confidence interval on a resolved source) as the $R_{\rm eff}$ upper limit. We expect that these disks are most likely limited by the resolution of the telescope, but take this conservative approach in order to not misinterpret disks that are large and faint (sensitivity limited).

Occasionally we notice walkers stuck within local minima of our posteriors. This appears to happen in less than 15% of our sources. Because not all of these stuck walkers are identifiable by eye, we make no attempt to remove them in order to safeguard against introducing systematic errors. However, we measured the impact of stuck walkers on several sources and found that the decision to leave the chains unaltered ultimately results in small changes, and slightly larger errors, in our $R_{\rm eff}$ estimates. For example, an estimation of R_{68} for J16000236-4222145 with, and without stuck walkers results in values of $81.67^{+1.97}_{-2.95}$ and $85.28^{+2.62}_{-2.30}$ arcsec respectively.

4.4.1 Subsample of systems with estimated disk sizes

While we have modeled all of the detected sources within the Lupus, Chamaeleon I, and USco regions, we do not use every source in the remainder of our analysis.

Unless otherwise noted, we have removed from our sample, disks around multiple star systems with separations $\leq$ 2.0" in order to make our sample consistent with those in Tripathi et al. (2017a) and Andrews et al. (2018b). These papers imposed

the separation threshold to exclude disks that might have their sizes truncated by dynamical interactions with their companions (see, e.g. Manara et al., 2019). However, we do not impose a flux cutoff of 2 mJy as in Andrews et al. (2018b).

Additionally, we find 15 disks with best-fit models that we do not trust, hence we remove them from our analysis. The details and further discussion of the excluded models is given in Appendix B.3. This leaves us with 152 disks: 50 from Lupus, 58 from Chamaeleon I and 44 from USco which we include in our analysis.

To better determine if our final disk samples are representative, or biased (being a subset of each region's complete disk population), we attempt to reproduce previously reported disk-host ($\log M_{\rm dust} - \log M_\star$) relationships with our subset of disks (using the equivalent $\log L_{\rm mm} - \log M_\star$ relationship). With the exception of Oph, this relationship has been quantified in Ansdell et al. (2016) and Pascucci et al. (2016), and we use the fitting slopes reported in Pascucci et al. (2016) for our comparison given that stellar masses in this paper are estimated in the same way. In those works, a larger sample size for each region (than we use here) is included in the analysis because they are able to include flux density non-detections. We find that for our subset of disks in each region, $\log L_{\rm mm} - \log M_\star$ is correlated for Lupus, Chamaeleon I and USco, and is not correlated for the regions Oph and Tau/Aur (see Appendix B.4; Figure B.4 and Table B.2). For the regions with correlations (Lupus, Chamaeleon I and USco) we find consistently shallower slopes as it is expected from samples lacking the faintest disks (see Section 4 in Pascucci et al. 2016). The results of our modeling for individual sources is given in Table B.4.

Appendix B.5 shows that R_{90} and R_{68} are strongly correlated and we derive an equation to convert R_{68} into R_{90} based on our modeling of the Lupus, Chamaeleon I and USco disks. Additionally, we compare in Appendix B.1.2 disk radii obtained here from those obtained at high-resolution for 26 sources and demonstrate that these lower resolution surveys are sufficient to determine dust disk sizes.

4.5 Results

We present a census of 199 homogeneously derived dust-disk sizes from five star-forming regions and associations. In this paper, we estimate the sizes of 152 disks: 50 from Lupus, 58 from Chamaeleon I and 44 from USco. Of the 152 disks we model, we find 85 to be resolved, and 67 to be unresolved. Of the unresolved disks, 20 are in Lupus, 25 in Chamaeleon I and 22 in USco[2]. To this we add the literature values for 20 Oph disks and 27 Tau/Aur disks; these disk size estimations were originally modeled in Tripathi et al. (2017a) but we use the updated values reported in Andrews et al. (2018b).

Table 4.2 summarizes the median and maximum R_{68} and R_{90} sizes of resolved disks within each region. Both interpretations of $R_{\rm eff}$ are useful to consider. R_{68} is necessary in order to compare all 5 regions, since only R_{68} sizes are available for Oph and Tau/Aur. Consequently, the majority of our analysis uses R_{68} as a proxy for $R_{\rm eff}$. However, R_{90} better approximates the full extent of the disk, and we find it useful to consider in the discussion (Section 4.6).

A comparison of the size distribution for each region is shown in Figure 4.4. Individual resolved disks within each region are shown as swarmplots with a shaded box surrounding the distribution's 25-75% quartiles and a horizontal line denoting the median disk size. Whiskers extend from the shaded boxes defining the 0-25% and 75-100% quartiles. While it may be tempting to infer a trend of decreasing disk size with age, it is important to recall that the Oph and Tau/Aur samples are biased towards higher luminosity disks, and therefore, a direct comparison of size distributions, in particular of the minimum and median size, between the SMA and ALMA samples is unjustified. The largest disks, being also among the brightest (see Section 5.1), are the least affected by the bias mentioned above, as well as by differences in survey sensitivity and spatial resolution. Table 4.2 and Figure 4.4 show that all regions, except USco, have multiple disks with R_{68} greater than 115 au (while USco has only one disk with R_{68} larger than 80 au), hinting that USco disks

[2]The modeling results of individual sources are given in Appendix B.6

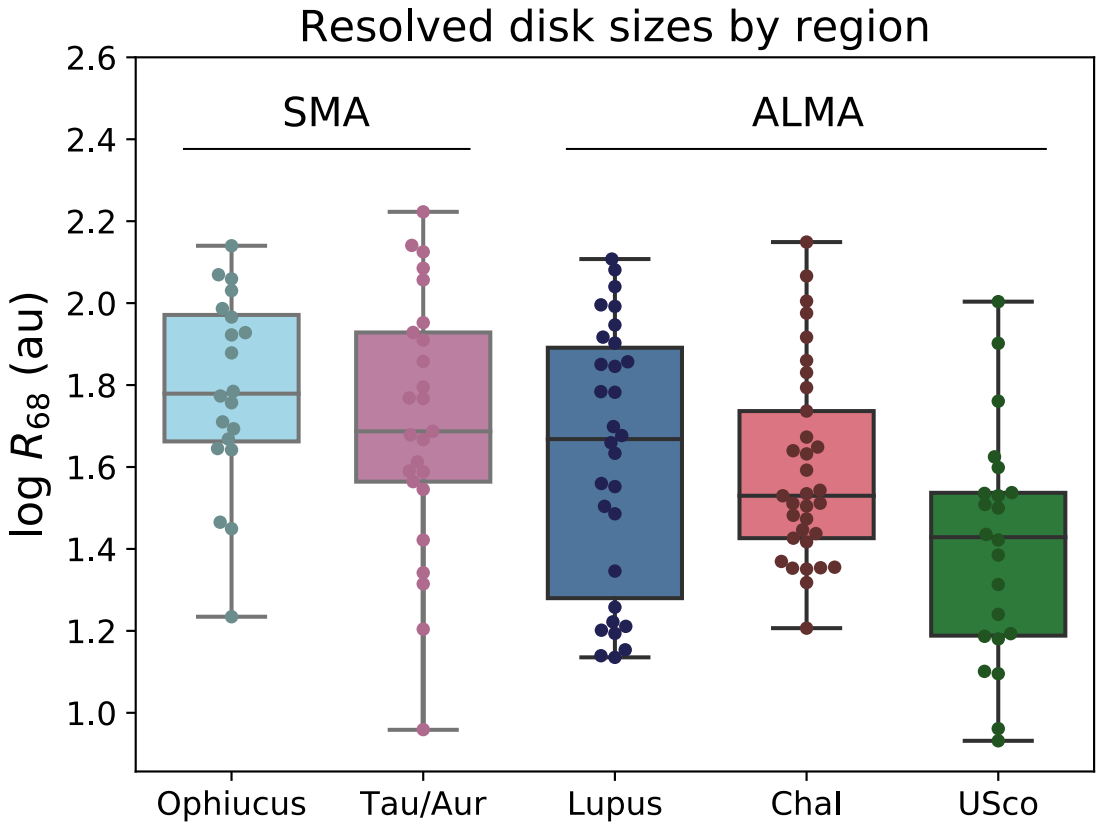

Figure 4.4 Swarmplots for resolved disks in different regions, ordered by age. The boxplots include a shaded region surrounding the R_{68} 25-75% quartiles, the horizontal line denotes the median disk size, while whiskers define the 0-25% and 75-100% quartiles. The regions observed with the SMA are greyed out because they are biased to the brightest millimeter disks, hence their size distributions should not be directly compared to the regions observed by ALMA.

Table 4.2. Summary statistics for resolved disks

		R_{68} (au)		R_{90} (au)	
region	count	median	max	median	max
Oph	20	60.1	138.0	...	...
Tau/Aur	25	48.6	167.0	...	...
Lupus	30	46.6	128.1	63.2	213.1
Chamaeleon I	33	33.9	140.9	43.1	231.3
USco	22	26.8	100.8	33.4	126.2

Note. — Oph and Tau/Aur R_{68} values are from Andrews et al. (2018b).

are smaller than those in other regions. This is in agreement with Barenfeld et al. (2017) who used a different approach to determine USco disk sizes[3] and concluded that that they are ~ 3 times smaller than those in Oph, Tau/Aur and the subset of the Lupus disks modelled by Tazzari et al. (2017).

To further examine if there is a difference in the observed distributions of the now homogeneously-derived disk sizes, we focus on the three ALMA regions observed with similar sensitivity and spatial resolution (Lupus, Chamaeleon I and USco) and show the R_{68} cumulative distribution functions (CDF) in Figure 4.5. Uncertainties on the CDF are determined using the Kaplan-Meier estimator[4] and include unresolved disks with upper limits. However, the CDF uncertainties do not consider our disk size uncertainties. There are two features in Figure 4.5 that are worth noting. First, there is a deficit of large disks in USco when compared to Lupus

[3]Barenfeld et al. (2017) fit power-law models to the dust surface density and carry out continuum radiative transfer calculations to compute the surface brightness and visibilities.

[4]We use the Python lifelines (Davidson-Pilon et al., 2019) Kaplan-Meier implementation.

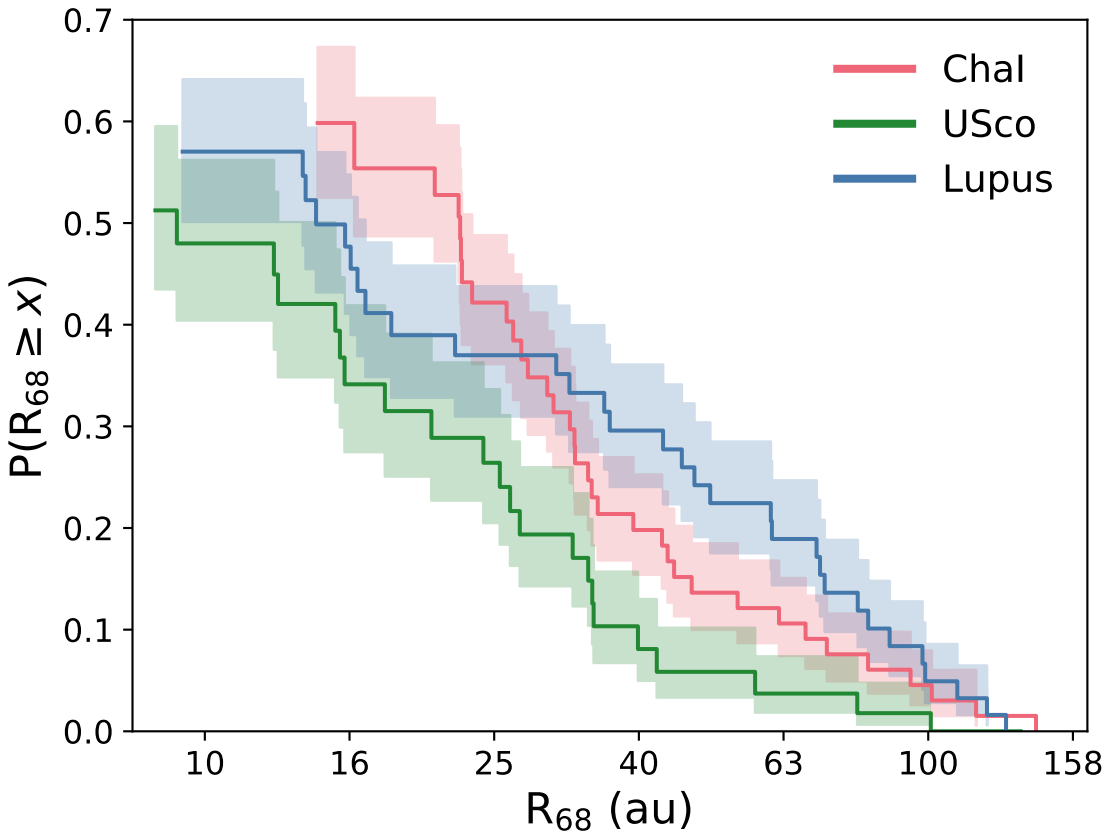

Figure 4.5 Cumulative disk sizes distributions for our modeled regions: Lupus, Chamaeleon I and USco. Shaded regions indicate 1σ confidence intervals.

and Chamaeleon I. Second, all regions host small disks (as small as $\sim 15\,\mathrm{au}$), and USco in particular appears to have a population of even smaller disks. However, the smaller end of the disk-size distributions are impacted by the source distance combined with the chosen beam size and sensitivity. For this reason we make no inferences regarding the smallest disks.

In order to test if two regions are drawn from the same empirical distribution function, we compare each region with every other using the Anderson-Darling test (Anderson and Darling, 1952). We report the Anderson-Darling statistic and significance level (sig.) in Table 4.3. The significance level is the level at which we cannot reject the null hypothesis that the samples are drawn from the same distribution. The small values of 0.013 and 0.014 suggest that the USco sample is unlikely to be drawn from the same parent disk-size distribution of Lupus and Chamaeleon I, respectively. With a significance level of 0.1 we are not able to determine if Lupus and Chamaeleon I are drawn from differing distributions or not with any high degree of confidence. Oph and Tau/Aur, with their similarly biased samples have a significance level $> 25\%$, suggesting that there is no difference in the distribution from which the two regions' brightest disks are drawn.

To test if these results depend on the selection of R_{68} or R_{90}, we produced a R_{90} version of Figure 4.5, and performed the Anderson-Darling tests on Lupus, Chamaeleon I and USco using our R_{90} disk sizes and found no significant change in the observed trends.

4.5.1 Relations between stellar and disk properties

The following two subsections examine the disk size-disk luminosity ($\log R_{\mathrm{eff}} - \log L_{\mathrm{mm}}$) and the disk size-stellar properties ($\log R_{\mathrm{eff}} - \log M_\star$ and $\log R_{\mathrm{eff}} - \log L_\star$) relations. In order to determine if empirical relationships can be established, we apply several statistical tests to the data.

We begin with the Shapiro−Wilk normality test (Shapiro and Wilk, 1965) to determine if the distribution of our bivariate data is normal or not. This is important as many correlation tests, e.g. the Pearson's r test, are based on the assumption

Table 4.3. Comparison of R_{68} size distributions

R_{68} Distributions		Anderson-Darling	
Region 1	Region 2	stat	sig.[a]
USco	Chamaeleon I	3.4	0.014
USco	Lupus	3.4	0.013
Chamaeleon I	Lupus	1.2	0.105
Lupus	Oph	1.2	0.104
Tau/Aur	Oph	-0.2	> 0.25

[a]sig., also known as the error rate, indicates the significance level at which the null hypothesis that samples are drawn from the same distribution cannot be rejected.

that the data follow a normal distribution. The Shapiro−Wilk p-value is the null hypothesis probability that the sample is normally distributed. In cases where the p-value is < 0.05 we reject the null hypothesis and conclude that the distribution is not normal. Otherwise, we conclude that the distribution is likely normal. The result of this determines which correlation test we use afterward and is described in further detail below.

For all regions we calculate both the Pearson correlation coefficient (hereafter Pearson r test) and Spearman's rank correlation coefficient (hereafter Spearman ρ test) and the corresponding p-values. For both tests, the p-value gives the probability of rejecting the null hypothesis that there is no statistically significant relationship between the variables, more specifically a linear relation for the Pearson's r test and a monotonic one for the Spearman ρ test. In cases where the p-value for the chosen statistic is < 0.05 we consider the data to be correlated. As mentioned above, the Pearson's r test requires the data to be bivariate normal. For this reason, we use the Pearson's r test to establish if there is a linear correlation only when our data are normally distributed, as found by the Shapiro−Wilk test. In all other cases, we rely on the Spearman ρ to test for the existence of a monotonic relationship between variables. Note that while the Spearman ρ does not need the variables to be normally distributed, it does require that they are converted into a rank-order (ordinal) data set.

A limitation of all these statistical tests is that they do not include upper-limits and uncertainties in the assessment. As such, and for comparison with results already reported in the literature, we might fit linear relationships even if our correlation tests result in a probability larger than 0.05 that the variables are not correlated.

Disk radii and millimeter luminosities

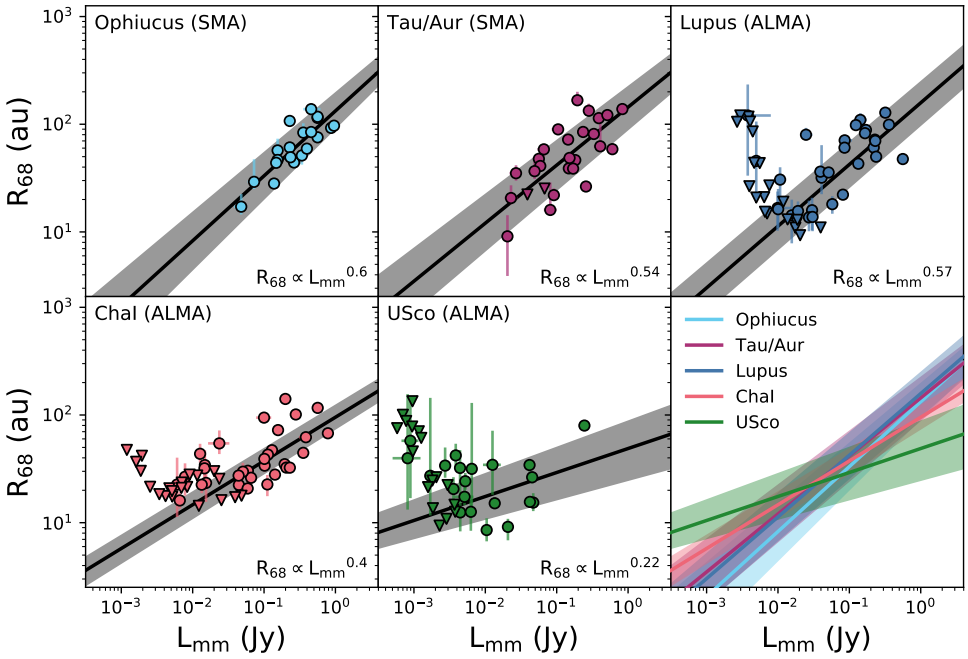

Figure 4.6 Fitting of $\log R_{\rm eff} - \log L_{\rm mm}$. The first 5 panels (left to right; top to bottom; ordered by region age) show the model results of each region as circles (resolved) and triangles (upper-limits). The best fit from MCMC linear regression is plotted as a black line, and surrounded by our 68% confidence intervals in grey. The last panel replots the bests fits of each region (and the corresponding 68% confidence intervals) so that they can be directly compared. Fit parameters for each region are given in Table 4.4.

Table 4.4. $\log R_{68} - \log L_{\rm mm}$ Statistical tests

Region	Shapiro $L_{\rm mm}$		Shapiro $R_{\rm eff}$		Pearson r		Spearman ρ		Regression Parameters			
	stat	p-value	stat	p-value	stat	p-value	stat	p-value	α	β	σ	$\hat{\rho}$
Oph	0.91	5.7e-02	0.96	5.9e-01	0.67	1.3e-03	0.75	1.4e-04	$2.11^{+0.06}_{-0.06}$	$0.60^{+0.11}_{-0.11}$	$0.14^{+0.03}_{-0.02}$	$0.92^{+0.04}_{-0.06}$
Tau/Aur	0.84	9.9e-04	0.91	3.4e-02	0.59	2.0e-03	0.70	1.0e-04	$2.16^{+0.11}_{-0.11}$	$0.53^{+0.12}_{-0.12}$	$0.24^{+0.05}_{-0.04}$	$0.86^{+0.05}_{-0.08}$
Lupus	0.81	8.8e-05	0.91	1.9e-02	0.44	1.4e-02	0.55	1.8e-03	$2.20^{+0.14}_{-0.13}$	$0.57^{+0.10}_{-0.10}$	$0.30^{+0.06}_{-0.05}$	$0.88^{+0.04}_{-0.05}$
Chamaeleon I	0.75	4.5e-06	0.77	1.3e-05	0.53	1.7e-03	0.64	7.7e-05	$1.97^{+0.08}_{-0.08}$	$0.40^{+0.06}_{-0.06}$	$0.21^{+0.03}_{-0.03}$	$0.90^{+0.03}_{-0.04}$
USco	0.45	7.7e-08	0.87	1.0e-02	0.60	4.1e-03	-0.27	2.4e-01	$1.68^{+0.23}_{-0.22}$	$0.22^{+0.11}_{-0.10}$	$0.28^{+0.07}_{-0.05}$	$0.67^{+0.12}_{-0.18}$

Note. — Values we consider unreliable are greyed out (see Section 4.5.1).

Recently, Andrews et al. (2018b) demonstrated that the dust disk effective radius ($R_{\rm eff}$) and the millimeter luminosity ($L_{\rm mm}$) scale in the same way for their Oph, Tau/Aur, and Lupus samples as $R_{\rm eff} \propto L_{\rm mm}^{0.5}$. Thus, one might infer that such a relationship is universal and apply to all star-forming regions. Here, we demonstrate that this is not the case and that the $\log R_{\rm eff} - \log L_{\rm mm}$ slope flattens moving from the younger to the older star-forming regions.

Figure 4.6 shows the inferred disk sizes (circles) or upper limits (downward triangles) as a function of $L_{\rm mm}$. Values for Oph and Tau/Aur are from Andrews et al. (2018b) while for the other three regions are from this work (see Sections 4.2.1 and 4.2.2). For all regions, we see the general trend of larger disk sizes for brighter disks, although USco covers a smaller range in $L_{\rm mm}$ than other regions and the scatter is large. Indeed, when we apply the non-parametric Spearman's rank correlation test to the disks with a measured dust radius (circles), we find positive values ($R_{\rm eff}$ increases with $L_{\rm mm}$) and probabilities (p-value) lower than 5% that the two quantities are uncorrelated in all regions except USco (see Table 4.4).

Next, following Andrews et al. (2018b), we fit the $\log R_{\rm eff} - \log L_{\rm mm}$ relation in each individual region taking into account measured $R_{\rm eff}$, the associated uncertainties, as well as upper limits in $R_{\rm eff}$. For this task we use the Bayesian method of linear regression described in Kelly (2007) (as implemented in the `linmix` code by Joshua E. Meyers) and specifically fit the following linear relation:

$$\log R_{\rm eff} = \alpha + \beta \log L_{\rm mm} \tag{4.2}$$

where α and β are the intercept and the slope, respectively. The best fit parameters for each region, together with the scatter of the relation (σ) and the correlation coefficient ($\hat{\rho}$), are reported in Table 4.4.

We find that $\hat{\rho}$, which is estimated accounting for uncertainties and upper limits (but assumes bivariate-normal data), is positive and larger than the Spearman ρ correlation coefficient in all regions. This may be particularly important for USco, where the Spearman ρ coefficient of -0.27 and large p-value suggest no $\log R_{\rm eff} - \log L_{\rm mm}$ correlation for sources with measured disk sizes, while the `linmix` $\hat{\rho}$ value

of 0.67 points to a positive correlation, albeit less strong than in the other younger star-forming regions. The first five panels of Figure 4.6 visualize the best fit for each region with the grey shadowing highlighting the 68% confidence intervals. The sixth panel of Figure 4.6 summarizes the results and emphasizes the main finding of our analysis that the $\log R_{\rm eff} - \log L_{\rm mm}$ relation is not universal.

We do not perform a fitting for the combined sample of all regions due to differences in the estimated disk size uncertainties between the SMA and the ALMA samples and our finding that not all regions share the same $\log R_{\rm eff} - \log L_{\rm mm}$ relation.

Disk radii and stellar properties

Several works have pointed out that $L_{\rm mm}$, which (if optically thin) probes the dust disk mass, is positively correlated with stellar properties like stellar bolometric luminosity ($L_\star$) and stellar mass ($M_\star$) in most star-forming regions, (e.g., Andrews et al., 2013; Ansdell et al., 2016; Pascucci et al., 2016). However, the relationship between $R_{\rm eff}$ and these same stellar properties has been less explored. Andrews et al. (2018b) find $\log R_{\rm eff} - \log M_\star$ and $\log R_{\rm eff} - \log L_\star$ to be correlated ($R_{\rm eff} \propto {M_\star}^{0.6} \propto {L_\star}^{0.3}$) for the combined Tau/Aur and Lupus samples but to a lesser degree than $\log R_{\rm eff} - \log L_{\rm mm}$. In this section we investigate whether such relations are present in individual regions.

Figures 4.7 and 4.8 show the inferred disk sizes (circles) or upper limits (downward triangles) as a function of $M_\star$ and $L_\star$, respectively. Tables 4.5 and 4.6 report the statistical tests described in Section 4.5.1 as well as the `linmix` best fit parameters and correlation coefficient $\hat{\rho}$. For the two regions that are most biased to bright millimeter disks (Oph and Tau/Aur), we can confidently conclude that there is no correlation in $\log R_{\rm eff} - \log M_\star$ nor in $\log R_{\rm eff} - \log L_\star$.

Interestingly, for Chamaeleon I, which covers the largest range in $L_\star$, we can rule out a $\log R_{\rm eff} - \log L_\star$ correlation with a high level of confidence (correlation coefficient=0.17 and p-value=0.35). The situation is different for USco where we can not rule out a weak $\log R_{\rm eff} - \log L_\star$ relation, the Spearman ρ correlation coefficient is 0.29 with a p-value of 0.19 and $\hat{\rho}$ is 0.72.

The $\log R_{\rm eff} - \log M_\star$ within Chamaeleon I suggests a weak relation with a correlation coefficient=0.37 and p-value=0.033. The two remaining regions (Lupus and USco) have Spearman ρ correlation coefficients (0.29 and 0.34) and p-values (0.07 and 0.19) where we can not completely rule out a weak or marginal correlation between R_{eff} and $M_\star$, but correlations are not strongly supported.

Finally, the Lupus region appears to have some degree of correlation in $\log R_{\rm eff} - \log L_\star$, but likely not in $\log R_{\rm eff} - \log M_\star$. When we combine the Oph, Tau/Aur, and Lupus samples and refit the $\log R_{\rm eff} - \log M_\star$ relation with `linmix` we find $\hat{\rho} = 0.63^{+0.07}_{-0.09}$, the same as for Lupus. Thus, we conclude that the weak $\log R_{\rm eff} - \log M_\star$ correlation reported by Andrews et al. (2018b) for the SMA+ALMA samples (mostly Oph, Tau/Aur, and Lupus) with a coefficient of $\hat{\rho} = 0.54$ is mostly driven by the Lupus sample. Similarly, when we combine Oph, Tau/Aur, and Lupus samples and refit the $\log R_{\rm eff} - \log L_\star$ relation, we find a coefficient of $\hat{\rho} = 0.64^{+0.07}_{-0.09}$, consistent with the findings in Andrews et al. (2018b) for the same joint sample.

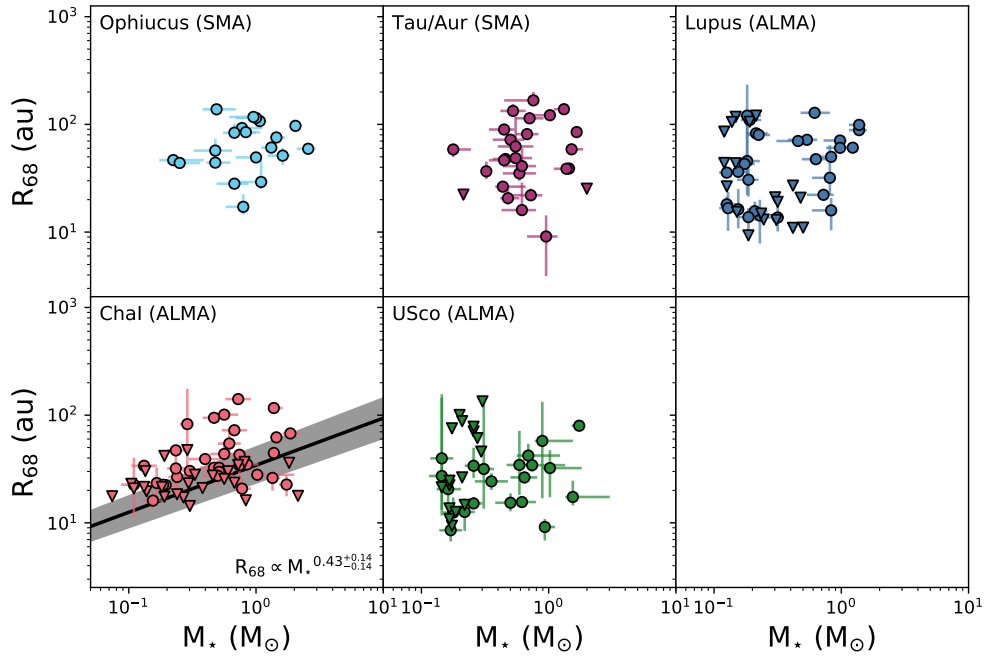

Figure 4.7 Fitting of $\log R_{\rm eff} - \log M_\star$. The first 5 panels (left to right; top to bottom; ordered by region age) show the model results of each region as circles (resolved) and triangles (upper-limits).

Table 4.5. $\log R_{68} - \log M_\star$ statistical tests

Region	Shapiro $M_\star$		Shapiro $R_{\rm eff}$		Pearson r		Spearman ρ		Regression Parameters			
	stat	p-value	stat	p-value	stat	p-value	stat	p-value	α	β	σ	$\hat{\rho}$
Oph	0.91	6.7e-02	0.96	5.9e-01	0.08	7.2e-01	0.24	3.2e-01	$1.81^{+0.06}_{-0.06}$	$0.20^{+0.25}_{-0.24}$	$0.24^{+0.05}_{-0.04}$	$0.47^{+0.22}_{-0.11}$
Tau/Aur	0.87	3.7e-03	0.91	3.4e-02	0.16	4.3e-01	0.18	3.8e-01	$1.71^{+0.08}_{-0.09}$	$0.18^{+0.30}_{-0.29}$	$0.34^{+0.07}_{-0.05}$	$0.38^{+0.23}_{-0.10}$
Lupus	0.82	2.3e-04	0.91	1.6e-02	0.31	1.0e-01	0.34	7.2e-02	$1.66^{+0.13}_{-0.13}$	$0.57^{+0.23}_{-0.22}$	$0.43^{+0.08}_{-0.06}$	$0.62^{+0.10}_{-0.14}$
Chamaeleon I	0.88	1.4e-03	0.80	2.7e-05	0.24	1.7e-01	0.37	3.3e-02	$1.55^{+0.07}_{-0.07}$	$0.44^{+0.13}_{-0.13}$	$0.31^{+0.05}_{-0.04}$	$0.69^{+0.08}_{-0.11}$
USco	0.56	7.4e-07	0.87	1.0e-02	0.13	5.8e-01	0.29	1.9e-01	$1.41^{+0.08}_{-0.08}$	$0.47^{+0.16}_{-0.15}$	$0.26^{+0.06}_{-0.05}$	$0.72^{+0.09}_{-0.13}$

Note. — Values we consider unreliable are greyed out (see Section 4.5.1).

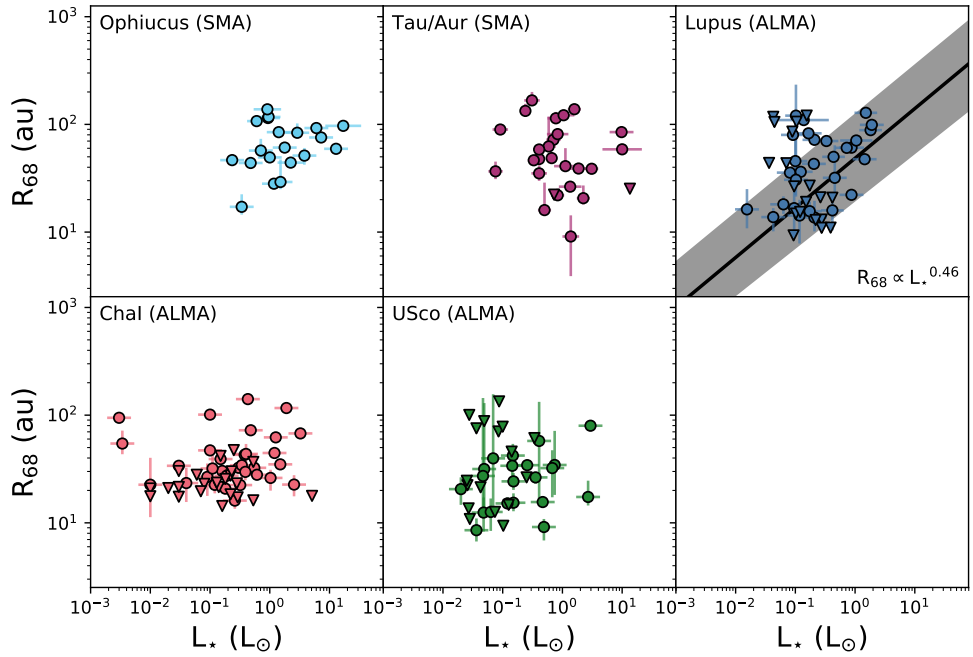

Figure 4.8 Fitting of $\log R_{\rm eff} - \log L_\star$. The first 5 panels (left to right; top to bottom; ordered by region age) show the model results of each region as circles (resolved) and triangles (upper-limits).

Table 4.6. $\log R_{68} - \log L_\star$ statistical tests

	Shapiro $L_\star$		Shapiro $R_{\rm eff}$		Pearson r		Spearman ρ		Regression Parameters			
Region	stat	p-value	stat	p-value	stat	p-value	stat	p-value	α	β	σ	$\hat{\rho}$
Oph	0.66	1.3e-05	0.96	5.9e-01	0.15	5.4e-01	0.17	4.6e-01	$1.77^{+0.06}_{-0.06}$	$0.14^{+0.13}_{-0.13}$	$0.24^{+0.05}_{-0.04}$	$0.54^{+0.19}_{-0.38}$
Tau/Aur	0.54	9.5e-08	0.91	3.4e-02	-0.02	9.3e-01	-0.18	3.9e-01	$1.67^{+0.07}_{-0.07}$	$-0.15^{+0.13}_{-0.14}$	$0.33^{+0.06}_{-0.05}$	nan^{+nan}_{-nan}
Lupus	0.75	1.4e-05	0.91	1.6e-02	0.45	1.4e-02	0.42	2.3e-02	$1.68^{+0.13}_{-0.13}$	$0.46^{+0.17}_{-0.16}$	$0.41^{+0.08}_{-0.06}$	$0.67^{+0.10}_{-0.13}$
Chamaeleon I	0.71	1.2e-06	0.77	1.3e-05	0.18	3.2e-01	0.17	3.5e-01	$1.45^{+0.08}_{-0.09}$	$0.10^{+0.09}_{-0.08}$	$0.36^{+0.06}_{-0.05}$	$0.45^{+0.15}_{-0.24}$
USco	0.57	8.9e-07	0.87	1.0e-02	0.45	3.9e-02	0.35	1.2e-01	$1.49^{+0.10}_{-0.10}$	$0.33^{+0.11}_{-0.10}$	$0.25^{+0.06}_{-0.05}$	$0.77^{+0.08}_{-0.12}$

Note. — Values we consider unreliable are greyed out (see Section 4.5.1), including the result of *nan* which denotes a value below the floating point precision of our analysis.

4.6 Discussion

In the following sections we compare the size distributions found in each region (Section 4.6.1), define and compare our inferred disk sizes with the outer edge of the Solar System (Section 4.6.2), and discuss disk-disk and disk-host scaling relations (Section 4.6.3).

4.6.1 Comparison between regions

In Section 4.5 we use several statistical approaches to assess how similar, or different, the distributions of disk sizes are in our sample regions.

When compared to other regions USco lacks large dust disks. The vast majority ($\geq$ 75%) of resolved disks within USco have sizes that fall below the Lupus and Chamaeleon I median disk sizes. Barenfeld et al. (2017) compared their USco disk sizes with the inhomogeneously derived sizes of Oph, Tau/Aur and Lupus [5] and concluded that USco disks are three times smaller. We also find that the typical disk in USco is smaller than the typical disk in Lupus or Chamaeleon I. However, the difference is not as great: the median disk size in USco is 1.7 times smaller than that in Lupus and 1.3 times smaller than that in Chamaeleon I. We believe that the difference between our results and Barenfeld et al. (2017) is due to the fact that the latter has used inhomogeneous disk size estimations as well as samples biased to the brightest disks in Oph, Tau/Aur, and Lupus. Because the disks from Oph and Tau/Aur are biased towards only the brightest disks, the only conclusion we can make is that USco lacks the large disks seen in both of those regions. The decrease in median disk size from the younger Lupus and Chamaeleon I to the older USco may be interpreted as an evolution of the disk outer edge caused by e.g. efficient inward drift of millimeter grains (Pinilla et al., 2013; Krijt et al., 2015; Pascucci

[5]The comparison by Barenfeld et al. (2017) made use of Lupus dust-disk sizes from Tazzari et al. (2018) which considered a sample that excluded edge-on disks, disks with sub-structures and disks with mm-flux $<$ 4mJy, resulting in $\sim$50% of the objects modelled in Andrews et al. (2018b) or this work.

et al., 2016); growth of millimeter grains into planetesimals (Barenfeld et al., 2017; Gerbig et al., 2019; Lenz et al., 2019); or external photoevaporation in the higher UV field of the USco OB association (Facchini et al., 2016; Barenfeld et al., 2017). Measuring gas disk sizes in these three regions should help to discriminate between internal vs external processes.

Eisner et al. (2018) reported that the population of disk sizes within Chamaeleon I was significantly smaller than that of disks in the younger regions of Oph, Tau/Aur, and Lupus. However, we do not arrive at the same conclusion. As previously mentioned, we find that Chamaeleon I disks are not significantly smaller than Lupus, and span a similar range in disk sizes. Chamaeleon I, when compared to Lupus in Figure 4.5, hints at a enhanced population of disks between 15 and 25 au, and a decreased population of disks between 30 and 65 au.

The differing result from Eisner et al. (2018) is likely due to several factors. First, their work compares inhomogeneously estimated disk sizes, e.g. FWHMs from Pascucci et al. (2016) for Cha I with exponential cutoff radii of a power-law disk from Tazzari et al. (2017) for Lupus. Second, the entire Chamaeleon I disk population is compared with luminosity biased samples in Oph, Tau/Aur, and even Lupus (only the sub-sample in Tazzari et al. (2017) was available at that time). Lastly, the cumulative disk-size distributions used for comparison in Eisner et al. (2018) are not consistently constructed, leading to a different definition for what a probability of unity means in each region. For instance, the Chamaeleon I sample appears to include all sources that were targeted in Pascucci et al. (2016), whether they were detected or not, the USco sample includes only resolved sources, while the Lupus sample appears to include detected sources, whether they were resolved or not.

4.6.2 The outer edge of the Solar System

Stellar encounters (e.g. Ida et al., 2000; Kenyon and Bromley, 2004) and external photoevaporation by massive stars within a star cluster (e.g. Adams et al., 2004) have been suggested as mechanisms connected to the formation of the Solar System's

outer edge. In this section we look into whether or not our results can test these models which utilize edge truncation to explain the size of the Solar System.

The region of the Solar System beyond Neptune (the trans-Neptune region or Edgeworth–Kuiper belt) is populated with icy bodies (TNOs) which fall into distinct classes based on their dynamical properties. There is a decrease in the population of TNOs beyond 48 au, and the population of objects with nearly circular orbits effectively ends at 45 au (e.g. Petit et al., 2011). This *outer edge* of the Kuiper belt appears well defined and is not an observational bias (Allen et al., 2001; Morbidelli et al., 2008). Because the region beyond this edge is dynamically stable on timescales longer than the Solar System's lifetime (Duncan et al., 1995), a primordial population of planetesimals beyond 45 au – had it existed – should have been retained.

Determining if the outer edge of the Solar System's primordial planetesimal disk was located at, beyond, or interior to the present Kuiper belt's edge would test hypotheses which evoke an outer-edge modifying event. This work does not directly probe the history of the Solar System. However, if we take the location of dust observed in our disks to be an indicator of the location of planetesimals (or planetesimal formation), and if we interpret the outer edge at 45-48 au to be primordial, we can compare the Solar System's outer edge with our inferred disk sizes. It is important to be aware that this comparison is between the location of dust emission in 1-3 Myr old disks and the location of a dynamical and occurrence-rate feature found within a distribution of 4.5 Gyr old planetesimals. The validity of this comparison ultimately relies on whether or not the Solar System's outer-edge is a feature inherited from its protoplanetary disk.

While stellar encounters and external photoevaporation by massive stars may impact disk sizes in high-mass star-forming regions, these two mechanisms are most likely not affecting the disk sizes in Lupus and Chamaeleon I. Winter et al. (2018) compared the effect of external photoevaporation and close stellar encounters on disk sizes in typical cluster environments and concluded that tidal truncation due to stellar encounters are unlikely. They find that significant truncation due to stellar

encounters requires a cluster stellar density of $5 \times 10^4 \mathrm{pc}^{-3}$; far larger than the current stellar densities of Lupus (Nakajima et al., 2000; Merín et al., 2008; Winter et al., 2018) ($< 500 \mathrm{pc}^{-3}$) and Chamaeleon I (Sacco et al., 2017). By comparing Gaia observations of the structural properties of Chamaeleon I with N-body simulations, Sacco et al. (2017) concluded that Chamaeleon I likely did not form in a high-density environment. The number of O- and B- stars in Lupus and Chamaeleon I is only 2 (Comerón, 2008) and 3 (Luhman, 2008), respectively, ruling out external photoevaporation as the dominant mechanism setting disk sizes in these low-mass star-forming regions.

The Solar System, on the other hand, may have formed in a high-density cluster environment. The review by Adams (2010) argues for a large cluster ($N = 10^3 - 10^4$) as birth environment, and required a nearby supernova to produce the inventory of short-lived radio isotopes found in the meteoritic record at the time of writing. However, more recently Wasserburg et al. (2017) showed that the short-lived radionuclide abundances of ^{26}Al, ^{60}Fe, ^{182}Hf, and ^{107}Pd found in meteorites are not consistent with being injected via sources of mass $> 5\,\mathrm{M}_\odot$ such as supernovae. A small fraction of presolar grains (X grains) may still link the early Solar System formation to a nearby supernova event (see Zinner, 2014), but how nearby the supernova would need to be is not known. Low-mass star-forming regions such as Lupus and Oph are known to have been influenced by external supernovae (e.g. Comerón, 2008). Therefore, it remains unclear if the presence of X grains limits the Solar System birth environment to that of a high-density cluster.

To compare our dust-disk sizes with the Solar System, we utilize the R_{90} estimates which better represent the full extent of the disk. In addition, we constrain ourselves to the younger and lower mass star-forming regions of Lupus and Chamaeleon I to exclude significant evolution and external processes affecting disk sizes. Figure 4.9 provides this comparison and shows that the Solar System's size falls within the range of R_{90} values found for both low-mass star-forming regions. We also test if the dust masses of the Lupus and Chamaeleon I disks is consistent, or discordant, with the Solar System. To get a rough estimate of the mass of the

primordial Solar System's dust disk, we sum the masses of solids locked up within the major planets ($\sim 30\,M_{\oplus}$). Dust disk masses are estimated assuming optically thin emission and a fixed temperature of 20 K for the emitting grains as in the 20 K dust-mass calculation described in Pascucci et al. (2016). Figure 4.9 shows that the mass of solids in the Solar System is larger than the average dust disk mass but still falls within the range of masses observed in other disks.

When compared to the disks in Lupus and Chamaeleon I, the Solar System doesn't appear to be an outlier. It is neither small, nor does it appear to be missing dust mass. If the initial sizes of protoplanetary disks within high-density and low-density regions are similar, our results show that the Solar system's primordial disk requires no external modification (e.g. stellar encounter or photoevaporation) to explain its size and mass since it is consistent with a population of disks lacking truncation. Radial drift of dust grains, which is common to all environments, may be setting disk sizes. However, if the Solar System formed in a high-density cluster, *and* the initial sizes of these disks is not similar to the initial sizes found in low-density regions, we can come to no conclusion about the history of the Solar System's outer edge.

4.6.3 Disk size scaling relations

In Section 4.5.1 we test for the existence of and, if found, quantify empirical relations between disk sizes ($R_{\rm eff}$), millimeter luminosities ($L_{\rm mm}$), stellar masses ($M_{\star}$), and stellar luminosities ($L_{\star}$). In this sub-section we discuss our findings in that order, starting with $\log R_{\rm eff} - \log L_{\rm mm}$.

We find that, in log scale, disk radii are linearly correlated with millimeter luminosities and that the slope of the $\log R_{\rm eff} - \log L_{\rm mm}$ relation is not the same for all regions investigated here (see Figure 4.6 and Table 4.4). The latter result is different from earlier works. Previous analysis by Tripathi et al. (2017a) and Andrews et al. (2018b) found a slope of ~ 0.5 to be common to the Oph, Tau/Aur, and Lupus star-forming regions. Using a different technique, Barenfeld et al. (2017) showed that disk sizes in USco, while being a factor of $\sim$3 times smaller than those in Oph

and Tau/Aur, plot on the same $\log R_{\rm eff} - \log L_{\rm mm}$ relation with slope 0.5. This result has led to speculation that the $\log R_{\rm eff} - \log L_{\rm mm}$ relationship could be universal (e.g., Rosotti et al., 2019). As the relation implies that the millimeter luminosity scales with the square of the dust radius, the most commonly adopted interpretation is that the millimeter emission is mostly optically thick.

Assuming a simple parameterization for the dust temperature profile, Andrews et al. (2018b) considered whether their $\log R_{\rm eff} - \log L_{\rm mm}$ and $\log L_{\rm mm} - \log L_\star$ relationships for Oph, Tau/Aur and Lupus were consistent with disks being optically thin or thick. Ultimately, they concluded that neither of the two scenarios could be ruled out. Here, we focus on the optically thick scenario and repeat Andrews et al. (2018b) approach for Chamaeleon I and USco. Using the following temperature profile:

$$T_d(r) \propto \left(\frac{L_\star}{L_\odot}\right)^{0.25} \left(\frac{r}{r_0}\right)^{-q} \tag{4.3}$$

where $r_0 = 10\,{\rm au}$ for a solar luminosity star, Andrews et al. (2018b) derived a relationship connecting the dust effective radius to the stellar luminosity and millimeter luminosity via the power law index (q) of the dust temperature profile:

$$R_{\rm eff} \propto {L_\star}^{-1/3(2-q)} {L_{\rm mm}}^{1/(2-q)} \tag{4.4}$$

We can then estimate q for each region using Equation 4.4 and our empirically measured $\log L_{\rm mm} - \log L_\star$ and $\log R_{\rm eff} - \log L_{\rm mm}$ relationships (see Table B.5 in Appendix B.7 and Table 4.4 in Section 4.5.1 respectively). With an estimate of q in hand, we can test if the resulting temperature profile is consistent with that expected for optically thin or thick disks. Doing so results in values of q of $0.32^{+0.33}_{-0.4}$ for Chamaeleon I and $-0.85^{+1.42}_{-3.1}$ for USco. At long millimeter wavelengths and in the case of optically thin emission, the radial temperature profile can be expressed as $T(r) \propto r^{-2/(4+\beta)}$ where β is the index of the dust absorption coefficient, e.g. Evans (1994). Thus, for the average β of 0.6 (Ricci et al., 2010), we find $T(r) \propto r^{-0.4}$ in the optically thin regime. Partially optically thick emission is characterized by a steeper dependence with radial distance (e.g., Fig. 5 in Pascucci et al., 2004) close

to $r^{-0.5}$ for the midplane of an accretion disk irradiated by the central star (D'Alessio et al., 1998). The upper bounds of the confidence intervals encompass the optically thin and thick temperature profiles both for Chamaeleon I and USco. However, the mostly negative values of q for USco imply a temperature profile increasing with disk radius, which is highly unlikely, suggesting that the disk emission is not optically thick.

Andrews et al. (2018b) report finding weak scaling relationships for their joint sample of Oph, Tau/Aur and Lupus for both $\log R_{\rm eff} - \log M_\star$ and $\log R_{\rm eff} - \log L_\star$. We determine that $\log R_{\rm eff} - \log M_\star$ is uncorrelated for all but one of our regions (Chamaeleon I, which has a weak $\log R_{\rm eff} - \log M_\star$ correlation), and for the $\log R_{\rm eff} - \log L_\star$ correlation we find a trend only for Lupus. Extending disk radii measurements to even smaller and less luminous stars could reveal trends also in other regions. This would require observations more sensitive than those adopted for the initial ALMA surveys of nearby star-forming regions.

Finally, we would like to speculate on the possible time evolution of the $\log R_{\rm eff} - \log L_{\rm mm}$ relation utilizing the three regions that have been observed at a similar sensitivity with ALMA, i.e. Lupus, Cha I and USco. While Chamaeleon I and Lupus have overlapping ages with large uncertainties (1-3 and 2-3 Myrs respectively), if we take these ages at face value, we see a flattening of the $\log R_{\rm eff} - \log L_{\rm mm}$ relation moving from the youngest to the oldest region.

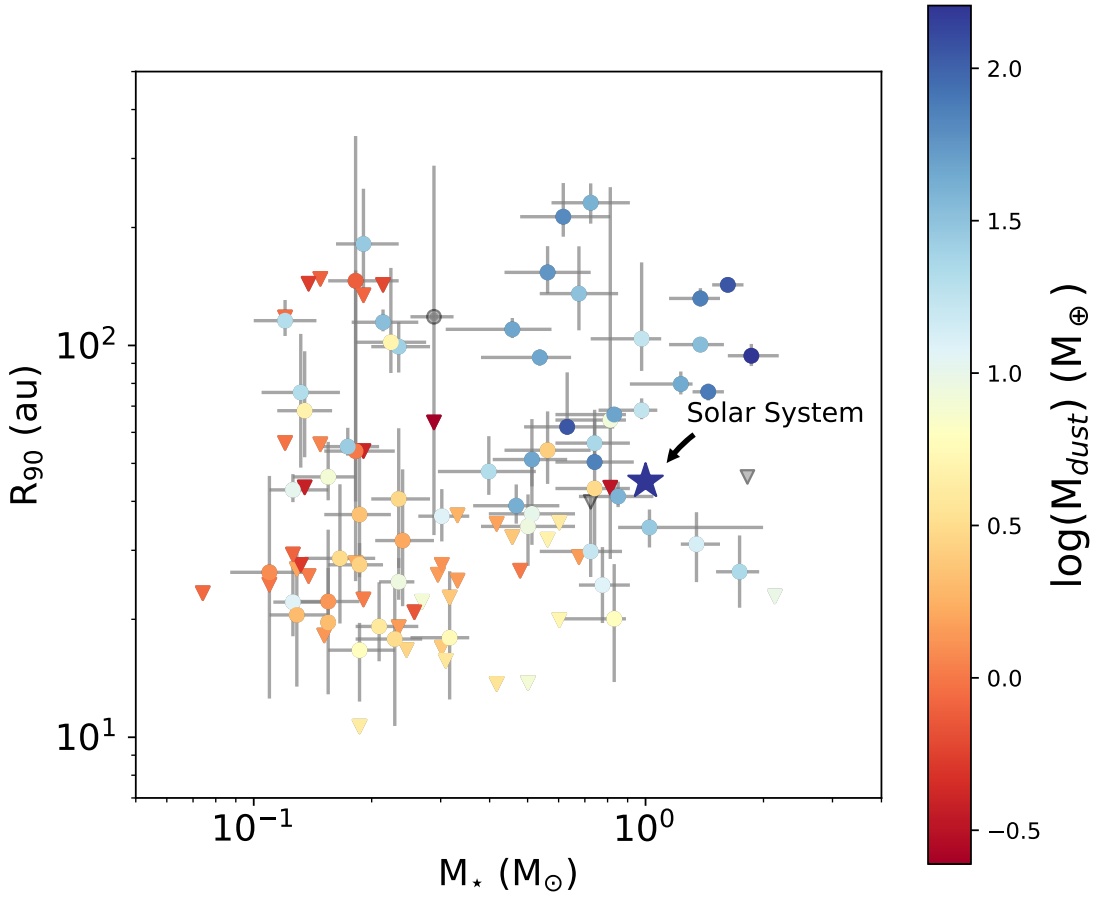

Figure 4.9 The R_{90} sizes and dust masses for disks in the 1-3 and 2-3 Myr old Lupus and Chamaeleon I star-forming regions are plotted along with the Solar System in order to determine if the Solar System (denoted in the figure with a star) should be considered *typical*, or a statistical outlier. Disks with constrained size estimates are shown as circles, and upper limits with triangles. The color of each symbol (including the Solar System) corresponds to the dust mass.

4.7 Summary

Using ALMA archival data, we estimate the sizes of 152 protoplanetary disks in the three star-forming regions of Lupus, Chamaeleon I and USco. This results in the first homogenous estimation of dust disk sizes between these regions. Because we use the same approach (visibility fitting using Nuker profiles) as in Tripathi et al. (2017a) and Andrews et al. (2018b), we add to our analysis their disk-size estimates for Oph and Tau/Aur, for a total of 199 disk sizes from 5 different regions. While the 5 regions have had their disk-sizes estimated in a consistent way, Oph and Tau/Aur were observed with the SMA, hence are biased towards the brightest millimeter disks.

These 5 nearby regions cover the age range over which disks disperse (Ophiuchus: 1-2 Myr; Taurus & Auriga Complex: 1-3 Myr; Lupus: 1-3 Myr; Chamaeleon I: 2-3 Myr; Upper Scorpius OB: 5-11 Myr) and host stars that span the entire stellar mass, 0.08 to 4.68 $M_\star$; with typical (16-84% quantile range) stellar masses of 0.17 to 0.89 $M_\star$.

Of the 199 disk-size estimates in our entire sample, there are 130 resolved disks and 69 unresolved disks for which we provide upper limits in the dust radii. Estimated R_{68} disk sizes for the entire sample range from 8.5 to 177 au with a median of 39 au. For the 3 regions with R_{90} estimates (Lupus, Chamaeleon I and USco), we find that R_{90} range from 10-231 au with a median of 43 au.

Our main results can be summarized as follows:

- For disks around near solar mass stars ($M_\star \in [0.85 - 1.15\, M\odot]$) R_{90} disk sizes range from 20-103 au. This suggests that the ~ 45 au outer-edge of the Solar System, if primordial in origin, is not an outlier when compared with typical 1-3 Myr disks, and that a truncating event (e.g. a stellar encounter or external photoevaporation) may not be required to explain its size. Additionally we find that the mass of solids in the Solar System falls within the range of estimated dust-disk masses estimated for our sample.

- We find that the disks in Chamaeleon I are not smaller than those in Lupus as

previously suggested in Eisner et al. (2018), whose comparison was based on a sub-sample of Lupus as well as samples from Oph and Tau/Aur all of which were biased towards higher luminosity sources.

- USco disk sizes are not drawn from the same distribution of disk sizes as Lupus and Chamaeleon I. In agreement with previous findings, the older USco region appears to have a population of smaller disks, albeit not by a factor of 3 as reported in Barenfeld et al. (2017). We find that USco disks are also smaller than those in Chamaeleon I; our homogeneous analysis finds a difference in the median values of ~ 1.5.

- Dust disk radii correlate with millimeter luminosity in each of the 5 regions. However, we find that the $\log R_{\rm eff} - \log L_{\rm mm}$ relation is not the same in all regions but rather becomes flatter for older regions. Uncertainties in each region's age, lack of dynamic range in ages, and different stellar environments, impedes our ability to conclude that disk-size evolution with time is conclusively seen.

- We find no evidence for a correlation between the dust-disk outer radius and stellar mass in any of the 5 regions we tested.

- Only in the Lupus star-forming region is there a modest correlation between the dust outer radius and the stellar luminosity.

In relation to the last two points, one should keep in mind that we are examining only a subset of the entire disk population in each region. While we find a correlation between $L_{\rm mm}$ and $M_\star$ for our sub-samples, in each region the correlation is shallower than when the entire population is included (see Section 4.4.1 and Appendix B.4). Therefore, we can conclude that dust radii correlate less with $M_\star$ and $L_\star$ than the millimeter luminosity. Deeper ALMA observations, especially of disks around low-mass stars, will be necessary to test if a modest correlation is present between dust disk sizes and stellar properties.

CHAPTER 5

Conclusion

During the period of this PhD work, the ALMA interferometer has been completed, providing views of protoplanetary disks that have impacted every area of protoplanetary disk research. While ALMA has tempted us with amazing observations of the resolved structures of dust disks, we are still attempting to understand the major questions of how, when and where planets form within these disks.

When studying disks, almost all disk properties must be estimated (as opposed to being measured directly), requiring starting assumptions to do so. For example, to estimate the disk mass ($M_{\rm dust}$) one must assume a disk temperature and an opacity for the dust grains (with the unknown dust opacity providing the largest uncertainty). $R_{\rm dust}$, unlike almost all other disk properties, is fundamentally measurable by an interferometer of sufficient resolution, sensitivity and UV coverage.

Most of the work of this PhD has been devoted to deriving basic physical properties of disks, with a particular focus on estimating $R_{\rm dust}$. Prior to the complete deployment of ALMA, SEDs of brown dwarf and very low mass stars were used to fit radiative transfer modeling. That work (Chapter 2) finds that disks around the smallest objects have a median $R_{\rm dust}$ of 3.2 au – an order of magnitude smaller than the median R_{90} values (33-63 au for Lupus, Chamaeleon I and USco) of T Tauri stars found in Chapter 4 of this thesis.

Using the high-spatial resolution and high-sensitivity data provided by ALMA of the transition source T Cha as a test-case, I developed a method of radial profile modeling and visibility fitting in order to estimate the location of the disk's multiple dust structures. Because T Cha possesses an inner disk, a gap, and a dust ring, it required the development of a flexible code-base capable of exploring the superposition of a variety of functions (e.g. delta, Gaussian, Nuker, exponentially tapered power law) in order to determine the correct modeling setup prior to performing

MCMC fitting. Because this approach uses visibilities, instead of a continuum map image, we were able to better estimate the location of the ring and in particular the inner disk size which appears unresolved in the cleaned image. When compared to the 1.6 μm ring observed by VLT/SPHERE, we find that the 3mm emission is located $\sim$7 au farther from the central star. We consider several mechanisms for the gap's formation, and find that the most likely scenario which explains the inner disk, the gap, and the radial offset of larger grains in the ring, is from planet-disk interactions.

I then further improved the radial profile modeling code for use in Long et al. (2018) to characterize the disk substructures observed by ALMA of disks within Taurus & Auriga Complex. As a result of (a) improving the efficiency of the modeling, (b) making the process easier to explore single- and multi-function radial profiles, and (c) integrating it with the GPU accelerated visibility fitting code `galario`, an increase in the complexity and number of disks which can be modeled for a given period of time was achieved.

These improvements in efficiency were necessary in order to perform the homogeneous analysis of disk sizes in multiple star-forming regions. Additionally, the management, extraction, and binning of visibilities for hundreds of sources within the ALMA archive was automated.

This work has shown that the older USco region has a size distribution that is unlike the four other regions. USco, with a deficit of larger disks, and the lowest median disk size, suggests that disks become smaller with time. An additional indication of the temporal evolution of disks may exist in our finding that the $\log R_{\rm eff} - \log L_{\rm mm}$ relation is not the same value for all regions, but instead has a slope that flattens for older regions. It was also shown that while Chamaeleon I and Lupus have differing $\log R_{\rm eff} - \log L_{\rm mm}$ relations, their size distributions are not significantly different as was previously suggested by an inhomogeneous comparison of disk sizes.

As a planetary scientist, perhaps the most satisfying pursuit was that of answering the simple question, "What is the typical size of a planetary disk, and how does the Solar System fit into that picture?". Early in my PhD, a value of 200 au was

commonly used for the outer radius when modeling T Tauri dust disks. What was *typical* was often given as something greater than 100 au. I have shown that the majority of disks around T Tauri (and in particular those around solar mass stars) are less than 100 au in size, with typical sizes (R_{90}) between 33 and 63 au, (a value that appears to decrease with age).

Finally I find that, both the location of the outer edge of the Solar System (as defined by the Kuiper Belt) and the mass of solids with the Solar System is consistent with the disk radii and dust masses of disks around solar mass stars in our 1-3Myr regions. In conclusion, if the Kuiper Belt reflects the location of the primordial Solar System's outer edge, a truncation event is not required to explain it's origin.

APPENDIX A

Hints for Small Disks around Very Low-Mass Stars and Brown Dwarfs

A.1 Appendix: Confidence interval calculations

Because some of our probability distributions are asymmetric, or even multimodal, we use a modified version of the shortest interval method for defining our confidence intervals (e.g. Barlow, 1989; Andrae, 2010). We restrict our confidence intervals to being continuous and move the intervals away from the probability peak such that higher probabilities are preferred until at least 68.27% of the pdf area is found.

Examples of our confidence intervals are shown for the two sources J04381486 and Cha Hα 1 in Figure A.1. These two sources represent two extrema in the SED coverage and illustrate how our confidence intervals prefer areas of higher probability (e.g. the $R_{\rm in}$ panels illustrate how the confidence intervals do not include the low probabilities to the right of the peak probabilities), and the importance of mm photometry to constraining the disk outer radius. Cha Hα 1 lacks photometry data (detections or upper-limits) beyond 100,μm and consequently the outer radius (and dust mass) is unconstrained by our modeling.

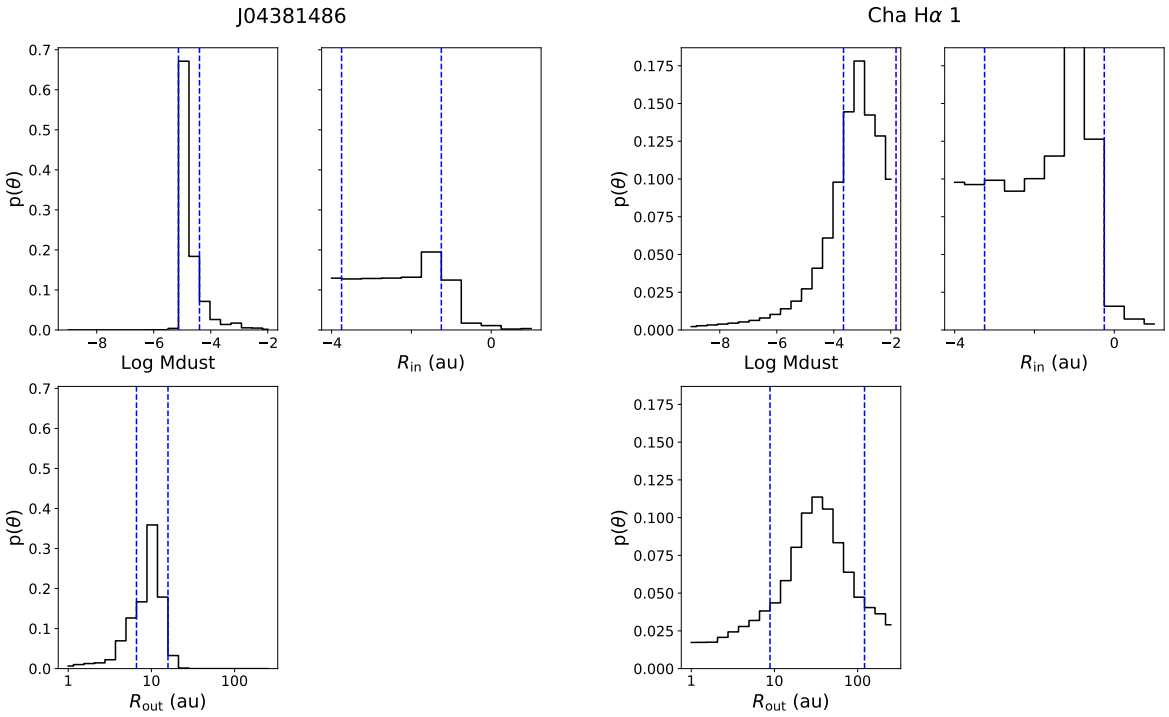

Figure A.1 Bayesian probability distributions of $M_{\rm dust}$, $R_{\rm in}$ and $R_{\rm out}$ for J04381486 and Cha Hα 1. For these examples, we show all three of our free parameters. The vertical dashed blue lines denote our 68.27% confidence interval.

A.2 Appendix: Effect of outer radius on sed

It has been suggested that the outer radius disk parameter has a minimal effect on the SEDs of brown dwarf disks (e.g. Harvey et al., 2012; Liu et al., 2015) and TT disks (e.g. Woitke et al., 2016). Because these previous works used parameterized scale heights and may not have extensively explored disk sizes down to very small radii (e.g. Harvey et al. (2012) explores 50-200 au), we explore the effect here. Figure A.2 shows the dependencies of the SED on the three disk parameters investigated in this work ($R_{\rm out}$, $R_{\rm in}$ and $M_{\rm dust}$). At wavelengths shorter than 10, μm the outer radius has some impact on the flux density, and beyond 10, μm it has significant influence on the flux density as well as the location of the Rayleigh limit. This example demonstrates that the outer disk radius is an important parameter to consider in

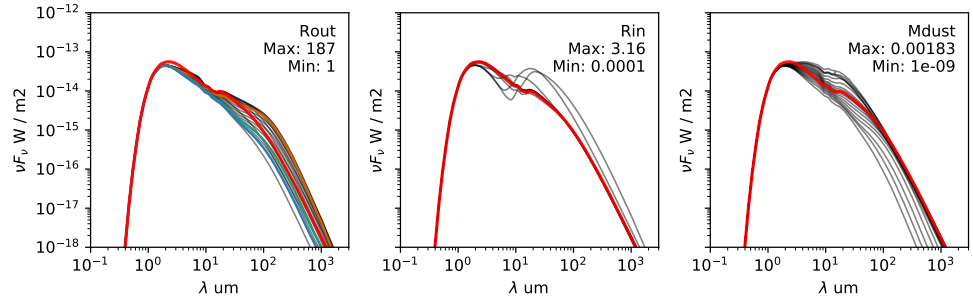

Figure A.2 In each panel we show the effect of varying the parameter ($R_{\rm out}$, $R_{\rm in}$ and $M_{\rm dust}$ respectively) while holding all other parameters to the value of the fiducial model (GM Tau; shown in red). Highlighted in the $R_{\rm out}$ plot are models with outer radii of 10 au (orange), 58 au (green) and 105 au (blue).

SED fitting of VLMO disks.

APPENDIX B

The evolution of dust-disk sizes from a homogeneous analysis of 1-10 Myr-old stars

B.1 Appendix: Comparison with literature results

B.1.1 Lupus: comparing Andrews et al. (2018b) with this work

Tripathi et al. (2017a) and Andrews et al. (2018b) have used the same modeling approach to infer disk sizes and their papers combined provide the largest compilation available in the literature. To further expand upon their work, we have applied the same steps to model the disks in Cha I and USco. However, there are bound to be small differences in chosen modeling and fitting parameters and techniques, as well as differences in determining uncertainties and upper-limits, hence our re-analysis of the Lupus dataset and the comparison presented here.

Figure B.1 shows our Lupus disk sizes vs those reported in Andrews et al. (2018b). For most models there is tight agreement in disk sizes between the two works and for almost all sources there is agreement within the uncertainties.

One caveat about Figure B.1 is that it does not compare disks for which only an upper limit to the disk size could be estimated. In general, our method results in larger uncertainties than those given in Andrews et al. (2018b). For this reason our upper limits are typically larger, and consequently for 10 disks which Andrews et al. (2018b) report a size for, we only provide an upper limit. Figure B.2 presents the results of Bayesian linear regression fitting (Kelly, 2007) of both modeling results with these differences in uncertainties and upper limits included. Our fitting of both the Andrews et al. (2018b) sample and our sample gives results that are consistent with each other, see values in Figure B.2 and in Table 1 of Andrews et al. (2018b).

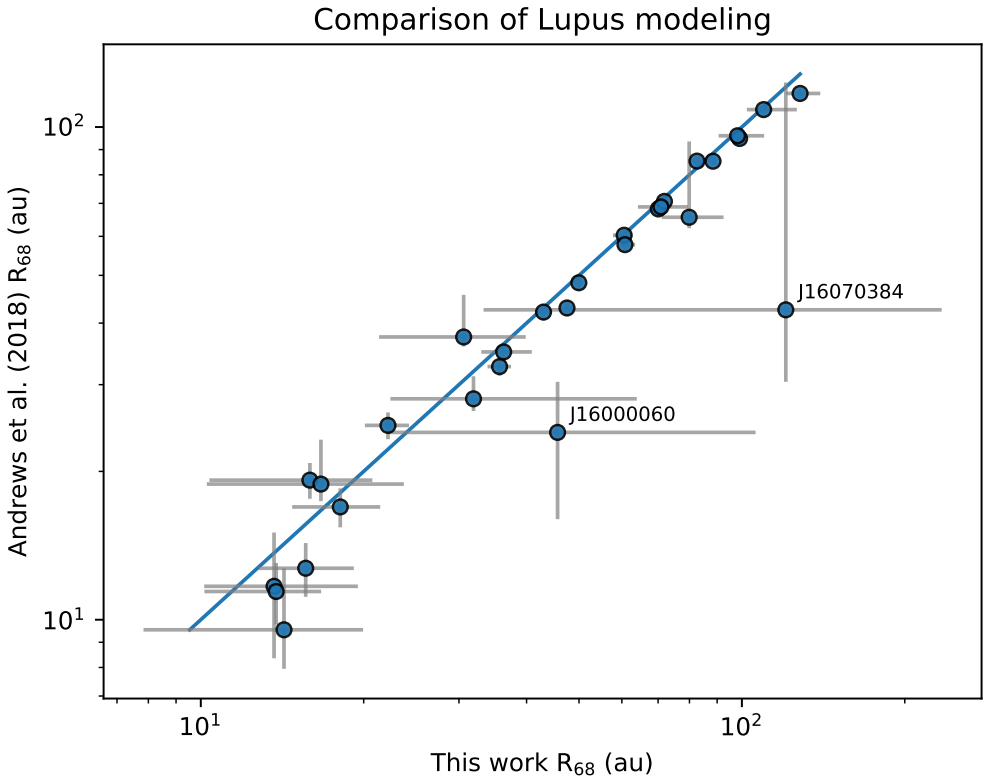

Figure B.1 A comparison of disk sizes calculated in this work with sizes from Andrews et al. (2018b). The 1:1 line is shown in blue.

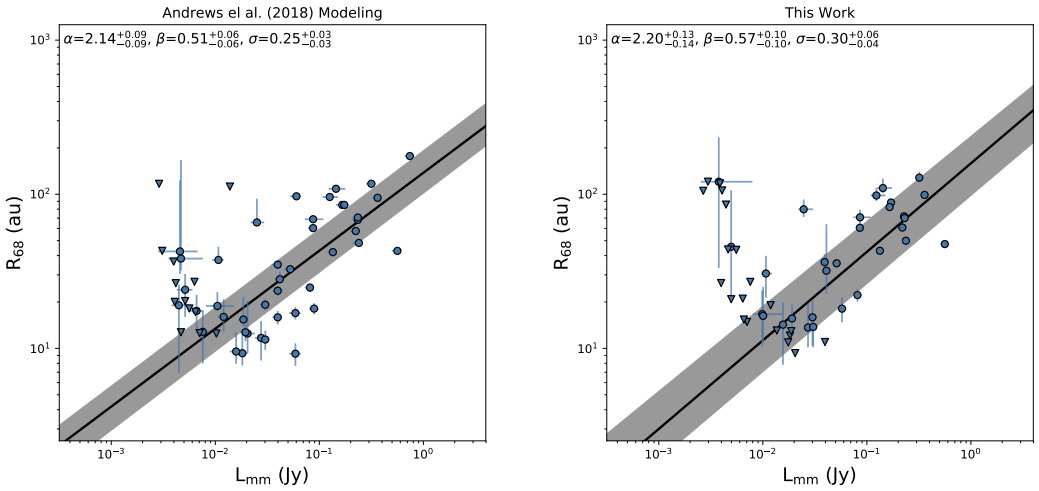

Figure B.2 Two panels showing the results of Bayesian linear regression fitting using disk sizes from Andrews et al. (2018b) (left) and this work (right). The upper-left corner of each panel includes the best fit parameters (α and β) and scatter of the relation (σ), see eq. 2 in the main text

.

B.1.2 High- vs medium-resolution observations

Due to the long exposure times required to make observations of disks at $\leq 0.1''$ like those in Long et al. (2018) and DSHARP (Andrews et al., 2018a), it is unlikely that large sample sizes required to compare disk demographics of star-forming regions will be available in the near-term at such high resolution. This means that medium-resolution observations, like those analyzed in this work, have an important role to play in establishing what are typical disk properties, e.g. disk sizes, and their spread. However, that can only be the case if these observations truly inform us about the disk size. Here, we test the agreement between disk sizes derived from high- and medium-resolution observations.

There are 26 Tau/Aur sources that are common between the high-resolution observations of Long et al. (2018), Huang et al. (2018) and Long et al. (2019) and the medium resolution observations of Tripathi et al. (2017a). The medium-resolution disk sizes used here are from Andrews et al. (2018b) who updated the Tripathi et al. (2017a) results by including GAIA DR2 distances. We use Eq. B.2 (see Appendix

B.5) to convert the Tripathi et al. (2017a) disk sizes from R_{68} to the R_{90} radii. It should be noted that the high-resolution disk sizes include a mix of R_{95} and R_{90} emission radii but these values are so close to each other that we do not attempt to derive an additional scaling.

We directly compare the high- and medium-resolution disk size data in Figure B.3 along with a 1:1 line (in blue) for reference. The relationship between the high-resolution ($R_{\rm high}$) and low-resolution ($R_{\rm low}$) disk sizes is fit using Bayesian linear regression fitting (Kelly, 2007) and the best-fit is shown in black with the corresponding 1σ confidence interval in gray. The relationship is also given as Eq. B.1.

$$R_{\rm high}(R_{\rm low}) = 0.95({\rm au}) + 0.88 R_{\rm low}({\rm au}) \tag{B.1}$$

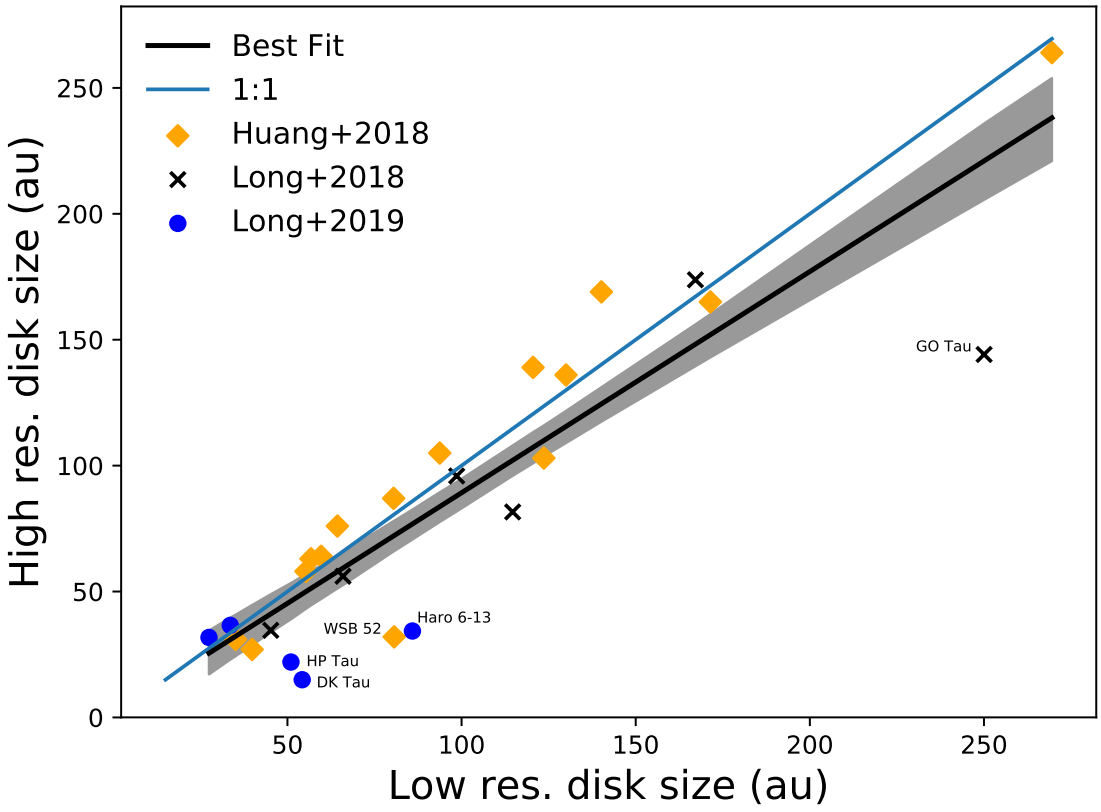

Figure B.3 A comparison of disk size measurements for Tau/Aur disks that have been resolved at both high-resolution (ALMA) and medium-resolution (SMA). The medium resolution observations are taken from Tripathi et al. (2017a). High-resolution observations are from Huang et al. (2018), Long et al. (2018) and Long et al. (2019) (indicated by a diamond, x and circle respectively). For each disk size measurement, the reported uncertainties are all 1 au or less. The best fit from Bayesian linear regression fitting is shown in black, while the corresponding 1σ confidence interval is shown in grey. A 1:1 relation line is shown in blue.

B.2 Appendix: Stellar and Disk Properties

Table B.1 lists stellar properties and derived stellar masses ($M_\star$) as described in Section 4.2.2. To derive stellar masses we follow the approach used in Pascucci et al. (2016) and assume an uncertainty of 0.02 dex in the stellar temperature for spectral types earlier than M3 and 0.01 dex for later spectral types, and a 0.1 dex uncertainty on all stellar luminosities.

Table B.1. Stellar and Disk Properties

2MASS	Region	Distance (pc)	$\log(L_\star)$ ($L_\odot$)	$T_{\rm eff}$ (K)	$\log(M_\star)$ ($M_\odot$)	$L_{\rm mm}$[a] (mJy)
J10533978-7712338	ChaI	$190.88^{+3.85}_{-3.70}$	$-1.70^{+0.01}_{-0.01}$	3560.00	$-0.42^{+0.09}_{-0.07}$	$6.95^{+0.59}_{-0.55}$
J10555973-7724399	ChaI	$184.11^{+1.07}_{-1.06}$	$-0.74^{+0.11}_{-0.11}$	4060.00	$-0.11^{+0.14}_{-0.10}$	$58.97^{+3.00}_{-2.93}$
J10561638-7630530	ChaI	$195.52^{+4.15}_{-3.98}$	$-1.10^{+0.05}_{-0.05}$	2935.00	$-0.98^{+0.02}_{-0.02}$	$7.78^{+0.66}_{-0.61}$
J10563044-7711393	ChaI	$182.12^{+0.65}_{-0.64}$	$-0.37^{+0.25}_{-0.25}$	4060.00	$-0.14^{+0.19}_{-0.15}$	$198.98^{+3.30}_{-3.25}$
J10580597-7711501	ChaI	$185.69^{+3.70}_{-3.56}$	$-2.00^{+0.01}_{-0.01}$	3060.00	$-0.96^{+0.03}_{-0.02}$	$4.71^{+0.48}_{-0.45}$
J10581677-7717170	ChaI	$188.83^{+1.50}_{-1.48}$	$0.07^{+0.68}_{-0.68}$	4900.00	$0.14^{+0.24}_{-0.12}$	$564.26^{+10.87}_{-10.60}$
J10590108-7722407	ChaI	$184.23^{+0.65}_{-0.65}$	$-0.42^{+0.22}_{-0.22}$	4060.00	$-0.13^{+0.17}_{-0.15}$	$113.14^{+3.77}_{-3.72}$
J10590699-7701404	ChaI	$186.47^{+0.80}_{-0.80}$	$0.51^{+1.91}_{-1.91}$	5110.00	$0.27^{+0.33}_{-0.24}$	$784.48^{+8.14}_{-8.03}$
J11004022-7619280	ChaI	$190.50^{+1.58}_{-1.55}$	$-1.00^{+0.06}_{-0.06}$	3270.00	$-0.63^{+0.05}_{-0.03}$	$129.15^{+2.47}_{-2.41}$
J11022491-7733357	ChaI	$175.38^{+1.17}_{-1.16}$	$0.16^{+0.85}_{-0.85}$	4900.00	$0.14^{+0.17}_{-0.15}$	$354.16^{+5.93}_{-5.80}$
J11025504-7721508	ChaI	$181.31^{+1.53}_{-1.50}$	$-0.82^{+0.09}_{-0.09}$	3200.00	$-0.72^{+0.02}_{-0.03}$	$1.95^{+0.31}_{-0.30}$
J11040425-7639328	ChaI	$191.36^{+3.53}_{-3.41}$	$-1.52^{+0.02}_{-0.02}$	3200.00	$-0.72^{+0.04}_{-0.04}$	$5.18^{+0.50}_{-0.47}$
J11040909-7627193	ChaI	$190.72^{+0.78}_{-0.77}$	$0.18^{+0.88}_{-0.88}$	4350.00	$-0.07^{+0.20}_{-0.18}$	$194.45^{+2.71}_{-2.67}$
J11044258-7741571	ChaI	$192.14^{+2.71}_{-2.64}$	$-1.05^{+0.05}_{-0.05}$	3270.00	$-0.62^{+0.05}_{-0.04}$	$7.82^{+0.53}_{-0.51}$
J11045701-7715569	ChaI	$193.46^{+3.24}_{-3.13}$	$-0.55^{+0.16}_{-0.16}$	3415.00	$-0.53^{+0.04}_{-0.03}$	$7.14^{+0.75}_{-0.71}$
J11062554-7633418	ChaI	$208.26^{+5.30}_{-5.04}$	$-1.52^{+0.02}_{-0.02}$	3060.00	$-0.88^{+0.03}_{-0.03}$	$101.91^{+5.60}_{-5.19}$
J11064510-7727023	ChaI	$184.49^{+1.28}_{-1.27}$	$-0.28^{+0.31}_{-0.31}$	4205.00	$-0.09^{+0.19}_{-0.17}$	$1.62^{+0.30}_{-0.30}$
J11065906-7718535	ChaI	$189.33^{+2.10}_{-2.06}$	$-0.49^{+0.19}_{-0.19}$	3200.00	$-0.71^{+0.04}_{-0.04}$	$44.41^{+1.65}_{-1.59}$
J11065939-7530559	ChaI	$195.30^{+4.40}_{-4.21}$	$-2.00^{+0.01}_{-0.01}$	3060.00	$-0.96^{+0.03}_{-0.02}$	$6.05^{+0.60}_{-0.56}$
J11070925-7718471	ChaI	$190.00^{+20.00}_{-20.00}$	$-0.60^{+0.15}_{-0.15}$	3415.00	$-0.54^{+0.04}_{-0.04}$	$1.20^{+0.65}_{-0.49}$
J11071206-7632232	ChaI	$194.65^{+0.84}_{-0.83}$	$-0.40^{+0.23}_{-0.23}$	3850.00	$-0.25^{+0.16}_{-0.13}$	$12.70^{+0.60}_{-0.59}$
J11071330-7743498	ChaI	$173.07^{+7.00}_{-6.48}$	$-0.66^{+0.13}_{-0.13}$	3342.00	$-0.62^{+0.05}_{-0.04}$	$3.41^{+0.55}_{-0.48}$
J11071860-7732516	ChaI	$198.81^{+13.57}_{-11.96}$	$-1.52^{+0.02}_{-0.02}$	3060.00	$-0.87^{+0.04}_{-0.03}$	$1.88^{+0.63}_{-0.50}$
J11072074-7738073	ChaI	$189.58^{+1.07}_{-1.06}$	$0.71^{+2.98}_{-2.98}$	5110.00	$0.33^{+0.37}_{-0.28}$	$48.34^{+3.26}_{-3.19}$
J11074366-7739411	ChaI	$193.76^{+2.21}_{-2.16}$	$-0.52^{+0.18}_{-0.18}$	3705.00	$-0.33^{+0.13}_{-0.10}$	$205.47^{+5.81}_{-5.60}$
J11074656-7615174	ChaI	$193.64^{+7.78}_{-7.21}$	$-2.00^{+0.01}_{-0.01}$	2935.00	$-1.13^{+0.03}_{-0.02}$	$4.17^{+0.67}_{-0.59}$
J11075730-7717262	ChaI	$187.37^{+12.74}_{-11.23}$	$-0.66^{+0.13}_{-0.13}$	3669.00	$-0.34^{+0.15}_{-0.11}$	$11.59^{+3.26}_{-2.61}$
J11075809-7742413	ChaI	$183.53^{+2.51}_{-2.44}$	$-0.80^{+0.09}_{-0.09}$	3415.00	$-0.52^{+0.05}_{-0.04}$	$12.22^{+0.62}_{-0.59}$
J11081509-7733531	ChaI	$190.00^{+20.00}_{-20.00}$	$0.10^{+0.74}_{-0.74}$	5110.00	$0.16^{+0.14}_{-0.13}$	$385.48^{+86.39}_{-77.52}$
J11083905-7716042	ChaI	$187.37^{+1.99}_{-1.95}$	$-0.48^{+0.19}_{-0.19}$	4060.00	$-0.08^{+0.72}_{-0.16}$	$25.27^{+1.98}_{-1.91}$
J11085367-7521359	ChaI	$187.26^{+0.82}_{-0.81}$	$-0.72^{+0.11}_{-0.11}$	3705.00	$-0.30^{+0.16}_{-0.12}$	$44.01^{+2.86}_{-2.81}$
J11085464-7702129	ChaI	$185.04^{+1.87}_{-1.83}$	$-0.89^{+0.08}_{-0.08}$	3780.00	$-0.17^{+0.55}_{-0.13}$	$7.04^{+0.43}_{-0.41}$
J11092379-7623207	ChaI	$191.25^{+0.83}_{-0.82}$	$-0.26^{+0.32}_{-0.32}$	3780.00	$-0.29^{+0.12}_{-0.11}$	$229.73^{+3.07}_{-3.02}$
J11094621-7634463	ChaI	$194.02^{+2.90}_{-2.82}$	$-1.22^{+0.04}_{-0.04}$	3415.00	$-0.48^{+0.07}_{-0.06}$	$9.08^{+1.84}_{-1.74}$
J11094742-7726290	ChaI	$192.14^{+5.47}_{-5.18}$	$-1.00^{+0.06}_{-0.06}$	3705.00	$-0.25^{+0.16}_{-0.13}$	$278.49^{+17.78}_{-16.34}$
J11095340-7634255	ChaI	$201.12^{+6.42}_{-6.04}$	$-0.32^{+0.28}_{-0.28}$	4060.00	$-0.17^{+0.18}_{-0.14}$	$157.05^{+14.20}_{-12.84}$
J11100369-7633291	ChaI	$199.94^{+3.21}_{-3.12}$	$-0.64^{+0.13}_{-0.13}$	3850.00	$-0.22^{+0.17}_{-0.13}$	$20.05^{+2.31}_{-2.18}$

Table B.1 (cont'd)

2MASS	Region	Distance (pc)	$\log(L_\star)$ ($L_\odot$)	$T_{\rm eff}$ (K)	$\log(M_\star)$ ($M_\odot$)	$L_{\rm mm}$[a] (mJy)
J11100469-7635452	ChaI	$193.92^{+0.93}_{-0.92}$	$-0.47^{+0.20}_{-0.20}$	4060.00	$-0.13^{+0.17}_{-0.15}$	$14.83^{+1.65}_{-1.62}$
J11101141-7635292	ChaI	$194.31^{+2.09}_{-2.05}$	$-0.21^{+0.36}_{-0.36}$	4350.00	$0.01^{+0.97}_{-0.17}$	$142.21^{+5.83}_{-5.62}$
J11104959-7717517	ChaI	$184.20^{+1.49}_{-1.47}$	$-0.82^{+0.09}_{-0.09}$	3560.00	$-0.40^{+0.13}_{-0.10}$	$101.04^{+4.19}_{-4.07}$
J11105333-7634319	ChaI	$193.60^{+1.14}_{-1.13}$	$-0.80^{+0.09}_{-0.09}$	3415.00	$-0.52^{+0.05}_{-0.04}$	$59.32^{+3.20}_{-3.13}$
J11105359-7725004	ChaI	$195.71^{+11.63}_{-10.41}$	$-1.40^{+0.02}_{-0.02}$	3125.00	$-0.78^{+0.04}_{-0.03}$	$15.40^{+2.63}_{-2.19}$
J11111083-7641574	ChaI	$190.00^{+20.00}_{-20.00}$	$-2.52^{+0.00}_{-0.00}$	3705.00	$-0.33^{+0.11}_{-0.09}$	$99.96^{+26.09}_{-22.52}$
J11113965-7620152	ChaI	$189.47^{+1.04}_{-1.03}$	$-0.54^{+0.17}_{-0.17}$	3340.00	$-0.57^{+0.03}_{-0.03}$	$39.34^{+1.91}_{-1.87}$
J11114632-7620092	ChaI	$191.45^{+0.89}_{-0.88}$	$0.01^{+0.60}_{-0.60}$	4900.00	$0.13^{+0.20}_{-0.12}$	$65.83^{+2.99}_{-2.94}$
J11120351-7726009	ChaI	$184.63^{+3.85}_{-3.69}$	$-1.15^{+0.04}_{-0.04}$	3060.00	$-0.86^{+0.02}_{-0.02}$	$5.13^{+0.51}_{-0.47}$
J11120984-7634366	ChaI	$192.18^{+1.89}_{-1.86}$	$-0.85^{+0.08}_{-0.08}$	3125.00	$-0.74^{+0.02}_{-0.02}$	$8.37^{+0.59}_{-0.57}$
J11122772-7644223	ChaI	$192.17^{+0.98}_{-0.97}$	$0.41^{+1.49}_{-1.49}$	5110.00	$0.24^{+0.21}_{-0.22}$	$111.26^{+3.60}_{-3.53}$
J11123092-7644241	ChaI	$194.92^{+1.79}_{-1.76}$	$-0.74^{+0.11}_{-0.11}$	3780.00	$-0.25^{+0.16}_{-0.13}$	$23.61^{+2.08}_{-2.01}$
J11132446-7629227	ChaI	$188.52^{+1.81}_{-1.78}$	$-0.96^{+0.06}_{-0.06}$	3270.00	$-0.63^{+0.05}_{-0.03}$	$14.63^{+1.74}_{-1.68}$
J11142454-7733062	ChaI	$188.00^{+2.94}_{-2.85}$	$-0.92^{+0.07}_{-0.07}$	3200.00	$-0.73^{+0.03}_{-0.03}$	$13.40^{+1.05}_{-1.00}$
J11160287-7624533	ChaI	$190.00^{+20.00}_{-20.00}$	$-2.47^{+0.00}_{-0.00}$	3955.00	$-0.21^{+0.14}_{-0.12}$	$23.63^{+9.02}_{-7.19}$
J11173700-7704381	ChaI	$187.36^{+0.86}_{-0.85}$	$-0.38^{+0.25}_{-0.25}$	3780.00	$-0.29^{+0.15}_{-0.11}$	$50.61^{+2.80}_{-2.75}$
J11183572-7935548	ChaI	$94.40^{+1.36}_{-1.32}$	$-0.59^{+0.15}_{-0.15}$	3125.00	$-0.81^{+0.03}_{-0.03}$	$6.60^{+0.36}_{-0.34}$
J11241186-7630425	ChaI	$183.82^{+2.48}_{-2.41}$	$-1.52^{+0.02}_{-0.02}$	3060.00	$-0.88^{+0.04}_{-0.03}$	$2.53^{+0.35}_{-0.33}$
J15354856-2958551	USco	$145.00^{+20.00}_{-20.00}$	$-0.60^{+0.15}_{-0.15}$	$3235.94^{+152.50}_{152.50}$	$-0.68^{+0.05}_{-0.04}$	$2.06^{+0.82}_{-0.65}$
J15392776-3446171	Lupus	$155.00^{+3.00}_{-3.00}$	$-0.06^{+0.51}_{-0.51}$	$4073.80^{+191.99}_{-183.35}$	$-0.17^{+0.18}_{-0.14}$	$81.27^{+4.32}_{-3.82}$
J15392828-3446180	Lupus	$156.00^{+4.00}_{-4.00}$	$-0.66^{+0.13}_{-0.13}$	$3388.44^{+78.93}_{-77.13}$	$-0.54^{+0.05}_{-0.04}$	$18.75^{+5.41}_{-1.18}$
J15450887-3417333	Lupus	$154.00^{+6.00}_{-6.00}$	$-1.20^{+0.04}_{-0.04}$	$3090.30^{+71.98}_{-70.34}$	$-0.83^{+0.04}_{-0.03}$	$57.72^{+5.50}_{-5.08}$
J15451741-3418283	Lupus	$154.00^{+3.00}_{-3.00}$	$-1.03^{+0.05}_{-0.05}$	$3235.94^{+75.37}_{-73.66}$	$-0.65^{+0.05}_{-0.03}$	$20.45^{+1.56}_{-1.25}$
J15464473-3430354	Lupus	$155.00^{+3.00}_{-3.00}$	$-0.48^{+0.19}_{-0.19}$	$3630.78^{+171.11}_{-163.41}$	$-0.38^{+0.12}_{-0.11}$	$230.69^{+10.93}_{-10.97}$
J15475062-3528353	Lupus	$155.00^{+3.00}_{-3.00}$	$-0.56^{+0.16}_{-0.16}$	$3548.13^{+167.22}_{-159.69}$	$-0.42^{+0.13}_{-0.09}$	$17.53^{+2.21}_{-1.14}$
J15475693-3514346	Lupus	$156.00^{+3.00}_{-3.00}$	$-0.34^{+0.27}_{-0.27}$	$4073.80^{+191.99}_{-183.35}$	$-0.07^{+0.73}_{-0.14}$	$40.85^{+3.01}_{-2.39}$
J15514032-2146103	USco	$141.66^{+2.15}_{-2.09}$	$-1.31^{+0.03}_{-0.03}$	$3235.94^{+152.50}_{152.50}$	$-0.68^{+0.04}_{-0.04}$	$0.78^{+0.19}_{-0.18}$
J15530132-2114135	USco	$145.81^{+2.58}_{-2.50}$	$-1.20^{+0.04}_{-0.04}$	$3235.94^{+152.50}_{152.50}$	$-0.66^{+0.04}_{-0.04}$	$6.27^{+0.38}_{-0.36}$
J15534211-2049282	USco	$135.25^{+3.48}_{-3.31}$	$-0.84^{+0.08}_{-0.08}$	$3311.31^{+156.06}_{156.06}$	$-0.59^{+0.04}_{-0.04}$	$2.73^{+0.43}_{-0.39}$
J15564230-3749154	Lupus	$159.00^{+3.00}_{-3.00}$	$0.16^{+0.85}_{-0.85}$	$4073.80^{+191.99}_{-183.35}$	$-0.20^{+0.16}_{-0.13}$	$561.21^{+23.12}_{-21.85}$
J15580252-3736026	Lupus	$152.00^{+3.00}_{-3.00}$	$-0.91^{+0.07}_{-0.07}$	$3162.28^{+73.66}_{-71.98}$	$-0.77^{+0.03}_{-0.03}$	$39.25^{+2.42}_{-2.21}$
J15582981-2310077	USco	$146.98^{+2.84}_{-2.74}$	$-1.31^{+0.03}_{-0.03}$	$3388.44^{+159.69}_{159.69}$	$-0.51^{+0.06}_{-0.05}$	$6.46^{+0.46}_{-0.43}$
J15583692-2257153	USco	$165.48^{+4.13}_{-3.94}$	$0.47^{+1.73}_{-1.73}$	$5623.41^{+0.00}_{0.00}$	$0.24^{+0.17}_{-0.22}$	$244.39^{+12.75}_{-11.86}$
J15591647-4157102	Lupus	$161.00^{+3.00}_{-3.00}$	$-0.36^{+0.26}_{-0.26}$	$4073.80^{+191.99}_{-183.35}$	$-0.07^{+0.70}_{-0.14}$	$237.39^{+10.16}_{-10.04}$
J15592838-4021513	Lupus	$158.00^{+4.00}_{-4.00}$	$0.28^{+1.11}_{-1.11}$	$4897.79^{+230.83}_{-220.44}$	$0.15^{+0.21}_{-0.15}$	$358.67^{+20.53}_{-19.26}$
J16000060-4221567	Lupus	$160.00^{+4.00}_{-4.00}$	$-1.00^{+0.06}_{-0.06}$	$3235.94^{+75.37}_{-73.66}$	$-0.65^{+0.05}_{-0.03}$	$4.96^{+1.07}_{-0.74}$
J16000236-4222145	Lupus	$164.00^{+4.00}_{-4.00}$	$-0.78^{+0.10}_{-0.10}$	$3235.94^{+75.37}_{-73.66}$	$-0.71^{+0.03}_{-0.13}$	$165.49^{+10.62}_{-9.28}$

Table B.1 (cont'd)

2MASS	Region	Distance (pc)	$\log(L_\star)$ ($L_\odot$)	$T_{\rm eff}$ (K)	$\log(M_\star)$ ($M_\odot$)	$L_{\rm mm}$[a] (mJy)
J16001844-2230114	USco	$138.05^{+8.95}_{-7.94}$	$-1.13^{+0.04}_{-0.04}$	$3162.28^{+149.03}_{149.03}$	$-0.73^{+0.04}_{-0.03}$	$3.78^{+0.67}_{-0.55}$
J16003103-4143369	Lupus	$160.00^{+3.00}_{-3.00}$	$-0.76^{+0.10}_{-0.10}$	$3548.13^{+167.22}_{-159.69}$	$-0.39^{+0.14}_{-0.10}$	$7.58^{+1.24}_{-0.78}$
J16004452-4155310	Lupus	$156.00^{+3.00}_{-3.00}$	$-0.06^{+0.51}_{-0.51}$	$5128.61^{+241.70}_{-230.83}$	$0.07^{+0.14}_{-0.10}$	$219.52^{+9.81}_{-9.32}$
J16004943-4130038	Lupus	$160.00^{+3.00}_{-3.00}$	$-0.82^{+0.09}_{-0.09}$	$3388.44^{+78.93}_{-77.13}$	$-0.53^{+0.05}_{-0.04}$	$11.89^{+1.26}_{-0.94}$
J16014086-2258103	USco	$145.00^{+20.00}_{-20.00}$	$-0.90^{+0.07}_{-0.07}$	$3235.94^{+152.50}_{152.50}$	$-0.66^{+0.04}_{-0.04}$	$3.70^{+1.29}_{-1.06}$
J16014157-2111380	USco	$144.20^{+2.54}_{-2.45}$	$-1.56^{+0.02}_{-0.02}$	$3235.94^{+152.50}_{152.50}$	$-0.70^{+0.04}_{-0.04}$	$0.70^{+0.18}_{-0.17}$
J16020757-2257467	USco	$139.73^{+1.26}_{-1.23}$	$-0.82^{+0.09}_{-0.09}$	$3467.37^{+163.41}_{163.41}$	$-0.45^{+0.12}_{-0.09}$	$5.24^{+0.37}_{-0.36}$
J16024152-2138245	USco	$141.30^{+2.58}_{-2.49}$	$-1.44^{+0.02}_{-0.02}$	$3162.28^{+149.03}_{149.03}$	$-0.77^{+0.04}_{-0.03}$	$10.44^{+0.58}_{-0.55}$
J16030161-2207523	USco	$143.71^{+3.57}_{-3.40}$	$-1.59^{+0.02}_{-0.02}$	$3162.28^{+149.03}_{149.03}$	$-0.78^{+0.04}_{-0.03}$	$2.96^{+0.28}_{-0.26}$
J16032939-4140018	Lupus	$153.00^{+18.00}_{-10.00}$	$0.02^{+0.61}_{-0.61}$	$4365.16^{+205.72}_{-196.46}$	$-0.03^{+0.21}_{-0.17}$	$85.99^{+23.06}_{-11.81}$
J16035767-2031055	USco	$142.00^{+0.79}_{-0.78}$	$-0.17^{+0.40}_{-0.40}$	$4365.16^{+101.68}_{101.68}$	$0.01^{+0.80}_{-0.13}$	$4.42^{+0.45}_{-0.45}$
J16041740-1942287	USco	$160.55^{+2.49}_{-2.42}$	$-1.07^{+0.05}_{-0.05}$	$3311.31^{+156.06}_{156.06}$	$-0.59^{+0.04}_{-0.04}$	$1.17^{+0.23}_{-0.21}$
J16052556-2035397	USco	$142.11^{+3.34}_{-3.20}$	$-1.37^{+0.02}_{-0.02}$	$3090.30^{+145.64}_{145.64}$	$-0.84^{+0.04}_{-0.03}$	$1.58^{+0.29}_{-0.27}$
J16063539-2516510	USco	$145.00^{+20.00}_{-20.00}$	$-1.60^{+0.01}_{-0.01}$	$3162.28^{+149.03}_{149.03}$	$-0.78^{+0.04}_{-0.03}$	$1.81^{+0.74}_{-0.59}$
J16064102-2455489	USco	$151.65^{+3.00}_{-2.89}$	$-1.70^{+0.01}_{-0.01}$	$3162.28^{+149.03}_{149.03}$	$-0.79^{+0.04}_{-0.03}$	$3.58^{+0.31}_{-0.29}$
J16064385-1908056	USco	$144.23^{+7.04}_{-6.43}$	$-0.39^{+0.24}_{-0.24}$	$4168.69^{+97.10}_{97.10}$	$-0.05^{+0.66}_{-0.12}$	$0.89^{+0.26}_{-0.22}$
J16070384-3911113	Lupus	$152.00^{+21.00}_{-11.00}$	$-0.99^{+0.06}_{-0.06}$	$3235.94^{+75.37}_{-73.66}$	$-0.65^{+0.05}_{-0.03}$	$3.77^{+4.17}_{-1.24}$
J16070854-3914075	Lupus	$175.00^{+17.00}_{-10.00}$	$-0.86^{+0.08}_{-0.08}$	$3235.94^{+75.37}_{-73.66}$	$-0.66^{+0.04}_{-0.03}$	$142.66^{+31.88}_{-17.37}$
J16071007-3911033	Lupus	$160.00^{+3.00}_{-3.00}$	$-0.38^{+0.24}_{-0.24}$	$4073.80^{+191.99}_{-183.35}$	$-0.07^{+0.70}_{-0.14}$	$30.04^{+1.95}_{-1.74}$
J16072625-2432079	USco	$142.25^{+1.99}_{-1.94}$	$-0.92^{+0.07}_{-0.07}$	$3311.31^{+156.06}_{156.06}$	$-0.59^{+0.04}_{-0.04}$	$13.55^{+0.64}_{-0.61}$
J16072747-2059442	USco	$145.00^{+20.00}_{-20.00}$	$-0.99^{+0.06}_{-0.06}$	$3162.28^{+149.03}_{149.03}$	$-0.76^{+0.04}_{-0.03}$	$2.28^{+0.84}_{-0.68}$
J16073773-3921388	Lupus	$173.00^{+7.00}_{-7.00}$	$-1.05^{+0.05}_{-0.05}$	$3090.30^{+71.98}_{-70.34}$	$-0.84^{+0.03}_{-0.02}$	$4.43^{+1.36}_{-0.91}$
J16075230-3858059	Lupus	$157.00^{+3.00}_{-3.00}$	$-0.58^{+0.15}_{-0.15}$	$3388.44^{+78.93}_{-77.13}$	$-0.55^{+0.04}_{-0.04}$	$6.41^{+0.90}_{-0.61}$
J16075475-3915446	Lupus	$153.00^{+22.00}_{-11.00}$	$-0.98^{+0.06}_{-0.06}$	$3235.94^{+75.37}_{-73.66}$	$-0.65^{+0.05}_{-0.03}$	$4.06^{+4.85}_{-0.87}$
J16075796-2040087	USco	$197.84^{+8.33}_{-7.69}$	$-0.82^{+0.09}_{-0.09}$	$3715.35^{+175.10}_{175.10}$	$-0.30^{+0.16}_{-0.12}$	$46.91^{+4.29}_{-3.80}$
J16080017-3902595	Lupus	$159.00^{+4.00}_{-4.00}$	$-1.44^{+0.02}_{-0.02}$	$3090.30^{+71.98}_{-70.34}$	$-0.85^{+0.04}_{-0.03}$	$4.64^{+0.64}_{-0.60}$
J16081263-3908334	Lupus	$156.00^{+3.00}_{-3.00}$	$-0.38^{+0.24}_{-0.24}$	$3715.35^{+175.10}_{-167.22}$	$-0.33^{+0.13}_{-0.11}$	$4.97^{+0.84}_{-0.55}$
J16081497-3857145	Lupus	$145.00^{+30.00}_{-12.00}$	$-1.02^{+0.06}_{-0.06}$	$3090.30^{+71.98}_{-70.34}$	$-0.84^{+0.03}_{-0.02}$	$9.87^{+5.60}_{-1.84}$
J16081566-2222199	USco	$139.66^{+1.61}_{-1.58}$	$-0.85^{+0.08}_{-0.08}$	$3388.44^{+159.69}_{159.69}$	$-0.53^{+0.05}_{-0.05}$	$0.97^{+0.14}_{-0.14}$
J16082180-3904214	Lupus	$157.00^{+3.00}_{-3.00}$	$-0.99^{+0.06}_{-0.06}$	$3311.31^{+77.13}_{-75.37}$	$-0.59^{+0.04}_{-0.04}$	$7.04^{+0.66}_{-0.63}$
J16082249-3904464	Lupus	$156.00^{+3.00}_{-3.00}$	$0.18^{+0.89}_{-0.89}$	$4073.80^{+191.99}_{-183.35}$	$-0.20^{+0.16}_{-0.13}$	$318.85^{+15.35}_{-14.18}$
J16082324-1930009	USco	$137.48^{+1.12}_{-1.10}$	$-0.59^{+0.15}_{-0.15}$	$3890.45^{+90.62}_{90.62}$	$-0.13^{+0.61}_{-0.12}$	$41.65^{+1.47}_{-1.43}$
J16082576-3906011	Lupus	$136.00^{+4.00}_{-4.00}$	$-1.09^{+0.05}_{-0.05}$	$3090.30^{+71.98}_{-70.34}$	$-0.85^{+0.03}_{-0.03}$	$51.24^{+3.66}_{-3.50}$
J16082751-1949047	USco	$145.00^{+20.00}_{-20.00}$	$-1.16^{+0.04}_{-0.04}$	$3090.30^{+145.64}_{145.64}$	$-0.84^{+0.03}_{-0.03}$	$0.82^{+0.42}_{-0.31}$
J16083026-3906111	Lupus	$159.00^{+4.00}_{-4.00}$	$-0.93^{+0.07}_{-0.07}$	$3311.31^{+77.13}_{-75.37}$	$-0.59^{+0.04}_{-0.04}$	$15.61^{+2.42}_{-1.14}$
J16083070-3828268	Lupus	$155.00^{+3.00}_{-3.00}$	$0.26^{+1.06}_{-1.06}$	$4897.79^{+230.83}_{-220.44}$	$0.15^{+0.29}_{-0.15}$	$170.75^{+8.07}_{-7.61}$
J16083081-3905488	Lupus	$165.00^{+4.00}_{-4.00}$	$-1.15^{+0.04}_{-0.04}$	$3090.30^{+71.98}_{-70.34}$	$-0.85^{+0.03}_{-0.03}$	$5.56^{+0.86}_{-0.66}$

Table B.1 (cont'd)

2MASS	Region	Distance (pc)	$\log(L_\star)$ ($L_\odot$)	$T_{\rm eff}$ (K)	$\log(M_\star)$ ($M_\odot$)	$L_{\rm mm}$[a] (mJy)
J16084940-3905393	Lupus	$159.00^{+6.00}_{-6.00}$	$-0.81^{+0.09}_{-0.09}$	$3311.31^{+77.13}_{-75.37}$	$-0.59^{+0.05}_{-0.04}$	$2.97^{+1.06}_{-0.46}$
J16085157-3903177	Lupus	$159.00^{+3.00}_{-3.00}$	$-0.76^{+0.10}_{-0.10}$	$3311.31^{+77.13}_{-75.37}$	$-0.60^{+0.04}_{-0.04}$	$19.09^{+1.66}_{-1.09}$
J16085324-3914401	Lupus	$167.00^{+4.00}_{-4.00}$	$-0.68^{+0.12}_{-0.12}$	$3388.44^{+78.93}_{-77.13}$	$-0.54^{+0.05}_{-0.04}$	$27.18^{+2.36}_{-1.69}$
J16085373-3914367	Lupus	$156.00^{+31.00}_{-14.00}$	$-1.02^{+0.06}_{-0.06}$	$3090.30^{+71.98}_{-70.34}$	$-0.84^{+0.03}_{-0.02}$	$3.97^{+2.63}_{-0.99}$
J16085468-3937431	Lupus	$157.00^{+3.00}_{-3.00}$	$-0.68^{+0.12}_{-0.12}$	$3715.35^{+175.10}_{-167.22}$	$-0.28^{+0.17}_{-0.13}$	$227.63^{+10.48}_{-10.19}$
J16085553-3902339	Lupus	$159.00^{+4.00}_{-4.00}$	$-0.92^{+0.07}_{-0.07}$	$3162.28^{+73.66}_{-71.98}$	$-0.77^{+0.03}_{-0.03}$	$6.58^{+1.01}_{-0.82}$
J16085780-3902227	Lupus	$163.00^{+4.00}_{-4.00}$	$-1.37^{+0.02}_{-0.02}$	$3235.94^{+75.37}_{-73.66}$	$-0.68^{+0.04}_{-0.04}$	$30.50^{+2.08}_{-1.99}$
J16090002-1908368	USco	$138.53^{+2.75}_{-2.65}$	$-1.33^{+0.03}_{-0.03}$	$3090.30^{+145.64}_{145.64}$	$-0.84^{+0.04}_{-0.03}$	$1.69^{+0.20}_{-0.19}$
J16090075-1908526	USco	$137.08^{+1.48}_{-1.45}$	$-0.45^{+0.21}_{-0.21}$	$3890.45^{+90.62}_{90.62}$	$-0.19^{+0.17}_{-0.14}$	$45.33^{+1.88}_{-1.81}$
J16090141-3925119	Lupus	$164.00^{+4.00}_{-4.00}$	$-1.04^{+0.05}_{-0.05}$	$3311.31^{+77.13}_{-75.37}$	$-0.58^{+0.05}_{-0.04}$	$24.70^{+5.68}_{-2.76}$
J16090185-3905124	Lupus	$162.00^{+3.00}_{-3.00}$	$-0.69^{+0.12}_{-0.12}$	$3162.28^{+73.66}_{-71.98}$	$-0.73^{+0.02}_{-0.02}$	$133.50^{+6.38}_{-5.80}$
J16093558-1828232	USco	$164.63^{+2.81}_{-2.72}$	$-1.06^{+0.05}_{-0.05}$	$3388.44^{+159.69}_{159.69}$	$-0.52^{+0.05}_{-0.04}$	$0.95^{+0.25}_{-0.23}$
J16094434-3913301	Lupus	$158.00^{+3.00}_{-3.00}$	$-0.56^{+0.16}_{-0.16}$	$3311.31^{+77.13}_{-75.37}$	$-0.62^{+0.04}_{-0.03}$	$13.63^{+1.18}_{-0.88}$
J16094864-3911169	Lupus	$163.00^{+3.00}_{-3.00}$	$-0.14^{+0.42}_{-0.42}$	$4365.16^{+205.72}_{-196.46}$	$0.01^{+0.88}_{-0.15}$	$85.54^{+4.44}_{-4.03}$
J16095628-3859518	Lupus	$156.00^{+4.00}_{-4.00}$	$-1.81^{+0.01}_{-0.01}$	$3019.95^{+70.34}_{-68.74}$	$-1.00^{+0.03}_{-0.02}$	$10.06^{+1.04}_{-0.86}$
J16101984-3836065	Lupus	$158.00^{+4.00}_{-4.00}$	$-1.35^{+0.03}_{-0.03}$	$2951.21^{+68.74}_{-67.18}$	$-1.09^{+0.02}_{-0.02}$	$2.67^{+1.61}_{-0.50}$
J16102955-3922144	Lupus	$163.00^{+4.00}_{-4.00}$	$-0.99^{+0.06}_{-0.06}$	$3235.94^{+75.37}_{-73.66}$	$-0.65^{+0.05}_{-0.03}$	$10.71^{+1.53}_{-1.04}$
J16104636-1840598	USco	$142.59^{+2.84}_{-2.73}$	$-1.57^{+0.02}_{-0.02}$	$3162.28^{+149.03}_{149.03}$	$-0.78^{+0.04}_{-0.03}$	$1.85^{+0.25}_{-0.23}$
J16122737-2009596	USco	$146.64^{+4.10}_{-3.88}$	$-1.44^{+0.02}_{-0.02}$	$3162.28^{+149.03}_{149.03}$	$-0.76^{+0.04}_{-0.03}$	$0.58^{+0.22}_{-0.20}$
J16124373-3815031	Lupus	$159.00^{+3.00}_{-3.00}$	$-0.41^{+0.23}_{-0.23}$	$3715.35^{+175.10}_{-167.22}$	$-0.32^{+0.14}_{-0.11}$	$39.60^{+2.58}_{-2.23}$
J16133650-2503473	USco	$145.00^{+20.00}_{-20.00}$	$-1.00^{+0.06}_{-0.06}$	$3311.31^{+156.06}_{156.06}$	$-0.59^{+0.04}_{-0.04}$	$0.94^{+0.54}_{-0.39}$
J16134410-3736462	Lupus	$159.00^{+4.00}_{-4.00}$	$-1.37^{+0.02}_{-0.02}$	$3162.28^{+73.66}_{-71.98}$	$-0.76^{+0.04}_{-0.03}$	$3.87^{+1.15}_{-0.56}$
J16141107-2305362	USco	$145.00^{+20.00}_{-20.00}$	$0.43^{+1.57}_{-1.57}$	$4897.79^{+230.83}_{230.83}$	$0.19^{+1.47}_{-0.20}$	$5.12^{+1.70}_{-1.43}$
J16142029-1906481	USco	$142.46^{+2.57}_{-2.48}$	$-0.33^{+0.27}_{-0.27}$	$3890.45^{+90.62}_{90.62}$	$-0.21^{+0.18}_{-0.14}$	$42.13^{+1.77}_{-1.67}$
J16143367-1900133	USco	$141.47^{+2.27}_{-2.20}$	$-0.47^{+0.20}_{-0.20}$	$3388.44^{+159.69}_{159.69}$	$-0.56^{+0.04}_{-0.04}$	$1.27^{+0.21}_{-0.20}$
J16153456-2242421	USco	$145.00^{+20.00}_{-20.00}$	$-0.13^{+0.43}_{-0.43}$	$3890.45^{+90.62}_{90.62}$	$-0.23^{+0.15}_{-0.12}$	$12.60^{+3.88}_{-3.33}$
J16154416-1921171	USco	$131.34^{+2.19}_{-2.12}$	$-0.31^{+0.29}_{-0.29}$	$4365.16^{+101.68}_{101.68}$	$-0.03^{+0.19}_{-0.08}$	$20.74^{+0.84}_{-0.80}$
J16163345-2521505	USco	$161.92^{+1.49}_{-1.46}$	$-0.83^{+0.09}_{-0.09}$	$3801.89^{+88.56}_{88.56}$	$-0.16^{+0.54}_{-0.13}$	$3.85^{+0.48}_{-0.46}$
J16181904-2028479	USco	$137.45^{+2.47}_{-2.39}$	$-1.32^{+0.03}_{-0.03}$	$3162.28^{+149.03}_{149.03}$	$-0.75^{+0.04}_{-0.03}$	$4.45^{+0.28}_{-0.27}$
J16270942-2148457	USco	$139.66^{+2.81}_{-2.70}$	$-1.55^{+0.02}_{-0.02}$	$3162.28^{+149.03}_{149.03}$	$-0.78^{+0.04}_{-0.03}$	$2.86^{+0.24}_{-0.22}$

[a]For consistency, our definition of $L_{\rm mm}$ is the same as found in Andrews et al. (2018b). It is a flux density scaled to 140 pc.

B.3 Appendix: Determination and removal of spurious modeling

During our model fitting we realized that low signal-to-noise data can result in Nuker profiles that fit the noise with a disk model that is typically extended, faint, highly inclined and/or ring-like. An example is shown in Figure B.4. In these cases the uncertainties on the disk sizes are large. In order to cull these models from our analysis, we examine by eye sources where the uncertainty in disk size is larger than 66% of the disk size. By observing the fitting in the UV plane, and comparing continuum images of the data and model, we can identify these cases. Of the 23 disks that meet this metric, we find 15 that are obviously problematic, and hence removed them from our analysis (see Section 4.4.1).

Sources removed from the Chamaeleon I sample are: J11100785-7727480, J11064180-7635489, J11092266-7634320, J11071206-7632232 and J11045701-7715569.

Sources removed from the USco sample are: J16095933-1800090, J16095361-1754474, J16115091-2012098, J16102857-1904469, J16073939-1917472, J15534211-2049282, J16035793-1942108, J16043916-1942459, J16135434-2320342 and J16303390-2428062

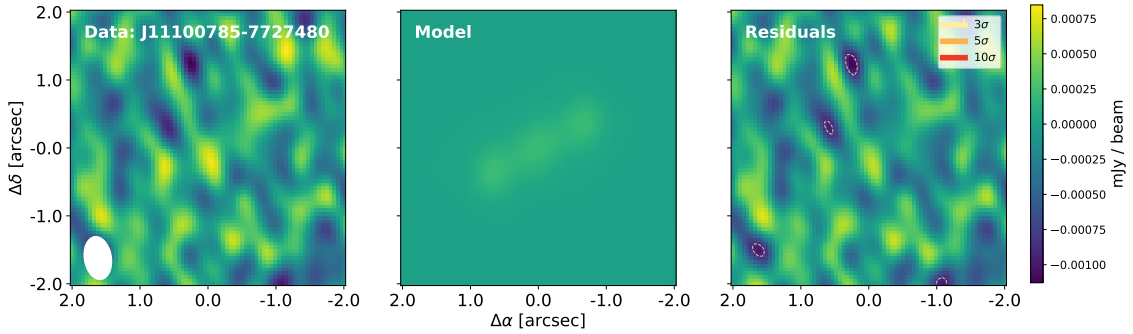

Figure B.4 Example of a Nuker profile fitting the noise and not the faint disk emission from J11100785-7727480. The flux density is only 0.49 ± 0.16 mJy (Pascucci et al., 2016), a marginal 3σ detection.

B.4 Appendix: $\log L_{\rm mm} - \log M_\star$ Relation

Our sample population is a subset of the entire disk population in each region, and is biased towards resolved sources. In order to understand this bias, we test our sample for a correlation between $L_{\rm mm}$ and $M_\star$ so that we can compare it to previously measured $L_{\rm mm}$–$M_\star$ correlations (e.g. Ansdell et al., 2016; Pascucci et al., 2016). We find a shallower slope for the $\log L_{\rm mm} - \log M_\star$ correlation, and discuss this in detail at the end of Section 4.4.

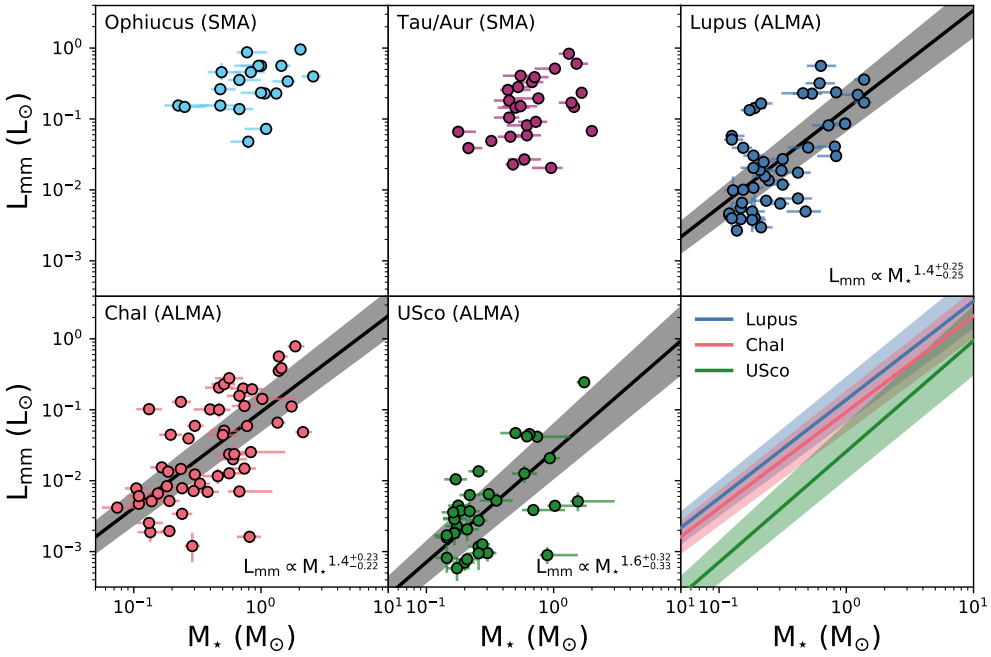

Figure B.5 Fitting of $\log L_{\rm mm} - \log M_\star$. The first 5 panels (left to right; top to bottom; ordered by region age) show the model results of each region as circles (resolved) and triangles (upper-limits). The best fit from MCMC linear regression is plotted as a black line, and surrounded by our 68% confidence intervals in grey. The last panel replots the bests fits of each region (and the corresponding 68% confidence intervals) so that they can be directly compared. Fit parameters for each region are given in Table B.2.

Table B.2. $\log L_{\rm mm} - \log M_\star$ statistical tests

Region	Shapiro $L_{\rm mm}$		Shapiro $M_\star$		Pearson r		Spearman ρ		Regression Parameters			
	stat	p-value	stat	p-value	stat	p-value	stat	p-value	α	β	σ	$\hat{\rho}$
Oph	0.91	6.71e-02	0.91	5.66e-02	0.38	9.86e-02	0.30	2.01e-01	$-0.53^{+0.083}_{-0.08}$	$0.49^{+0.36}_{-0.36}$	$0.35^{+0.074}_{-0.056}$	$0.61^{+0.17}_{-0.28}$
Tau/Aur	0.87	3.25e-03	0.82	2.86e-04	0.37	6.06e-02	0.37	5.54e-02	$-0.77^{+0.1}_{-0.1}$	$0.75^{+0.36}_{-0.36}$	$0.43^{+0.074}_{-0.058}$	$0.66^{+0.12}_{-0.18}$
Lupus	0.77	2.89e-07	0.67	3.46e-09	0.56	3.82e-05	0.61	3.94e-06	$-0.86^{+0.2}_{-0.1}$	$1.4^{+0.2}_{-0.2}$	$0.51^{+0.06}_{-0.05}$	$0.81^{+0.05}_{-0.06}$
Chamaeleon I	0.8	1.19e-07	0.6	1.35e-11	0.61	2.78e-07	0.55	6.20e-06	$-1^{+0.1}_{-0.1}$	$1.4^{+0.2}_{-0.2}$	$0.56^{+0.06}_{-0.06}$	$0.82^{+0.05}_{-0.06}$
USco	0.45	8.04e-11	0.34	7.70e-12	0.29	7.48e-02	0.49	1.81e-03	$-1.9^{+0.2}_{-0.2}$	$1.1^{+0.3}_{-0.3}$	$0.52^{+0.07}_{-0.06}$	$0.75^{+0.08}_{-0.1}$

Note. — Values we consider unreliable are greyed out (see Section 4.5.1).

B.5 Appendix: Correlation of R_{90} and R_{68}

Different emission fractions have been used to define the location of $R_{\rm eff}$ in past works. For example, Tripathi et al. (2017a) and Andrews et al. (2018b), who analyze low- and medium-resolution SMA and ALMA data, calculate the radius containing 68% of the total flux (R_{68}). However, high-resolution ALMA images have shown that R_{68} does not properly capture the radial extent of the disk, several sub-structures are left out, hence more recent works compute and analyze the 90% (R_{90}) or 95% (R_{95}) dust radius (see Long et al. 2018 and Huang et al. 2018). In order to compare the results of this work with disk sizes from the literature, we are interested in understanding if R_{68} is a reliable predictor of R_{90}.

The 68% and 90% emission radii we measure from modeled disks in Lupus, Chamaeleon I, and USco are shown in Figure B.6. Visual inspection suggests that the two disk sizes are strongly correlated. We calculate the Spearman ρ rank-order correlation coefficient[1] to test the null hypothesis that the two variables are uncorrelated. As shown in Table B.3, the correlation coefficient is nearly unity (positive rank order) with an extremely low probability (p-value) that R_{68} and R_{90} are uncorrelated.

We then fit the data using the Bayesian linear regression method developed by Kelly (2007) and report the results in Table B.3. Using these best fitting parameters, we can convert the R_{68} to a R_{90} disk size:.

[1]We cannot apply the Pearson correlation test, which tests for a linear relationship between two quantities, because we find that R_{68} and R_{90} are not bivariate normally distributed.

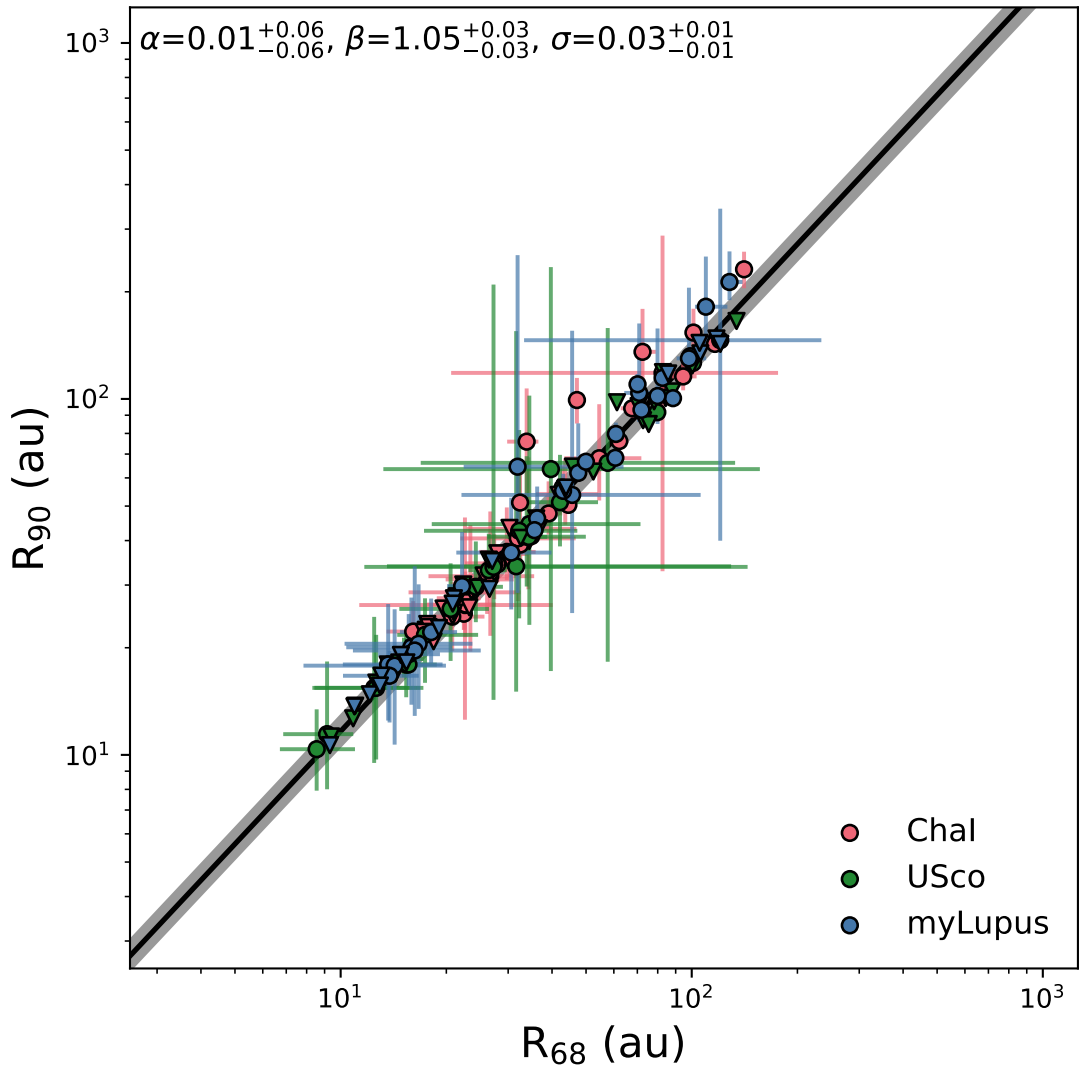

Figure B.6 Here we compare our R_{68} dust-disk size estimates with the R_{90} size for each disk. Constrained disks sizes are plotted as circles while upper-limits are given as triangles. Symbols are color coded according to their associated region. The correlation between R_{68} and R_{90} is measured by fitting the values using linmix. The best fit is shown as a black line, with a 1-sigma confidence interval in gray. The parameters resulting from the mcmc chain are given in the upper left of the figure (see Equation B.2).

Table B.3. R_{90} vs R_{68} statistical analysis and fitting

	Shapiro R_{68}		Shapiro R_{90}		Spearman ρ		Regression Parameters			
	stat	p-value	stat	p-value	stat	p-value	α	β	σ	corr
R_{90} vs R_{68}	0.87	3.1e-07	0.84	4.1e-08	0.98	2.6e-63	$0.01^{+0.06}_{-0.06}$	$1.05^{+0.03}_{-0.03}$	$0.03^{+0.01}_{-0.01}$	$1.00^{+0.00}_{-0.00}$

$$\log R_{90} = -0.037(\text{au}) + 1.1 \log R_{68}(\text{au}) \tag{B.2}$$

B.6 Appendix: Individual modeling results

Table B.4. Modeling Parameters

2MASS	R_{68} $''$	R_{90} $''$	R_t $''$	f_0 (Jy/Sr)	α	β	γ	i (°)	PA (°)	dDec ($''$)	dRA ($''$)	lnwcorr
J10533978-7712338	< 0.11	< 0.13	$0.11^{+0.05}_{-0.05}$	$9.98^{+0.52}_{-0.35}$	$60.00^{+32.12}_{-40.13}$	$9.37^{+3.55}_{-3.31}$	$-2.03^{+1.69}_{-2.69}$	$51.64^{+24.41}_{-28.56}$	$58.51^{+58.02}_{-37.85}$	$-0.01^{+0.03}_{-0.03}$	$-0.45^{+0.03}_{-0.03}$	$-0.96^{+0.00}_{-0.00}$
J10555973-7724399	$0.11^{+0.03}_{-0.01}$	$0.13^{+0.03}_{-0.03}$	$0.10^{+0.02}_{-0.02}$	$10.84^{+0.44}_{-0.16}$	$52.10^{+36.53}_{-26.66}$	$8.68^{+3.24}_{-3.09}$	$-2.75^{+2.09}_{-2.20}$	$43.74^{+11.77}_{-13.83}$	$88.60^{+29.78}_{-26.10}$	$-0.07^{+0.01}_{-0.01}$	$-0.07^{+0.01}_{-0.01}$	$-3.79^{+0.01}_{-0.01}$
J10561638-7630530	< 0.12	< 0.14	$0.10^{+0.04}_{-0.04}$	$10.23^{+0.49}_{-0.51}$	$56.36^{+35.09}_{-41.50}$	$9.79^{+3.28}_{-4.37}$	$-2.55^{+1.85}_{-1.57}$	$41.79^{+25.26}_{-17.18}$	$62.34^{+25.32}_{-23.98}$	$-0.07^{+0.02}_{-0.03}$	$-0.37^{+0.02}_{-0.01}$	$-0.49^{+0.01}_{-0.00}$
J10563044-7711393	$0.77^{+0.03}_{-0.03}$	$1.27^{+0.15}_{-0.15}$	$0.54^{+0.05}_{-0.04}$	$10.01^{+0.05}_{-0.10}$	$65.43^{+31.18}_{-46.05}$	$4.27^{+0.44}_{-0.36}$	$-3.57^{+1.37}_{-1.73}$	$51.64^{+1.27}_{-1.09}$	$167.35^{+1.46}_{-1.92}$	$0.06^{+0.01}_{-0.01}$	$-0.41^{+0.01}_{-0.01}$	$-3.88^{+0.01}_{-0.01}$
J10580597-7711501	< 0.11	< 0.13	$0.11^{+0.03}_{-0.05}$	$10.01^{+0.47}_{-0.70}$	$62.61^{+28.85}_{-29.76}$	$9.59^{+2.91}_{-3.74}$	$-2.06^{+1.74}_{-2.43}$	$55.33^{+18.43}_{-23.39}$	$147.06^{+17.04}_{-29.60}$	$-0.02^{+0.03}_{-0.03}$	$-0.37^{+0.03}_{-0.03}$	$-0.48^{+0.00}_{-0.00}$
J10581677-7717170	$0.62^{+0.01}_{-0.01}$	$0.76^{+0.03}_{-0.02}$	$0.57^{+0.02}_{-0.03}$	$10.43^{+0.06}_{-0.03}$	$65.83^{+27.95}_{-24.66}$	$7.60^{+1.27}_{-0.75}$	$-3.74^{+0.49}_{-0.86}$	$42.01^{+0.98}_{-0.77}$	$157.12^{+1.36}_{-1.56}$	$-0.06^{+0.00}_{-0.00}$	$-0.38^{+0.00}_{-0.00}$	$-4.10^{+0.01}_{-0.01}$
J10590108-7722407	$0.23^{+0.01}_{-0.01}$	$0.31^{+0.05}_{-0.03}$	$0.21^{+0.04}_{-0.04}$	$10.53^{+0.16}_{-0.29}$	$42.87^{+43.72}_{-29.18}$	$7.36^{+3.85}_{-2.48}$	$-2.89^{+2.14}_{-1.64}$	$31.40^{+4.96}_{-3.37}$	$-16.22^{+34.30}_{-5.49}$	$-0.16^{+0.01}_{-0.01}$	$-0.42^{+0.01}_{-0.00}$	$-3.82^{+0.01}_{-0.01}$
J10590699-7701404	$0.36^{+0.01}_{-0.03}$	$0.50^{+0.04}_{-0.03}$	$0.36^{+0.03}_{-0.04}$	$10.45^{+0.11}_{-0.05}$	$52.69^{+38.02}_{-28.69}$	$5.83^{+1.27}_{-1.10}$	$0.13^{+0.02}_{-0.04}$	$31.47^{+1.48}_{-1.86}$	$36.46^{+4.42}_{-3.16}$	$0.16^{+0.00}_{-0.00}$	$-0.42^{+0.00}_{-0.00}$	$-4.47^{+0.01}_{-0.01}$
J11004022-7619280	$0.25^{+0.01}_{-0.01}$	$0.52^{+0.08}_{-0.07}$	$0.16^{+0.07}_{-0.04}$	$10.29^{+0.26}_{-0.29}$	$35.15^{+50.60}_{-21.38}$	$3.68^{+0.85}_{-0.32}$	$-0.70^{+0.78}_{-2.17}$	$3.67^{+3.80}_{-2.35}$	$82.69^{+17.18}_{-24.61}$	$-0.01^{+0.00}_{-0.00}$	$-0.27^{+0.00}_{-0.00}$	$-0.58^{+0.00}_{-0.01}$
J11022491-7733357	$0.25^{+0.01}_{0.00}$	$0.29^{+0.01}_{-0.01}$	$0.25^{+0.02}_{-0.01}$	$10.97^{+0.07}_{-0.22}$	$49.20^{+35.35}_{-23.69}$	$12.16^{+1.94}_{-2.07}$	$-4.34^{+2.17}_{-1.31}$	$10.92^{+8.31}_{-5.57}$	$83.72^{+27.61}_{-20.18}$	$0.10^{+0.00}_{-0.00}$	$-0.49^{+0.00}_{-0.00}$	$-4.14^{+0.01}_{-0.01}$
J11023265-7729129	$0.42^{+0.48}_{-0.32}$	$0.61^{+0.87}_{-0.44}$	$0.39^{+0.31}_{-0.29}$	$8.02^{+0.75}_{-0.37}$	$58.20^{+24.08}_{-32.81}$	$9.00^{+3.82}_{-4.73}$	$-3.07^{+1.84}_{-2.06}$	$62.73^{+15.22}_{-44.60}$	$113.53^{+47.12}_{-76.85}$	$-1.56^{+0.23}_{-0.25}$	$-0.72^{+0.20}_{-0.23}$	$-0.96^{+0.00}_{-0.01}$
J11025504-7721508	< 0.23	< 0.30	$0.15^{+0.13}_{-0.09}$	$8.82^{+0.63}_{-0.64}$	$42.36^{+35.01}_{-23.83}$	$5.55^{+5.11}_{-2.67}$	$-2.69^{+1.91}_{-2.08}$	$53.30^{+19.94}_{-19.75}$	$162.52^{+21.91}_{-30.27}$	$0.01^{+0.13}_{-0.14}$	$-0.39^{+0.05}_{-0.09}$	$-0.47^{+0.00}_{-0.00}$
J11040425-7639328	< 0.09	< 0.12	$0.10^{+0.05}_{-0.04}$	$9.65^{+0.36}_{-1.37}$	$33.01^{+41.65}_{-21.70}$	$6.96^{+5.53}_{-3.20}$	$-0.33^{+0.56}_{-2.77}$	$33.79^{+15.48}_{-21.42}$	$54.00^{+24.09}_{-31.55}$	$-0.09^{+0.04}_{-0.04}$	$-0.40^{+0.03}_{-0.02}$	$-0.48^{+0.00}_{-0.00}$
J11040909-7627193	$0.18^{+0.01}_{-0.02}$	$0.22^{+0.02}_{-0.01}$	$0.18^{+0.02}_{-0.03}$	$10.77^{+0.27}_{-0.21}$	$65.72^{+30.64}_{-34.34}$	$9.05^{+3.19}_{-2.22}$	$-1.25^{+1.06}_{-2.99}$	$38.95^{+8.11}_{-16.83}$	$47.79^{+16.20}_{-8.93}$	$-0.08^{+0.00}_{-0.00}$	$-0.22^{+0.00}_{-0.00}$	$-3.96^{+0.01}_{-0.01}$
J11044258-7741571	$0.14^{+0.05}_{-0.05}$	$0.17^{+0.09}_{-0.05}$	$0.13^{+0.06}_{-0.05}$	$9.91^{+0.54}_{-0.62}$	$58.33^{+24.87}_{-32.95}$	$10.16^{+2.68}_{-4.19}$	$-3.01^{+3.09}_{-2.38}$	$58.40^{+12.25}_{-20.78}$	$79.18^{+19.56}_{-25.18}$	$-0.03^{+0.04}_{-0.03}$	$-0.30^{+0.02}_{-0.03}$	$-0.49^{+0.01}_{-0.01}$
J11045701-7715569	< 0.12	< 0.13	$0.09^{+0.06}_{-0.04}$	$10.06^{+0.99}_{-0.40}$	$47.21^{+28.55}_{-29.89}$	$10.09^{+3.52}_{-5.78}$	$-2.35^{+1.62}_{-2.26}$	$39.82^{+32.66}_{-24.64}$	$72.86^{+74.29}_{-46.51}$	$-0.06^{+0.03}_{-0.02}$	$-0.37^{+0.03}_{-0.03}$	$-0.95^{+0.00}_{-0.00}$
J11062554-7633418	$0.16^{+0.01}_{-0.02}$	$0.36^{+0.15}_{-0.13}$	$0.08^{+0.05}_{-0.02}$	$10.97^{+0.20}_{-0.32}$	$35.82^{+50.57}_{-16.53}$	$3.36^{+1.07}_{-0.41}$	$-2.35^{+1.41}_{-2.05}$	$53.42^{+4.13}_{-4.12}$	$31.46^{+4.63}_{-5.70}$	$-0.05^{+0.00}_{-0.00}$	$-0.42^{+0.00}_{-0.00}$	$-0.56^{+0.00}_{-0.00}$
J11064510-7727023	< 0.20	< 0.23	$0.19^{+0.08}_{-0.08}$	$9.14^{+0.67}_{-0.29}$	$44.01^{+28.92}_{-27.20}$	$8.23^{+3.17}_{-3.43}$	$-3.01^{+2.41}_{-1.68}$	$45.30^{+29.90}_{-31.16}$	$108.46^{+47.09}_{-69.55}$	$0.02^{+0.06}_{-0.04}$	$-0.06^{+0.06}_{-0.06}$	$-0.96^{+0.00}_{-0.01}$
J11065906-7718535	$0.12^{+0.01}_{-0.01}$	$0.13^{+0.02}_{-0.01}$	$0.10^{+0.01}_{-0.01}$	$10.76^{+0.12}_{-0.12}$	$72.57^{+26.67}_{-34.22}$	$10.71^{+2.73}_{-4.10}$	$-3.74^{+1.89}_{-1.75}$	$28.95^{+16.85}_{-7.13}$	$161.66^{+27.46}_{-34.25}$	$0.12^{+0.01}_{-0.00}$	$-0.48^{+0.00}_{-0.00}$	$-0.50^{+0.00}_{-0.00}$
J11065939-7530559	$0.12^{+0.09}_{-0.06}$	$0.13^{+0.10}_{-0.07}$	$0.10^{+0.07}_{-0.07}$	$9.71^{+0.67}_{-1.59}$	$78.46^{+13.10}_{-44.02}$	$10.45^{+2.36}_{-4.76}$	$-1.04^{+1.31}_{-2.80}$	$49.93^{+20.30}_{-30.04}$	$110.40^{+54.41}_{-70.98}$	$-0.05^{+0.06}_{-0.02}$	$-0.29^{+0.02}_{-0.03}$	$-0.48^{+0.01}_{-0.00}$
J11070925-7718471	< 0.25	< 0.33	$0.25^{+0.48}_{-0.17}$	$8.14^{+0.90}_{-0.46}$	$43.94^{+39.25}_{-37.28}$	$9.34^{+4.01}_{-3.74}$	$-3.90^{+2.80}_{-1.39}$	$41.62^{+33.89}_{-30.66}$	$99.42^{+44.00}_{-59.84}$	$0.14^{+0.30}_{-0.16}$	$-0.49^{+0.20}_{-0.28}$	$-0.96^{+0.00}_{-0.00}$
J11071206-7632232	$0.22^{+0.05}_{-0.04}$	$0.28^{+0.07}_{-0.05}$	$0.23^{+0.08}_{-0.05}$	$9.72^{+0.45}_{-0.45}$	$60.96^{+25.12}_{-35.79}$	$9.68^{+3.42}_{-2.72}$	$-2.49^{+2.15}_{-2.61}$	$63.02^{+11.34}_{-31.70}$	$114.64^{+10.45}_{-19.65}$	$-0.01^{+0.02}_{-0.02}$	$-0.42^{+0.01}_{-0.02}$	$-0.97^{+0.00}_{-0.00}$
J11071330-7743498	< 0.11	< 0.12	$0.09^{+0.09}_{-0.05}$	$10.17^{+0.86}_{-0.81}$	$66.05^{+18.58}_{-34.88}$	$11.24^{+2.73}_{-4.16}$	$-2.11^{+1.62}_{-2.64}$	$64.44^{+13.87}_{-31.30}$	$70.54^{+63.54}_{-56.50}$	$0.13^{+0.03}_{-0.03}$	$-0.65^{+0.03}_{-0.03}$	$-0.96^{+0.00}_{-0.00}$
J11071860-7732516	< 0.15	< 0.22	$0.13^{+0.21}_{-0.09}$	$8.53^{+1.28}_{-0.73}$	$48.93^{+45.19}_{-31.94}$	$9.72^{+2.96}_{-3.76}$	$-3.82^{+2.59}_{-1.29}$	$34.73^{+20.86}_{-21.95}$	$96.82^{+22.82}_{-34.87}$	$0.09^{+0.19}_{-0.22}$	$-0.45^{+0.14}_{-0.19}$	$-0.48^{+0.00}_{-0.00}$

Table B.4 (cont'd)

2MASS	R_{68} $''$	R_{90} $''$	R_t $''$	f_0 (Jy/Sr)	α	β	γ	i (°)	PA (°)	dDec ($''$)	dRA ($''$)	lnwcorr
J11072074-7738073	< 0.09	< 0.12	$0.06^{+0.03}_{-0.03}$	$10.05^{+1.22}_{-1.52}$	$66.39^{+20.46}_{-38.85}$	$6.78^{+1.87}_{-3.30}$	$0.13^{+0.19}_{-1.19}$	$45.33^{+17.53}_{-22.49}$	$37.64^{+103.18}_{-26.28}$	$-0.02^{+0.01}_{-0.01}$	$-0.42^{+0.01}_{-0.01}$	$-3.77^{+0.01}_{-0.01}$
J11074366-7739411	$0.17^{+0.01}_{-0.01}$	$0.20^{+0.03}_{-0.02}$	$0.16^{+0.06}_{-0.02}$	$11.06^{+0.12}_{-0.68}$	$75.09^{+23.28}_{-33.11}$	$8.62^{+3.88}_{-1.51}$	$-3.33^{+3.40}_{-1.50}$	$38.59^{+5.65}_{-14.07}$	$129.89^{+4.70}_{-7.51}$	$-0.05^{+0.00}_{-0.00}$	$-0.35^{+0.00}_{-0.00}$	$-3.93^{+0.01}_{-0.01}$
J11074656-7615174	< 0.09	< 0.12	$0.10^{+0.07}_{-0.04}$	$10.03^{+0.49}_{-0.68}$	$54.66^{+38.40}_{-36.42}$	$8.21^{+3.30}_{-3.48}$	$-1.92^{+1.90}_{-2.33}$	$63.22^{+14.18}_{-15.23}$	$93.97^{+25.73}_{-29.82}$	$0.10^{+0.04}_{-0.05}$	$-0.31^{+0.03}_{-0.03}$	$-0.48^{+0.01}_{-0.01}$
J11075730-7717262	< 0.15	< 0.17	$0.15^{+0.05}_{-0.07}$	$9.56^{+0.44}_{-1.68}$	$34.05^{+41.33}_{-21.32}$	$8.32^{+2.69}_{-3.65}$	$-1.29^{+1.58}_{-3.67}$	$30.10^{+17.99}_{-15.69}$	$-4.06^{+42.06}_{-22.15}$	$-0.05^{+0.05}_{-0.07}$	$-0.41^{+0.03}_{-0.05}$	$-3.75^{+0.01}_{-0.01}$
J11075809-7742413	< 0.08	< 0.09	$0.07^{+0.05}_{-0.03}$	$10.58^{+0.98}_{-0.41}$	$56.38^{+29.16}_{-33.71}$	$9.59^{+4.01}_{-3.14}$	$-2.10^{+1.53}_{-2.12}$	$43.35^{+31.28}_{-30.26}$	$86.70^{+62.10}_{-46.34}$	$-0.02^{+0.01}_{-0.01}$	$-0.35^{+0.02}_{-0.01}$	$-0.96^{+0.00}_{-0.00}$
J11080002-7717304	< 0.13	< 0.16	$0.09^{+0.24}_{-0.08}$	$8.16^{+1.87}_{-0.45}$	$44.31^{+24.98}_{-35.08}$	$7.64^{+4.66}_{-3.73}$	$-2.68^{+2.04}_{-2.25}$	$47.22^{+32.04}_{-33.39}$	$93.32^{+68.02}_{-65.02}$	$0.46^{+0.19}_{-0.27}$	$0.53^{+0.18}_{-0.23}$	$-0.96^{+0.00}_{-0.00}$
J11081509-7733531	$0.33^{+0.02}_{-0.01}$	$0.40^{+0.02}_{-0.02}$	$0.31^{+0.06}_{-0.03}$	$10.65^{+0.11}_{-0.22}$	$65.90^{+27.72}_{-33.73}$	$8.55^{+4.66}_{-2.32}$	$-2.30^{+1.54}_{-1.62}$	$37.60^{+1.85}_{-2.40}$	$163.18^{+3.00}_{-3.62}$	$-0.25^{+0.00}_{-0.00}$	$0.99^{+0.00}_{-0.00}$	$-4.05^{+0.01}_{-0.01}$
J11083905-7716042	< 0.09	< 0.11	$0.08^{+0.10}_{-0.06}$	$10.05^{+0.77}_{-2.06}$	$28.11^{+42.67}_{-10.53}$	$12.44^{+1.59}_{-3.04}$	$-0.13^{+0.49}_{-3.26}$	$38.78^{+13.11}_{-21.39}$	$103.29^{+35.77}_{-17.28}$	$0.09^{+0.02}_{-0.02}$	$-0.38^{+0.01}_{-0.02}$	$-3.78^{+0.01}_{-0.01}$
J11085367-7521359	$0.15^{+0.03}_{-0.03}$	$0.18^{+0.04}_{-0.04}$	$0.15^{+0.04}_{-0.04}$	$10.39^{+0.28}_{-0.26}$	$49.40^{+28.33}_{-28.05}$	$10.10^{+3.06}_{-2.96}$	$-1.36^{+0.93}_{-2.58}$	$37.83^{+15.49}_{-22.38}$	$131.42^{+16.13}_{-18.44}$	$-0.02^{+0.01}_{-0.01}$	$-0.25^{+0.01}_{-0.01}$	$-3.81^{+0.01}_{-0.01}$
J11085464-7702129	< 0.13	< 0.16	$0.10^{+0.06}_{-0.03}$	$10.15^{+0.45}_{-0.41}$	$43.94^{+32.82}_{-27.15}$	$9.43^{+3.50}_{-3.63}$	$-3.16^{+2.03}_{-2.19}$	$49.12^{+27.85}_{-36.95}$	$66.05^{+73.92}_{-35.02}$	$-0.11^{+0.02}_{-0.02}$	$-0.15^{+0.02}_{-0.02}$	$-0.96^{+0.00}_{-0.01}$
J11092379-7623207	$0.17^{+0.01}_{-0.01}$	$0.27^{+0.07}_{-0.04}$	$0.14^{+0.02}_{-0.03}$	$10.87^{+0.15}_{-0.18}$	$60.40^{+38.00}_{-26.92}$	$5.19^{+2.21}_{-1.17}$	$-1.87^{+1.44}_{-2.12}$	$15.63^{+8.15}_{-10.29}$	$55.18^{+26.51}_{-33.20}$	$-0.05^{+0.01}_{-0.00}$	$-0.35^{+0.00}_{-0.00}$	$-3.94^{+0.01}_{-0.01}$
J11094621-7634463	< 0.14	< 0.19	$0.13^{+0.06}_{-0.05}$	$9.62^{+0.46}_{-0.28}$	$44.13^{+45.34}_{-25.03}$	$9.95^{+3.74}_{-5.10}$	$-2.03^{+1.65}_{-2.58}$	$23.95^{+14.42}_{-12.36}$	$148.16^{+34.58}_{-26.08}$	$-0.05^{+0.04}_{-0.07}$	$-0.43^{+0.03}_{-0.06}$	$-3.76^{+0.01}_{-0.01}$
J11094742-7726290	$0.53^{+0.02}_{-0.02}$	$0.80^{+0.13}_{-0.09}$	$0.49^{+0.06}_{-0.04}$	$9.87^{+0.06}_{-0.05}$	$69.02^{+26.36}_{-39.19}$	$4.83^{+1.58}_{-0.57}$	$0.12^{+0.02}_{-0.02}$	$54.12^{+1.27}_{-1.93}$	$29.37^{+1.85}_{-1.74}$	$-0.07^{+0.00}_{-0.01}$	$-0.41^{+0.00}_{-0.01}$	$-3.87^{+0.01}_{-0.01}$
J11095340-7634255	$0.36^{+0.03}_{-0.02}$	$0.67^{+0.22}_{-0.13}$	$0.24^{+0.05}_{-0.05}$	$10.24^{+0.20}_{-0.16}$	$55.32^{+32.30}_{-28.08}$	$3.76^{+0.66}_{-0.50}$	$-1.09^{+0.89}_{-3.16}$	$51.26^{+2.78}_{-3.23}$	$134.18^{+4.55}_{-3.08}$	$0.10^{+0.01}_{-0.01}$	$-0.33^{+0.01}_{-0.01}$	$-3.84^{+0.01}_{-0.01}$
J11100369-7633291	< 0.15	< 0.18	$0.14^{+0.34}_{-0.05}$	$10.16^{+0.99}_{-2.00}$	$33.46^{+34.57}_{-19.37}$	$6.84^{+3.87}_{-1.81}$	$-1.50^{+1.78}_{-2.86}$	$64.77^{+12.54}_{-13.92}$	$131.01^{+25.56}_{-20.69}$	$0.03^{+0.02}_{-0.02}$	$-0.31^{+0.02}_{-0.02}$	$-3.77^{+0.02}_{-0.01}$
J11100469-7635452	$0.18^{+0.07}_{-0.06}$	$0.22^{+0.13}_{-0.07}$	$0.18^{+0.22}_{-0.08}$	$9.88^{+0.47}_{-1.47}$	$54.18^{+38.14}_{-30.42}$	$8.77^{+3.62}_{-4.67}$	$-0.34^{+0.62}_{-2.60}$	$60.67^{+15.98}_{-25.29}$	$89.84^{+27.43}_{-14.71}$	$0.03^{+0.02}_{-0.03}$	$-0.34^{+0.02}_{-0.03}$	$-3.78^{+0.01}_{-0.01}$
J11101141-7635292	$0.14^{+0.02}_{-0.01}$	$0.18^{+0.02}_{-0.02}$	$0.15^{+0.01}_{-0.02}$	$11.01^{+0.17}_{-0.11}$	$55.55^{+36.09}_{-25.75}$	$12.14^{+1.53}_{-2.95}$	$-2.25^{+1.39}_{-2.33}$	$56.71^{+7.33}_{-13.78}$	$173.68^{+8.69}_{-11.46}$	$-0.02^{+0.01}_{-0.01}$	$-0.34^{+0.00}_{-0.00}$	$-3.91^{+0.01}_{-0.01}$
J11104959-7717517	$0.21^{+0.02}_{-0.02}$	$0.26^{+0.06}_{-0.03}$	$0.19^{+0.04}_{-0.03}$	$10.71^{+0.20}_{-0.09}$	$34.67^{+28.82}_{-21.56}$	$9.84^{+3.51}_{-5.33}$	$-1.64^{+1.16}_{-1.55}$	$61.71^{+10.22}_{-6.47}$	$59.76^{+6.48}_{-5.12}$	$0.04^{+0.01}_{-0.01}$	$-0.37^{+0.01}_{-0.00}$	$-3.82^{+0.01}_{-0.01}$
J11105333-7634319	$0.16^{+0.02}_{-0.03}$	$0.19^{+0.03}_{-0.03}$	$0.16^{+0.02}_{-0.02}$	$10.57^{+0.16}_{-0.30}$	$57.66^{+46.03}_{-23.44}$	$10.04^{+3.79}_{-2.97}$	$-2.81^{+2.39}_{-2.46}$	$46.76^{+13.83}_{-10.38}$	$24.56^{+20.27}_{-33.11}$	$-0.02^{+0.01}_{-0.01}$	$-0.27^{+0.01}_{-0.00}$	$-3.79^{+0.01}_{-0.01}$
J11105359-7725004	$0.12^{+0.05}_{-0.04}$	$0.15^{+0.08}_{-0.05}$	$0.11^{+0.02}_{-0.03}$	$10.35^{+0.26}_{-0.37}$	$45.16^{+34.71}_{-25.38}$	$10.26^{+3.62}_{-3.66}$	$-2.01^{+1.40}_{-2.70}$	$44.83^{+17.14}_{-13.10}$	$178.45^{+20.47}_{-25.86}$	$-0.07^{+0.01}_{-0.01}$	$-0.38^{+0.01}_{-0.01}$	$-0.49^{+0.01}_{-0.00}$
J11111083-7641574	$0.50^{+0.05}_{-0.05}$	$0.61^{+0.08}_{-0.05}$	$0.54^{+0.05}_{-0.11}$	$9.97^{+0.44}_{-0.20}$	$61.70^{+34.34}_{-22.59}$	$11.75^{+2.37}_{-5.96}$	$-0.01^{+0.12}_{-2.75}$	$76.72^{+5.65}_{-2.61}$	$144.14^{+1.42}_{-1.45}$	$0.30^{+0.01}_{-0.01}$	$-0.23^{+0.01}_{-0.01}$	$-3.80^{+0.01}_{-0.01}$
J11113965-7620152	< 0.09	< 0.12	$0.07^{+0.03}_{-0.01}$	$10.92^{+0.17}_{-0.19}$	$58.88^{+36.70}_{-33.35}$	$9.22^{+3.61}_{-2.72}$	$-3.21^{+2.34}_{-1.81}$	$24.03^{+18.42}_{-11.46}$	$113.13^{+26.59}_{-24.76}$	$0.33^{+0.02}_{-0.01}$	$-0.18^{+0.01}_{-0.01}$	$-3.79^{+0.01}_{-0.01}$
J11114632-7620092	$0.14^{+0.03}_{-0.03}$	$0.16^{+0.03}_{-0.03}$	$0.14^{+0.03}_{-0.03}$	$10.78^{+0.22}_{-0.20}$	$60.10^{+27.72}_{-38.03}$	$10.12^{+2.33}_{-3.63}$	$-2.14^{+1.83}_{-2.78}$	$56.51^{+8.03}_{-12.05}$	$136.42^{+15.63}_{-14.32}$	$0.40^{+0.01}_{-0.01}$	$-0.22^{+0.01}_{-0.01}$	$-3.80^{+0.01}_{-0.01}$
J11120351-7726009	< 0.11	< 0.14	$0.11^{+0.05}_{-0.04}$	$9.86^{+0.35}_{-0.28}$	$54.25^{+29.08}_{-30.04}$	$9.33^{+3.66}_{-4.09}$	$-3.19^{+2.07}_{-1.98}$	$47.71^{+16.94}_{-20.25}$	$125.17^{+24.64}_{-30.24}$	$0.06^{+0.03}_{-0.03}$	$-0.40^{+0.03}_{-0.02}$	$-0.49^{+0.01}_{-0.01}$

Table B.4 (cont'd)

2MASS	R_{68} $''$	R_{90} $''$	R_t $''$	f_0 (Jy/Sr)	α	β	γ	i (°)	PA (°)	dDec ($''$)	dRA ($''$)	lnwcorr
J11120984-7634366	< 0.11	< 0.14	$0.09^{+0.03}_{-0.04}$	$10.15^{+1.22}_{-0.28}$	$59.80^{+33.80}_{-37.59}$	$7.58^{+3.50}_{-2.14}$	$-1.81^{+1.19}_{-2.11}$	$43.50^{+11.75}_{-16.12}$	$156.92^{+24.31}_{-25.69}$	$0.09^{+0.03}_{-0.03}$	$-0.37^{+0.01}_{-0.01}$	$-0.48^{+0.01}_{-0.00}$
J11122772-7644223	$0.12^{+0.03}_{-0.03}$	$0.14^{+0.03}_{-0.03}$	$0.12^{+0.02}_{-0.04}$	$11.07^{+0.66}_{-0.16}$	$60.33^{+34.92}_{-19.22}$	$10.48^{+3.42}_{-3.11}$	$-1.93^{+1.22}_{-2.95}$	$51.81^{+10.91}_{-14.38}$	$144.73^{+23.25}_{-10.26}$	$0.17^{+0.01}_{-0.00}$	$-0.34^{+0.00}_{-0.00}$	$-3.87^{+0.01}_{-0.01}$
J11123092-7644241	< 0.13	< 0.16	$0.11^{+0.05}_{-0.05}$	$10.18^{+1.04}_{-0.34}$	$66.55^{+27.31}_{-43.58}$	$9.34^{+3.31}_{-4.64}$	$-2.27^{+1.75}_{-2.75}$	$24.56^{+19.26}_{-12.67}$	$102.37^{+30.73}_{-29.99}$	$0.29^{+0.03}_{-0.03}$	$-0.26^{+0.02}_{-0.02}$	$-3.80^{+0.01}_{-0.01}$
J11124268-7722230	< 0.18	< 0.23	$0.13^{+0.22}_{-0.10}$	$8.48^{+0.91}_{-0.67}$	$49.46^{+34.43}_{-34.07}$	$8.24^{+4.69}_{-4.88}$	$-2.72^{+1.83}_{-2.02}$	$59.40^{+22.88}_{-38.71}$	$73.10^{+57.56}_{-45.85}$	$-0.61^{+0.18}_{-0.26}$	$0.55^{+0.21}_{-0.18}$	$-0.96^{+0.01}_{-0.01}$
J11132446-7629227	$0.17^{+0.08}_{-0.05}$	$0.22^{+0.11}_{-0.07}$	$0.16^{+0.09}_{-0.05}$	$9.98^{+0.61}_{-0.36}$	$56.72^{+30.98}_{-39.50}$	$8.81^{+3.94}_{-3.82}$	$-1.82^{+1.39}_{-2.34}$	$59.91^{+14.46}_{-16.45}$	$19.33^{+25.92}_{-21.64}$	$-0.07^{+0.03}_{-0.04}$	$-0.40^{+0.02}_{-0.03}$	$-3.81^{+0.01}_{-0.01}$
J11142454-7733062	$0.12^{+0.01}_{-0.02}$	$0.15^{+0.02}_{-0.03}$	$0.11^{+0.02}_{-0.03}$	$10.20^{+0.12}_{-0.18}$	$58.92^{+33.74}_{-29.72}$	$9.73^{+2.64}_{-3.48}$	$-3.83^{+2.29}_{-1.48}$	$16.54^{+14.51}_{-10.42}$	$121.04^{+31.24}_{-34.91}$	$-0.19^{+0.02}_{-0.02}$	$-0.40^{+0.01}_{-0.01}$	$-0.48^{+0.01}_{-0.01}$
J11160287-7624533	$0.29^{+0.09}_{-0.06}$	$0.36^{+0.15}_{-0.09}$	$0.26^{+0.12}_{-0.10}$	$9.87^{+0.25}_{-0.28}$	$74.33^{+28.01}_{-43.73}$	$8.55^{+4.15}_{-4.08}$	$-2.32^{+1.92}_{-2.44}$	$70.85^{+7.85}_{-12.53}$	$132.49^{+10.80}_{-8.06}$	$-0.01^{+0.03}_{-0.03}$	$-0.40^{+0.03}_{-0.03}$	$-3.79^{+0.01}_{-0.01}$
J11173700-7704381	$0.16^{+0.03}_{-0.03}$	$0.20^{+0.07}_{-0.03}$	$0.13^{+0.04}_{-0.05}$	$10.57^{+0.13}_{-0.20}$	$38.63^{+30.55}_{-19.49}$	$6.06^{+4.39}_{-2.14}$	$-2.18^{+1.58}_{-1.53}$	$43.77^{+15.80}_{-19.46}$	$130.76^{+11.03}_{-16.15}$	$0.01^{+0.01}_{-0.01}$	$-0.42^{+0.01}_{-0.01}$	$-3.82^{+0.01}_{-0.01}$
J11183572-7935548	$0.17^{+0.03}_{-0.03}$	$0.24^{+0.05}_{-0.04}$	$0.14^{+0.04}_{-0.03}$	$10.36^{+0.51}_{-0.13}$	$69.16^{+33.69}_{-43.66}$	$6.19^{+3.07}_{-1.36}$	$-3.48^{+2.32}_{-1.96}$	$66.21^{+6.50}_{-10.60}$	$115.53^{+6.93}_{-11.50}$	$-0.33^{+0.01}_{-0.01}$	$0.19^{+0.01}_{-0.01}$	$-0.48^{+0.01}_{-0.01}$
J11241186-7630425	< 0.12	< 0.15	$0.13^{+0.06}_{-0.06}$	$9.35^{+0.34}_{-0.58}$	$46.26^{+36.29}_{-30.11}$	$10.78^{+2.75}_{-4.04}$	$-2.54^{+1.98}_{-2.01}$	$45.78^{+18.66}_{-23.68}$	$133.99^{+24.02}_{-36.09}$	$-0.17^{+0.11}_{-0.09}$	$-0.36^{+0.08}_{-0.05}$	$-0.48^{+0.01}_{-0.00}$
J15354856-2958551	< 0.18	< 0.24	$0.09^{+0.15}_{-0.04}$	$10.27^{+0.67}_{-0.80}$	$70.53^{+21.38}_{-38.19}$	$8.98^{+4.72}_{-3.81}$	$-1.64^{+1.55}_{-3.08}$	$70.45^{+15.50}_{-11.95}$	$88.67^{+33.06}_{-30.91}$	$-0.67^{+0.05}_{-0.03}$	$-0.95^{+0.03}_{-0.05}$	$-0.48^{+0.00}_{-0.00}$
J15392776-3446171	$0.14^{+0.01}_{-0.01}$	$0.19^{+0.08}_{-0.03}$	$0.13^{+0.05}_{-0.04}$	$10.93^{+0.28}_{-0.56}$	$45.10^{+37.82}_{-35.09}$	$6.66^{+4.01}_{-2.84}$	$-1.49^{+1.60}_{-3.09}$	$52.06^{+4.21}_{-2.30}$	$114.24^{+4.49}_{-2.16}$	$-0.17^{+0.00}_{-0.00}$	$-0.36^{+0.00}_{-0.00}$	$-0.53^{+0.01}_{-0.00}$
J15392828-3446180	< 0.08	< 0.10	$0.10^{+0.07}_{-0.04}$	$10.61^{+0.61}_{-1.40}$	$46.41^{+42.76}_{-35.89}$	$11.94^{+3.18}_{-4.90}$	$-0.95^{+1.18}_{-3.12}$	$40.45^{+21.22}_{-14.97}$	$59.51^{+22.40}_{-33.76}$	$-0.16^{+0.01}_{-0.01}$	$-0.26^{+0.01}_{-0.01}$	$-0.62^{+0.01}_{-0.01}$
J15450634-3417378	< 0.08	< 0.10	$0.07^{+0.03}_{-0.03}$	$11.13^{+0.34}_{-0.55}$	$63.22^{+23.66}_{-25.38}$	$11.48^{+2.89}_{-5.92}$	$-2.07^{+1.73}_{-2.61}$	$64.91^{+15.69}_{-18.01}$	$75.16^{+20.65}_{-32.65}$	$-0.11^{+0.01}_{-0.01}$	$-0.22^{+0.02}_{-0.02}$	$-0.49^{+0.01}_{-0.01}$
J15450887-3417333	$0.12^{+0.02}_{-0.02}$	$0.14^{+0.03}_{-0.03}$	$0.11^{+0.03}_{-0.03}$	$10.92^{+0.17}_{-0.24}$	$50.75^{+34.01}_{-34.13}$	$10.46^{+4.35}_{-5.14}$	$-1.82^{+1.39}_{-2.77}$	$44.12^{+19.76}_{-16.44}$	$95.87^{+19.09}_{-20.55}$	$-0.12^{+0.01}_{-0.00}$	$-0.34^{+0.01}_{-0.01}$	$-0.52^{+0.01}_{-0.01}$
J15451741-3418283	< 0.06	< 0.07	$0.06^{+0.03}_{-0.02}$	$11.03^{+0.36}_{-0.21}$	$40.13^{+32.86}_{-21.38}$	$11.96^{+3.80}_{-4.81}$	$-3.11^{+1.92}_{-2.12}$	$35.07^{+24.57}_{-14.42}$	$12.72^{+30.06}_{-18.83}$	$-0.17^{+0.01}_{-0.01}$	$-0.33^{+0.01}_{-0.01}$	$-0.50^{+0.01}_{-0.01}$
J15464473-3430354	$0.45^{+0.02}_{-0.01}$	$0.71^{+0.05}_{-0.04}$	$0.90^{+0.32}_{-0.48}$	$10.18^{+0.11}_{-0.12}$	$1.98^{+2.74}_{-0.40}$	$11.71^{+3.31}_{-7.10}$	$0.13^{+0.03}_{-0.03}$	$40.00^{+2.02}_{-1.99}$	$31.12^{+4.16}_{-3.18}$	$-0.57^{+0.00}_{-0.00}$	$-0.18^{+0.00}_{-0.00}$	$-0.53^{+0.01}_{-0.00}$
J15475062-3528353	< 0.07	< 0.09	$0.06^{+0.03}_{-0.02}$	$11.31^{+0.54}_{-0.47}$	$34.03^{+29.40}_{-18.95}$	$11.50^{+2.74}_{-4.60}$	$-3.06^{+2.33}_{-1.81}$	$57.75^{+19.03}_{-16.38}$	$6.92^{+27.88}_{-24.18}$	$-0.36^{+0.01}_{-0.01}$	$-0.21^{+0.01}_{-0.01}$	$-0.49^{+0.01}_{-0.01}$
J15475693-3514346	$0.20^{+0.21}_{-0.06}$	$0.41^{+1.21}_{-0.23}$	$0.12^{+0.06}_{-0.09}$	$10.69^{+0.55}_{-0.57}$	$43.40^{+33.13}_{-17.56}$	$5.15^{+9.58}_{-2.67}$	$-2.72^{+2.75}_{-2.14}$	$57.54^{+13.46}_{-12.25}$	$101.55^{+10.91}_{-18.96}$	$-0.38^{+0.01}_{-0.01}$	$-0.21^{+0.02}_{-0.01}$	$-0.51^{+0.01}_{-0.01}$
J15514032-2146103	< 0.62	< 0.74	$0.60^{+0.30}_{-0.49}$	$7.39^{+0.94}_{-2.34}$	$60.14^{+26.46}_{-32.17}$	$10.52^{+3.59}_{-4.55}$	$-3.36^{+3.17}_{-1.79}$	$43.60^{+19.65}_{-17.88}$	$82.04^{+21.65}_{-35.17}$	$-1.00^{+0.16}_{-0.22}$	$-0.50^{+0.15}_{-0.20}$	$-0.48^{+0.01}_{-0.01}$
J15530132-2114135	$0.09^{+0.03}_{-0.03}$	$0.11^{+0.04}_{-0.04}$	$0.08^{+0.04}_{-0.03}$	$10.40^{+0.52}_{-0.20}$	$54.80^{+32.54}_{-30.49}$	$11.13^{+4.30}_{-5.56}$	$-2.48^{+1.99}_{-2.15}$	$59.33^{+11.13}_{-17.32}$	$41.35^{+36.81}_{-24.02}$	$-0.30^{+0.01}_{-0.01}$	$-0.23^{+0.01}_{-0.01}$	$-0.48^{+0.01}_{-0.01}$
J15534211-2049282	$0.25^{+0.12}_{-0.06}$	$0.30^{+0.21}_{-0.08}$	$0.22^{+0.08}_{-0.08}$	$9.50^{+0.84}_{-0.49}$	$54.90^{+23.14}_{-31.97}$	$10.96^{+4.73}_{-7.06}$	$-2.34^{+2.12}_{-1.98}$	$74.77^{+7.75}_{-11.52}$	$78.06^{+14.60}_{-15.65}$	$-0.48^{+0.02}_{-0.04}$	$-0.62^{+0.07}_{-0.04}$	$-4.12^{+0.00}_{-0.01}$
J15564230-3749154	$0.30^{+0.01}_{-0.01}$	$0.39^{+0.15}_{-0.02}$	$0.30^{+0.02}_{-0.12}$	$10.54^{+0.40}_{-0.03}$	$33.60^{+38.78}_{-26.10}$	$6.44^{+1.66}_{-2.77}$	$0.16^{+0.01}_{-0.40}$	$15.59^{+5.05}_{-2.98}$	$89.58^{+9.33}_{-8.27}$	$-0.34^{+0.00}_{-0.00}$	$-0.18^{+0.00}_{-0.00}$	$-0.67^{+0.01}_{-0.01}$
J15580252-3736026	$0.24^{+0.03}_{-0.02}$	$0.30^{+0.07}_{-0.04}$	$0.23^{+0.03}_{-0.05}$	$10.54^{+0.22}_{-0.20}$	$56.50^{+26.56}_{-36.41}$	$7.85^{+6.67}_{-3.14}$	$-1.60^{+1.26}_{-2.94}$	$75.67^{+2.86}_{-6.93}$	$164.68^{+3.00}_{-2.63}$	$-0.40^{+0.01}_{-0.01}$	$-0.32^{+0.01}_{-0.01}$	$-0.50^{+0.01}_{-0.01}$

Table B.4 (cont'd)

2MASS	R_{68} $''$	R_{90} $''$	R_t $''$	f_0 (Jy/Sr)	α	β	γ	i (°)	PA (°)	dDec ($''$)	dRA ($''$)	lnwcorr
J15582981-2310077	$0.17^{+0.57}_{-0.09}$	$0.23^{+0.82}_{-0.13}$	$0.15^{+0.47}_{-0.08}$	$9.75^{+0.89}_{-3.02}$	$37.91^{+46.30}_{-23.55}$	$14.07^{+1.84}_{-6.70}$	$-0.04^{+0.41}_{-3.93}$	$46.74^{+24.83}_{-35.41}$	$100.51^{+43.05}_{-63.03}$	$-0.33^{+0.01}_{-0.01}$	$-0.09^{+0.02}_{-0.01}$	$-0.49^{+0.01}_{-0.01}$
J15583692-2257153	$0.48^{+0.00}_{0.00}$	$0.55^{+0.00}_{-0.00}$	$0.53^{+0.01}_{-0.01}$	$9.96^{+0.01}_{-0.01}$	$68.28^{+20.64}_{-23.50}$	$14.38^{+1.47}_{-2.23}$	$-0.25^{+0.03}_{-0.04}$	$29.86^{+0.86}_{-1.02}$	$150.26^{+1.81}_{-1.54}$	$-0.29^{+0.00}_{-0.00}$	$-0.31^{+0.00}_{-0.00}$	$-0.61^{+0.01}_{-0.00}$
J15591647-4157102	$0.31^{+0.00}_{-0.00}$	$0.41^{+0.01}_{-0.02}$	$0.36^{+0.12}_{-0.06}$	$10.26^{+0.10}_{-0.04}$	$6.54^{+68.11}_{-3.12}$	$9.12^{+6.41}_{-3.36}$	$0.12^{+0.01}_{-0.03}$	$31.38^{+1.98}_{-1.81}$	$155.57^{+4.85}_{-4.37}$	$-0.37^{+0.00}_{-0.00}$	$-0.26^{+0.00}_{-0.00}$	$-0.52^{+0.01}_{-0.01}$
J15592838-4021513	$0.63^{+0.01}_{-0.01}$	$0.83^{+0.05}_{-0.04}$	$0.55^{+0.03}_{-0.03}$	$10.55^{+0.31}_{-0.09}$	$11.12^{+48.79}_{-5.74}$	$6.32^{+1.27}_{-0.71}$	$-2.02^{+0.46}_{-0.79}$	$67.71^{+0.60}_{-0.53}$	$108.87^{+0.52}_{-0.57}$	$-0.30^{+0.00}_{-0.00}$	$-0.23^{+0.01}_{-0.00}$	$-0.52^{+0.01}_{-0.01}$
J16000060-4221567	$0.29^{+0.38}_{-0.15}$	$0.34^{+0.64}_{-0.18}$	$0.23^{+0.23}_{-0.15}$	$9.39^{+0.80}_{-0.98}$	$41.71^{+42.75}_{-25.67}$	$7.53^{+7.14}_{-3.62}$	$-2.59^{+1.82}_{-2.52}$	$65.32^{+16.90}_{-16.68}$	$144.36^{+22.85}_{-27.36}$	$0.45^{+0.11}_{-0.10}$	$-0.41^{+0.10}_{-0.12}$	$-0.49^{+0.01}_{-0.01}$
J16000236-4222145	$0.50^{+0.01}_{-0.01}$	$0.70^{+0.05}_{-0.04}$	$0.59^{+0.27}_{-0.14}$	$9.97^{+0.09}_{-0.03}$	$5.43^{+45.97}_{-2.37}$	$8.28^{+6.51}_{-3.39}$	$0.12^{+0.01}_{-0.03}$	$64.53^{+1.05}_{-1.00}$	$161.71^{+1.24}_{-1.68}$	$0.53^{+0.00}_{-0.01}$	$-0.34^{+0.01}_{-0.00}$	$-0.50^{+0.01}_{-0.01}$
J16001844-2230114	< 0.09	< 0.12	$0.10^{+0.03}_{-0.03}$	$10.12^{+0.42}_{-0.23}$	$51.18^{+33.81}_{-32.93}$	$11.19^{+3.45}_{-4.83}$	$-2.60^{+1.89}_{-1.19}$	$50.37^{+14.94}_{-16.32}$	$47.61^{+22.85}_{-24.34}$	$-0.31^{+0.01}_{-0.01}$	$-0.30^{+0.02}_{-0.02}$	$-0.48^{+0.01}_{-0.00}$
J16003103-4143369	< 0.17	< 0.22	$0.17^{+0.71}_{-0.09}$	$9.35^{+1.01}_{-5.12}$	$55.34^{+34.25}_{-36.34}$	$10.46^{+4.01}_{-4.95}$	$-2.39^{+3.01}_{-4.96}$	$36.57^{+33.68}_{-27.55}$	$88.05^{+47.57}_{-55.56}$	$-0.11^{+0.04}_{-0.05}$	$-0.32^{+0.06}_{-0.08}$	$-0.50^{+0.01}_{-0.01}$
J16004452-4155310	$0.39^{+0.02}_{-0.01}$	$0.51^{+0.04}_{-0.03}$	$0.42^{+0.04}_{-0.05}$	$10.45^{+0.09}_{-0.06}$	$31.68^{+37.60}_{-25.04}$	$7.54^{+5.31}_{-1.99}$	$0.10^{+0.02}_{-0.03}$	$72.59^{+1.22}_{-1.56}$	$58.40^{+1.15}_{-0.91}$	$-0.07^{+0.00}_{-0.00}$	$-0.31^{+0.01}_{-0.00}$	$-0.52^{+0.01}_{-0.01}$
J16004943-4130038	< 0.12	< 0.14	$0.10^{+0.04}_{-0.03}$	$10.36^{+0.53}_{-0.32}$	$56.39^{+25.64}_{-30.87}$	$10.11^{+5.16}_{-4.29}$	$-2.52^{+1.89}_{-2.33}$	$52.46^{+20.39}_{-23.42}$	$133.70^{+36.12}_{-22.10}$	$-0.16^{+0.02}_{-0.02}$	$0.02^{+0.01}_{-0.02}$	$-0.49^{+0.01}_{-0.01}$
J16011549-4152351	$0.61^{+0.07}_{-0.05}$	$0.81^{+0.47}_{-0.11}$	$0.59^{+0.08}_{-0.12}$	$9.58^{+0.08}_{-0.06}$	$44.48^{+41.46}_{-22.33}$	$5.28^{+6.49}_{-1.86}$	$0.19^{+0.01}_{-0.02}$	$65.86^{+2.16}_{-3.71}$	$160.00^{+3.77}_{-3.51}$	$-0.24^{+0.02}_{-0.01}$	$-0.25^{+0.01}_{-0.01}$	$-0.51^{+0.01}_{-0.01}$
J16014086-2258103	< 0.10	< 0.13	$0.07^{+0.07}_{-0.06}$	$9.87^{+0.51}_{-0.78}$	$63.93^{+19.10}_{-36.07}$	$12.97^{+1.77}_{-7.25}$	$-2.18^{+2.38}_{-2.32}$	$32.85^{+14.07}_{-9.38}$	$176.94^{+18.10}_{-39.30}$	$-0.79^{+0.02}_{-0.02}$	$-0.27^{+0.01}_{-0.02}$	$-0.48^{+0.01}_{-0.01}$
J16014157-2111380	< 0.70	< 0.86	$0.49^{+0.53}_{-0.38}$	$7.92^{+0.77}_{-1.99}$	$35.64^{+32.39}_{-27.54}$	$10.71^{+4.44}_{-7.30}$	$-3.09^{+1.77}_{-2.32}$	$54.98^{+22.73}_{-16.15}$	$83.79^{+16.55}_{-29.24}$	$-0.32^{+0.20}_{-0.25}$	$1.82^{+0.20}_{-0.18}$	$-4.12^{+0.00}_{-0.00}$
J16020757-2257467	$0.17^{+0.03}_{-0.03}$	$0.21^{+0.07}_{-0.04}$	$0.16^{+0.04}_{-0.05}$	$9.66^{+0.23}_{-0.38}$	$57.05^{+29.61}_{-35.71}$	$10.90^{+4.47}_{-6.81}$	$-1.90^{+1.92}_{-2.08}$	$30.54^{+16.72}_{-13.37}$	$113.57^{+21.26}_{-30.65}$	$-0.50^{+0.02}_{-0.02}$	$-0.27^{+0.02}_{-0.03}$	$-0.47^{+0.00}_{-0.00}$
J16024152-2138245	$0.06^{+0.02}_{-0.01}$	$0.07^{+0.02}_{-0.02}$	$0.06^{+0.02}_{-0.01}$	$10.71^{+0.34}_{-0.16}$	$38.53^{+36.59}_{-22.45}$	$9.18^{+5.44}_{-4.10}$	$-1.79^{+1.33}_{-1.37}$	$28.22^{+16.15}_{-10.52}$	$54.55^{+17.28}_{-33.49}$	$-0.42^{+0.01}_{-0.01}$	$-0.15^{+0.01}_{-0.00}$	$-4.19^{+0.00}_{-0.01}$
J16030161-2207523	< 0.16	< 0.21	$0.12^{+0.56}_{-0.08}$	$6.36^{+3.63}_{-1.79}$	$65.09^{+26.58}_{-43.33}$	$11.15^{+3.73}_{-7.06}$	$0.47^{+0.17}_{-0.99}$	$43.88^{+23.88}_{-19.22}$	$88.41^{+30.56}_{-31.72}$	$-0.44^{+0.02}_{-0.01}$	$-0.23^{+0.02}_{-0.02}$	$-4.18^{+0.01}_{-0.00}$
J16032939-4140018	$0.46^{+0.06}_{-0.04}$	$0.68^{+0.39}_{-0.12}$	$0.40^{+0.14}_{-0.16}$	$10.29^{+0.34}_{-0.27}$	$47.70^{+34.85}_{-37.27}$	$4.30^{+4.30}_{-1.18}$	$-0.01^{+0.13}_{-4.15}$	$77.72^{+2.89}_{-3.24}$	$126.45^{+1.78}_{-1.76}$	$0.59^{+0.01}_{-0.01}$	$-0.43^{+0.01}_{-0.01}$	$-0.51^{+0.01}_{-0.01}$
J16035767-2031055	$0.23^{+0.11}_{-0.11}$	$0.30^{+0.28}_{-0.13}$	$0.14^{+0.15}_{-0.08}$	$9.91^{+0.72}_{-0.63}$	$52.69^{+35.75}_{-35.09}$	$6.61^{+6.06}_{-3.22}$	$-1.88^{+1.47}_{-3.06}$	$49.71^{+24.31}_{-40.38}$	$128.62^{+37.57}_{-87.70}$	$-0.41^{+0.07}_{-0.06}$	$-0.16^{+0.03}_{-0.03}$	$-0.91^{+0.00}_{-0.00}$
J16041740-1942287	< 0.44	< 0.59	$0.33^{+0.72}_{-0.25}$	$6.89^{+2.51}_{-1.98}$	$49.61^{+39.53}_{-42.15}$	$10.27^{+4.59}_{-5.29}$	$-2.00^{+1.52}_{-3.09}$	$44.96^{+23.80}_{-10.79}$	$53.95^{+39.25}_{-16.13}$	$-0.46^{+0.15}_{-0.11}$	$-0.01^{+0.17}_{-0.18}$	$-4.13^{+0.00}_{-0.00}$
J16042165-2130284	$0.67^{+0.00}_{-0.00}$	$0.84^{+0.01}_{-0.01}$	$0.60^{+0.00}_{-0.00}$	$10.13^{+0.01}_{-0.01}$	$83.89^{+11.75}_{-21.31}$	$7.30^{+0.20}_{-0.16}$	$-5.88^{+0.16}_{-0.09}$	$10.15^{+1.33}_{-1.80}$	$137.28^{+7.30}_{-8.48}$	$-0.42^{+0.00}_{-0.00}$	$-0.19^{+0.00}_{-0.00}$	$-0.70^{+0.01}_{-0.01}$
J16052556-2035397	< 0.15	< 0.20	$0.14^{+0.16}_{-0.08}$	$9.33^{+0.76}_{-1.12}$	$46.03^{+29.90}_{-25.98}$	$8.34^{+4.89}_{-4.00}$	$-2.09^{+1.82}_{-3.00}$	$50.67^{+21.85}_{-35.96}$	$89.38^{+57.34}_{-57.41}$	$0.06^{+0.05}_{-0.08}$	$-0.23^{+0.10}_{-0.10}$	$-0.49^{+0.01}_{-0.01}$
J16062196-1928445	< 0.22	< 0.28	$0.24^{+0.52}_{-0.14}$	$9.37^{+0.56}_{-2.37}$	$55.02^{+31.31}_{-39.00}$	$9.14^{+5.56}_{-5.99}$	$-2.69^{+2.04}_{-1.57}$	$39.73^{+31.57}_{-25.91}$	$117.60^{+42.22}_{-72.48}$	$-0.14^{+0.10}_{-0.39}$	$-0.31^{+1.07}_{-0.13}$	$-1.04^{+0.01}_{-0.01}$
J16062277-2011243	< 0.55	< 0.79	$0.56^{+0.63}_{-0.40}$	$6.22^{+1.23}_{-0.96}$	$57.01^{+24.12}_{-35.17}$	$11.88^{+3.65}_{-5.25}$	$-2.71^{+2.30}_{-2.28}$	$41.50^{+28.70}_{-32.35}$	$71.68^{+57.65}_{-48.38}$	$-0.24^{+1.78}_{-1.00}$	$-0.09^{+1.16}_{-1.15}$	$-0.48^{+0.01}_{-0.01}$
J16063539-2516510	< 0.17	< 0.20	$0.14^{+0.08}_{-0.06}$	$9.52^{+0.31}_{-0.29}$	$48.11^{+36.77}_{-30.68}$	$10.02^{+5.43}_{-5.48}$	$-3.45^{+2.03}_{-1.54}$	$36.18^{+20.95}_{-23.03}$	$21.28^{+24.00}_{-26.96}$	$-0.54^{+0.05}_{-0.05}$	$-0.18^{+0.06}_{-0.03}$	$-0.48^{+0.01}_{-0.01}$

Table B.4 (cont'd)

2MASS	R_{68} $''$	R_{90} $''$	R_t $''$	f_0 (Jy/Sr)	α	β	γ	i (°)	PA (°)	dDec ($''$)	dRA ($''$)	lnwcorr
J16064102-2455489	$0.14^{+0.04}_{-0.04}$	$0.17^{+0.06}_{-0.05}$	$0.12^{+0.04}_{-0.04}$	$9.71^{+0.34}_{-0.21}$	$44.89^{+37.28}_{-25.99}$	$8.94^{+5.17}_{-4.37}$	$-3.39^{+2.72}_{-1.69}$	$38.69^{+9.99}_{-20.50}$	$118.27^{+25.38}_{-30.34}$	$-0.43^{+0.03}_{-0.02}$	$-0.25^{+0.02}_{-0.03}$	$-0.48^{+0.01}_{-0.01}$
J16064385-1908056	$0.40^{+0.52}_{-0.28}$	$0.46^{+0.64}_{-0.33}$	$0.37^{+0.45}_{-0.29}$	$7.95^{+1.11}_{-2.26}$	$41.61^{+23.74}_{-24.68}$	$11.10^{+4.37}_{-5.37}$	$-3.13^{+2.52}_{-2.13}$	$66.43^{+16.05}_{-9.29}$	$71.31^{+41.22}_{-26.62}$	$-0.48^{+0.15}_{-0.22}$	$-0.11^{+0.13}_{-0.15}$	$-4.12^{+0.00}_{-0.00}$
J16070384-3911113	$0.79^{+0.75}_{-0.57}$	$0.96^{+1.29}_{-0.70}$	$0.75^{+0.46}_{-0.45}$	$7.43^{+1.16}_{-1.16}$	$51.22^{+30.49}_{-32.87}$	$8.58^{+5.39}_{-4.83}$	$-2.65^{+2.28}_{-2.02}$	$60.84^{+20.15}_{-19.13}$	$134.06^{+33.79}_{-23.94}$	$0.28^{+0.15}_{-0.16}$	$-0.85^{+0.20}_{-0.16}$	$-0.49^{+0.01}_{-0.01}$
J16070854-3914075	$0.63^{+0.10}_{-0.04}$	$1.04^{+0.40}_{-0.25}$	$0.50^{+0.09}_{-0.07}$	$9.96^{+0.12}_{-0.09}$	$43.70^{+36.45}_{-33.33}$	$4.16^{+2.22}_{-0.72}$	$-0.35^{+0.30}_{-0.82}$	$72.41^{+1.92}_{-1.86}$	$154.02^{+1.74}_{-1.62}$	$-0.20^{+0.01}_{-0.02}$	$-0.37^{+0.01}_{-0.01}$	$-0.49^{+0.01}_{-0.01}$
J16071007-3911033	$0.10^{+0.03}_{-0.03}$	$0.13^{+0.05}_{-0.04}$	$0.08^{+0.04}_{-0.04}$	$11.05^{+0.55}_{-0.36}$	$54.50^{+34.57}_{-23.66}$	$11.47^{+3.63}_{-5.84}$	$-2.80^{+1.74}_{-1.87}$	$54.83^{+13.51}_{-17.46}$	$142.63^{+14.62}_{-34.49}$	$-0.15^{+0.01}_{-0.01}$	$-0.27^{+0.01}_{-0.01}$	$-0.49^{+0.01}_{-0.01}$
J16072625-2432079	$0.11^{+0.01}_{-0.01}$	$0.13^{+0.02}_{-0.01}$	$0.10^{+0.02}_{-0.01}$	$10.52^{+0.23}_{-0.20}$	$51.36^{+34.46}_{-30.42}$	$9.66^{+3.74}_{-3.28}$	$-3.32^{+2.50}_{-1.60}$	$28.83^{+24.92}_{-13.94}$	$180.44^{+27.74}_{-35.05}$	$-0.29^{+0.00}_{-0.01}$	$-0.15^{+0.01}_{-0.01}$	$-0.50^{+0.00}_{-0.01}$
J16072747-2059442	< 0.06	< 0.08	$0.06^{+0.04}_{-0.02}$	$9.90^{+0.45}_{-1.26}$	$39.15^{+27.41}_{-21.54}$	$13.41^{+2.58}_{-5.83}$	$-0.77^{+1.00}_{-3.36}$	$32.71^{+19.26}_{-19.84}$	$135.41^{+26.56}_{-16.57}$	$-0.27^{+0.01}_{-0.02}$	$-0.38^{+0.02}_{-0.02}$	$-4.17^{+0.00}_{-0.01}$
J16073773-3921388	< 0.50	< 0.68	$0.33^{+0.41}_{-0.25}$	$7.84^{+1.25}_{-1.76}$	$60.04^{+22.91}_{-32.76}$	$9.67^{+5.00}_{-5.26}$	$-2.10^{+1.34}_{-1.99}$	$22.78^{+19.36}_{-15.70}$	$159.82^{+32.94}_{-33.13}$	$-0.34^{+0.22}_{-0.18}$	$-0.08^{+0.23}_{-0.14}$	$-0.49^{+0.01}_{-0.01}$
J16075230-3858059	< 0.13	< 0.18	$0.11^{+0.10}_{-0.06}$	$10.17^{+0.53}_{-0.76}$	$49.98^{+34.64}_{-32.76}$	$9.72^{+5.10}_{-4.90}$	$-2.20^{+2.05}_{-2.14}$	$61.56^{+21.48}_{-14.71}$	$126.46^{+24.47}_{-25.22}$	$-0.19^{+0.04}_{-0.03}$	$-0.26^{+0.04}_{-0.04}$	$-0.49^{+0.01}_{-0.01}$
J16075475-3915446	< 0.69	< 0.88	$0.72^{+0.77}_{-0.53}$	$6.03^{+2.17}_{-2.15}$	$57.05^{+31.59}_{-40.88}$	$10.33^{+3.42}_{-6.63}$	$-6.16^{+4.88}_{-4.02}$	$42.12^{+33.31}_{-26.17}$	$91.82^{+49.25}_{-71.76}$	$0.02^{+1.90}_{-1.88}$	$0.10^{+2.00}_{-2.03}$	$-0.50^{+0.01}_{-0.01}$
J16075796-2040087	$0.08^{+0.02}_{-0.01}$	$0.09^{+0.02}_{-0.02}$	$0.09^{+0.05}_{-0.03}$	$10.84^{+0.68}_{-0.44}$	$75.57^{+18.48}_{-25.98}$	$10.94^{+3.00}_{-2.44}$	$-0.16^{+0.28}_{-2.26}$	$68.28^{+7.65}_{-17.95}$	$209.14^{+6.16}_{-8.62}$	$-0.37^{+0.00}_{-0.00}$	$-0.22^{+0.00}_{-0.00}$	$-4.19^{+0.00}_{-0.00}$
J16080017-3902595	< 0.28	< 0.35	$0.21^{+0.65}_{-0.14}$	$8.97^{+1.26}_{-1.65}$	$43.46^{+34.16}_{-28.27}$	$11.02^{+4.83}_{-5.88}$	$-2.17^{+2.50}_{-2.13}$	$47.97^{+25.03}_{-10.51}$	$164.31^{+30.23}_{-31.60}$	$-0.16^{+0.06}_{-0.08}$	$-0.55^{+0.05}_{-0.13}$	$-0.50^{+0.01}_{-0.01}$
J16081263-3908334	< 0.13	< 0.17	$0.12^{+0.07}_{-0.06}$	$10.09^{+0.60}_{-0.52}$	$50.37^{+30.45}_{-29.82}$	$9.62^{+4.49}_{-4.42}$	$-3.60^{+2.69}_{-1.47}$	$51.93^{+19.93}_{-21.14}$	$114.13^{+27.52}_{-31.65}$	$-0.33^{+0.06}_{-0.04}$	$-0.02^{+0.04}_{-0.04}$	$-0.50^{+0.01}_{-0.01}$
J16081497-3857145	$0.11^{+0.05}_{-0.04}$	$0.14^{+0.07}_{-0.05}$	$0.12^{+0.06}_{-0.05}$	$10.34^{+0.51}_{-0.41}$	$62.27^{+26.07}_{-37.10}$	$11.93^{+3.78}_{-4.25}$	$-1.92^{+1.89}_{-3.04}$	$55.60^{+18.60}_{-13.70}$	$96.02^{+26.98}_{-33.34}$	$-0.42^{+0.02}_{-0.01}$	$-0.00^{+0.03}_{-0.01}$	$-0.49^{+0.01}_{-0.01}$
J16081566-2222199	< 0.34	< 0.46	$0.29^{+0.29}_{-0.29}$	$5.54^{+2.26}_{-1.01}$	$39.99^{+48.68}_{-21.85}$	$1.25^{+4.02}_{-0.81}$	$0.50^{+0.12}_{-0.15}$	$12.18^{+6.11}_{-7.00}$	$107.65^{+41.52}_{-7.87}$	$-0.46^{+0.05}_{-0.04}$	$0.02^{+0.02}_{-0.02}$	$-4.16^{+0.00}_{-0.00}$
J16082180-3904214	< 0.09	< 0.12	$0.10^{+0.16}_{-0.05}$	$10.30^{+0.62}_{-1.60}$	$49.37^{+25.94}_{-30.68}$	$11.45^{+3.77}_{-5.23}$	$-1.24^{+1.49}_{-2.33}$	$73.54^{+10.24}_{-15.73}$	$75.93^{+21.21}_{-29.81}$	$-0.35^{+0.03}_{-0.02}$	$0.01^{+0.04}_{-0.03}$	$-0.49^{+0.01}_{-0.01}$
J16082249-3904464	$0.82^{+0.07}_{-0.05}$	$1.37^{+0.30}_{-0.15}$	$1.11^{+0.49}_{-0.66}$	$9.92^{+0.12}_{-0.03}$	$2.09^{+7.25}_{-0.49}$	$6.29^{+2.91}_{-3.78}$	$0.15^{+0.02}_{-0.03}$	$46.79^{+0.63}_{-2.21}$	$108.55^{+4.00}_{-0.98}$	$-0.85^{+0.00}_{-0.01}$	$-0.23^{+0.00}_{-0.01}$	$-0.51^{+0.00}_{-0.00}$
J16082324-1930009	$0.25^{+0.03}_{-0.03}$	$0.30^{+0.05}_{-0.03}$	$0.23^{+0.04}_{-0.05}$	$10.63^{+0.42}_{-0.20}$	$42.35^{+35.50}_{-22.51}$	$9.41^{+3.61}_{-3.63}$	$-3.14^{+1.48}_{-1.68}$	$70.25^{+1.74}_{-3.81}$	$126.62^{+4.08}_{-5.36}$	$-0.29^{+0.00}_{-0.01}$	$-0.28^{+0.01}_{-0.01}$	$-0.99^{+0.00}_{-0.00}$
J16082576-3906011	$0.26^{+0.01}_{-0.01}$	$0.31^{+0.03}_{-0.02}$	$0.24^{+0.04}_{-0.03}$	$10.43^{+0.14}_{-0.19}$	$40.97^{+43.85}_{-26.69}$	$8.52^{+5.18}_{-1.87}$	$-3.30^{+1.99}_{-1.85}$	$47.06^{+3.16}_{-4.05}$	$63.48^{+4.04}_{-2.13}$	$-0.55^{+0.01}_{-0.00}$	$-0.16^{+0.01}_{-0.00}$	$-0.49^{+0.01}_{-0.01}$
J16082751-1949047	$0.27^{+0.80}_{-0.18}$	$0.44^{+1.18}_{-0.32}$	$0.34^{+0.72}_{-0.26}$	$6.99^{+1.77}_{-1.42}$	$46.67^{+30.26}_{-31.94}$	$10.47^{+4.27}_{-5.61}$	$-3.39^{+2.05}_{-2.00}$	$40.76^{+29.70}_{-28.67}$	$100.52^{+55.92}_{-78.33}$	$0.11^{+0.92}_{-0.93}$	$-0.09^{+1.33}_{-1.35}$	$-0.49^{+0.01}_{-0.01}$
J16083026-3906111	$0.09^{+0.04}_{-0.04}$	$0.11^{+0.05}_{-0.04}$	$0.08^{+0.04}_{-0.04}$	$10.79^{+1.03}_{-0.44}$	$64.68^{+23.14}_{-32.66}$	$9.60^{+4.08}_{-4.45}$	$-1.98^{+1.50}_{-2.39}$	$50.40^{+15.19}_{-17.47}$	$41.26^{+23.72}_{-30.95}$	$-0.43^{+0.01}_{-0.01}$	$-0.05^{+0.01}_{-0.01}$	$-0.50^{+0.00}_{-0.01}$
J16083070-3828268	$0.57^{+0.01}_{-0.01}$	$0.65^{+0.03}_{-0.02}$	$0.56^{+0.02}_{-0.04}$	$10.52^{+0.12}_{-0.07}$	$45.33^{+29.45}_{-30.86}$	$11.71^{+2.81}_{-3.18}$	$-3.69^{+0.80}_{-1.56}$	$72.43^{+0.67}_{-0.61}$	$106.19^{+0.97}_{-0.71}$	$-0.43^{+0.01}_{-0.01}$	$-0.19^{+0.01}_{-0.01}$	$-0.51^{+0.01}_{-0.01}$
J16083081-3905488	< 0.26	< 0.34	$0.21^{+0.23}_{-0.14}$	$9.44^{+0.77}_{-2.13}$	$54.15^{+30.48}_{-32.23}$	$7.55^{+5.14}_{-5.18}$	$-1.51^{+1.85}_{-2.57}$	$57.95^{+22.14}_{-12.70}$	$127.29^{+31.51}_{-29.13}$	$-0.46^{+0.09}_{-0.11}$	$-0.13^{+0.09}_{-0.05}$	$-0.49^{+0.01}_{-0.01}$
J16084940-3905393	< 0.76	< 0.90	$0.53^{+0.73}_{-0.35}$	$6.85^{+0.94}_{-1.43}$	$50.43^{+35.35}_{-31.90}$	$9.77^{+5.79}_{-6.88}$	$-3.85^{+2.27}_{-1.53}$	$54.39^{+18.29}_{-21.24}$	$99.98^{+31.99}_{-22.74}$	$0.82^{+0.20}_{-0.16}$	$0.77^{+0.17}_{-0.21}$	$-0.49^{+0.01}_{-0.01}$

Table B.4 (cont'd)

2MASS	R_{68} $''$	R_{90} $''$	R_t $''$	f_0 (Jy/Sr)	α	β	γ	i (°)	PA (°)	dDec ($''$)	dRA ($''$)	lnwcorr
J16085157-3903177	$0.10^{+0.02}_{-0.02}$	$0.12^{+0.04}_{-0.02}$	$0.09^{+0.03}_{-0.04}$	$10.63^{+0.25}_{-0.24}$	$42.58^{+38.37}_{-26.72}$	$8.73^{+4.71}_{-4.21}$	$-1.95^{+1.58}_{-2.00}$	$32.42^{+15.68}_{-23.90}$	$174.60^{+26.49}_{-32.31}$	$-0.35^{+0.01}_{-0.01}$	$-0.14^{+0.01}_{-0.01}$	$-0.49^{+0.01}_{-0.01}$
J16085324-3914401	$0.08^{+0.04}_{-0.02}$	$0.11^{+0.05}_{-0.03}$	$0.09^{+0.08}_{-0.03}$	$11.03^{+0.51}_{-1.27}$	$49.31^{+37.43}_{-31.06}$	$10.62^{+4.01}_{-5.22}$	$-2.11^{+2.28}_{-2.95}$	$57.03^{+13.55}_{-7.57}$	$114.61^{+28.86}_{-17.42}$	$-0.24^{+0.00}_{-0.01}$	$-0.05^{+0.01}_{-0.00}$	$-0.50^{+0.01}_{-0.01}$
J16085373-3914367	< 0.17	< 0.19	$0.18^{+0.38}_{-0.13}$	$9.72^{+0.87}_{-1.37}$	$68.14^{+17.99}_{-46.11}$	$9.96^{+4.80}_{-5.19}$	$-2.14^{+2.34}_{-2.77}$	$66.88^{+15.97}_{-21.31}$	$33.52^{+25.02}_{-29.54}$	$-0.51^{+0.05}_{-0.04}$	$-0.10^{+0.07}_{-0.06}$	$-0.51^{+0.01}_{-0.01}$
J16085468-3937431	$0.46^{+0.00}_{-0.00}$	$0.59^{+0.03}_{-0.03}$	$0.40^{+0.02}_{-0.02}$	$10.46^{+0.06}_{-0.04}$	$49.98^{+33.64}_{-28.32}$	$6.43^{+0.90}_{-0.47}$	$-2.90^{+0.51}_{-0.75}$	$54.92^{+0.67}_{-0.65}$	$45.07^{+0.92}_{-1.00}$	$0.41^{+0.00}_{-0.00}$	$-0.10^{+0.00}_{-0.00}$	$-0.50^{+0.01}_{-0.01}$
J16085553-3902339	< 0.10	< 0.11	$0.09^{+0.15}_{-0.04}$	$10.01^{+0.48}_{-1.99}$	$63.01^{+26.75}_{-41.13}$	$12.53^{+3.10}_{-7.37}$	$-2.81^{+2.92}_{-2.33}$	$19.04^{+12.36}_{-10.86}$	$33.32^{+32.70}_{-21.07}$	$-0.40^{+0.04}_{-0.03}$	$-0.04^{+0.03}_{-0.03}$	$-0.49^{+0.01}_{-0.01}$
J16085780-3902227	$0.08^{+0.02}_{-0.02}$	$0.10^{+0.02}_{-0.03}$	$0.08^{+0.02}_{-0.02}$	$11.30^{+0.38}_{-0.41}$	$47.83^{+30.74}_{-16.04}$	$10.12^{+5.46}_{-4.34}$	$-3.03^{+2.20}_{-1.75}$	$61.03^{+15.60}_{-16.71}$	$21.46^{+11.03}_{-21.76}$	$-0.52^{+0.00}_{-0.01}$	$-0.12^{+0.01}_{-0.01}$	$-0.50^{+0.01}_{-0.01}$
J16090002-1908368	$0.20^{+0.84}_{-0.11}$	$0.24^{+1.27}_{-0.14}$	$0.26^{+0.91}_{-0.16}$	$7.44^{+2.03}_{-1.67}$	$49.66^{+27.64}_{-35.40}$	$9.28^{+4.64}_{-6.85}$	$0.24^{+0.19}_{-3.40}$	$39.24^{+28.55}_{-19.50}$	$74.74^{+61.76}_{-41.78}$	$-0.32^{+0.02}_{-0.03}$	$-0.05^{+0.03}_{-0.04}$	$-0.48^{+0.01}_{-0.01}$
J16090075-1908526	$0.19^{+0.02}_{-0.02}$	$0.24^{+0.06}_{-0.03}$	$0.17^{+0.03}_{-0.04}$	$10.73^{+0.17}_{-0.10}$	$53.55^{+28.03}_{-22.66}$	$7.74^{+6.80}_{-2.85}$	$-4.12^{+1.09}_{-1.22}$	$56.46^{+8.60}_{-12.23}$	$155.81^{+7.58}_{-6.82}$	$-0.42^{+0.01}_{-0.01}$	$-0.11^{+0.01}_{-0.00}$	$-1.03^{+0.01}_{-0.01}$
J16090141-3925119	$0.49^{+0.08}_{-0.05}$	$0.62^{+0.34}_{-0.10}$	$0.45^{+0.10}_{-0.09}$	$9.53^{+0.31}_{-0.22}$	$44.83^{+42.34}_{-28.01}$	$7.92^{+5.83}_{-4.01}$	$-0.64^{+0.54}_{-1.94}$	$72.99^{+5.41}_{-6.41}$	$0.31^{+4.62}_{-4.56}$	$-0.40^{+0.05}_{-0.04}$	$0.07^{+0.01}_{-0.02}$	$-0.50^{+0.01}_{-0.01}$
J16090185-3905124	$0.27^{+0.01}_{-0.01}$	$0.34^{+0.04}_{-0.02}$	$0.28^{+0.04}_{-0.02}$	$9.97^{+0.05}_{-0.04}$	$46.78^{+36.06}_{-34.80}$	$7.54^{+4.49}_{-1.89}$	$0.17^{+0.01}_{-0.01}$	$6.46^{+6.52}_{-4.95}$	$59.17^{+35.54}_{-34.78}$	$-0.30^{+0.00}_{-0.00}$	$-0.05^{+0.00}_{-0.00}$	$-0.51^{+0.01}_{-0.01}$
J16093558-1828232	< 0.81	< 1.01	$0.43^{+0.59}_{-0.30}$	$5.23^{+1.73}_{-1.10}$	$54.52^{+25.51}_{-35.54}$	$7.80^{+4.87}_{-5.19}$	$-1.61^{+1.37}_{-1.65}$	$36.12^{+17.25}_{-16.17}$	$60.56^{+35.44}_{-29.42}$	$1.34^{+0.15}_{-0.23}$	$-0.48^{+0.16}_{-0.17}$	$-4.11^{+0.00}_{-0.00}$
J16094098-2217594	< 0.50	< 0.60	$0.38^{+0.66}_{-0.29}$	$6.68^{+1.59}_{-1.54}$	$48.52^{+41.80}_{-34.87}$	$6.96^{+8.29}_{-3.24}$	$-1.53^{+1.69}_{-1.84}$	$32.66^{+19.08}_{-23.26}$	$38.64^{+19.30}_{-44.57}$	$1.82^{+0.18}_{-0.17}$	$-0.94^{+0.14}_{-0.24}$	$-4.15^{+0.00}_{-0.00}$
J16094434-3913301	< 0.08	< 0.11	$0.09^{+0.69}_{-0.04}$	$9.48^{+1.78}_{-3.01}$	$54.51^{+29.21}_{-41.53}$	$10.56^{+4.51}_{-4.43}$	$0.18^{+0.33}_{-3.49}$	$67.50^{+8.65}_{-20.27}$	$47.89^{+25.89}_{-37.43}$	$-0.21^{+0.01}_{-0.01}$	$0.12^{+0.02}_{-0.01}$	$-0.49^{+0.01}_{-0.01}$
J16094864-3911169	$0.37^{+0.01}_{-0.02}$	$0.42^{+0.03}_{-0.02}$	$0.37^{+0.03}_{-0.02}$	$10.40^{+0.15}_{-0.16}$	$48.20^{+35.71}_{-29.52}$	$11.89^{+3.63}_{-3.73}$	$-3.30^{+1.65}_{-1.82}$	$67.23^{+1.99}_{-3.21}$	$-5.42^{+3.07}_{-2.46}$	$-0.35^{+0.01}_{-0.01}$	$0.01^{+0.01}_{-0.01}$	$-0.49^{+0.01}_{-0.01}$
J16095441-1906551	< 0.62	< 0.74	$0.69^{+0.58}_{-0.40}$	$6.88^{+1.30}_{-1.60}$	$46.94^{+30.36}_{-31.55}$	$7.69^{+5.71}_{-4.48}$	$-2.74^{+1.65}_{-1.83}$	$63.71^{+15.14}_{-22.13}$	$25.31^{+47.22}_{-16.71}$	$-0.37^{+0.24}_{-0.18}$	$-0.88^{+0.23}_{-0.20}$	$-4.11^{+0.00}_{-0.01}$
J16095628-3859518	$0.10^{+0.06}_{-0.03}$	$0.13^{+0.09}_{-0.04}$	$0.10^{+0.03}_{-0.04}$	$10.58^{+0.54}_{-0.45}$	$43.44^{+39.70}_{-31.49}$	$10.17^{+5.03}_{-4.21}$	$-2.23^{+1.94}_{-2.78}$	$67.40^{+17.49}_{-22.68}$	$123.20^{+32.04}_{-17.48}$	$-0.22^{+0.01}_{-0.02}$	$-0.07^{+0.02}_{-0.02}$	$-0.50^{+0.00}_{-0.01}$
J16101984-3836065	< 0.67	< 0.91	$0.36^{+0.53}_{-0.29}$	$6.68^{+1.73}_{-1.10}$	$56.45^{+25.11}_{-38.65}$	$9.11^{+4.83}_{-6.01}$	$-2.43^{+1.96}_{-2.32}$	$25.28^{+16.32}_{-14.77}$	$21.98^{+27.49}_{-34.72}$	$-1.73^{+0.21}_{-0.19}$	$-1.16^{+0.16}_{-0.25}$	$-0.48^{+0.01}_{-0.01}$
J16102955-3922144	$0.19^{+0.06}_{-0.06}$	$0.23^{+0.10}_{-0.07}$	$0.16^{+0.06}_{-0.07}$	$10.16^{+0.70}_{-0.35}$	$58.96^{+25.92}_{-29.58}$	$11.85^{+3.41}_{-4.47}$	$-3.06^{+1.98}_{-2.02}$	$67.79^{+18.56}_{-13.62}$	$106.52^{+14.67}_{-19.58}$	$-0.14^{+0.02}_{-0.02}$	$-0.38^{+0.05}_{-0.03}$	$-0.49^{+0.01}_{-0.01}$
J16104636-1840598	< 0.10	< 0.13	$0.07^{+0.07}_{-0.03}$	$10.01^{+0.62}_{-0.64}$	$52.74^{+27.81}_{-32.04}$	$11.95^{+3.80}_{-4.52}$	$-2.03^{+1.43}_{-2.54}$	$52.98^{+19.81}_{-18.77}$	$159.03^{+16.50}_{-38.36}$	$-0.40^{+0.04}_{-0.04}$	$-0.06^{+0.04}_{-0.03}$	$-4.12^{+0.01}_{-0.00}$
J16122737-2009596	< 0.51	< 0.58	$0.66^{+0.39}_{-0.57}$	$6.59^{+2.58}_{-1.40}$	$62.71^{+30.08}_{-53.55}$	$8.24^{+6.99}_{-5.68}$	$-2.66^{+2.46}_{-1.07}$	$46.61^{+13.39}_{-24.06}$	$1.56^{+25.77}_{-27.75}$	$-0.34^{+0.13}_{-0.20}$	$-0.36^{+0.25}_{-0.11}$	$-4.12^{+0.00}_{-0.00}$
J16124373-3815031	< 0.07	< 0.09	$0.07^{+0.09}_{-0.02}$	$11.18^{+0.52}_{-0.87}$	$38.87^{+48.12}_{-26.63}$	$10.23^{+4.00}_{-3.67}$	$-1.38^{+1.52}_{-2.06}$	$62.94^{+12.24}_{-18.12}$	$40.32^{+23.78}_{-31.92}$	$-0.12^{+0.01}_{-0.01}$	$-0.13^{+0.01}_{-0.01}$	$-0.50^{+0.01}_{-0.01}$
J16133650-2503473	< 0.54	< 0.68	$0.39^{+0.32}_{-0.25}$	$6.95^{+1.76}_{-1.68}$	$49.93^{+31.99}_{-31.41}$	$7.97^{+6.61}_{-4.95}$	$-2.48^{+2.36}_{-1.87}$	$76.04^{+10.73}_{-10.22}$	$7.97^{+23.73}_{-23.57}$	$-0.53^{+0.17}_{-0.16}$	$-0.11^{+0.17}_{-0.21}$	$-0.47^{+0.01}_{-0.01}$
J16134410-3736462	< 0.74	< 0.93	$0.58^{+0.45}_{-0.37}$	$6.43^{+1.98}_{-0.96}$	$53.64^{+31.61}_{-35.07}$	$10.31^{+4.16}_{-6.53}$	$-2.15^{+1.50}_{-2.83}$	$54.84^{+22.10}_{-15.26}$	$39.97^{+37.93}_{-23.10}$	$-1.46^{+0.19}_{-0.20}$	$-1.58^{+0.22}_{-0.15}$	$-0.48^{+0.01}_{-0.01}$
J16141107-2305362	$0.12^{+0.03}_{-0.02}$	$0.15^{+0.04}_{-0.04}$	$0.13^{+0.20}_{-0.02}$	$9.93^{+0.28}_{-1.67}$	$40.14^{+28.70}_{-22.93}$	$13.54^{+2.46}_{-4.16}$	$-3.46^{+3.66}_{-1.59}$	$31.19^{+46.25}_{-18.34}$	$115.44^{+46.88}_{-73.21}$	$-0.35^{+0.01}_{-0.01}$	$-0.05^{+0.02}_{-0.02}$	$-0.48^{+0.01}_{-0.01}$

Table B.4 (cont'd)

2MASS	R_{68} $''$	R_{90} $''$	R_t $''$	f_0 (Jy/Sr)	α	β	γ	i (°)	PA (°)	dDec ($''$)	dRA ($''$)	lnwcorr
J16142029-1906481	$0.11^{+0.01}_{-0.01}$	$0.13^{+0.02}_{-0.01}$	$0.11^{+0.01}_{-0.01}$	$10.78^{+0.12}_{-0.19}$	$76.16^{+16.01}_{-33.28}$	$12.96^{+2.33}_{-3.65}$	$-0.85^{+0.58}_{-1.26}$	$22.53^{+16.05}_{-13.81}$	$36.50^{+100.49}_{-21.42}$	$-0.21^{+0.00}_{-0.00}$	$-0.32^{+0.00}_{-0.00}$	$-0.52^{+0.00}_{-0.01}$
J16143367-1900133	< 0.43	< 0.69	$0.50^{+0.74}_{-0.34}$	$6.06^{+1.75}_{-1.35}$	$58.66^{+30.44}_{-37.66}$	$8.70^{+5.63}_{-5.04}$	$-3.36^{+2.91}_{-1.41}$	$72.69^{+11.20}_{-14.28}$	$53.51^{+21.99}_{-41.12}$	$-0.52^{+0.12}_{-0.21}$	$-0.27^{+0.17}_{-0.20}$	$-4.12^{+0.00}_{-0.00}$
J16153456-2242421	$0.24^{+0.26}_{-0.11}$	$0.31^{+0.40}_{-0.15}$	$0.18^{+0.17}_{-0.06}$	$9.46^{+0.67}_{-0.95}$	$47.51^{+35.11}_{-25.59}$	$10.17^{+5.04}_{-5.57}$	$0.20^{+0.11}_{-0.08}$	$64.31^{+10.66}_{-12.92}$	$12.79^{+20.97}_{-10.54}$	$-0.99^{+0.00}_{-0.00}$	$0.02^{+0.01}_{-0.01}$	$-4.18^{+0.00}_{-0.00}$
J16154416-1921171	$0.07^{+0.01}_{-0.02}$	$0.09^{+0.05}_{-0.03}$	$0.05^{+0.02}_{-0.01}$	$11.47^{+0.26}_{-0.14}$	$49.00^{+23.45}_{-33.60}$	$6.89^{+4.34}_{-3.26}$	$-3.01^{+2.35}_{-1.99}$	$75.97^{+8.96}_{-8.28}$	$14.36^{+7.52}_{-7.92}$	$-0.54^{+0.00}_{-0.00}$	$-0.03^{+0.00}_{-0.00}$	$-4.19^{+0.01}_{-0.00}$
J16163345-2521505	$0.26^{+0.07}_{-0.06}$	$0.32^{+0.11}_{-0.08}$	$0.25^{+0.07}_{-0.07}$	$9.26^{+0.22}_{-0.23}$	$49.80^{+26.27}_{-29.24}$	$9.38^{+4.68}_{-4.77}$	$-2.61^{+1.85}_{-2.34}$	$66.19^{+14.42}_{-20.11}$	$61.35^{+14.04}_{-17.68}$	$-0.35^{+0.06}_{-0.03}$	$-0.20^{+0.05}_{-0.04}$	$-4.17^{+0.00}_{-0.00}$
J16181904-2028479	$0.09^{+0.03}_{-0.03}$	$0.11^{+0.07}_{-0.04}$	$0.07^{+0.03}_{-0.03}$	$10.85^{+0.24}_{-0.55}$	$59.77^{+21.80}_{-29.83}$	$10.30^{+4.71}_{-5.00}$	$-3.82^{+1.96}_{-1.51}$	$60.38^{+18.35}_{-13.79}$	$110.06^{+26.14}_{-32.21}$	$-0.28^{+0.01}_{-0.01}$	$-0.07^{+0.01}_{-0.01}$	$-4.17^{+0.01}_{-0.00}$
J16215466-2043091	< 0.48	< 0.58	$0.38^{+0.48}_{-0.30}$	$6.62^{+1.49}_{-2.07}$	$63.75^{+23.79}_{-35.42}$	$7.11^{+6.00}_{-4.51}$	$-3.08^{+2.23}_{-2.27}$	$34.72^{+13.58}_{-19.22}$	$59.71^{+23.64}_{-27.95}$	$-1.55^{+0.15}_{-0.12}$	$-0.03^{+0.17}_{-0.24}$	$-4.18^{+0.01}_{-0.00}$
J16270942-2148457	< 0.07	< 0.09	$0.06^{+0.04}_{-0.02}$	$10.37^{+0.26}_{-0.53}$	$43.26^{+35.76}_{-34.38}$	$12.60^{+3.39}_{-6.75}$	$-2.71^{+2.11}_{-1.41}$	$21.20^{+13.06}_{-12.60}$	$105.01^{+36.92}_{-27.81}$	$-0.34^{+0.02}_{-0.02}$	$-0.22^{+0.01}_{-0.01}$	$-4.17^{+0.00}_{-0.01}$

B.7 Appendix: $\log L_{\rm mm} - \log L_\star$ Relation

In our discussion on disk sizes scaling relations (see Section 4.6.3), we reproduce the temperature power law index (q) estimation following the method given in Andrews et al. (2018b). This approach requires us to know the $\log L_{\rm mm} - \log L_\star$ for our samples, which we provide here using the statistical methods described in Section 4.5.

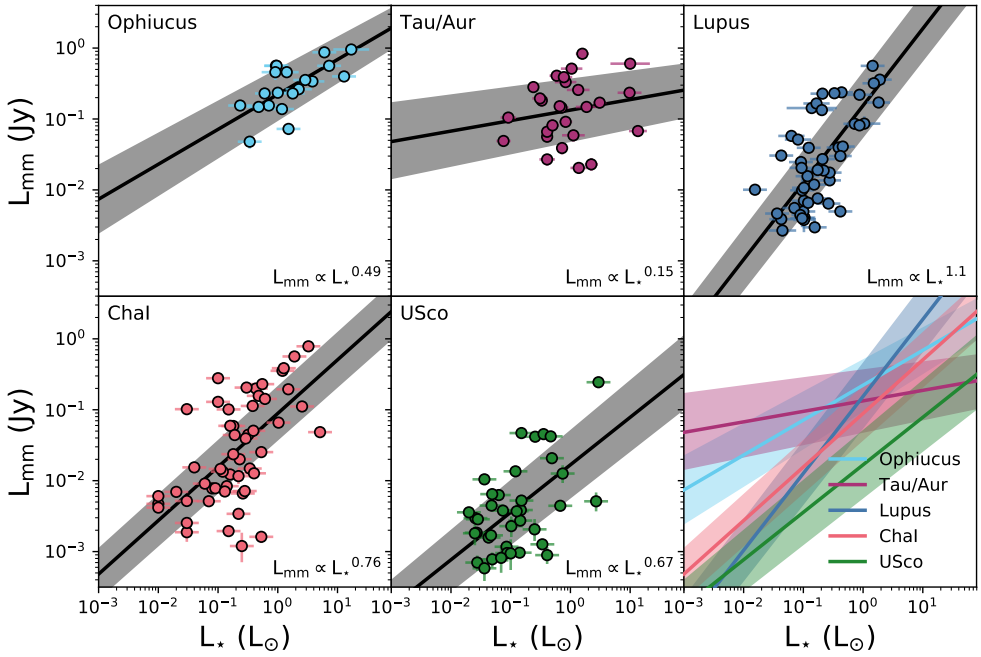

Figure B.7 Fitting of $\log L_{\rm mm} - \log L_\star$. The first 5 panels (left to right; top to bottom; ordered by region age) show the model results of each region as circles (resolved) and triangles (upper-limits). The best fit from MCMC linear regression is plotted as a black line, and surrounded by our 68% confidence intervals in grey. The last panel replots the bests fits of each region (and the corresponding 68% confidence intervals) so that they can be directly compared. Fit parameters for each region are given in Table B.7.

Table B.5. $\log L_{\rm mm} - \log L_\star$ statistical tests

Region	Shapiro $L_{\rm mm}$		Shapiro $L_\star$		Pearson r		Spearman ρ		Regression Parameters			
	stat	p-value	stat	p-value	stat	p-value	stat	p-value	α	β	σ	$\hat{\rho}$
Oph	0.66	1.3e-05	0.90	5.0e-02	0.66	1.6e-03	0.57	8.7e-03	$-0.65^{+0.07}_{-0.07}$	$0.49^{+0.2}_{-0.2}$	$0.27^{+0.07}_{-0.05}$	$0.84^{+0.08}_{-0.1}$
Tau/Aur	0.55	6.2e-08	0.82	3.5e-04	0.15	4.6e-01	0.16	4.2e-01	$-0.88^{+0.09}_{-0.09}$	$0.15^{+0.2}_{-0.2}$	$0.46^{+0.08}_{-0.06}$	$0.42^{+0.2}_{-0.2}$
Lupus	0.66	3.0e-09	0.67	3.5e-09	0.73	3.4e-09	0.63	1.7e-06	$-0.81^{+0.1}_{-0.1}$	$1.1^{+0.2}_{-0.2}$	$0.47^{+0.06}_{-0.06}$	$0.86^{+0.04}_{-0.06}$
Chamaeleon I	0.54	7.3e-12	0.62	1.1e-10	0.52	4.5e-05	0.54	1.8e-05	$-1.1^{+0.1}_{-0.1}$	$0.76^{+0.1}_{-0.1}$	$0.59^{+0.07}_{-0.06}$	$0.79^{+0.06}_{-0.07}$
USco	0.45	1.0e-10	0.34	7.7e-12	0.69	1.6e-06	0.46	3.9e-03	$-1.8^{+0.2}_{-0.2}$	$0.67^{+0.2}_{-0.2}$	$0.53^{+0.08}_{-0.06}$	$0.75^{+0.08}_{-0.1}$

Note. — Values we consider unreliable are greyed out (see Section 4.5.1).

REFERENCES

Adams, F. C. (2010). The Birth Environment of the Solar System. *ARA&A*, **48**, pp. 47–85. doi:10.1146/annurev-astro-081309-130830.

Adams, F. C., D. Hollenbach, G. Laughlin, and U. Gorti (2004). Photoevaporation of Circumstellar Disks Due to External Far-Ultraviolet Radiation in Stellar Aggregates. *ApJ*, **611**, pp. 360–379. doi:10.1086/421989.

Ahmic, M., R. Jayawardhana, A. Brandeker, A. Scholz, M. H. van Kerkwijk, E. Delgado-Donate, and D. Froebrich (2007). Multiplicity among Young Brown Dwarfs and Very Low Mass Stars. *ApJ*, **671**, pp. 2074–2081. doi:10.1086/522875.

Alcalá, J. M., A. Natta, C. F. Manara, L. Spezzi, B. Stelzer, A. Frasca, K. Biazzo, E. Covino, S. Randich, E. Rigliaco, L. Testi, F. Comerón, G. Cupani, and V. D'Elia (2014). X-shooter spectroscopy of young stellar objects. IV. Accretion in low-mass stars and substellar objects in Lupus. *A&A*, **561**, A2. doi:10.1051/0004-6361/201322254.

Alexander, R., I. Pascucci, S. Andrews, P. Armitage, and L. Cieza (2014). The Dispersal of Protoplanetary Disks. In Beuther, H., R. S. Klessen, C. P. Dullemond, and T. Henning (eds.) *Protostars and Planets VI*, p. 475. doi:10.2458/azu_uapress_9780816531240-ch021.

Allen, R. L., G. M. Bernstein, and R. Malhotra (2001). The Edge of the Solar System. *ApJ*, **549**(2), pp. L241–L244. doi:10.1086/319165.

Anderson, T. W. and D. A. Darling (1952). Asymptotic theory of certain" goodness of fit" criteria based on stochastic processes. *The annals of mathematical statistics*, **23**(2), pp. 193–212.

Andrae, R. (2010). Error estimation in astronomy: A guide. *ArXiv e-prints*.

Andrews, S. M., J. Huang, L. M. Pérez, A. Isella, C. P. Dullemond, N. T. Kurtovic, V. V. Guzmán, J. M. Carpenter, D. J. Wilner, S. Zhang, Z. Zhu, T. Birnstiel, X.-N. Bai, M. Benisty, A. M. Hughes, K. I. Öberg, and L. Ricci (2018a). The Disk Substructures at High Angular Resolution Project (DSHARP). I. Motivation, Sample, Calibration, and Overview. *ApJ*, **869**(2), L41. doi:10.3847/2041-8213/aaf741.

Andrews, S. M., K. A. Rosenfeld, A. L. Kraus, and D. J. Wilner (2013). The Mass Dependence between Protoplanetary Disks and their Stellar Hosts. *ApJ*, **771**, 129. doi:10.1088/0004-637X/771/2/129.

Andrews, S. M., M. Terrell, A. Tripathi, M. Ansdell, J. P. Williams, and D. J. Wilner (2018b). Scaling Relations Associated with Millimeter Continuum Sizes in Protoplanetary Disks. *ApJ*, **865**(2), 157. doi:10.3847/1538-4357/aadd9f.

Andrews, S. M., D. J. Wilner, A. M. Hughes, C. Qi, and C. P. Dullemond (2009). Protoplanetary Disk Structures in Ophiuchus. *ApJ*, **700**, pp. 1502–1523. doi:10.1088/0004-637X/700/2/1502.

Andrews, S. M., D. J. Wilner, A. M. Hughes, C. Qi, and C. P. Dullemond (2010). Protoplanetary Disk Structures in Ophiuchus. II. Extension to Fainter Sources. *ApJ*, **723**, pp. 1241–1254. doi:10.1088/0004-637X/723/2/1241.

Ansdell, M., J. P. Williams, N. van der Marel, J. M. Carpenter, G. Guidi, M. Hogerheijde, G. S. Mathews, C. F. Manara, A. Miotello, A. Natta, I. Oliveira, M. Tazzari, L. Testi, E. F. van Dishoeck, and S. E. van Terwisga (2016). ALMA Survey of Lupus Protoplanetary Disks. I. Dust and Gas Masses. *ApJ*, **828**(1), 46. doi:10.3847/0004-637X/828/1/46.

Apai, D., I. Pascucci, J. Bouwman, A. Natta, T. Henning, and C. P. Dullemond (2005). The Onset of Planet Formation in Brown Dwarf Disks. *Science*, **310**, pp. 834–836. doi:10.1126/science.1118042.

Bailer-Jones, C. A. L., J. Rybizki, M. Fouesneau, G. Mantelet, and R. Andrae (2018). Estimating Distance from Parallaxes. IV. Distances to 1.33 Billion Stars in Gaia Data Release 2. *AJ*, **156**(2), 58. doi:10.3847/1538-3881/aacb21.

Baraffe, I., G. Chabrier, F. Allard, and P. H. Hauschildt (1998). Evolutionary models for solar metallicity low-mass stars: mass-magnitude relationships and color-magnitude diagrams. *A&A*, **337**, pp. 403–412.

Baraffe, I., D. Homeier, F. Allard, and G. Chabrier (2015). New evolutionary models for pre-main sequence and main sequence low-mass stars down to the hydrogen-burning limit. *A&A*, **577**, A42. doi:10.1051/0004-6361/201425481.

Barenfeld, S. A., J. M. Carpenter, L. Ricci, and A. Isella (2016). ALMA Observations of Circumstellar Disks in the Upper Scorpius OB Association. *ApJ*, **827**(2), 142. doi:10.3847/0004-637X/827/2/142.

Barenfeld, S. A., J. M. Carpenter, A. I. Sargent, A. Isella, and L. Ricci (2017). Measurement of Circumstellar Disk Sizes in the Upper Scorpius OB Association with ALMA. *ApJ*, **851**(2), 85. doi:10.3847/1538-4357/aa989d.

Barlow, R. J. (1989). *Statistics: a guide to the use of statistical methods in the physical sciences*, volume 29. John Wiley & Sons.

Bate, M. R. (2012). Stellar, brown dwarf and multiple star properties from a radiation hydrodynamical simulation of star cluster formation. *MNRAS*, **419**, pp. 3115–3146. doi:10.1111/j.1365-2966.2011.19955.x.

Beckwith, S. V. W., A. I. Sargent, R. S. Chini, and R. Guesten (1990). A survey for circumstellar disks around young stellar objects. *AJ*, **99**, pp. 924–945. doi:10.1086/115385.

Berger, J. P. and D. Segransan (2007). An introduction to visibility modeling. *NewAR*, **51**(8-9), pp. 576–582. doi:10.1016/j.newar.2007.06.003.

Biazzo, K., A. Frasca, J. M. Alcalá, M. Zusi, E. Covino, S. Randich, M. Esposito, C. F. Manara, S. Antoniucci, B. Nisini, E. Rigliaco, and F. Getman (2017). X-shooter spectroscopy of young stellar objects in Lupus. Lithium, iron, and barium elemental abundances. *A&A*, **605**, A66. doi:10.1051/0004-6361/201730850.

Billot, N., M. Morales-Calderón, J. R. Stauffer, S. T. Megeath, and B. Whitney (2012). Herschel Far-infrared Photometric Monitoring of Protostars in the Orion Nebula Cluster. *ApJ*, **753**, L35. doi:10.1088/2041-8205/753/2/L35.

Brauer, F., C. P. Dullemond, and T. Henning (2008). Coagulation, fragmentation and radial motion of solid particles in protoplanetary disks. *A&A*, **480**(3), pp. 859–877. doi:10.1051/0004-6361:20077759.

Bulger, J., J. Patience, K. Ward-Duong, C. Pinte, H. Bouy, F. Ménard, and J.-L. Monin (2014). The Taurus Boundary of Stellar/Substellar (TBOSS) Survey. I. Far-IR disk emission measured with Herschel. *A&A*, **570**, A29. doi:10.1051/0004-6361/201323088.

Carpenter, J. M., L. Ricci, and A. Isella (2014). An ALMA Continuum Survey of Circumstellar Disks in the Upper Scorpius OB Association. *ApJ*, **787**(1), 42. doi:10.1088/0004-637X/787/1/42.

Chiang, E. I. and P. Goldreich (1997). Spectral Energy Distributions of T Tauri Stars with Passive Circumstellar Disks. *ApJ*, **490**(1), pp. 368–376. doi:10.1086/304869.

Comerón, F. (2008). *The Lupus Clouds*, volume 5, p. 295.

Cutri, R. M., M. F. Skrutskie, S. van Dyk, C. A. Beichman, J. M. Carpenter, T. Chester, L. Cambresy, T. Evans, J. Fowler, J. Gizis, E. Howard, J. Huchra, T. Jarrett, E. L. Kopan, J. D. Kirkpatrick, R. M. Light, K. A. Marsh, H. McCallon, S. Schneider, R. Stiening, M. Sykes, M. Weinberg, W. A. Wheaton, S. Wheelock, and N. Zacarias (2003). VizieR Online Data Catalog: 2MASS All-Sky Catalog of Point Sources (Cutri+ 2003). *VizieR Online Data Catalog*, **2246**.

Daemgen, S., A. Natta, A. Scholz, L. Testi, R. Jayawardhana, J. Greaves, and D. Eastwood (2016). Brown dwarf disks with Herschel: Linking far-infrared and (sub)-mm fluxes. *A&A*, **594**, A83. doi:10.1051/0004-6361/201628431.

D'Alessio, P., J. Cantö, N. Calvet, and S. Lizano (1998). Accretion Disks around Young Objects. I. The Detailed Vertical Structure. *ApJ*, **500**(1), pp. 411–427. doi:10.1086/305702.

Davidson-Pilon, C., J. Kalderstam, P. Zivich, B. Kuhn, A. Fiore-Gartland, L. Moneda, Gabriel, D. WIlson, A. Parij, K. Stark, S. Anton, L. Besson, Jona, H. Gadgil, D. Golland, S. Hussey, R. Kumar, J. Noorbakhsh, A. Klintberg, J. Kaluzka, I. Slavitt, E. Martin, E. Ochoa, D. Albrecht, dhuynh, D. Zgonjanin, D. Chen, C. Fournier, Arturo, and A. F. Rendeiro (2019). CamDavidsonPilon/lifelines: v0.21.3. doi:10.5281/zenodo.3240536.

Davies, C. L., S. G. Gregory, and J. S. Greaves (2014). Accretion discs as regulators of stellar angular momentum evolution in the ONC and Taurus-Auriga. *MNRAS*, **444**, pp. 1157–1176. doi:10.1093/mnras/stu1488.

de Gregorio-Monsalvo, I., F. Ménard, W. Dent, C. Pinte, C. López, P. Klaassen, A. Hales, P. Cortés, M. G. Rawlings, K. Tachihara, L. Testi, S. Takahashi, E. Chapillon, G. Mathews, A. Juhasz, E. Akiyama, A. E. Higuchi, M. Saito, L.-Å. Nyman, N. Phillips, J. Rodón, S. Corder, and T. Van Kempen (2013). Unveiling the gas-and-dust disk structure in HD 163296 using ALMA observations. *A&A*, **557**, A133. doi:10.1051/0004-6361/201321603.

de Juan Ovelar, M., M. Min, C. Dominik, C. Thalmann, P. Pinilla, M. Benisty, and T. Birnstiel (2013). Imaging diagnostics for transitional discs. *A&A*, **560**, A111. doi:10.1051/0004-6361/201322218.

de Zeeuw, P. T., R. Hoogerwerf, J. H. J. de Bruijne, A. G. A. Brown, and A. Blaauw (1999). A HIPPARCOS Census of the Nearby OB Associations. *AJ*, **117**(1), pp. 354–399. doi:10.1086/300682.

Dent, W. R. F., W. F. Thi, I. Kamp, J. P. Williams, F. Menard, S. Andrews, D. Ardila, G. Aresu, J.-C. Augereau, D. Barrado y Navascues, S. Brittain, A. Carmona, D. Ciardi, W. Danchi, J. Donaldson, G. Duchene, C. Eiroa, D. Fedele, C. Grady, I. de Gregorio-Molsalvo, C. Howard, N. Huélamo, A. Krivov, J. Lebreton, R. Liseau, C. Martin-Zaidi, G. Mathews, G. Meeus, I. Mendigutía, B. Montesinos, M. Morales-Calderon, A. Mora, H. Nomura, E. Pantin, I. Pascucci, N. Phillips, C. Pinte, L. Podio, S. K. Ramsay, B. Riaz, P. Riviere-Marichalar, A. Roberge, G. Sandell, E. Solano, I. Tilling, J. M. Torrelles, B. Vandenbusche, S. Vicente, G. J. White, and P. Woitke (2013). GASPS—A Herschel Survey of Gas and Dust in Protoplanetary Disks: Summary and Initial Statistics. *PASP*, **125**, pp. 477–505. doi:10.1086/670826.

Dong, R. and J. Fung (2017). What is the Mass of a Gap-opening Planet? *ApJ*, **835**(2), 146. doi:10.3847/1538-4357/835/2/146.

Dong, R., N. van der Marel, J. Hashimoto, E. Chiang, E. Akiyama, H. B. Liu, T. Muto, G. R. Knapp, T. Tsukagoshi, J. Brown, S. Bruderer, S. Koyamatsu, T. Kudo, N. Ohashi, E. Rich, M. Satoshi, M. Takami, J. Wisniewski, Y. Yang, Z. Zhu, and M. Tamura (2017). The Sizes and Depletions of the Dust and Gas Cavities in the Transitional Disk J160421.7-213028. *ApJ*, **836**(2), 201. doi:10.3847/1538-4357/aa5abf.

Dullemond, C. P. and C. Dominik (2004). The effect of dust settling on the appearance of protoplanetary disks. *A&A*, **421**, pp. 1075–1086. doi:10.1051/0004-6361:20040284.

Dullemond, C. P., D. Hollenbach, I. Kamp, and P. D'Alessio (2007). Models of the Structure and Evolution of Protoplanetary Disks. In Reipurth, B., D. Jewitt, and K. Keil (eds.) *Protostars and Planets V*, p. 555.

Duncan, M. J., H. F. Levison, and S. M. Budd (1995). The Dynamical Structure of the Kuiper Belt. *AJ*, **110**, p. 3073. doi:10.1086/117748.

Eisner, J. A., H. G. Arce, N. P. Ballering, J. Bally, S. M. Andrews, R. D. Boyden, J. Di Francesco, M. Fang, D. Johnstone, J. S. Kim, R. K. Mann, B. Matthews, I. Pascucci, L. Ricci, P. D. Sheehan, and J. P. Williams (2018). Protoplanetary Disk Properties in the Orion Nebula Cluster: Initial Results from Deep, High-resolution ALMA Observations. *ApJ*, **860**(1), 77. doi:10.3847/1538-4357/aac3e2.

Ercolano, B. and I. Pascucci (2017). The dispersal of planet-forming discs: theory confronts observations. *Royal Society Open Science*, **4**(4), 170114. doi:10.1098/rsos.170114.

Espaillat, C., J. Muzerolle, J. Najita, S. Andrews, Z. Zhu, N. Calvet, S. Kraus, J. Hashimoto, A. Kraus, and P. D'Alessio (2014). An Observational Perspective of Transitional Disks. In Beuther, H., R. S. Klessen, C. P. Dullemond, and T. Henning (eds.) *Protostars and Planets VI*, p. 497. doi:10.2458/azu_uapress_9780816531240-ch022.

Evans, A. (1994). *The dusty universe*.

Facchini, S., C. J. Clarke, and T. G. Bisbas (2016). External photoevaporation of protoplanetary discs in sparse stellar groups: the impact of dust growth. *MNRAS*, **457**(4), pp. 3593–3610. doi:10.1093/mnras/stw240.

Feiden, G. A. (2016). Magnetic inhibition of convection and the fundamental properties of low-mass stars. III. A consistent 10 Myr age for the Upper Scorpius OB association. *A&A*, **593**, A99. doi:10.1051/0004-6361/201527613.

Flock, M., J. P. Ruge, N. Dzyurkevich, T. Henning, H. Klahr, and S. Wolf (2015). Gaps, rings, and non-axisymmetric structures in protoplanetary disks. From simulations to ALMA observations. *A&A*, **574**, A68. doi:10.1051/0004-6361/201424693.

Foreman-Mackey, D., D. W. Hogg, D. Lang, and J. Goodman (2013a). emcee: The MCMC Hammer. *PASP*, **125**(925), p. 306. doi:10.1086/670067.

Foreman-Mackey, D., D. W. Hogg, D. Lang, and J. Goodman (2013b). emcee: The MCMC Hammer. *PASP*, **125**(925), p. 306. doi:10.1086/670067.

Frasca, A., K. Biazzo, J. M. Alcalá, C. F. Manara, B. Stelzer, E. Covino, and S. Antoniucci (2017). X-shooter spectroscopy of young stellar objects in Lupus. Atmospheric parameters, membership, and activity diagnostics. *A&A*, **602**, A33. doi:10.1051/0004-6361/201630108.

Gerbig, K., C. T. Lenz, and H. Klahr (2019). Linking planetesimal and dust content in protoplanetary disks via a local toy model. *A&A*, **629**, A116. doi:10.1051/0004-6361/201935278.

Gillon, M., E. Jehin, S. M. Lederer, L. Delrez, J. de Wit, A. Burdanov, V. Van Grootel, A. J. Burgasser, A. H. M. J. Triaud, C. Opitom, B.-O. Demory, D. K. Sahu, D. Bardalez Gagliuffi, P. Magain, and D. Queloz (2016). Temperate Earth-sized planets transiting a nearby ultracool dwarf star. *Nature*, **533**, pp. 221–224. doi:10.1038/nature17448.

Gillon, M., A. H. M. J. Triaud, B.-O. Demory, E. Jehin, E. Agol, K. M. Deck, S. M. Lederer, J. de Wit, A. Burdanov, J. G. Ingalls, E. Bolmont, J. Leconte, S. N. Raymond, F. Selsis, M. Turbet, K. Barkaoui, A. Burgasser, M. R. Burleigh, S. J. Carey, A. Chaushev, C. M. Copperwheat, L. Delrez, C. S. Fernandes, D. L. Holdsworth, E. J. Kotze, V. Van Grootel, Y. Almleaky, Z. Benkhaldoun, P. Magain, and D. Queloz (2017). Seven temperate terrestrial planets around the nearby ultracool dwarf star TRAPPIST-1. *Nature*, **542**, pp. 456–460. doi:10.1038/nature21360.

Greenwood, A. J., I. Kamp, L. B. F. M. Waters, P. Woitke, W.-F. Thi, C. Rab, G. Aresu, and M. Spaans (2017). Thermochemical modelling of brown dwarf discs. *ArXiv e-prints*.

Guieu, S., C. Dougados, J.-L. Monin, E. Magnier, and E. L. Martín (2006). Seventeen new very low-mass members in Taurus. The brown dwarf deficit revisited. *A&A*, **446**, pp. 485–500. doi:10.1051/0004-6361:20053493.

Guieu, S., C. Pinte, J.-L. Monin, F. Ménard, M. Fukagawa, D. L. Padgett, A. Noriega-Crespo, S. J. Carey, L. M. Rebull, T. Huard, and M. Guedel (2007).

On the circum(sub)stellar environment of brown dwarfs in Taurus. *A&A*, **465**, pp. 855–864. doi:10.1051/0004-6361:20066140.

Guilloteau, S., A. Dutrey, V. Piétu, and Y. Boehler (2011). A dual-frequency sub-arcsecond study of proto-planetary disks at mm wavelengths: first evidence for radial variations of the dust properties. *A&A*, **529**, A105. doi:10.1051/0004-6361/201015209.

Harvey, P. M., T. Henning, F. Ménard, S. Wolf, Y. Liu, L. A. Cieza, N. J. Evans, I. Pascucci, B. Merín, and C. Pinte (2012). A Herschel Search for Cold Dust in Brown Dwarf Disks: First Results. *ApJ*, **744**, L1. doi:10.1088/2041-8205/744/1/L1.

Harvey, P. M., D. T. Jaffe, K. Allers, and M. Liu (2010). A Spitzer Search for Planetary-mass Brown Dwarfs with Circumstellar Disks: Candidate selection. *ApJ*, **720**, pp. 1374–1379. doi:10.1088/0004-637X/720/2/1374.

Helled, R., P. Bodenheimer, M. Podolak, A. Boley, F. Meru, S. Nayakshin, J. J. Fortney, L. Mayer, Y. Alibert, and A. P. Boss (2014). Giant Planet Formation, Evolution, and Internal Structure. In Beuther, H., R. S. Klessen, C. P. Dullemond, and T. Henning (eds.) *Protostars and Planets VI*, p. 643. doi:10.2458/azu_uapress_9780816531240-ch028.

Herczeg, G. J. and L. A. Hillenbrand (2008). UV Excess Measures of Accretion onto Young Very Low Mass Stars and Brown Dwarfs. *ApJ*, **681**, 594-625. doi:10.1086/586728.

Howard, C. D., G. Sandell, W. D. Vacca, G. Duchêne, G. Mathews, J.-C. Augereau, D. Barrado, W. R. F. Dent, C. Eiroa, C. Grady, I. Kamp, G. Meeus, F. Ménard, C. Pinte, L. Podio, P. Riviere-Marichalar, A. Roberge, W.-F. Thi, S. Vicente, and J. P. Williams (2013). Herschel/PACS Survey of Protoplanetary Disks in Taurus/Auriga—Observations of [O I] and [C II], and Far-infrared Continuum. *ApJ*, **776**, 21. doi:10.1088/0004-637X/776/1/21.

Huang, J., S. M. Andrews, C. P. Dullemond, A. Isella, L. M. Pérez, V. V. Guzmán, K. I. Öberg, Z. Zhu, S. Zhang, X.-N. Bai, M. Benisty, T. Birnstiel, J. M. Carpenter, A. M. Hughes, L. Ricci, E. Weaver, and D. J. Wilner (2018). The Disk Substructures at High Angular Resolution Project (DSHARP). II. Characteristics of Annular Substructures. *ApJ*, **869**(2), L42. doi:10.3847/2041-8213/aaf740.

Ida, S., J. Larwood, and A. Burkert (2000). Evidence for Early Stellar Encounters in the Orbital Distribution of Edgeworth-Kuiper Belt Objects. *ApJ*, **528**, pp. 351–356. doi:10.1086/308179.

Isella, A., J. M. Carpenter, and A. I. Sargent (2009). Structure and Evolution of Pre-main-sequence Circumstellar Disks. *ApJ*, **701**, pp. 260–282. doi:10.1088/0004-637X/701/1/260.

Kamp, I., P. Woitke, C. Pinte, I. Tilling, W.-F. Thi, F. Menard, G. Duchene, and J.-C. Augereau (2011). Continuum and line modelling of discs around young stars. II. Line diagnostics for GASPS from the DENT grid. *A&A*, **532**, A85. doi:10.1051/0004-6361/201016399.

Keane, J. T., I. Pascucci, C. Espaillat, P. Woitke, S. Andrews, I. Kamp, W.-F. Thi, G. Meeus, and W. R. F. Dent (2014). Herschel Evidence for Disk Flattening or Gas Depletion in Transitional Disks. *ApJ*, **787**, 153. doi:10.1088/0004-637X/787/2/153.

Kelly, B. C. (2007). Some Aspects of Measurement Error in Linear Regression of Astronomical Data. *ApJ*, **665**, pp. 1489–1506. doi:10.1086/519947.

Kenyon, S. J. and B. C. Bromley (2004). Stellar encounters as the origin of distant Solar System objects in highly eccentric orbits. *Nature*, **432**, pp. 598–602. doi:10.1038/nature03136.

Klein, R., D. Apai, I. Pascucci, T. Henning, and L. B. F. M. Waters (2003). First Detection of Millimeter Dust Emission from Brown Dwarf Disks. *ApJ*, **593**, pp. L57–L60. doi:10.1086/377729.

Krijt, S., C. W. Ormel, C. Dominik, and A. G. G. M. Tielens (2015). Erosion and the limits to planetesimal growth. *A&A*, **574**, A83. doi:10.1051/0004-6361/201425222.

Lada, C. J. (1987). Star formation: from OB associations to protostars. In Peimbert, M. and J. Jugaku (eds.) *Star Forming Regions*, volume 115 of *IAU Symposium*, p. 1.

Lada, C. J. and B. A. Wilking (1984). The nature of the embedded population in the rho Ophiuchi dark cloud : mid-infrared observations. *ApJ*, **287**, pp. 610–621. doi:10.1086/162719.

Lauer, T. R., E. A. Ajhar, Y. I. Byun, A. Dressler, S. M. Faber, C. Grillmair, J. Kormendy, D. Richstone, and S. Tremaine (1995a). The Centers of Early-Type Galaxies with HST.I.An Observational Survey. *AJ*, **110**, p. 2622. doi:10.1086/117719.

Lauer, T. R., E. A. Ajhar, Y. I. Byun, A. Dressler, S. M. Faber, C. Grillmair, J. Kormendy, D. Richstone, and S. Tremaine (1995b). The Centers of Early-Type Galaxies with HST.I.An Observational Survey. *AJ*, **110**, p. 2622. doi:10.1086/117719.

Lenz, C. T., H. Klahr, and T. Birnstiel (2019). Planetesimal Population Synthesis: Pebble Flux-regulated Planetesimal Formation. *ApJ*, **874**(1), 36. doi:10.3847/1538-4357/ab05d9.

Liu, Y., V. Joergens, A. Bayo, M. Nielbock, and H. Wang (2015). A homogeneous analysis of disks around brown dwarfs. *A&A*, **582**, A22. doi:10.1051/0004-6361/201526153.

Long, F., G. J. Herczeg, D. Harsono, P. Pinilla, M. Tazzari, C. F. Manara, I. Pascucci, S. Cabrit, B. Nisini, D. Johnstone, S. Edwards, C. Salyk, F. Menard, G. Lodato, Y. Boehler, G. N. Mace, Y. Liu, G. D. Mulders, N. Hendler, E. Ragusa, W. J. Fischer, A. Banzatti, E. Rigliaco, G. van de Plas, G. Dipierro, M. Gully-Santiago, and R. Lopez-Valdivia (2019). Compact Disks in a High-resolution ALMA Survey of Dust Structures in the Taurus Molecular Cloud. *ApJ*, **882**(1), 49. doi:10.3847/1538-4357/ab2d2d.

Long, F., G. J. Herczeg, I. Pascucci, D. Apai, T. Henning, C. F. Manara, G. D. Mulders, L. Szűcs, and N. P. Hendler (2018). An ALMA Survey of Faint Disks in the Chamaeleon I Star-forming Region: Why Are Some Class II Disks so Faint? *ApJ*, **863**(1), 61. doi:10.3847/1538-4357/aacce9.

Luhman, K. L. (2000). The Initial Mass Function of Low-Mass Stars and Brown Dwarfs in Taurus. *ApJ*, **544**, pp. 1044–1055. doi:10.1086/317232.

Luhman, K. L. (2004). New Brown Dwarfs and an Updated Initial Mass Function in Taurus. *ApJ*, **617**(2), pp. 1216–1232. doi:10.1086/425647.

Luhman, K. L. (2008). *Chamaeleon*, p. 169.

Luhman, K. L., L. Adame, P. D'Alessio, N. Calvet, K. K. McLeod, C. J. Bohac, W. J. Forrest, L. Hartmann, B. Sargent, and D. M. Watson (2007). Hubble and Spitzer Observations of an Edge-on Circumstellar Disk around a Brown Dwarf. *ApJ*, **666**, pp. 1219–1225. doi:10.1086/520712.

Luhman, K. L., L. E. Allen, P. R. Allen, R. A. Gutermuth, L. Hartmann, E. E. Mamajek, S. T. Megeath, P. C. Myers, and G. G. Fazio (2008). The Disk Population of the Chamaeleon I Star-forming Region. *ApJ*, **675**, 1375-1406. doi:10.1086/527347.

Luhman, K. L., P. R. Allen, C. Espaillat, L. Hartmann, and N. Calvet (2010). The Disk Population of the Taurus Star-Forming Region. *ApJS*, **186**, pp. 111–174. doi:10.1088/0067-0049/186/1/111.

Luhman, K. L., C. Briceño, J. R. Stauffer, L. Hartmann, D. Barrado y Navascués, and N. Caldwell (2003). New Low-Mass Members of the Taurus Star-forming Region. *ApJ*, **590**, pp. 348–356. doi:10.1086/374983.

Luhman, K. L., E. E. Mamajek, P. R. Allen, and K. L. Cruz (2009). An Infrared/X-Ray Survey for New Members of the Taurus Star-Forming Region. *ApJ*, **703**, pp. 399–419. doi:10.1088/0004-637X/703/1/399.

Luhman, K. L., E. E. Mamajek, S. J. Shukla, and N. P. Loutrel (2017). A Survey for New Members of the Taurus Star-forming Region with the Sloan Digital Sky Survey. *AJ*, **153**, 46. doi:10.3847/1538-3881/153/1/46.

Luhman, K. L. and G. H. Rieke (1999). Low-Mass Star Formation and the Initial Mass Function in the ρ Ophiuchi Cloud Core. *ApJ*, **525**(1), pp. 440–465. doi:10.1086/307891.

Manara, C. F., D. Fedele, G. J. Herczeg, and P. S. Teixeira (2016). X-Shooter study of accretion in Chamaeleon I. *A&A*, **585**, A136. doi:10.1051/0004-6361/201527224.

Manara, C. F., M. Tazzari, F. Long, G. J. Herczeg, G. Lodato, A. A. Rota, P. Cazzoletti, G. van der Plas, P. Pinilla, G. Dipierro, S. Edwards, D. Harsono, D. Johnstone, Y. Liu, F. Menard, B. Nisini, E. Ragusa, Y. Boehler, and S. Cabrit (2019). Observational constraints on dust disk sizes in tidally truncated protoplanetary disks in multiple systems in the Taurus region. *A&A*, **628**, A95. doi:10.1051/0004-6361/201935964.

Manara, C. F., L. Testi, G. J. Herczeg, I. Pascucci, J. M. Alcalá, A. Natta, S. Antoniucci, D. Fedele, G. D. Mulders, T. Henning, S. Mohanty, T. Prusti, and E. Rigliaco (2017). X-shooter study of accretion in Chamaeleon I. II. A steeper increase of accretion with stellar mass for very low-mass stars? *A&A*, **604**, A127. doi:10.1051/0004-6361/201630147.

Martín, E. L., C. Dougados, E. Magnier, F. Ménard, A. Magazzù, J.-C. Cuillandre, and X. Delfosse (2001). Four Brown Dwarfs in the Taurus Star-Forming Region. *ApJ*, **561**, pp. L195–L198. doi:10.1086/324754.

Mathis, J. S., P. G. Mezger, and N. Panagia (1983). Interstellar radiation field and dust temperatures in the diffuse interstellar matter and in giant molecular clouds. *A&A*, **128**, pp. 212–229.

McMullin, J. P., B. Waters, D. Schiebel, W. Young, and K. Golap (2007a). *CASA Architecture and Applications*, volume 376 of *Astronomical Society of the Pacific Conference Series*, p. 127.

McMullin, J. P., B. Waters, D. Schiebel, W. Young, and K. Golap (2007b). CASA Architecture and Applications. In Shaw, R. A., F. Hill, and D. J. Bell (eds.) *Astronomical Data Analysis Software and Systems XVI*, volume 376 of *Astronomical Society of the Pacific Conference Series*, p. 127.

Merín, B., J. Jørgensen, L. Spezzi, J. M. Alcalá, I. Evans, Neal J., P. M. Harvey, T. Prusti, N. Chapman, T. Huard, E. F. van Dishoeck, and F. Comerón (2008). The Spitzer c2d Survey of Large, Nearby, Interstellar Clouds. XI. Lupus Observed with IRAC and MIPS. *ApJS*, **177**(2), pp. 551–583. doi:10.1086/588042.

Min, M., C. P. Dullemond, C. Dominik, A. de Koter, and J. W. Hovenier (2009). Radiative transfer in very optically thick circumstellar disks. *A&A*, **497**, pp. 155–166. doi:10.1051/0004-6361/200811470.

Mohanty, S., J. Greaves, D. Mortlock, I. Pascucci, A. Scholz, M. Thompson, D. Apai, G. Lodato, and D. Looper (2013). Protoplanetary Disk Masses from Stars to Brown Dwarfs. *ApJ*, **773**, 168. doi:10.1088/0004-637X/773/2/168.

Monin, J.-L., E. T. Whelan, B. Lefloch, C. Dougados, and C. Alves de Oliveira (2013). A molecular outflow driven by the brown dwarf binary FU Tauri. *A&A*, **551**, L1. doi:10.1051/0004-6361/201220973.

Morbidelli, A., H. F. Levison, and R. Gomes (2008). *The Dynamical Structure of the Kuiper Belt and Its Primordial Origin*, pp. 275–292.

Mordasini, C., Y. Alibert, W. Benz, H. Klahr, and T. Henning (2012). Extrasolar planet population synthesis . IV. Correlations with disk metallicity, mass, and lifetime. *A&A*, **541**, A97. doi:10.1051/0004-6361/201117350.

Mulders, G. D. and C. Dominik (2012). Probing the turbulent mixing strength in protoplanetary disks across the stellar mass range: no significant variations. *A&A*, **539**, A9. doi:10.1051/0004-6361/201118127.

Mulders, G. D., I. Pascucci, and D. Apai (2015). A Stellar-mass-dependent Drop in Planet Occurrence Rates. *ApJ*, **798**(2), 112. doi:10.1088/0004-637X/798/2/112.

Muto, T., C. A. Grady, J. Hashimoto, M. Fukagawa, J. B. Hornbeck, M. Sitko, R. Russell, C. Werren, M. Curé, T. Currie, N. Ohashi, Y. Okamoto, M. Momose, M. Honda, S. Inutsuka, T. Takeuchi, R. Dong, L. Abe, W. Brandner, T. Brandt, J. Carson, S. Egner, M. Feldt, T. Fukue, M. Goto, O. Guyon, Y. Hayano, M. Hayashi, S. Hayashi, T. Henning, K. W. Hodapp, M. Ishii, M. Iye, M. Janson, R. Kandori, G. R. Knapp, T. Kudo, N. Kusakabe, M. Kuzuhara, T. Matsuo, S. Mayama, M. W. McElwain, S. Miyama, J. I. Morino, A. Moro-Martin, T. Nishimura, T. S. Pyo, E. Serabyn, H. Suto, R. Suzuki, M. Takami, N. Takato, H. Terada, C. Thalmann, D. Tomono, E. L. Turner, M. Watanabe, J. P. Wisniewski, T. Yamada, H. Takami, T. Usuda, and M. Tamura (2012). Discovery of Small-scale Spiral Structures in the Disk of SAO 206462 (HD 135344B): Implications for the Physical State of the Disk from Spiral Density Wave Theory. *ApJ*, **748**(2), L22. doi:10.1088/2041-8205/748/2/L22.

Nakajima, Y., M. Tamura, Y. Oasa, and T. Nakajima (2000). A Near-Infrared Imaging Survey of the Lupus 3 Dark Cloud: A Modest Cluster of Low-Mass, Pre-Main-Sequence Stars. *AJ*, **119**(2), pp. 873–881. doi:10.1086/301222.

Olofsson, J., M. Benisty, J. C. Augereau, C. Pinte, F. Ménard, E. Tatulli, J. P. Berger, F. Malbet, B. Merín, E. F. van Dishoeck, S. Lacour, K. M. Pontoppidan, J. L. Monin, J. M. Brown, and G. A. Blake (2011). Warm dust resolved in the cold disk around T Chamaeleontis with VLTI/AMBER. *A&A*, **528**, L6. doi:10.1051/0004-6361/201016074.

Olofsson, J., M. Benisty, J. B. Le Bouquin, J. P. Berger, S. Lacour, F. Ménard, T. Henning, A. Crida, L. Burtscher, G. Meeus, T. Ratzka, C. Pinte, J. C. Augereau, F. Malbet, B. Lazareff, and W. Traub (2013). Sculpting the disk around T Chamaeleontis: an interferometric view. *A&A*, **552**, A4. doi:10.1051/0004-6361/201220675.

Ormel, C. W., B. Liu, and D. Schoonenberg (2017). Formation of TRAPPIST-1 and other compact systems. *A&A*, **604**, A1. doi:10.1051/0004-6361/201730826.

Ott, S. (2010). The Herschel Data Processing System — HIPE and Pipelines — Up and Running Since the Start of the Mission. In Mizumoto, Y., K.-I. Morita, and M. Ohishi (eds.) *Astronomical Data Analysis Software and Systems XIX*, volume 434 of *Astronomical Society of the Pacific Conference Series*, p. 139.

Pascucci, I., D. Apai, K. Luhman, T. Henning, J. Bouwman, M. R. Meyer, F. Lahuis, and A. Natta (2009). The Different Evolution of Gas and Dust in Disks around Sun-Like and Cool Stars. *ApJ*, **696**, pp. 143–159. doi:10.1088/0004-637X/696/1/143.

Pascucci, I., U. Gorti, and D. Hollenbach (2012). Free-Free Emission and Radio Recombination Lines from Photoevaporating Disks. *ApJ*, **751**(2), L42. doi:10.1088/2041-8205/751/2/L42.

Pascucci, I., G. D. Mulders, A. Gould, and R. Fernand es (2018). A Universal Break in the Planet-to-star Mass-ratio Function of Kepler MKG Stars. *ApJ*, **856**(2), L28. doi:10.3847/2041-8213/aab6ac.

Pascucci, I., L. Ricci, U. Gorti, D. Hollenbach, N. P. Hendler, K. J. Brooks, and Y. Contreras (2014). Low Extreme-ultraviolet Luminosities Impinging on Protoplanetary Disks. *ApJ*, **795**(1), 1. doi:10.1088/0004-637X/795/1/1.

Pascucci, I. and M. Sterzik (2009). Evidence for Disk Photoevaporation Driven by the Central Star. *ApJ*, **702**(1), pp. 724–732. doi:10.1088/0004-637X/702/1/724.

Pascucci, I., L. Testi, G. J. Herczeg, F. Long, C. F. Manara, N. Hendler, G. D. Mulders, S. Krijt, F. Ciesla, T. Henning, S. Mohanty, E. Drabek-Maunder, D. Apai, L. Szűcs, G. Sacco, and J. Olofsson (2016). A Steeper than Linear Disk Mass-Stellar Mass Scaling Relation. *ApJ*, **831**, 125. doi:10.3847/0004-637X/831/2/125.

Pascucci, I., S. Wolf, J. Steinacker, C. P. Dullemond, T. Henning, G. Niccolini, P. Woitke, and B. Lopez (2004). The 2D continuum radiative transfer problem. Benchmark results for disk configurations. *A&A*, **417**, pp. 793–805. doi:10.1051/0004-6361:20040017.

Pecaut, M. J., E. E. Mamajek, and E. J. Bubar (2012). A Revised Age for Upper Scorpius and the Star Formation History among the F-type Members of the Scorpius-Centaurus OB Association. *ApJ*, **746**(2), 154. doi:10.1088/0004-637X/746/2/154.

Pérez, L. M., A. Isella, J. M. Carpenter, and C. J. Chandler (2014). Large-scale Asymmetries in the Transitional Disks of SAO 206462 and SR 21. *ApJ*, **783**(1), L13. doi:10.1088/2041-8205/783/1/L13.

Petit, J.-M., J. J. Kavelaars, B. J. Gladman, R. L. Jones, J. W. Parker, C. Van Laerhoven, P. Nicholson, G. Mars, P. Rousselot, O. Mousis, B. Marsden, A. Bieryla, M. Taylor, M. L. N. Ashby, P. Benavidez, A. Campo Bagatin, and G. Bernabeu (2011). The Canada-France Ecliptic Plane Survey—Full Data Release: The Orbital Structure of the Kuiper Belt. *AJ*, **142**, 131. doi:10.1088/0004-6256/142/4/131.

Pilbratt, G. L., J. R. Riedinger, T. Passvogel, G. Crone, D. Doyle, U. Gageur, A. M. Heras, C. Jewell, L. Metcalfe, S. Ott, and M. Schmidt (2010). Herschel Space Observatory. An ESA facility for far-infrared and submillimetre astronomy. *A&A*, **518**, L1. doi:10.1051/0004-6361/201014759.

Pinilla, P., M. Benisty, T. Birnstiel, L. Ricci, A. Isella, A. Natta, C. P. Dullemond, L. H. Quiroga-Nuñez, T. Henning, and L. Testi (2014). Millimetre spectral indices of transition disks and their relation to the cavity radius. *A&A*, **564**, A51. doi:10.1051/0004-6361/201323322.

Pinilla, P., T. Birnstiel, M. Benisty, L. Ricci, A. Natta, C. P. Dullemond, C. Dominik, and L. Testi (2013). Explaining millimeter-sized particles in brown dwarf disks. *A&A*, **554**, A95. doi:10.1051/0004-6361/201220875.

Pinilla, P., M. Flock, M. d. J. Ovelar, and T. Birnstiel (2016a). Can dead zones create structures like a transition disk? *A&A*, **596**, A81. doi:10.1051/0004-6361/201628441.

Pinilla, P., L. Klarmann, T. Birnstiel, M. Benisty, C. Dominik, and C. P. Dullemond (2016b). A tunnel and a traffic jam: How transition disks maintain a detectable warm dust component despite the presence of a large planet-carved gap. *A&A*, **585**, A35. doi:10.1051/0004-6361/201527131.

Pinilla, P., N. van der Marel, L. M. Pérez, E. F. van Dishoeck, S. Andrews, T. Birnstiel, G. Herczeg, K. M. Pontoppidan, and T. van Kempen (2015). Testing particle trapping in transition disks with ALMA. *A&A*, **584**, A16. doi: 10.1051/0004-6361/201526655.

Poglitsch, A., C. Waelkens, N. Geis, H. Feuchtgruber, B. Vandenbussche, L. Rodriguez, O. Krause, E. Renotte, C. van Hoof, P. Saraceno, J. Cepa, F. Kerschbaum, P. Agnèse, B. Ali, B. Altieri, P. Andreani, J.-L. Augueres, Z. Balog, L. Barl, O. H. Bauer, N. Belbachir, M. Benedettini, N. Billot, O. Boulade, H. Bischof, J. Blommaert, E. Callut, C. Cara, R. Cerulli, D. Cesarsky, A. Contursi, Y. Creten, W. De Meester, V. Doublier, E. Doumayrou, L. Duband, K. Exter, R. Genzel, J.-M. Gillis, U. Grözinger, T. Henning, J. Herreros, R. Huygen, M. Inguscio, G. Jakob, C. Jamar, C. Jean, J. de Jong, R. Katterloher, C. Kiss, U. Klaas, D. Lemke, D. Lutz, S. Madden, B. Marquet, J. Martignac, A. Mazy, P. Merken, F. Montfort, L. Morbidelli, T. Müller, M. Nielbock, K. Okumura, R. Orfei, R. Ottensamer, S. Pezzuto, P. Popesso, J. Putzeys, S. Regibo, V. Reveret, P. Royer, M. Sauvage, J. Schreiber, J. Stegmaier, D. Schmitt, J. Schubert, E. Sturm, M. Thiel, G. Tofani, R. Vavrek, M. Wetzstein, E. Wieprecht, and E. Wiezorrek (2010). The Photodetector Array Camera and Spectrometer (PACS) on the Herschel Space Observatory. *A&A*, **518**, L2. doi:10.1051/0004-6361/201014535.

Pohl, A., E. Sissa, M. Langlois, A. Müller, C. Ginski, R. G. van Holstein, A. Vigan, D. Mesa, A. L. Maire, T. Henning, R. Gratton, J. Olofsson, R. van Boekel, M. Benisty, B. Biller, A. Boccaletti, G. Chauvin, S. Daemgen, J. de Boer, S. Desidera, C. Dominik, A. Garufi, M. Janson, Q. Kral, F. Ménard, C. Pinte, T. Stolker, J. Szulágyi, A. Zurlo, M. Bonnefoy, A. Cheetham, M. Cudel, M. Feldt, M. Kasper, A. M. Lagrange, C. Perrot, and F. Wildi (2017). New constraints on the disk characteristics and companion candidates around T Chamaeleontis with VLT/SPHERE. *A&A*, **605**, A34. doi:10.1051/0004-6361/201630234.

Preibisch, T., A. G. A. Brown, T. Bridges, E. Guenther, and H. Zinnecker (2002). Exploring the Full Stellar Population of the Upper Scorpius OB Association. *AJ*, **124**(1), pp. 404–416. doi:10.1086/341174.

Raymond, S. N., J. Scalo, and V. S. Meadows (2007). A Decreased Probability of Habitable Planet Formation around Low-Mass Stars. *ApJ*, **669**, pp. 606–614. doi:10.1086/521587.

Rebull, L. M., D. L. Padgett, C.-E. McCabe, L. A. Hillenbrand, K. R. Stapelfeldt, A. Noriega-Crespo, S. J. Carey, T. Brooke, T. Huard, S. Terebey, M. Audard, J.-L. Monin, M. Fukagawa, M. Güdel, G. R. Knapp, F. Menard, L. E. Allen, J. R. Angione, C. Baldovin-Saavedra, J. Bouvier, K. Briggs, C. Dougados, N. J. Evans, N. Flagey, S. Guieu, N. Grosso, A. M. Glauser, P. Harvey, D. Hines, W. B. Latter, S. L. Skinner, S. Strom, J. Tromp, and S. Wolf (2010). The Taurus Spitzer Survey: New Candidate Taurus Members Selected Using Sensitive Mid-Infrared Photometry. *ApJS*, **186**, pp. 259–307. doi:10.1088/0067-0049/186/2/259.

Ribas, Á., B. Merín, H. Bouy, and L. T. Maud (2014). Disk evolution in the solar neighborhood. I. Disk frequencies from 1 to 100 Myr. *A&A*, **561**, A54. doi: 10.1051/0004-6361/201322597.

Ricci, L., A. Isella, J. M. Carpenter, and L. Testi (2013). CARMA Interferometric Observations of 2MASS J044427+2512: The First Spatially Resolved Observations of Thermal Emission of a Brown Dwarf Disk. *ApJ*, **764**, L27. doi: 10.1088/2041-8205/764/2/L27.

Ricci, L., L. Testi, A. Natta, R. Neri, S. Cabrit, and G. J. Herczeg (2010). Dust properties of protoplanetary disks in the Taurus-Auriga star forming region from millimeter wavelengths. *A&A*, **512**, A15. doi:10.1051/0004-6361/200913403.

Ricci, L., L. Testi, A. Natta, A. Scholz, I. de Gregorio-Monsalvo, and A. Isella (2014). Brown Dwarf Disks with ALMA. *ApJ*, **791**, 20. doi:10.1088/0004-637X/791/1/20.

Riviere-Marichalar, P., B. Merín, I. Kamp, C. Eiroa, and B. Montesinos (2016). Herschel-PACS observations of far-IR lines in young stellar objects. I. [OI] and H_2O at 63 μm. *A&A*, **594**, A59. doi:10.1051/0004-6361/201527829.

Roccatagliata, V., G. G. Sacco, E. Franciosini, and S. Rand ich (2018). The double population of Chamaeleon I detected by Gaia DR2. *A&A*, **617**, L4. doi:10.1051/0004-6361/201833890.

Rosotti, G. P., R. A. Booth, M. Tazzari, C. Clarke, G. Lodato, and L. Testi (2019). On the millimetre continuum flux-radius correlation of proto-planetary discs. *MNRAS*, **486**(1), pp. L63–L68. doi:10.1093/mnrasl/slz064.

Ruge, J. P., M. Flock, S. Wolf, N. Dzyurkevich, S. Fromang, T. Henning, H. Klahr, and H. Meheut (2016). Gaps, rings, and non-axisymmetric structures in protoplanetary disks: Emission from large grains. *A&A*, **590**, A17. doi:10.1051/0004-6361/201526616.

Sacco, G. G., E. Flaccomio, I. Pascucci, F. Lahuis, B. Ercolano, J. H. Kastner, G. Micela, B. Stelzer, and M. Sterzik (2012). High-resolution Spectroscopy of

Ne II Emission from Young Stellar Objects. *ApJ*, **747**(2), 142. doi:10.1088/0004-637X/747/2/142.

Sacco, G. G., L. Spina, S. Randich, F. Palla, R. J. Parker, R. D. Jeffries, R. Jackson, M. R. Meyer, M. Mapelli, A. C. Lanzafame, R. Bonito, F. Damiani, E. Franciosini, A. Frasca, A. Klutsch, L. Prisinzano, E. Tognelli, S. Degl'Innocenti, P. G. Prada Moroni, E. J. Alfaro, G. Micela, T. Prusti, D. Barrado, K. Biazzo, H. Bouy, L. Bravi, J. Lopez-Santiago, N. J. Wright, A. Bayo, G. Gilmore, A. Bragaglia, E. Flaccomio, S. E. Koposov, E. Pancino, A. R. Casey, M. T. Costado, P. Donati, A. Hourihane, P. Jofré, C. Lardo, J. Lewis, L. Magrini, L. Monaco, L. Morbidelli, S. G. Sousa, C. C. Worley, and S. Zaggia (2017). The Gaia-ESO Survey: Structural and dynamical properties of the young cluster Chamaeleon I. *A&A*, **601**, A97. doi:10.1051/0004-6361/201629698.

Sawicki, M. (2012). SEDfit: Software for Spectral Energy Distribution Fitting of Photometric Data. *PASP*, **124**, p. 1208. doi:10.1086/668636.

Schaefer, G. H., A. Dutrey, S. Guilloteau, M. Simon, and R. J. White (2009). A Millimeter-wave Interferometric Study of Dust and CO Disks Around Late Spectral Type Stars in Taurus-Auriga. *ApJ*, **701**, pp. 698–709. doi:10.1088/0004-637X/701/1/698.

Shapiro, S. S. and M. B. Wilk (1965). An analysis of variance test for normality (complete samples)†. *Biometrika*, **52**(3-4), pp. 591–611. ISSN 0006-3444. doi:10.1093/biomet/52.3-4.591.

Slesnick, C. L., L. A. Hillenbrand, and J. M. Carpenter (2008). A Large-Area Search for Low-Mass Objects in Upper Scorpius. II. Age and Mass Distributions. *ApJ*, **688**(1), pp. 377–397. doi:10.1086/592265.

Soderblom, D. R., L. A. Hillenbrand, R. D. Jeffries, E. E. Mamajek, and T. Naylor (2014). Ages of Young Stars. In Beuther, H., R. S. Klessen, C. P. Dullemond, and T. Henning (eds.) *Protostars and Planets VI*, p. 219. doi:10.2458/azu_uapress_9780816531240-ch010.

Stamatellos, D. and A. P. Whitworth (2009). The role of thermodynamics in disc fragmentation. *MNRAS*, **400**(3), pp. 1563–1573. doi:10.1111/j.1365-2966.2009.15564.x.

Stassun, K. G., G. A. Feiden, and G. Torres (2014). Empirical tests of pre-main-sequence stellar evolution models with eclipsing binaries. *NewAR*, **60**, pp. 1–28. doi:10.1016/j.newar.2014.06.001.

Strom, K. M., S. E. Strom, S. Edwards, S. Cabrit, and M. F. Skrutskie (1989). Circumstellar Material Associated with Solar-Type Pre-Main-Sequence Stars: A

Possible Constraint on the Timescale for Planet Building. *AJ*, **97**, p. 1451. doi: 10.1086/115085.

Szűcs, L., D. Apai, I. Pascucci, and C. P. Dullemond (2010). Stellar-mass-dependent Disk Structure in Coeval Planet-forming Disks. *ApJ*, **720**, pp. 1668–1673. doi: 10.1088/0004-637X/720/2/1668.

Tazzari, M. (2017). mtazzari/uvplot: v0.1.1. doi:10.5281/zenodo.1003113.

Tazzari, M., F. Beaujean, and L. Testi (2018). GALARIO: a GPU accelerated library for analysing radio interferometer observations. *MNRAS*, **476**(4), pp. 4527–4542. doi:10.1093/mnras/sty409.

Tazzari, M., L. Testi, A. Natta, M. Ansdell, J. Carpenter, G. Guidi, M. Hogerheijde, C. F. Manara, A. Miotello, N. van der Marel, E. F. van Dishoeck, and J. P. Williams (2017). Physical properties of dusty protoplanetary disks in Lupus: evidence for viscous evolution? *A&A*, **606**, A88. doi:10.1051/0004-6361/201730890.

Terebey, S., F. H. Shu, and P. Cassen (1984). The collapse of the cores of slowly rotating isothermal clouds. *ApJ*, **286**, pp. 529–551. doi:10.1086/162628.

Testi, L., A. Natta, A. Scholz, M. Tazzari, L. Ricci, and I. de Gregorio Monsalvo (2016). Brown dwarf disks with ALMA: Evidence for truncated dust disks in Ophiuchus. *A&A*, **593**, A111. doi:10.1051/0004-6361/201628623.

Torres, R. M., L. Loinard, A. J. Mioduszewski, and L. F. Rodríguez (2007). VLBA Determination of the Distance to Nearby Star-forming Regions. II. Hubble 4 and HDE 283572 in Taurus. *ApJ*, **671**, pp. 1813–1819. doi:10.1086/522924.

Torres, R. M., L. Loinard, A. J. Mioduszewski, and L. F. Rodríguez (2009). VLBA Determination of the Distance to Nearby Star-Forming Regions. III. HP TAU/G2 and the Three-Dimensional Structure of Taurus. *ApJ*, **698**, pp. 242–249. doi: 10.1088/0004-637X/698/1/242.

Tripathi, A., S. M. Andrews, T. Birnstiel, and D. J. Wilner (2017a). A millimeter Continuum Size-Luminosity Relationship for Protoplanetary Disks. *ApJ*, **845**(1), 44. doi:10.3847/1538-4357/aa7c62.

Tripathi, A., S. M. Andrews, T. Birnstiel, and D. J. Wilner (2017b). A millimeter Continuum Size-Luminosity Relationship for Protoplanetary Disks. *ApJ*, **845**(1), 44. doi:10.3847/1538-4357/aa7c62.

Ubach, C., S. T. Maddison, C. M. Wright, D. J. Wilner, D. J. P. Lommen, and B. Koribalski (2012). Grain growth signatures in the protoplanetary discs of Chamaeleon and Lupus. *MNRAS*, **425**(4), pp. 3137–3161. doi:10.1111/j.1365-2966.2012.21603.x.

van Boekel, R., T. Henning, J. Menu, J. de Boer, M. Langlois, A. Müller, H. Avenhaus, A. Boccaletti, H. M. Schmid, C. Thalmann, M. Benisty, C. Dominik, C. Ginski, J. H. Girard, D. Gisler, A. Lobo Gomes, F. Menard, M. Min, A. Pavlov, A. Pohl, S. P. Quanz, P. Rabou, R. Roelfsema, J. F. Sauvage, R. Teague, F. Wildi, and A. Zurlo (2017). Three Radial Gaps in the Disk of TW Hydrae Imaged with SPHERE. *ApJ*, **837**(2), 132. doi:10.3847/1538-4357/aa5d68.

van der Marel, N., E. F. van Dishoeck, S. Bruderer, S. M. Andrews, K. M. Pontoppidan, G. J. Herczeg, T. van Kempen, and A. Miotello (2016). Resolved gas cavities in transitional disks inferred from CO isotopologs with ALMA. *A&A*, **585**, A58. doi:10.1051/0004-6361/201526988.

van der Plas, G., F. Ménard, K. Ward-Duong, J. Bulger, P. M. Harvey, C. Pinte, J. Patience, A. Hales, and S. Casassus (2016). Dust Masses of Disks around 8 Brown Dwarfs and Very Low-mass Stars in Upper Sco OB1 and Ophiuchus. *ApJ*, **819**, 102. doi:10.3847/0004-637X/819/2/102.

Wasserburg, G. J., A. I. Karakas, and M. Lugaro (2017). Intermediate-mass Asymptotic Giant Branch Stars and Sources of ^{26}Al, ^{60}Fe, ^{107}Pd, and ^{182}Hf in the Solar System. *ApJ*, **836**(1), 126. doi:10.3847/1538-4357/836/1/126.

Winter, A. J., C. J. Clarke, G. Rosotti, J. Ih, S. Facchini, and T. J. Haworth (2018). Protoplanetary disc truncation mechanisms in stellar clusters: comparing external photoevaporation and tidal encounters. *MNRAS*, **478**(2), pp. 2700–2722. doi:10.1093/mnras/sty984.

Woitke, P., I. Kamp, and W.-F. Thi (2009). Radiation thermo-chemical models of protoplanetary disks. I. Hydrostatic disk structure and inner rim. *A&A*, **501**, pp. 383–406. doi:10.1051/0004-6361/200911821.

Woitke, P., M. Min, C. Pinte, W.-F. Thi, I. Kamp, C. Rab, F. Anthonioz, S. Antonellini, C. Baldovin-Saavedra, A. Carmona, C. Dominik, O. Dionatos, J. Greaves, M. Güdel, J. D. Ilee, A. Liebhart, F. Ménard, L. Rigon, L. B. F. M. Waters, G. Aresu, R. Meijerink, and M. Spaans (2016). Consistent dust and gas models for protoplanetary disks. I. Disk shape, dust settling, opacities, and PAHs. *A&A*, **586**, A103. doi:10.1051/0004-6361/201526538.

Woitke, P., C. Pinte, I. Tilling, F. Ménard, I. Kamp, W.-F. Thi, G. Duchêne, and J.-C. Augereau (2010). Continuum and line modelling of discs around young stars - I. 300000 disc models for HERSCHEL/GASPS. *MNRAS*, **405**, pp. L26–L30. doi:10.1111/j.1745-3933.2010.00852.x.

Wright, E. L., P. R. M. Eisenhardt, A. K. Mainzer, M. E. Ressler, R. M. Cutri, T. Jarrett, J. D. Kirkpatrick, D. Padgett, R. S. McMillan, M. Skrutskie, S. A.

Stanford, M. Cohen, R. G. Walker, J. C. Mather, D. Leisawitz, T. N. Gautier, III, I. McLean, D. Benford, C. J. Lonsdale, A. Blain, B. Mendez, W. R. Irace, V. Duval, F. Liu, D. Royer, I. Heinrichsen, J. Howard, M. Shannon, M. Kendall, A. L. Walsh, M. Larsen, J. G. Cardon, S. Schick, M. Schwalm, M. Abid, B. Fabinsky, L. Naes, and C.-W. Tsai (2010). The Wide-field Infrared Survey Explorer (WISE): Mission Description and Initial On-orbit Performance. *AJ*, **140**, 1868-1881. doi:10.1088/0004-6256/140/6/1868.

Zhu, Z., R. P. Nelson, L. Hartmann, C. Espaillat, and N. Calvet (2011). Transitional and Pre-transitional Disks: Gap Opening by Multiple Planets? *ApJ*, **729**(1), 47. doi:10.1088/0004-637X/729/1/47.

Zinner, E. (2014). *Presolar Grains*, volume 1, pp. 181–213.